Multi-object Astronomical Spectroscopy with Optical Fibres

Frederick Garnett Watson

Doctor of Philosophy

University of Edinburgh

1987

Declaration

I hereby declare that this thesis is my own composition, and that the work reported in it is my own, except where it is clearly indicated otherwise. In those sections where collaborative work is reported, my contribution has been a substantial one; the extent of my contribution is fully documented in the text.

F G Watson
30 Apr 1987

Abstract

A full account is given of the relatively new astronomical technique of multi-object spectroscopy with optical fibre lightguides. The thesis begins with a survey of the number densities of a wide range of astronomical object classes, and, after comparing the merits of the various techniques for multi-object spectroscopy, shows (by defining the "effective aperture" of a multiple fibre-coupled telescope) that the multi-fibre technique is very well-suited to the real distribution of celestial objects.

A review of the properties of optical fibres is given, together with an exposition of the important considerations in the design of fibre feeds for astronomy. This is followed by a description of the requirements in the design of telescopes, spectrographs and detectors to render them suitable for the multi-fibre technique. Equations are derived for the performance of these systems in terms of signal-to-noise ratio, and an example is given.

A survey of the equipment that has been built for multi-fibre spectroscopy at observatories throughout the world is presented, and special attention is paid to the FOCAP fibre system at the 3.9-metre Anglo-Australian telescope. The thesis gives an example of the use of FOCAP in work carried out by the writer to investigate the kinematics of RR Lyrae variables in the nuclear bulge of the Galaxy. Evidence is found in the preliminary results for the existence of non-circular motions along the galactic centre line-of-sight.

A description is then given of the FLAIR wide-field fibre-coupled multi-object spectroscopy system built by the writer for the 1.2-metre UK Schmidt Telescope. Reports are presented on a series of observational programmes designed to test the system, including the classification of stars in the Chamaeleon dark cloud, spectroscopy of Orion cluster flare stars, spectroscopy of objects in the Large Magellanic Cloud, the measurement of galaxy redshifts, and the observation of quasar candidates. An experiment in time-resolved multi-object photometry is also described. It is shown that for spectroscopy, the prototype system will perform well on stellar targets to V~16-17, but, although galaxy redshifts have been obtained, its usefulness for the systematic measurement of redshifts is hampered by its low sensitivity in the blue region of the spectrum. An account is then given of the relatively simple steps needed to rectify this, together with a brief description of a proposed, fully-optimised FLAIR system.

Finally, the future prospects for multi-fibre astronomical spectroscopy are briefly reviewed, from the point of view of the new instrumentation becoming available, and the astronomical results that will be produced.

To Helen and Anna

Preface

The work reported in this thesis has been carried out, for the most part, during a tour of duty by the writer at the UK Schmidt telescope at Coonabarabran, Australia. The work has been done on a part-time basis, although much of it has also formed a part of the writer's duties at the telescope.

Work that is not original to the writer is fully referenced throughout the text, and the writer's role in the collaborative work described in Chapters 5 and 7 is fully documented. In addition to this, it may be noted that the early planning of a multi-fibre system for the UKST was carried out in collaboration with John Dawe.

It may be pointed out that no formal consistency has been maintained with regard to units, etc, where the terminology has been determined largely by the context. Some confusion may arise regarding the terminology used to describe the configuration in which plane diffraction gratings are used: the description "Ebert" is adopted when referring to any system where the incident and diffracted rays do not have the same azimuth with respect to the grating, even though a spectrograph using this configuration may not, technically, be an Ebert spectrograph.

Finally, references appear at the end of each chapter, while a list of abbreviations and acronyms, together with a full glossary of symbols, is given at the end of the thesis.

Acknowledgements

The success of the work described in this thesis owes much to the help given by a large number of people. First, it is a pleasure to thank my supervisors, Malcolm Longair, Russell Cannon and Don Morton, for their interest and encouragement throughout the period of the work. Second, I should like to thank all members of staff of the UK Schmidt Telescope Unit over the past four and a half years for their assistance with, and tolerance of the development of FLAIR. Much credit is due to John Dawe for recognising the potential of a wide-field multi-fibre system for the UKST in the first place, and to Eric Coyte for his expertise in turning vague ideas into solid metal. Other technical help at the UKST has come from Magnus Paterson, Colin Willcock, Ken Russell, Brian Plummer and Jack Gilligan. Assistance with FLAIR has also come from colleagues outside the UKST, and it is a particular pleasure to thank Peter Gray of the AAO. Valuable contributions have also been made by Ian McLean, David Malin, Ray Sharples, Paul Lindner and Steve Lee.

I thank my collaborators in the projects described in Chapter 7: Doug Whittet, Peter Bunclark, Brad Carter, Rich Robinson, David Morgan, Bruce

Peterson, and, in particular, Tom Shanks and Paddy Oates, without whom we would have no CCD. It is also a pleasure to thank Mike Breare, Nick Waltham, John Webster and Ian Parry for their work on the CCD system.

I owe a special debt of gratitude to Victor Clube, but for whom my first-hand experience of astronomical research would probably have remained within the confines of planetary motions. Our collaborative work on the galactic centre RR Lyrae stars was helped by many people, including Don Matthewson, John Alexander, David Carter, Richard Ellis, Gerry Gillmore, Tom Lloyd Evans, David Pike, Keith Taylor, Roger Clowes and members of UKSTU at ROE. Particular thanks are due to Paul Murdin, whose help in the early stages got the project off to a good start, and to Tony Weston, who has helped with the reduction of the latest data.

Finally, no words can express my gratitude to Trish McKenzie, without whose constant support, encouragement and help this thesis would not have become a reality.

Contents

Contents (continued)

Contents (continued)

List of Tables

"A good idea is worth more than a large telescope"

R O Redman

CHAPTER 1

Introduction: the role of multi-object spectroscopy.

1.1 Prologue: optical astronomy

Contemporary astrophysics is, perhaps, most succinctly characterised by its access to observational data from almost every region of the electromagnetic spectrum. Since the beginnings of radio astronomy in the 1940s, the invisible wavebands have been opened up for observation, one by one, by the arrival of new technologies such as Earth satellites, cryogenic solid-state infrared detectors and superconducting microwave devices. Similar advances have taken place in the particle astronomies, and it is immediately apparent that much of this progress has resulted from the application of technology not originally destined for astronomical research - a theme that will be seen to underlie the main topic of this thesis.

It goes without saying that optical astronomy predates every other branch of the science by a third of a millenium, even discounting the vast quantity of naked-eye data accumulated before Galileo applied Lippershey's new telescope to celestial observation. Yet, despite its antiquity, optical astronomy continues to make a vigorous contribution to modern astrophysics. There appear to be several reasons for this. Perhaps the most basic is

concerned with the temperatures at which we observe 'ordinary' matter in the Universe (Longair, 1985). Such material, at temperatures between 3,000 and 10,000 K, radiates in the optical waveband, so that optical observations remain of singular importance in building up the coherent picture of the Universe that is the ultimate aim of astrophysics.

Other, more circumstantial reasons exist. A recent review (Watson, 1980a) highlights the stimulus created by the new astronomies themselves (together with - again - the application of new technology to optical astronomy), so that discoveries in any region of the electromagnetic spectrum are likely to prompt optical observations. Longair (1982), reviewing the scientific prospects for the Hubble Space Telescope (HST), outlines a number of basic astrophysical questions under the headings of stellar evolution, star formation, the interstellar medium, galaxies, active galaxies and cosmology. In all these areas, the HST appears set to make a significant contribution and, while its useful wavelength range of 1100 to 11,000 Å (with first generation instruments) certainly embraces rather more than the usual definition of visible light, it is nevertheless basically an optical telescope. Separately, high sensitivity, high spatial resolution and high spectral resolution - all attributes of the HST - do not uniquely characterise optical observations. At radio wavelengths, for example, millijansky sensitivities are commonplace, very large aperture synthesis arrays are capable of resolving tenths of milliseconds of arc (far better than optical telescopes), while million-channel spectrum analysers are becoming operational. Rather, it appears to be the simultaneous combination of these that contributes to the continuing importance of optical astronomy: the information content per single optical observation remains

higher than that for other wavebands.

Optical astronomy from space is likely to produce some extremely valuable and spectacular results. However, it cannot fulfil all the requirements of optical observers. For example, the absence of seeing, low background intensity and optical excellence of the telescope mean that the HST will improve the quality of optical imaging by at least an order of magnitude. But with a limited field of a few minutes of arc, and running costs of the order of \$US 10^5 per hour (Illingworth, 1986), only a relatively small number of very high-priority objects will be observed. Much is still to be achieved by ground-based observation, as witnessed by the new generation of very large optical telescopes currently being planned. Observations well-suited to ground-based telescopes include spectroscopy of all but the faintest objects, high time-resolution observations and, returning to the topic of this thesis, observations of large numbers of objects. Clearly, therefore, in this exciting era of exploration of the Universe over the widest possible range of wavebands, there remains a place for the modern counterpart of Galileo's astronomy.

1.2 Astronomical spectroscopy

The generalized astronomical observation consists of a measurement of the intensity of electromagnetic radiation (or particle flux) as a function of direction, wavelength (or energy), polarization and/or time. In particular, the optical spectrum of an object is the intensity of the excess of radiation from the direction of that object over the background sky, measured as a function of wavelength in some range within the (approximate)

limits 3300 to 10,000 Å defined by the visible atmospheric transmission window at sea level (see Figure 1.1). This region of the electromagnetic spectrum is rich in atomic and certain molecular lines, and the optical spectrum of an object remains one of the most informative signatures of its true nature, its dynamical condition and, often, its environment.

Historically, the classification of celestial objects on the basis of their spectra (eg, Secchi, 1867; Vogel, 1874) and the first stellar radial velocity measurements (Huggins, 1868, 1872) marked the dawn of astrophysics. The remaining years of the 19th century were characterised by the identification of lines in the spectra of celestial objects, culminating in the discovery of helium. The subsequent paramount role of optical spectroscopy in astronomy resulted in a long series of major advances, and some well-known highlights, from 1900 to the present day, are shown in Table 1.1.

Although the table makes no claims of historical completeness, a number of general conclusions can be drawn. First, as might be expected, discoveries have often been made at the limits of sensitivity of the equipment of the time. Slipher's (1917) measurements of the redshifts of the objects then known as spiral nebulae, for example, required photographic exposure times of 20 to 40 hours per object with the Lowell 24-inch (0.6-m) refractor. (Slipher's paper presents measurements of the redshifts of 25 such nebulae!) Table 1.1 thus presents a picture based on observations of successively fainter objects. By contrast, there is no similar overall trend of increasing spectral resolution, some of the highest-dispersion observations figuring in the table being those made in the 1930s (eg, Minnaert and

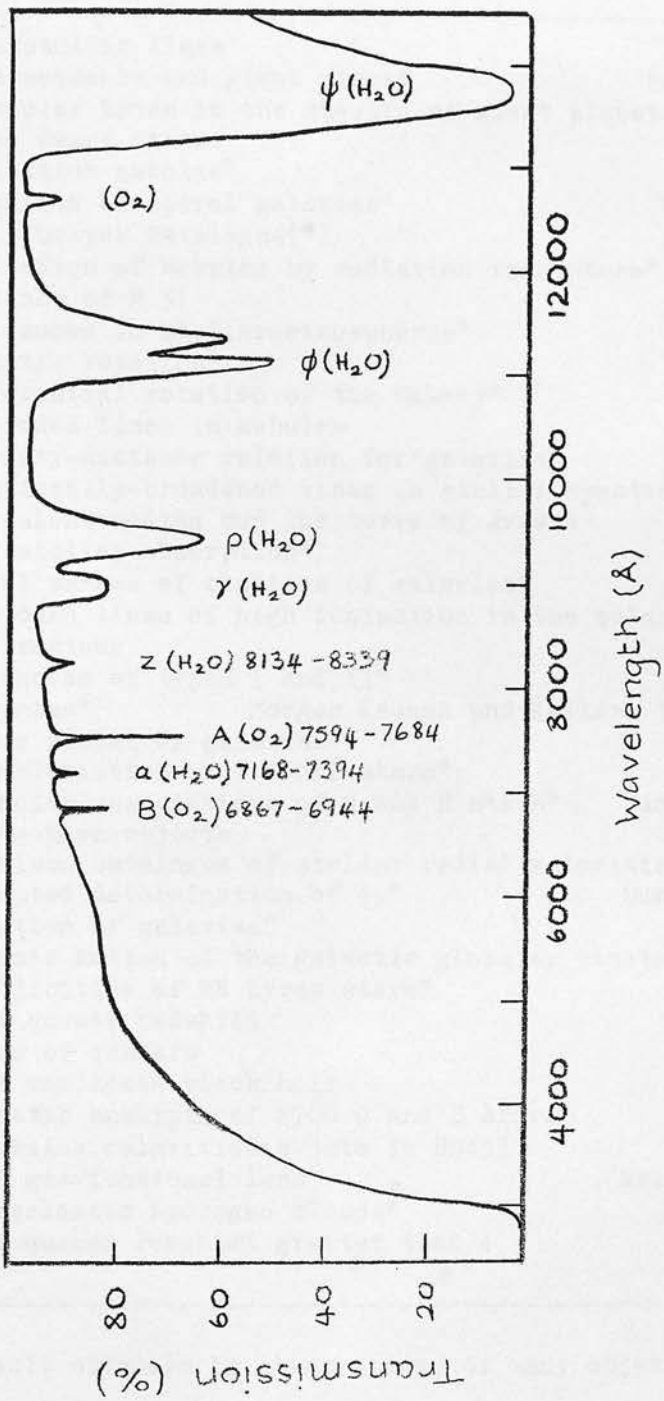

Figure 1.1 Atmospheric transmission at sea-level for an object at the zenith, as a function of wavelength. The blue cut-off is mainly due to scattering, while the near-infrared is dominated by absorption bands of O_2 and H_2O. The strength of the water-vapour features may vary significantly with time. (After Eccles, Sim and Tritton, 1983, p6; Allen, 1973, p129; Seitter, 1970)

Table 1.1 Some landmarks in astronomical spectroscopy since 1900

Interstellar lines	Hartmann 1904
Main sequence and giant stars*	Hertzsprung 1905; Russell 1914
Molecular bands in the spectra of giant planets	Slipher 1909; Dunham 1933
White dwarf stars	Adams 1914; 1915
Reflection nebulae*	Slipher 1916
Redshifts of spiral galaxies*	Slipher 1917
Henry Draper Catalogue(*)	Cannon and Pickering 1918-24
Excitation of nebulae by radiation from stars*	Hubble 1922
Distance of M 31	Opik 1922
Abundances in stellar atmospheres*	Payne 1925
Galactic rotation*	Lindblad 1925
Differential rotation of the Galaxy*	Oort 1927
Forbidden lines in nebulae	Bowen 1928
Velocity-distance relation for galaxies*	Hubble 1929
Rotationally-broadened lines in stellar spectra	Shajn and Struve 1929
Equivalent widths and the curve of growth	Minnaert and Mulders 1930
Interstellar absorption*	Trumpler 1930
Virial masses of clusters of galaxies*	Zwicky 1937
Forbidden lines of high ionisation in the solar corona	Grotrian 1939
H II regions	Struve and Elvey 1939
Supernovae of types I and II*	Minkowski 1941
MK system*	Morgan Keenan and Kellman 1943; Johnson and Morgan 1953
Active nuclei of galaxies*	Seyfert 1943
Characteristics of T Tauri stars*	Joy 1945
Expanding associations of O and B stars*	Ambartsumian 1949; Blaauw 1952
Herbig-Haro objects	Herbig 1951; Haro 1952
Mt Wilson catalogue of stellar radial velocities(*)	Wilson 1953
Attempted determination of q_o*	Humason Mayall and Sandage 1956
Evolution of galaxies*	Ambartsumian 1958
Systemic motion of the galactic globular clusters*	Kinman 1959
Metallicities of RR Lyrae stars*	Preston 1959
First quasar redshift	Schmidt 1963
Nature of quasars	Greenstein and Schmidt 1964
First candidate black hole	Webster and Murdin 1972
Kinematic analysis of 2700 O and B stars*	Balona and Feast 1974
Precessing relativistic jets in SS433	Margon et al. 1979
First gravitational lens	Walsh Carswell and Weymann 1979
Intergalactic hydrogen clouds*	Sargent et al. 1980
First quasar redshift greater than 4	Warren et al. 1987

* Result obtained by observations of many objects

Mulders, 1930; Dunham 1933). Sensitivity and spectral resolution are, of course, very closely related, but it is evident that, in recent times at least, the most far-reaching discoveries have not come from the highest dispersion work (1).

A second, and equally self-evident remark concerns the high proportion of investigations (indicated in the table) that have used observations of large numbers of objects. Attempts to measure some of the most basic parameters (eg Humason, Mayall and Sandage, 1956; Balona and Feast, 1974) have needed the spectra of several hundreds of objects, sometimes collected over very many years. In these two examples, the target objects are merely test particles used to explore basic trends, a method employed in much of astronomy and clearly underlining its fundamentally statistical nature.

All the above remarks may equally be applied to contemporary astronomical spectroscopy. The current thrust is, as ever, towards obtaining the spectra of yet fainter objects, and/or obtaining the spectra of large numbers of objects of specific type. Both these trends are particularly easy to understand in the light of present-day astrophysical problems. In our own Galaxy - the only representative galaxy whose structure, chemistry and evolution we can study in detail - some of the more interesting results are coming from objects remote from the solar neighbourhood, and therefore

---

(1) This general statement is in no degree intended to underrate the importance of modern high-dispersion spectroscopy, rather merely to indicate the overall picture.

faint. (Examples include the evolution of globular clusters (Cannon, 1982), the presence of a thick disc (Gilmore and Reid, 1983) and the possibility of systematic non-circular motions in the halo (Clube and Watson, 1979; Frenk and White, 1980).) Nearer, intrinsically faint objects are also important (eg, "brown dwarfs" (Hawkins, 1986), perhaps accounting for the hidden matter in galaxies). In extragalactic astronomy, the emphasis on faint objects is principally to provide long look-back times for studies like the determination of the cosmological parameters H_o and q_o, the study of the large-scale structure of the Universe (eg, Shanks et al., 1983), the evolution of normal and radio galaxies (eg, Longair, 1984; Peacock, 1985), active galaxies, the dynamics of clusters of galaxies, and so on. In addition, there are again faint, relatively nearby objects of interest (eg, dwarf galaxies; Zinnecker et al., 1985).

The need for observations of large samples in all these areas has also never been greater. Spectroscopic data sets, perhaps more than any others, are, in general, highly incomplete, and marred by selection effects of a variety of kinds. The most mundane of these arises simply because spectroscopy is expensive in telescope time, so that an investigator with only a limited allocation of that commodity will restrict his observations to those which promise to be the most productive. Objects that have been selected for observation on the basis of some attribute (eg, position, colour) thus have a second or third (and perhaps more arbitrary) selection criterion imposed upon them. The result is that collections of spectroscopic data are frequently strongly biassed towards the brighter end of any given magnitude range, and are often patchy throughout (2). It is not possible to carry out definitive studies in many of the areas mentioned above

---

(2) Again, this is not to denigrate the quality of major spectroscopic sur-

without well-defined, complete sets of good-quality spectroscopic data.

1.3 Multi-object spectroscopy and number densities

1.3.1 In recent years, a number of spectroscopic techniques have been developed which allow the simultaneous observation of several - sometimes very many - objects within the field of view of a single telescope, thus promising substantial gains in efficiency. The instrumental aspects of multi-object spectroscopy are introduced in the next section of this chapter, but it is first appropriate to examine the relevant characteristics of classes of celestial objects likely to be of interest, so as to be able to establish whether, in practice, there are advantages to be gained. The important parameters are those concerned with the distribution of objects on the sky: for any class of objects C, we require the number of objects A(m,C) at apparent magnitude m, per unit magnitude interval, per deg^2. A is usually a function of the direction of observation, (l,b), so that there may be large-scale variations over the sky. In certain cases, where objects are clumped or clustered, it may also be necessary to know the typical areal extent at a given number density.

---

veys (eg, the Henry Draper Catalogue (Cannon and Pickering, 1918-24) or the Mount Wilson-Palomar-Lick lists of galaxy redshifts (Humason, Mayall and Sandage, 1956)). However, completeness nearly always implies a relatively bright limiting magnitude (8.5 and 11.6 respectively in these two examples).

The quantity A is a differential number density and from it we can obtain the integrated number density N(m,C), the cumulative number of objects per deg^2 having apparent magnitudes less than or equal to m. Thus

$$N(m,C) = \int_{-\infty}^{m} A(m,C)\, dm. \qquad (1.1)$$

Both A and N are important parameters for multi-object spectroscopy. For a telescope with a field of view of area F deg^2, the product F.N(m,C) is indicative of the total number of target objects of type C which might be observed to a given limiting magnitude, m, while F.A(m,C)dm specifies the number of targets available with apparent magnitudes in the range m to m+dm - an important parameter when (as often happens) instrumental considerations dictate that objects with only a limited range of magnitudes be observed simultaneously.

We remark in passing that the apparent number density of celestial objects of a given type in a given direction (l,b) is, of course, a consequence of the space density $\nu(r,M,C)$ of objects of absolute magnitude M at heliocentric distances r along the line of sight (l,b), where ν is in objects per unit volume. It is usual to represent ν as the product of a relative density function D(r,C) in units of the local density, and a luminosity function $\phi(M,C)$ in objects per unit volume, so that

$$\nu(r,M,C)\, dMdV = \phi(M,C)dM\, D(r,C)dV \qquad (1.2)$$

where dM and dV are elemental increments of absolute magnitude and volume respectively. It is then straightforward to show that

$$A(m,C) = \omega\int_0^\infty \phi(m+5-5\log(r)-a(r),C)\ D(r,C)r^2dr \qquad (1.3)$$

where ω is a solid angle of one deg^2 ($=(\pi/180)^2$ steradians) and $a(r)$ is the absorption in magnitudes along the line of sight (see, eg, Mihalas and Binney, 1981, Section 4.2). This equation relates the observed magnitude distribution of objects to their true spatial and luminosity distributions, with the important proviso that the latter (the luminosity function, ϕ) is assumed to remain constant along the line of sight.

The observational determination of number densities has been of fundamental importance since the days of Herschel, and a considerable body of data exists in the literature (3). We restrict ourselves here to an account of the overall density characteristics of the main classes of object likely to be of spectroscopic interest. In some cases, specific areas of sky are discussed, and it should be borne in mind that not all the objects mentioned will be accessible to all ground-based telescopes.

1.3.2 Beginning with galactic objects, Figure 1.2 shows a logarithmic plot of the integrated number density $N(m,C')$ in the range m=4 to 21 for two classes, C', of stars distinguished only by their galactic latitude, b. The plots are given for both visual and photographic magnitudes, and their general features are very much in accordance with intuitive expectation.

---

(3) An important new review of star counts and their uses (Bahcall, 1986) has appeared since the bulk of this chapter was written.

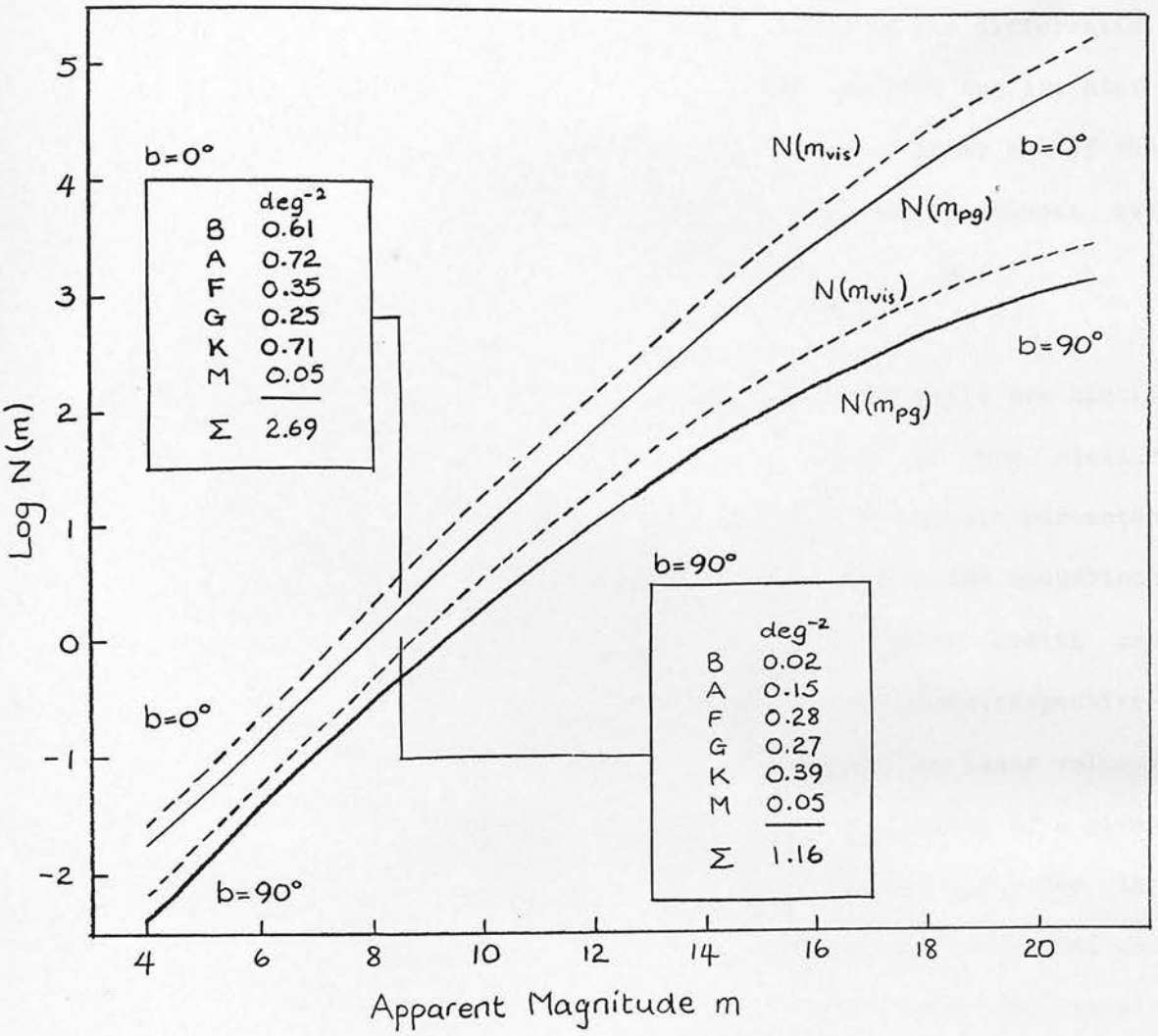

Figure 1.2 Integrated number densities of stars in the visible and photographic wavebands, plotted for the galactic equator and the galactic pole. The insets show the approximate distribution of number density with spectral type at the magnitude limit of the Henry Draper Catalogue. (Allen, 1973, p243; Nort, 1950)

In particular, N increases by a factor of three per magnitude at the brighter end of the range, falling to approximately two at the fainter end (2.3 for b=0 deg, 1.7 for b=90 deg). Also, the values of the differential number density, A (the derivative of N), for b=0 deg and b=90 deg are similar for bright stars (within a factor of 4), but at the fainter end of the range, the value of A for b=0 deg exceeds that for b=90 deg by almost two orders of magnitude.

From the point of view of multi-object spectroscopy, these plots are highly indiscriminate, but do indicate the overall limits of the stellar number-density distribution. For the moment, the only telescopic parameter we shall consider will be the field area F, and we remark for comparison that most telescopes have F in the range 1 to 40 deg^2. (These limits are typified by conventional reflectors and Schmidt-type telescopes respectively, and the distribution is very strongly biassed towards the lower value.) Thus it can be seen that a complete stellar spectroscopic survey of a given area of sky could be undertaken by multi-object techniques provided the limiting magnitude were approximately 8 or fainter - precisely what was accomplished in the objective-prism survey for the Henry Draper (HD) catalogue (see King, 1955, p. 294).

The insets to Figure 1.2 break down the integrated number density by spectral type at the magnitude limit of the HD catalogue, and reveal the large range in frequency for the various classes, from one object per 50 deg^2 for B stars at b=90 deg to one per 1.4 deg^2 for A stars at b=0 deg. The data show clearly that early-type stars are strongly concentrated to the galactic plane while (with the exception of K stars) the later spectral

types are not. Because we are sampling a distribution of space densities, $\nu(r,M,C)$, as discussed earlier, the relative proportions of different types, C, do not remain constant in the overall N(m,C') distribution plotted in Figure 1.2. It is from N(m,C) data (such as those presented in the insets), obtained over a range of magnitudes, m, that it is possible to solve Equation 1.3 for the density function D(r,C), given a knowledge of the luminosity function $\phi(M,C)$ and absorption a(r). If D(r,C) is expressed as a vertical density gradient D(z,C) (where z is distance above the galactic plane), we can conveniently summarize the relative concentrations of various types of object to the galactic plane in terms of a scale height $\beta(C)$, defined by

$$D(z,C) = D(0,C)\ \exp(-\frac{|z|}{\beta(C)}). \qquad (1.4)$$

Table 1.2 presents values of $\beta(C)$ for the main classes of star and several other galactic object classes, together with a total surface density

$$\Sigma(C) = \int_{-\infty}^{\infty} D(z,C)\ dz \qquad (1.5)$$

(tabulated logarithmically) to give some indication of their relative frequencies. Taking them in order of scale-height for convenience, we may now summarize the relevant properties of some of those object-classes in Table 1.2 which are likely to be of interest spectroscopically:

Classical cepheid variables. The General Catalogue of Variable Stars (GCVS) (Kukarkin et al., 1969) lists some 700 (galactic) stars of this type to an unspecified magnitude (in fact, approximately 15, with no indication

Table 1.2 Scale height β and surface density Σ for galactic objects (see text)

Object class C	$\beta(C)$ (pc)	$\log \Sigma(C)$ (pc^{-2})
O stars	50	-5.8
Classical cepheids	50	-5.1
B stars	60	-2.2
Open clusters	80	-
Interstellar dust and gas	120	-
A stars	120	-1.2
F stars	190	-0.2
Planetary nebulae	260	-
gK stars	270	-2.9
Novae	300	-
dG stars	340	0.3
dK stars	350	0.5
dM stars	350	1.3
gG stars	400	-1.2
White dwarfs	500	1.1
Long-period variables (M5-M8)	700	-
RR Lyrae variables (P<0.5 d)	900	-
Long-period variables (M0-M4)	1000	-
RR Lyrae variables (P>0.5 d)	2000	-
W Virginis variables (Pop II Cepheids)	2000	-
Subdwarfs	2000	-
Globular clusters	3000	-

(After Mihalas and Binney, 1981, p252)

of completeness). Given that their distribution in longitude is reasonably uniform (eg, Kraft, 1965) we infer an average number density of order 0.1 deg^{-2}, somewhat low to contemplate multi-object spectroscopy. Fernie and Hube (1968) have catalogued spectroscopic data for 162 galactic cepheids; radial velocities in particular are of value in studies of the internal kinematics of the Galaxy (eg, Crampton and Fernie, 1969).

OB stars. Likewise important for kinematic investigations (eg, Balona and Feast, 1974; Ovenden and Byl, 1976), these stars occur at the rate of one per 1.6 deg^2 in the galactic plane at a limiting magnitude of 8.5 (Figure 1.2). This limit (which is approximately the same as that of the radial-velocity catalogue of Balona and Feast (1974)) corresponds to an approximate distance of 2 kpc; the increase in N beyond this limit reflects the overall trend of Figure 1.2 (McCuskey, 1965). The distribution with magnitude of these stars is thus potentially favourable for multi-object spectroscopy and, given the uncertainties still remaining in fundamental quantities such as Oort's constant A (eg, Kerr and Lynden-Bell, 1986), much stands to be gained. (It should be noted, however, that for kinematic studies of this kind, reasonably uniform coverage in galactic longitude is required; also, much of the remaining uncertainty in the galactic constants is due to uncertainties in the distances of the test-objects themselves, which are, at most, only partially determined by spectroscopic observations (eg, Balona and Crampton, 1974).) In addition to the early-type stars in the field, there are also some 50 known O-associations containing up to 1000 stars (Allen, 1973, p. 277) and representing significant local increases in number-density.

Approximately 1000 open clusters are known in the Galaxy, containing a wide range of star-types for which spectroscopic data are of interest. Because of their widely varying distances and, to a lesser extent, their differing linear sizes, open clusters present a range of number densities (Allen, 1973, p278). At large distances (of order 2kpc) are M 103 (having N=2700 stars deg^{-2}, but extending over only 0.011 deg^2) and h Persei (with 2100 stars deg^{-2} extending over 0.14 deg^2). The mean visual magnitude of stars in both these clusters is approximately 10.5. Nearer clusters include the Pleiades (38 stars deg^{-2} spread over 3.1 deg^2) and the Hyades (2.9 stars deg^{-2} over 35 deg^2). The mean visual magnitude in these clusters is about 6. Clearly, there is potential for carrying out multi-object spectroscopy in open clusters, though telescopic field size and cluster angular diameter may be matched for only a limited number of targets.

Coupled with the star-forming regions of dust and gas (Table 1.2) are T-associations, rich in T Tauri variables and presenting an opportunity to study objects in a very early, pre-main-sequence phase. Typical number densities range from N=5 deg^{-2} (in the Gum nebula at 400 pc; Pettersson, 1986) to 18 deg^{-2} (Chamaeleon dark cloud at 140 pc; Whittet et al., 1987), with an approximate magnitude limit of 16. The areas surveyed for T Tauri stars in these two examples were about 2 and 3 deg^2 respectively. Also of interest in the study of such regions of nebulosity is the spectroscopic investigation of background field stars, to determine reddening parameters for the intervening dust cloud, for example. The obscuration reduces the values of N expected from Figure 1.2 to a level comparable with the T Tauri stars themselves. Some star-forming regions contain cluster-type flare stars, which provide a unique opportunity to study chromospheric activity

in young, late-type stars (see, eg, Ambartsumian and Mirzoyan, 1975; Haro, 1976; Mirzoyan, 1984). Time-resolved multi-object spectroscopy of samples of these stars is a particularly attractive proposition. Some 1200 cluster-type flare stars are known, with over 450 occurring in Orion, where N exceeds 20 deg^{-2} (to an approximate V magnitude of 19) in the region of M42 (Haro, 1968; Mirzoyan, 1984).

A stars account for 27 per cent of the total number of objects in the HD catalogue, making them the second most common type of star at the HD magnitude limit (Shapley and Cannon, 1924). Like the OB stars, their number density shows the increasing trend of Figure 1.2, making them suitable targets for multi-object spectroscopy. The space-motions of brighter A stars show kinematic structure in the solar neighbourhood (eg, Eggen's (1963) moving groups); similarly coherent localized motions at greater distances can be expected in the radial velocities of fainter A stars.

The distribution of galactic planetary nebulae is presented in detail by Perek and Kohoutek (1967) and shows a strong concentration towards the galactic centre, where number densities up to 4 deg^{-2} at R~16 are found. Spectroscopic data exist for a substantial fraction of known galactic planetaries, though radial velocities remain more sparse (33 per cent in the Perek and Kohoutek catalogue) and, towards the galactic centre, are a possible application for multi-object spectroscopy.

Of the remaining types of common stars in Table 1.2, the most numerous are the M dwarfs, with a luminosity function that peaks with a value of $\sim 2 \times 10^{-2}$ pc^{-3} (the highest of any star type) at approximately $M_B = 15.7$, and

falls for fainter absolute magnitudes (Luyten, 1968). The suspicion that this peak value underestimates the total number of M dwarfs (Sanduleak, 1976) has been demonstrated to be unlikely (eg, by Reid and Gilmore, 1982), but Hawkins (1986) has recently raised the exciting possibility that the luminosity function begins to increase again for fainter magnitudes (specifically for $M_R \gtrsim 15$). This has significant implications for our understanding of the dynamics of the Galaxy (perhaps suggesting a very large and almost invisible population of "brown dwarfs"), and spectroscopy of these cool, extremely red stars is clearly desirable. The number densities are sufficiently high to contemplate multi-object spectroscopy; using relatively simple methods, Hawkins (1986) measured 7 stars deg^{-2} later than M0 (on the basis of their R-I colour) to be within 80 pc at a limiting apparent magnitude of R=20. Some credence is lent to the possibility of the existence of a large population of very faint stars by the extension to the stellar number density distribution (Figure 1.2) shown in Figure 1.3. These number counts, obtained by machine analysis of deep plates, show a marked increase for stars with (photographic) magnitudes fainter than about 22. It should be noted, however, that there is nothing in the data of Figure 1.3 to distinguish these objects from faint quasars.

Turning now to objects in the galactic halo (ie, having $\beta \gtrsim 1$ kpc in Table 1.2), the RR Lyrae stars are, in general, distributed at a relatively low number density. The GCVS lists approximately 4400 spread over the whole sky representing a mean number density of 0.1 deg^{-2}, although this value is artificially low because of the incompleteness of the catalogue. (Deep surveys at high galactic latitudes reveal a substantially larger number: eg, N=0.4 stars deg^{-2} to B=17 in a survey for a-type RR Lyraes near the NGP

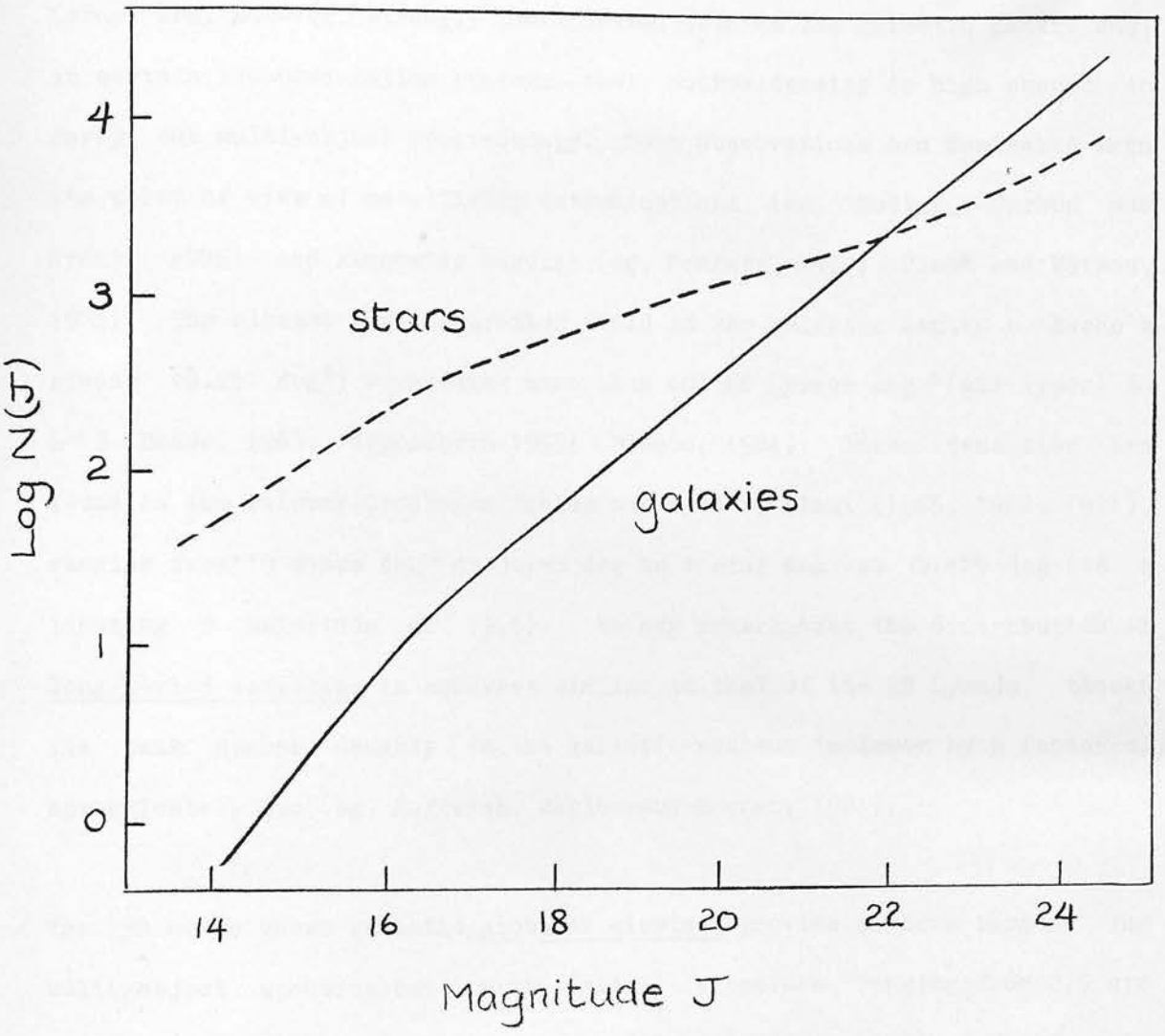

Figure 1.3 Integrated number densities of stars and galaxies to limiting (photographic) magnitude J, scaled to the north galactic pole (from Tyson and Jarvis, 1979). The data were obtained by digitizing KPNO 4-metre telescope plates of nine selected areas (each 37.2 arcmin square) with a PDS machine, using image detection and classification software to obtain the number counts. Similar results in good agreement have been presented by Peterson et al. (1979) (stars and galaxies), Ellis (1980) and Karachentsev (1980) (galaxies only), and more recently by Ellis (1986) and Koo (1986).

(Kinman, Wirtanen and Janes, 1966); N=1.5 stars deg^{-2} to B=21 in the south galactic cap (Hawkins, 1984; see also Stobie, Bishop and King, 1986).) RR Lyraes are, however, strongly concentrated towards the galactic centre and, in certain low-obscuration regions, their number density is high enough to carry out multi-object spectroscopy. Such observations are desirable from the point of view of metallicity determinations (eg, Butler, Carbon and Kraft, 1976) and kinematic studies (eg, Rodgers, 1977; Clube and Watson, 1978). The closest low-obscuration field to the galactic centre - Baade's window (0.25 deg^2) - contains more than 400 RR Lyraes deg^{-2} (all types) to B=19 (Baade, 1963; Gaposchkin 1955; Blanco, 1984); lower densities are found in the Palomar-Groningen fields surveyed by Plaut (1966, 1968, 1971), ranging from 19 stars deg^{-2} at $|b|=8$ deg to 1 star deg^{-2} at $|b|=29$ deg (to a limiting B magnitude of 19.5). We may remark that the distribution of long-period variables is somewhat similar to that of the RR Lyraes, though the peak number density in the galactic nucleus is lower by a factor of approximately two (eg, Hartwick, Barlow and Hesser, 1981).

The 130 or so known galactic globular clusters provide obvious targets for multi-object spectroscopy, with (tidal) diameters ranging from 2.5 arc minutes (Pal 13) to almost two degrees (ωCen) (Madore, 1980), and extremely high star densities (eg, King, 1980). For example, variable stars alone (90 per cent of which are RR Lyraes) may have densities of many hundreds per deg^2. (M62 has ~900 variables deg^{-2} at approximately V=16 (Sawyer-Hogg, 1973).) Spectroscopic studies of globular cluster members yield a wealth of data on stellar evolution, abundances and dynamics (see, eg, Hanes and Madore, 1980, Chapters 3, 4, 5, 14 and 20); of particular interest also are the globular clusters that have been identified as X-ray sources.

Finally, a number of relatively rare objects, which are clearly not suitable for multi-object observation, exists in the Galaxy. Mention might be made of pulsars (only two known to radiate at optical wavelengths), novae (sporadic) and, at a less exotic level, the 159 known galactic Wolf-Rayet stars (Hidayat, Supelli and van der Hucht, 1982) and certain rare classes of variable stars such as short-period Population II cepheids (BL Her stars), which may be expected to occur at a rate of one per 100 RR Lyrae stars (Watson, 1980b). Unless they are incorporated within samples of other, more numerous objects, there is no possibility of observing any of these by multi-object methods.

1.3.3 From the point of view of multi-object spectroscopy, extra-galactic objects fall into two categories: those near enough to allow the observation of individual targets within them, and those for which only the integrated properties may be observed. This division is clearly not a fundamental one, and will depend on instrumental parameters such as telescope plate scale and the size of the sampling aperture, but it is convenient for the present discussion on number densities.

Beginning with the former category, the Magellanic clouds are the Galaxy's closest companions (LMC 51 kpc; SMC 58 kpc (Stothers, 1983)) and, while the objects within them may have similar space densities to their galactic counterparts, the effect of their distance is obviously an increase in number densities with a corresponding (numerical) increase in apparent magnitudes. Furthermore, since the thickness of each cloud is small compared with its distance, the number-density distribution of any given class of objects mimics its luminosity function.

Confining our remarks mainly to the LMC for brevity, we note first that the total integrated stellar luminosity function $\phi(M_v)$ (where ϕ is the number of stars with absolute magnitude brighter than M_v) is given approximately by

$$\log \phi(M_v) = 6.3 + 0.5M_v \qquad (1.6)$$

in the range V = 9.0 to 17.0 (ie, M_v= -9.5 to -1.5; see Hodge and Wright, 1967; Stothers, 1983). This resembles the luminosity function of Population I stars in the Galaxy, and those of other nearby galaxies (Freedman, 1986). If the LMC is assumed to occupy approximately 80 deg^2 (Hodge and Wright, 1967), the luminosity function may be compared, as an apparent number-density distribution, with Figure 1.2. (See also the star counts by Brück, 1984.) It may be noted that spectroscopic catalogues comparable in quality to the HD catalogue and containing many LMC stars do already exist (eg, Rousseau et al. 1978).

The LMC contains a large number (>2000) of known variable stars, of which the largest population are classical cepheids. The number densities of these objects can exceed 200 deg^{-2} to magnitude 18 (Feast, 1984). RR Lyraes have also been found (in the vicinity of LMC clusters) at a density of 100 deg^{-2} at V=19.2 (Graham, 1984); both these classes of LMC variables play a major role in the determination of the extragalatic distance scale, and are important candidates for spectroscopy. Long-period variables occur at up to 100 deg^{-2}.

The star clusters found in the Magellanic Clouds do not fall readily into the "open" and "globular" categories found in the Galaxy. Of the 1200 or

so clusters in the LMC (Hodge and Wright, 1967), only 17 are identified by Harris and Racine (1979) as having the characteristics of galactic globular clusters. A population of blue (young) globular clusters also exists. Radial velocity data on all these objects are extremely sparse, and they are clearly suitable for multi-object observations.

Some 400 HII regions populate the LMC (Hodge and Wright, 1967), together with approximately 130 unresolved planetary nebulae (Sanduleak, 1984) which have objective prism excitation classes (Morgan, 1984) but again, for the most part, no radial velocities. Other emission-line objects for which slit spectroscopy is desirable include some 80 Wolf-Rayet stars (Fehrenbach, Duflot and Acker, 1976).

Turning now to the other members of the Local Group, all these objects are near enough (within some 600 kpc) for their brighter members, at least, to be resolved and, as with the Magellanic Clouds, all are relatively compact as seen from the Galaxy, so that the number densities of individually-resolved objects are high. The similarity of their luminosity functions (Freedman, 1986) has already been remarked upon. Many classes of object of spectroscopic interest are seen in the large (~10 deg^2) spiral M31 including supergiants, cepheid variables, open clusters, HII regions, RR Lyrae variables and some 300 globular clusters (Sargent et al., 1977). While all these objects are faint (to ~20th magnitude), they do lend themselves to multi-object methods. Likewise with other Local Group members; for example, M33 and the dwarf ellipticals NGC 147, 185 and 205 each contain half a dozen or so known globular clusters (typically 17-18th magnitude) with almost no spectroscopic data (Harris and Racine, 1979).

The nearby dwarf spheroidal galaxies (eg, Carina, Sculptor) occupy typically ~1 deg^2, and are rich in population II objects. There is interest in K giants (eg, Armandroff and Da Costa, 1986), RR Lyraes (eg, Zinn, 1980, and references therein) and carbon stars (eg, Lynden-Bell, Cannon and Godwin, 1983) in these systems and, since previous spectroscopy has hinted at anomalous mass-to-light ratios, there is much scope for further work.

Beyond the Local Group, many other nearby galaxies contain objects which might be considered as candidates for multi-object spectroscopy. Cepheids can be seen in some 30 galaxies to roughly 6 Mpc (corresponding to V~23) and supergiants in galaxies to about 25 Mpc. HII regions can be resolved to somewhat greater distances. Perhaps the most numerous discrete objects encountered in these galaxies are globular clusters, present in a large number of moderately nearby galaxies (Harris and Racine, 1979). The Virgo cluster is particularly rich in known globular cluster systems with seven galaxies known to have more than 100 globulars, and two with more than 1000. The B magnitudes of these objects lie in the range 21 to 23 (Hanes, 1980) and their number densities are in excess of 1000 deg^{-2}.

1.3.4. Considering now the distribution of galaxies themselves, we return to Figure 1.3 which presents machine-analysed integrated number densities to (integrated magnitude) J=24. The salient features of the galaxy number density distribution are that it is linear from about J=17, with a slope of 0.41 (equivalent to a factor of 2.6 increase in N per magnitude), that it exceeds the number density distribution of stars from J=22, and that its maximum value of 17100 deg^{-2} at J=24 (Tyson and Jarvis, 1979) corresponds to a mean (ie, unclustered) separation of galaxies of only ~30 arcsec (see

also Jarvis and Tyson, 1981). It may be noted that the observed number-density distribution is a consequence of a galaxy luminosity function (see, eg, Schechter, 1976) as described in Section 1.3.1, and also that its shape is influenced by the rate of galaxy luminosity evolution (Brown and Tinsley, 1974) and, at the fainter end of Figure 1.3, by the cosmological deceleration parameter q_o (Sandage, 1961a; Peebles, 1980). The study of galaxy number counts, especially in more than one colour (eg Shanks et al., 1984), is thus a useful end in itself and ranks in importance with the extension of the Hubble diagram. It may also provide data on the isotropy of the Universe.

Complete spectroscopic surveys, particularly for redshifts, have been and are being undertaken already. The Mount Wilson-Palomar-Lick survey (Humason, Mayall and Sandage, 1956) has already been mentioned; the most important contemporary survey is the Harvard-Smithsonian Center for Astrophysics (CfA) survey (Huchra et al, 1983) which is complete to B=14.5 in the (unobscured) northern sky. It may be noted from Figure 1.3 that it is only beyond this magnitude limit that multi-object techniques begin to become practicable. Clusters of galaxies represent local increases of number density above the mean value, and their suitability for multi-object spectroscopy at a given limiting magnitude is thus enhanced. Clustering occurs over a wide range of scales; discussion of its investigation using the two-point correlation function is beyond the scope of this work, but we remark that the technique may be applied in three dimensions (using redshifts) as well as two (using only position on the sky), thus providing additional motivation for complete redshift surveys (eg, Shanks et al., 1983).

Turning now to the characteristics of specific galaxy types, we present in Figure 1.4 the apparent mix of normal galaxies with limiting J magnitude. (Note that at the brighter limit of the Hubble Atlas of Galaxies (Sandage, 1961b), the mix is E:SO:S:Irr = 13:22:62:3.) It will be seen that, at faint limiting magnitudes, the distribution is dominated by late-type spirals. The true mix at a given redshift, a consequence of the sum of the luminosity functions for each type, is not known with certainty (Ellis, 1980).

The properties of active galaxies are presented in a comprehensive review by Osterbrock and Mathews (1986). Optical activity in galactic nuclei is seen on a wide variety of levels, ranging from that commonly seen (eg, Keel, 1983) in spiral galaxies (HII region galaxies (French, 1980), starburst galaxies (Balzano, 1983) and liners (low-ionization nuclear emission-line regions; Heckman, 1980)) to rarer Seyfert 1 galaxies and quasars. The lists of galaxies with a UV continuum published by Markarian from objective-prism surveys with the 1-metre Byurakan Schmidt (for references see, eg, Weedman, 1977) have proved to contain many emission-line galaxies of a wide range of types. The Markarian galaxies have number densities of $\sim$1 deg^{-2} at B$\sim$16, and the type is estimated to comprise 10 percent of all galaxies with $M_B > -21$ (Huchra and Sargent, 1973). French (1980) estimates that 70 percent of Markarians are HII region galaxies, and Huchra (1977) estimates that 85 percent require only stars and hot gas ionized by stars (ie, no nonthermal sources) to produce the observed emission features. Starburst galaxies are thus also part of this large fraction. More recent work (eg, Diaz, Pagel and Wilson, 1985) suggests that up to one third of all galaxies are liners, which may form a continuous sequence with the Seyferts. It is clear from the foregoing that these low-excitation

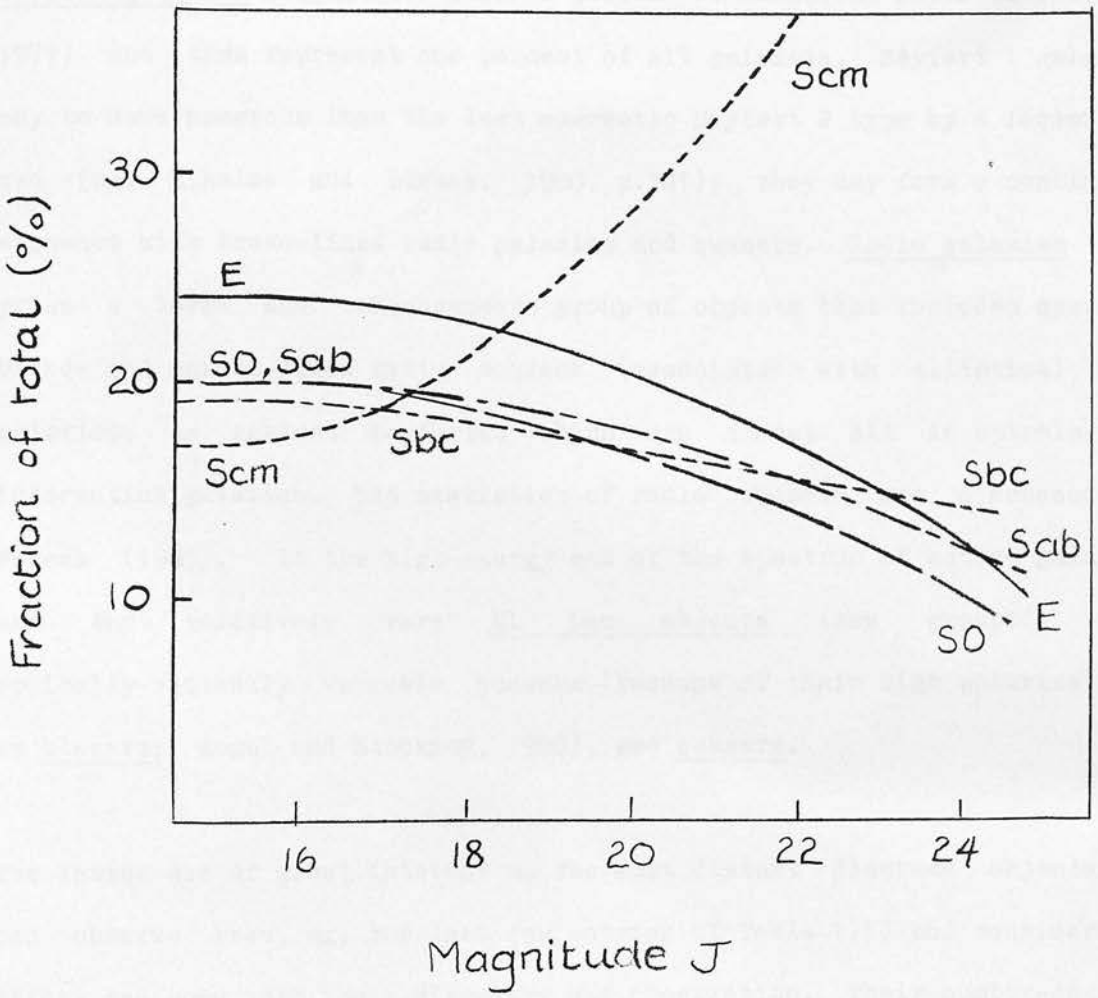

Figure 1.4 Apparent mix of galaxy types with limiting J magnitude (from Ellis, 1980; no source quoted).

nuclear emission objects are themselves closely related.

Seyfert galaxies account for some 10 percent of Markarian galaxies (Huchra, 1977) and thus represent one percent of all galaxies. Seyfert 1 galaxies may be more numerous than the less energetic Seyfert 2 type by a factor of two (eg, Mihalas and Binney, 1980, p.301); they may form a continuous sequence with broad-lined radio galaxies and quasars. Radio galaxies comprise a large and inhomogeneous group of objects that includes quasars, broad- and narrow-lined radio sources (associated with elliptical host galaxies, as against Seyferts, which are almost all in spirals) and interacting galaxies. The statistics of radio objects are discussed by Porcas (1985). At the high-energy end of the spectrum of active galaxies are the relatively rare BL Lac objects (now grouped with optically-violently variable quasars (because of their high polarization) as blazars; Angel and Stockman, 1980), and quasars.

The latter are of great interest as the most distant discrete objects we can observe (see, eg, the last few entries of Table 1.1) and considerable effort has gone into their discovery and observation. Their number-density distribution is thus reasonably well-known, and we show in Figure 1.5 the number counts of quasars discovered by one particular technique (stellar images with UV excess) and confirmed by slit spectroscopy. Redshifts of these UVX objects are typically less than 2.3 (Boyle et al., 1986). It is quite clear that at faint magnitudes ($B \gtrsim 19$), multi-object spectroscopy offers a powerful method for gathering large samples of data on quasars.

1.3.5 In the foregoing discussion, we have presented number-density data

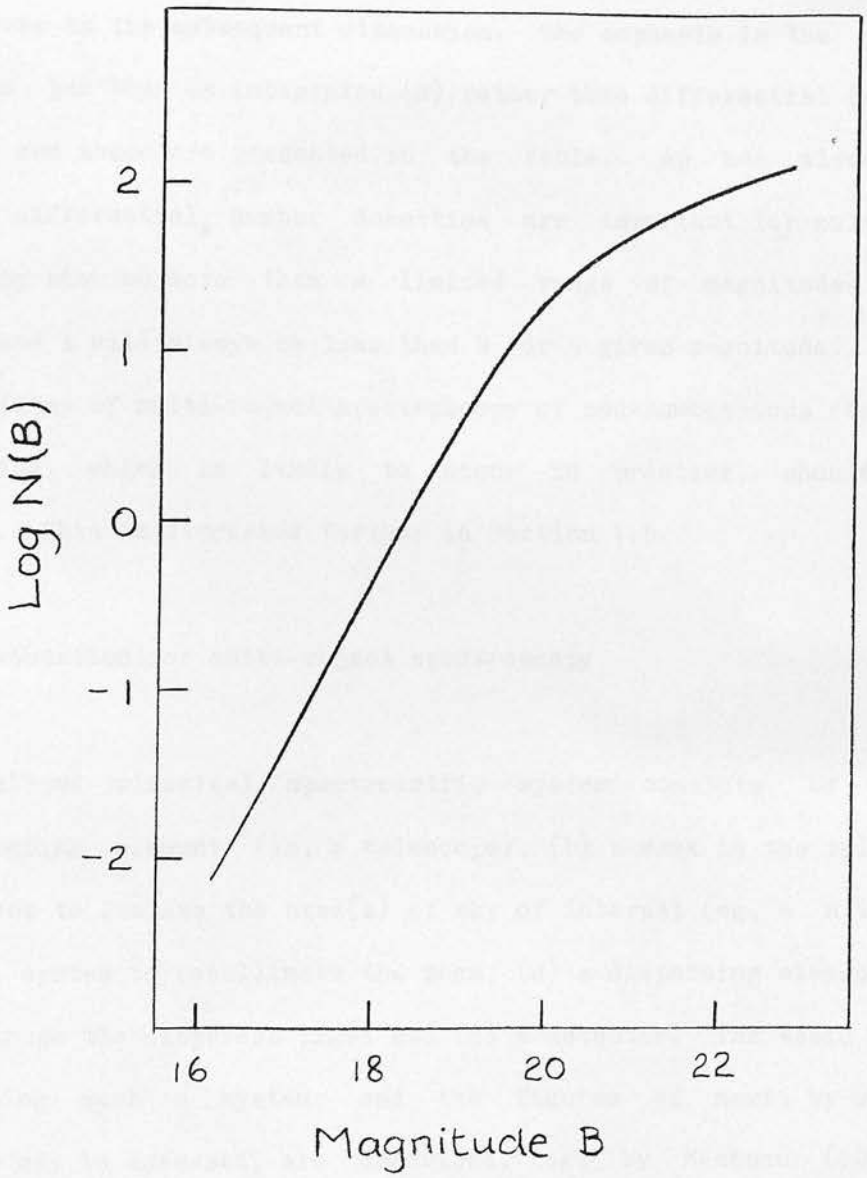

Figure 1.5 Integrated number densities of quasars identified from their ultraviolet excess and slit spectroscopy (data from several authors; see Boyle et al., 1985; Boyle et al., 1986).

for a wide variety of objects ranging from nearby stars to quasars. These are now summarized in Table 1.3 to provide a working guide for the application of multi-object spectroscopy over a range of telescopic field sizes and apertures in the subsequent discussion. The emphasis in the preceding subsections has been on integrated (N) rather than differential (A) number densities, and these are presented in the table. As has already been remarked, differential number densities are important for multi-object spectroscopy when no more than a limited range of magnitudes can be observed, and A will always be less than N for a given magnitude. However, the possibility of multi-object spectroscopy of non-homogeneous (but similar) samples, which is likely to occur in practice, should not be overlooked. This is discussed further in Section 1.5.

1.4 Instrumentation for multi-object spectroscopy

The generalized classical spectrometric system consists of (a) a light-collecting element (ie, a telescope), (b) a mask in the telescope's focal surface to isolate the area(s) of sky of interest (eg, a slit), (c) an optical system to recollimate the beam, (d) a dispersing element, (e) a camera to image the dispersed light and (f) a detector. The basic parameters defining such a system, and the figures of merit by which its performance may be assessed, are described, eg, by Meaburn (1976) and Kitchen (1984); some of these are presented in detail in Chapter 3 of this thesis. For the moment, we restrict ourselves to a qualitative account of the requirements for multi-object systems.

A few definitions are first necessary. We have already alluded to the

Table 1.3 Number densities of objects discussed in Section 1.3

$N(m,C)$ (deg^{-2})	Object class C and limiting magnitude m
<0.1	Common stars to B~5 (b=0) and B~6 (b=90). M stars to B~8.5. B stars to B~8.5 (b=90). Galactic novae, Wolf-Rayet stars, BL Her stars, etc. Blazars. Quasars to B~17.
0.1	Common stars to B~6 (b=0) and B~7 (b=90). F stars to B~8.5. G stars to B~8.5. A stars to B~8.5 (b=90). K stars to B~8.5 (b=90). Galactic cepheids to ~15. RR Lyrae stars to ~18 (b=90). Seyfert galaxies to ~16. Quasars to B~17.5.
1	Common stars to B~8 (b=0) and B~9 (b=90). B stars to B~8.5 (b=0). A stars to B~8.5 (b=0). K stars to B~8.5 (b=0). Stars in nearby (galactic) open clusters. Planetary nebulae towards the galactic centre, to R~16. RR Lyraes ~30 deg above galactic nucleus to B~19. LMC planetary nebulae. LMC Wolf-Rayet stars. Normal galaxies to J~14. Markarian galaxies to B~16. Seyfert galaxies to ~19. Quasars to B~19.
10	Common stars to B~10 (b=0) and B~12 (b=90). Stars in T-associations to ~16. Flare stars in Orion to V~19. M dwarfs within 80 pc to R~20. RR Lyraes ~10 deg below galactic nucleus to B~19. Common stars in LMC to V~12. LMC star clusters. LMC HII regions. Local Group globular clusters. K giants, RR Lyraes, carbon stars in nearby dwarf spheroidal galaxies. Normal galaxies to J~16. Markarian galaxies to B~19. Quasars to B~20.
100	Common stars to B~12 (b=0) and B~15 (b=90). Faint M dwarfs? RR Lyraes ~4 deg below galactic nucleus to B~19. Long-period variables near galactic nucleus to B~19. RR Lyraes in (galactic) globular clusters. Common stars in LMC to V~14. LMC variable stars to ~19. Normal galaxies to J~19. Quasars to B~22.
1000	Common stars to B~15 (b=0) and B~19 (b=90). Stars in distant (galactic) open clusters. Common stars in LMC to V~16. Virgo cluster globulars to B~23. Normal galaxies to J~21.
>1000	Common stars to limits fainter than B~16 (b=0) and B~23 (b=90). Stars in (galactic) globular clusters. Normal galaxies to limits fainter than J~22.

definition of multi-object spectroscopy (in 1.3.1) as the simultaneous spectroscopic observation of several objects within the field of view of a single telescope; to this might be added the further ingredient that all the elements of each spectrum are themselves observed simultaneously. Thus, we are not concerned with the use of filters, or scanning Fabry-Perot devices like TAURUS (Taylor and Atherton, 1980) which are more suitable for the investigation of relatively large extended objects at low spectral resolution (or with limited spectral coverage); ie, when the spatial content of the data predominates over the spectral content. In what is normally understood by multi-object spectroscopy, the reverse is true, so that the spectra of a relatively limited number of discrete points are obtained in some detail. (In some multi-object systems, there is nothing to prevent those discrete points from being samples of a single extended object.)

We will denote the number of discrete points that can be observed simultaneously with a multi-object system as j (which may be understood as a multiplex advantage over a single-object system). As we shall see, in some cases, j (although finite) is not defined, and we may wish to consider the number, i, of discrete points that are actually observed in a single exposure or integration. In the spectrograph itself, x will refer to the direction of dispersion and y to the perpendicular (vertical) direction normal to the optical axis. These definitions are rather loose, but have a precise meaning in the plane of the detector, where ambiguity might otherwise arise (eg, with the "rows" and "columns" of a charge-coupled device (CCD), or the "channels" and "increments" of Boksenberg's (1972) image photon counting system (IPCS)). Note that in the detector plane of some

(indeed, most) multi-object spectroscopy systems, x includes spatial as well as wavelength information, and so is not merely equivalent to λ.

We turn now to the generalized spectrometric system, and begin at the detector, which, for any kind of multi-object capability, must be two-dimensional in format. Thus, photographic plates, image-tube cameras (with photographic or electronic detection - eg, the IPCS), CCD cameras (see, eg, Mackay, 1986) or other hybrid imaging devices (see, eg, Ford, 1979) may be suitable, whereas one-dimensional (eg, Reticons; Ford, 1979) or zero-dimensional (eg, photomultiplier tubes; see Griffin, 1967) detectors are not (4). It may be noted that the use of (two-dimensional) photographic plates gave the spectrographs used in many of the early investigations presented in Table 1.1 a rudimentary multi-object capability in that they could record simultaneously the spectra of target objects and comparison lamps. Also, of course, because the telescope and camera focal surfaces are optically conjugate in the classical spectrograph described above, spatial features along the slit are imaged through the system, so that simultaneous spectroscopy of close pairs of objects (eg, double stars) has long been possible where the spectrograph slit can be rotated in position angle.

---

(4) It is, in fact, possible to imagine a fibre-coupled multi-object analogue of Griffin's (1967) radial-velocity spectrometer using a one-dimensional Reticon array aligned in the y-direction; however, its optical configuration would not be straightforward, and its usefulness probably limited.

Because spectra are extended objects, spectrograph cameras have traditionally been made fast, and the same requirement obviously holds for multi-object systems. An additional prerequisite is that the camera must have significant imaging capability in the y-direction; the construction of many conventional spectrographs would cause serious vignetting of vertically off-axis beams. The criteria for the choice of dispersing element are similar for multi-object work as for conventional observation, so prisms, grisms and gratings are all acceptable; however, collimator design may be very strongly modified by multi-object requirements. In particular, the collimator must again have a significant field of view, and it may be necessary to incorporate a field lens. Finally, the main consideration in telescopes for multi-object work (apart from aperture, which we shall here denote by a) is, as we have seen in the preceding section, the field area, F. These are the basic requirements for multi-object systems, and many of them will be discussed further in Chapter 3 of this thesis.

Considering now the practical realization of these concepts, we describe the various schemes that are in use for carrying out multi-object spectroscopy. We begin with the case where j is undefined: that of slitless spectroscopy, which may be considered as the true spectroscopic survey mode, since targets are selected on the basis of no other criteria than their position in the sky (ie, within the field of the telescope) and their magnitude (ie, within the range usefully covered by the particular observation). This type of spectroscopy contrasts strongly with the discriminate nature of most spectroscopic observation (single or multiple object), where targets are selected as being potentially interesting on the basis of an earlier observation. The selection effects (as discussed in Section 1.2)

associated with data obtained by slitless spectroscopy are perhaps the most straightforward of any, although there are subtleties (eg, in the way the response of a particular photographic emulsion may affect the appearance of spectra in surveys for particular types of object; see Savage et al., 1985).

The most common slitless technique is that of the objective prism, which dispenses with elements (a) to (c) of the generalized spectrometric system and turns the telescope itself into the spectrograph camera (e). As examples, we may quote the 2480 and 830 Å/mm (at H_γ) objective prisms of the UK Schmidt telescope (see Tritton et al., 1983), which have proved spectacularly effective as survey instruments for a variety of object classes (see, eg, Clowes, Cooke and Beard, 1984; Morgan and Good, 1985; see also the atlas by Savage et al., 1985). To a lesser extent, work of a "follow-up" nature has also been undertaken (eg, Cooke et al., 1981); the very effective use of the COSMOS (MacGillivray and Stobie, 1984) and APM (Kibblewhite et al., 1975) high-speed automatic plate-measuring machines for the analysis of these objective-prism spectra may also be mentioned.

The UK Schmidt telescope (UKST) has a=1.2 metres and F=40 deg^2, and uses 356 mm square photographic plates as detectors. When exposed to the sky limit (ie, so as to have a background density D of 1.0 above the chemical fog level (5)) using the lower-dispersion prism, such a plate may contain

---

(5) Photographic density D is defined by D = -log T, where T is the transmission of the plate (ie, the fraction of normally-incident light that

short ($\lesssim$1 mm) spectra of i~10^5 objects. In this respect, it resembles the filter/TAURUS technique, mentioned earlier, as much as conventional multi-object spectroscopy. An example of UKST objective-prism spectra is reproduced in Figure 1.6(a).

A number of well-known drawbacks are associated with objective-prism spectroscopy. The first of these is the possible overlapping of spectra, which may be particularly serious at higher dispersions and in crowded fields. On the UKST, it is possible to adjust the prisms in position angle to exert some degree of control over this; for example, two plates taken with orthogonal prism position angles but otherwise identical may partially overcome the problem. A second drawback is the difficulty of providing comparison spectra for wavelength calibration. At low dispersions, as on the UKST, this may be achieved by careful absolute calibration of the dispersion of the prism, the sharply-defined red cutoff of the emulsion sensitivity then providing a zero-point. At higher dispersions, other methods must be adopted; for example, Fehrenbach (1966) has described the use of a compound zero-deviation objective prism which may be rotated in position angle through 180 deg between double exposures on the same plate, thus enabling stellar radial-velocity measurements to be made. A third disadvantage of objective-prism spectroscopy, which may be particularly acute at low dispersions, is that the spectral resolution is directly related to the diameter of the seeing disc, and may be substantially degraded in poor conditions. Finally, and most seriously for faint-object

---

passes through it).

Figure 1.6 Examples of multi-object spectra (following pages)

(a) Positive reproduction from a 2 cm square portion of a low-dispersion (2480 Å/mm) 1.2-metre UK Schmidt telescope objective-prism plate, showing stars in the region of the Horsehead Nebula. Wavelength increases to the right.

(b) 2000 Å/mm grens spectra of the field of 3C 36, obtained with the 3.6-metre Canada-France-Hawaii telescope using an electronographic camera. The quasar (arrowed) has a B magnitude of 22.1. Wavelength increases to the left. (From Lelièvre, 1983.)

(c) CCD image of spectra obtained with the multi-slit low-dispersion survey spectrograph (LDSS) on the 3.9-metre Anglo-Australian telescope. Each of the slits produces a zero-order image with the first-order spectrum to its right. The spectra clearly show [OI] and NaI night-sky emission lines together with the continua of the target objects, which range in B magnitude from 21.0 to 23.5. The reciprocal dispersion is 850 Å/mm, and the exposure time was 4000 seconds. (From Taylor and Ellis, 1986.)

(d) Photographic spectra of bright (B<12.5) stars at 190 Å/mm obtained with the fibre-linked array-image reformatter (FLAIR) on the 1.2-metre UK Schmidt telescope. Wavelength increases from left to right, and covers the range 4000 to 7000 Å. Features visible include the Balmer lines of hydrogen, the G band and, in the spectrum of an M star (fourth from top), TiO bands.

(a)

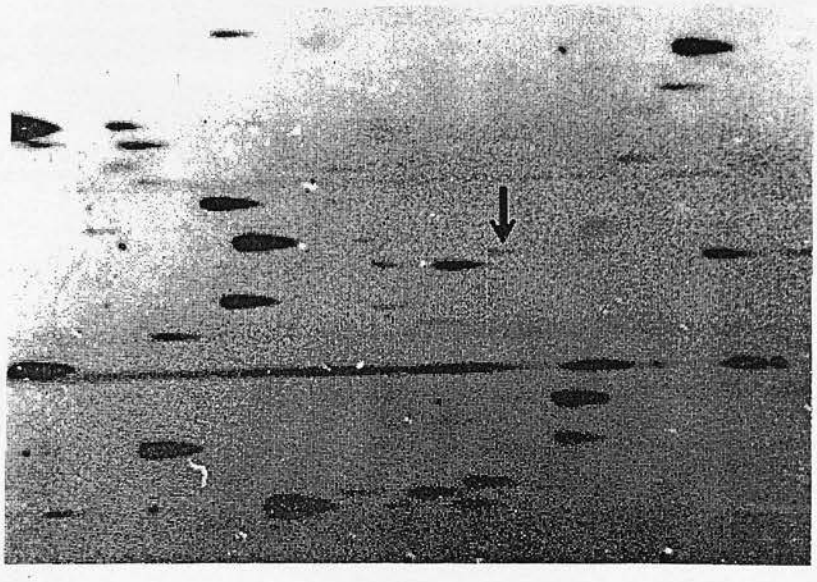

(b)

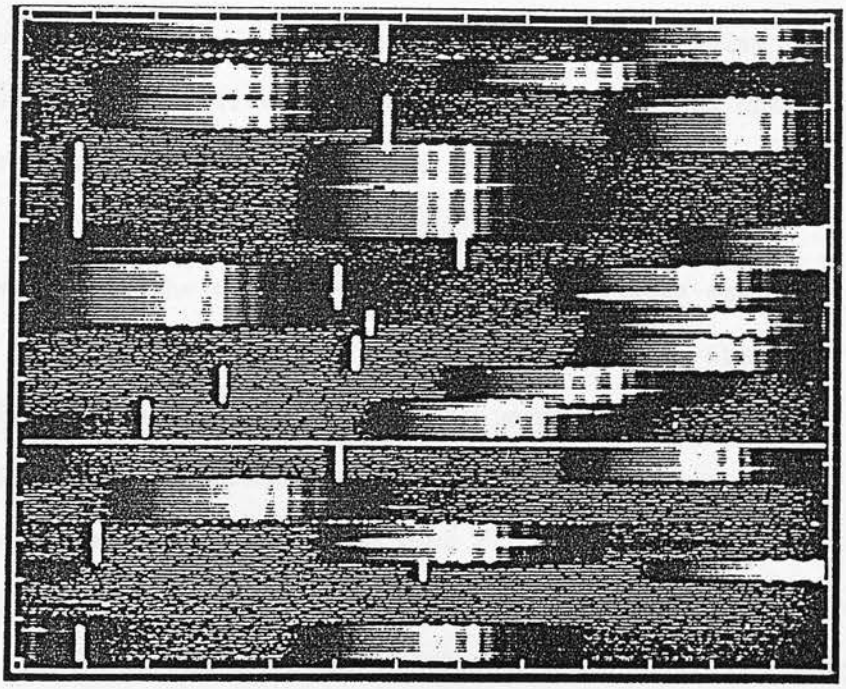

(c)

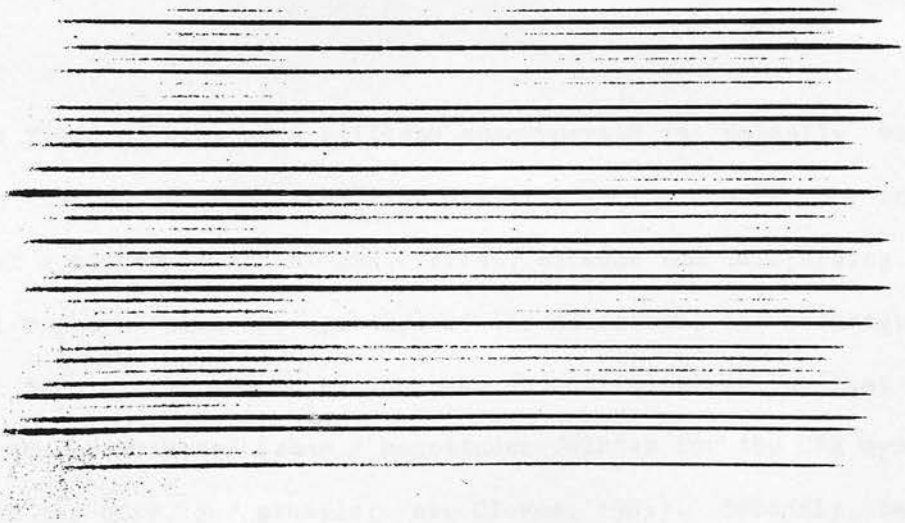

(α)

spectroscopy, the sky background is undispersed and may be very bright compared with the spectrum of the target object; this problem is aggravated by the use of (non-linear) photographic plates, and constitutes a real limit to the sensitivity of objective-prisms.

Closely related to the objective prism is the slitless spectrograph, which has all the elements of the generalized classical spectrometric system except (b), the mask or slit. Thus, all images in that portion of the field of the telescope common to the field of the collimator are dispersed, frequently by means of a low-dispersion zero-deviation element, such as a grism. (Usually, only a small area of the telescope field is used, since a physically large collimator field would imply excessively bulky spectrograph optics.) An example of this type of system is the grens (grating-lens) spectrograph on the 3.6-metre Canada-France-Hawaii telescope (CFHT); typical spectra obtained with this instrument are shown in Figure 1.6(b).

While the field of view of a slitless spectrograph is normally very much less than that of an objective-prism system like the UKST's, the instrument does offer a number of advantages. First, because the dispersing element is small compared with the aperture of the telescope, the technique can be used with much larger apertures than can objective prisms, so that fainter objects can be detected (some 2 magnitudes fainter for the CFH system compared with the UKST, for example; see Clowes, 1985). Secondly, because of the relatively small size of the final image (6), the sensitivity can be

---

(6) The final image is demagnified in these systems because the focal ratio

further increased by using an electronic detector (eg, a CCD), whose linearity will also help to improve the subtraction of the severe sky contamination. This is still present, of course, along with all the other drawbacks of objective prisms, but we shall see how the addition of a simple multi-slit mask can considerably improve the situation.

First, though, we digress briefly to consider some of the relevant properties of single-slit systems. It may be remarked that the "degenerate case" of multi-object spectroscopy is represented, not by a single slit (as element (b) of the generalized spectrometric system), but by an aperture approximately matching the seeing disc imaged by the telescope. Here, j is strictly equal to one, as there is no possibility of simultaneous observation of anything else at all - not even empty sky. This situation is, in fact, encountered in practice, when the aperture is replaced by a single optical fibre feeding a stationary spectrograph (eg, Heacox, 1986). The configuration offers certain advantages for radial-velocity measurements of bright objects, and will be discussed in subsequent chapters.

We have already seen how a single (long) slit can achieve limited ($i \sim 2$) multi-object capability when used with a two-dimensional detector. Of more immediate interest for faint-object spectroscopy, however, is the use of a

---

of the collimator is constrained to match that of the telescope beam (typically f/8 at Cassegrain focus), while that of the camera is usually very much lower. The system thus acts as a focal reducer.

long slit to provide simultaneous samples of the sky spectrum adjacent to the target object, so that this can be subtracted from the object's spectrum. The detrimental effect of noise due to spatial variations in the sky signal are thus minimised. It is also usual to attempt to reduce the effects of temporal variations in the sky signal and inhomogeneity in the instrumental throughput (ie, the differences in detected signal resulting from the same light flux falling on different points (y) along the slit) by frequent beamswitching, so that the target object is moved between two positions on the slit between successive exposures. The observations are thus obtained in pairs and, in good conditions, instrumental efficiency variations will be cancelled out in the sky subtraction, leaving only the effects of Poisson noise (= $(\text{signal})^{1/2}$) in the object and sky signals reaching the detector (see Appendix to Chapter 5). The subject of sky noise in faint-object spectroscopy is dealt with in some detail by Parry (1986); we will return to it in Chapter 3 of this thesis.

The insertion of a suitably-pierced mask in the telescope/collimator focal surface of the slitless spectrograph described above turns it into a multi-slit or multi-aperture spectrograph. The mask must be manufactured with high precision to form a number of short slits (or holes) whose configuration matches that of the (preselected) targets in a chosen field. Note that j here is variable (and equal to i), and that the instrument is no longer operating in the survey mode described for the slitless techniques - although this can, of course, be regained simply by removing the mask. The advantages offered by this instrument over the slitless spectrograph are, first, that the overlapping of spectra can be avoided (although this clearly places limitations on the positioning of the slits); second, that

comparison spectra can be obtained simply by illuminating the input side of the mask with a calibration lamp; third, that spectral resolution is independent of seeing and, finally, that the target spectra no longer lie on undispersed sky, so that efficient sky-subtraction can be performed using the methods described above for single-slit observations - hence the preferred use of slits in the mask, rather than merely holes.

Against these, the drawbacks of the technique compared with slitless spectroscopy are, first, that the mask has to be prepared in advance, and second, that the method has to incorporate some means of registering the slit mask with the sky (involving adjustments in RA, Dec and position angle). Neither of these drawbacks is serious, and some ingenuity is going into methods of minimising the lead time for mask preparation, including "on-the-spot" fabrication from the direct CCD image (at CFHT; Fort et al., 1986) and the use of computer-controlled, mechanically-driven "slitlets" (on the 2.5-metre Isaac Newton telescope (INT); Breare et al., 1986), thus, incidentally, fixing the value of j.

A version of this system has been developed for the 4-metre Mayall telescope at Kitt Peak National Observatory (KPNO) (Butcher, 1982) using aperture plates drilled with circular holes. These are prepared automatically using a numerically-controlled milling machine. Separate sky holes are included, either adjacent to each object (preferable) or elsewhere in the field if the number density of target objects is high. A new multi-slit spectrograph with a 12 arcmin field has recently been commissioned (Taylor and Ellis, 1986) on the 3.9-metre Anglo-Australian telescope (AAT). Known as the low-dispersion survey spectrograph (LDSS; see Taylor,

1983), the instrument is designed for use with large-format CCDs (~1500 pixels square, compared with current versions of ~500) to obtain low-resolution spectra of objects with V in the range 20-24. It is designed to be versatile, with interchangeable detectors and capabilities for slitless, direct (with filters) and single long-slit work. Using currently-available CCDs, the instrument has j~20, but this should eventually increase to ~200; an example of spectra produced by this instrument is shown in Figure 1.6(c).

The multi-slit spectrograph clearly promises to be a powerful tool for the rapid collection of data on very faint sources, but it does have two disadvantages. These are, first, the restriction on j imposed by the need to avoid overlapping images at the detector and, more seriously, the relatively small field area that can be covered. For example, the AAT's f/8 Ritchey-Chrétien focus has a useful field 40 arcmin in diameter, but the physical diameter of this is approximately 360 mm, so that an impossibly large spectrograph with an equally impossible CCD would be required to be mounted at the Cassegrain position to enable multi-slit observations to be made over the full field.

The solution to both these problems lies in the use of a fibre-optics coupler, or multiple-fibre feed, to replace the mask (b) in the generalized spectrometric system, and turn it into a fibre-coupled multi-object spectrograph. The technique relies on the low intrinsic losses and extreme flexibility of optical fibres developed for the communications industry; the fibres are used as single apertures with their input ends matching the configuration of the target images in the telescope focal surface, and

their output ends aligned to form a "slit" in the collimator focus of the spectrograph, a short distance away. The multiple fibre feed thus acts as a reformatting device, producing, from a random distribution of target objects in the telescope field, a stack of spectra such as that shown in Figure 1.6(d), which maximizes the area of the detector actually used. There are no fundamental limitations on the placing of fibres in the telescope's focal surface; both disadvantages of the multi-slit system are thereby eliminated. Furthermore, the collimator field need not be excessively large, and there are no limitations on the dispersion that may be used. Values of j are typically in the range 40 to 80 and are limited primarily by detector sizes. It is, however, possible to feed more than one spectrograph simultaneously, and multiplex advantages of more than 1000 may eventually be achieved. This technique was first described by Hill et al. (1980), and is now in use at a number of telescopes (including the AAT), with a variety of methods for supporting the fibres in the focal surface (see Chapter 4 of this thesis). An attractive extension to the technique is to lengthen the fibres so that the spectrograph may be removed from the telescope altogether and used in a stationary position (preferably in a controlled environment), to produce considerable gains in stability and accessibility. The fibres then have the dual role of reformatting the images and acting as a pseudo-coudé feed; so far as is known, the only fully-operational example of this arrangement is the fibre-linked array-image reformatter (FLAIR) developed by the author at the UKST (described in Chapter 6).

Since the multi-fibre technique forms the main topic of this thesis, we will defer further discussion of its technical and observational aspects to

subsequent chapters. To facilitate comparison with the other multi-object techniques described in the present section, however, we may mention in conclusion that its drawbacks include the need to set up the fibres in their correct configuration prior to observing, and then to align them in exact registration with the telescope field (both common to the multi-slit technique). More seriously, it is possible that fibre-to-fibre transmission differences may prevent perfect sky subtraction, and, for very faint objects, this could limit the ultimate performance of fibre-coupled systems in comparison with multi-slit systems (Parry, 1986; Chapter 3 of this thesis).

1.5 Spectroscopy with fibre-coupled multi-object systems

The survey of multi-object spectroscopic techniques in Section 1.4 has revealed the strengths and weaknesses of the instrumentation currently available, and has clearly demonstrated that the multi-fibre technique offers most promise in terms of field coverage, versatility of spectral range and resolution, efficiency of detector use and ultimate multiplex advantage. The only question appears to be whether imperfect sky subtraction may limit its use for very faint objects. It is now possible to consider how applicable the technique might be in practice, given the real distribution of objects presented in Table 1.3. Since multi-fibre spectroscopy can be carried out on any telescope with an appreciable field of view, it is necessary to introduce a figure of merit that will allow us to compare instruments with different apertures a and field areas F. A previous paper (Dawe and Watson, 1984) defined the effective aperture, α, of a telescope (7) as

---

(7) This is derived from the more fundamental definition of "effective

$$\alpha = i^{1/2}a, \qquad (1.7)$$

where i is now the number of fibres in use at a given time, from a total number, j, available. (Since there are no inherent limitations on the positioning of the fibres in the field, i and j may be regarded simply as the numbers of channels in use and available in a general, spatially-multiplexed observing system.)

Consider now the behaviour of α with N, the number density of target objects. There are three cases that arise, depending on the value of N; they are:

(a) $N<1/F$, so that only one object can be observed at a time; we then have

$$\alpha = a; \qquad (1.8a)$$

(b) $1/F<N<j/F$; then i fibres may be used, and

$$\alpha = (FN)^{1/2}a; \qquad (1.8b)$$

(c) $N>j/F$; then all the fibres may be used, and

---

light grasp" (= ia^2).

$$\alpha = j^{1/2}a. \qquad (1.8c)$$

In Figure 1.7 we plot Equations 1.8 for a number of telescope/fibre combinations. Two existing configurations are plotted: the UKST with j=40 fibres (a) and the AAT with j=64 fibres (c). For the first, the multiplex advantage begins to take effect at N=0.025 deg^{-2}, and all the fibres are in use when $N \geqslant 1.0$ deg^{-2}, the effective aperture α then becoming 7.6 metres. For the AAT, with fibres at the 40 arcmin Ritchey-Chrétien focus, objects with $N < 2.25$ deg^{-2} must be observed one at a time, and the full potential of the system is not reached until N=144 deg^{-2}, when α=31.2 metres. It will be seen that there is a range of number densties, between 0.26 and 8.5 deg^{-2}, where the UKST is actually working more efficiently than the AAT in terms of effective aperture; this is entirely due to the wide field of the telescope and indicates the region of the number-density distribution where multi-object spectroscopy on the UKST will be most effective. It may eventually be possible to increase the number of fibres on the UKST to 400, and the effect of this is shown as line (b). It will be seen that the UKST's advantage in effective aperture is now maintained to N=85 deg^{-2}, and its maximum value of α=24.0 metres is comparable with that for the existing AAT system.

In discussing these diagrams, it has to be remembered that N is not a free variable, but is itself a two-dimensional function of object class, C, and limiting magnitude, m. The effect of the dependence on the first of these is to permit the mixing of object classes in a single observation (so that N(C) values are summed over C) to avoid the need to work on the rising section of the diagram (ie, with not all the fibres in use, a situation which

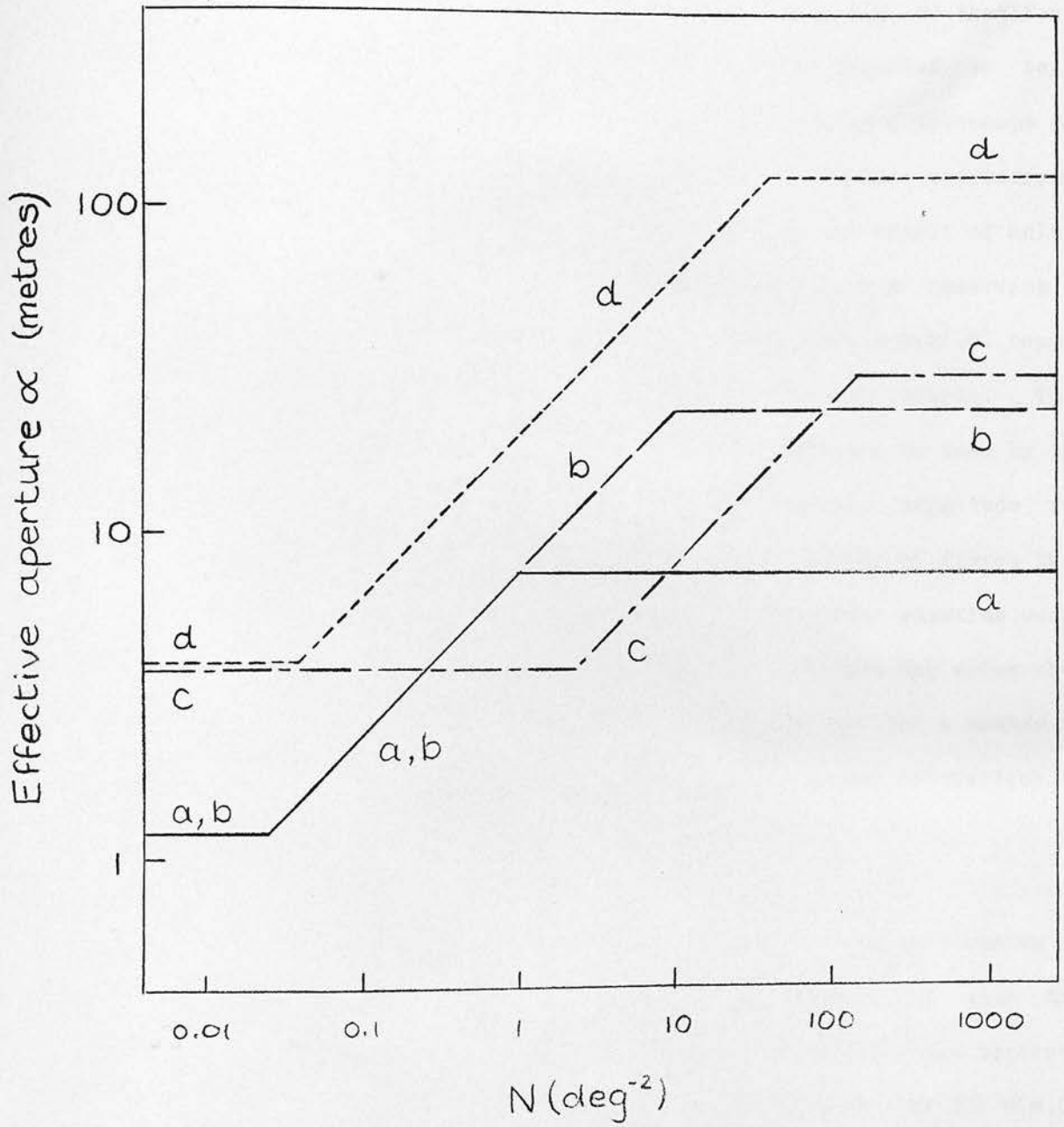

Figure 1.7 Effective aperture $\propto$ plotted against number density N for a variety of telescope/fibre combinations (see text).

(a) UK Schmidt telescope, a=1.2 metres, F=40 deg^2, j=40 fibres;
(b) UK Schmidt telescope, a=1.2 metres, F=40 deg^2, j=400 fibres;
(c) Anglo-Australian telescope, a=3.9 metres, F=0.44 deg^2, j=64 fibres;
(d) Proposed Willstrop telescope, a=4.0 metres (equiv.), F=25 deg^2, j=1000 fibres.

is unlikely to be allowed to happen in practice). The dependence of N on limiting magnitude, m, is always monotonically increasing, so that for a given object class, the abscissa of Figure 1.7 may be regarded as being loosely equivalent to m. The limiting magnitude, m', of a telescope for multi-object spectroscopy is, of course, dependent on the true aperture, a, rather than the effective aperture, α, which is merely the result of multiplexing. Thus, for a given telescope of limiting magnitude m' observing a single class C of objects, there will be a number density N(m',C) beyond which it is not possible to observe all the objects in the sample. This places an ultimate limit on the number of fibres that can be used by the telescope; for example, suppose the UKST has a limiting magnitude for multi-fibre spectroscopy of B'~18, then the maximum number of fibres that could be employed for the measurement of redshifts of normal galaxies would be ~1600 (from Figure 1.3). A further consideration that may arise when faint objects close to the sky limit are being observed is that a number of sky fibres will be required, up to a maximum of i/2 if sky subtraction by beamswitching is used (see Chapter 5).

Bearing these considerations in mind, we may now compare the performance of existing fibre-coupled telescopes presented in Figure 1.7 with the number-density data summarized in Table 1.3, and it is immediately apparent that the technique is very well suited to the problem, for all N(m,C) values higher than about 0.1 deg^{-2}. In particular, the low number-density range (0.1 to 10 deg^{-2}) of relatively bright objects is well catered for by the UKST with its wide field and modest aperture, while the fainter objects with number densities above 10 deg^{-2} can be satisfactorily observed with 4-metre class telescopes like the AAT (assumed to have a limiting magnitude

m' for fibres work of somewhat fainter than 20).

It has been remarked before (eg, Edmunds and Ellis, 1986) that large fields and large apertures have traditionally been mutually exclusive features of telescopes, but a new design has recently been presented (Willstrop, 1984, 1985, 1987) that goes some way towards changing this. The currently-favoured design of the Willstrop telescope has a 5-metre primary mirror (though the 3-metre central obstruction reduces its equivalent aperture to a=4 metres) and a field of view of area F=25 deg^2. The design has a number of attractive properties, and may be adopted for a next-generation survey telescope, in which case it will certainly be used in a multi-fibre configuration with a high order of multiplexing. Line (d) in Figure 1.7 is the effective-aperture diagram of such a telescope equipped with 1000 fibres (thus having a maximum α of 126.5 metres), and it is evident that its performance exceeds both the present UKST and AAT configurations. It is likely that such an instrument would be used for survey spectroscopy of moderately faint objects (V~20) at relatively high number densities (~100 deg^{-2}), but it would also have a role in observing rarer objects (eg, quasars) at limiting magnitudes fainter than that of the UKST. The Willstrop telescope will be discussed further in subsequent chapters.

Having introduced the technique and investigated the potential of fibre-coupled multi-object spectroscopy, the aim of this thesis is now to give a full account of its technical aspects (Chapters 2, 3, 4 and 6) with particular emphasis on two contrasting systems:

(a) A moderately large-aperture, modest-field system, with a relatively

slow focal ratio and coarse plate-scale, which uses a telescope-mounted medium-to-high dispersion spectrograph. This is the AAT's FOCAP multi-fibre system, built by Peter Gray (described in Chapter 4).

(b) A modest-aperture, wide-field system with fast focal ratio and fine plate-scale, using a floor-mounted low-to-medium dispersion spectrograph (ie, the UKST FLAIR system, devised and built by the writer, and described in Chapter 6).

Astronomical results have been obtained by the author using both these systems and they are presented in Chapters 5 and 7. Finally, in Chapter 8, we shall look to the future of multi-object fibre-optics spectroscopy.

References for Chapter 1

Adams WS, 1914. PASP 26, 198
Adams WS, 1915. PASP 27, 236
Allen CW, 1973. Astrophysical Quantities, 3rd Ed. Athlone, London
Ambartsumian VA, 1949. Astronomicheskii zhurnal 26, 1
Ambartsumian VA, 1958. In La Structure...de l'Univers, p. 241, Brussels
Ambartsumian VA, Mirzoyan LV, 1975. In Vbl.Stars and Stellar Ev. Reidel
Angel JRP, Stockman HS, 1980. Ann.Rev.Astr.Astrophys. 18, 321
Armandroff TE, Da Costa GS, 1986. AJ 92, 777

Baade W, 1963. Evolution of Stars and Galaxies, Ch 21. Harvard
Bahcall JN, 1986. Ann.Rev.Astron.Astrophys. 24, 577
Balona L, Crampton D, 1974. MNRAS 166, 203
Balona LA, Feast MW, 1974. MNRAS 167, 621
Balzano VA, 1983. Ap J 268, 602
Blaauw A, 1952. BAN 11, 405
Blanco BM, 1984. AJ 89, 1836
Boksenberg A, 1972. In Proc ESO/CERN Conf on Aux.Inst., p.295, Geneva
Bowen IS, 1928. Ap J 67, 1
Boyle BJ, Fong R, Shanks T, Clowes RG, 1985. MNRAS 216, 623
Boyle BJ, Fong R, Shanks T, Peterson BA, 1986. In Struc.and Ev.of AGN,R'del
Breare JM, Ellis RS, Purvis A, Miller W, Webb DA, 1986. Proc SPIE 627, 278
Brown GS, Tinsley BM, 1974. ApJ 194, 555
Brück MT, 1984. In Struc. and Ev. of the Mag. Clouds, p.97, Reidel
Butcher H, 1982. Proc SPIE 331, 296
Butler D, Carbon D, Kraft RP, 1976. Ap J 210, 120

Cannon AJ, Pickering EC, 1918-24. Harvard Annals 91-99
Cannon RD, 1982. In Highlights in Astronomy (IAU) 6, 109
Clowes RG, 1985. In Roy.Obs.Edin.Research and Facilities, p.10, ROE
Clowes RG, Cooke JA, Beard SM, 1984. MNRAS 207, 99
Clube SVM, Watson FG, 1978. Observatory 98, 124
Clube SVM, Watson FG, 1979. MNRAS 187, 863
Cooke JA, EmersonD,KellyBD,MacgillivrayHT,DoddRJ, 1981. MNRAS 196, 397
Crampton D, Fernie JD, 1969. AJ 74, 53

Dawe JA, Watson FG, 1984. In Astr.with Schmidt-type Tels., p.181, Reidel
Diaz AI, Pagel BEJ, Wilson IRG, 1985. In Active Gal.Nuclei,p171,Manchester
Dunham T, 1933. PASP 45, 202

Eccles MJ, Sim ME, Tritton KP, 1983. Low Light-level Det.in Astr.,Cambridge
Edmunds MG, Ellis RS, 1986. A UK strtgy for fut.grnd-based tels.(SERC rep.)
Eggen OJ, 1963. AJ 68, 697
Ellis RS, 1980. In Objects of High Redshift (IAU Sym. 92), p.23, Reidel
Ellis RS, 1986. Observational Cosmology, Beijing

Feast MW, 1984. In Struc.and Ev.of the Mag.Clouds, p.157, Reidel
Fehrenbach Ch, 1966. Advances in Astron. and Astrophys. 4, 1
Fehrenbach Ch, Duflot M, Acker A, 1976. Astron.Astrophys.Supp 24, 379
Fernie JD, Hube JO, 1968. AJ 73, 492
Ford WK, 1979. Ann.Rev.Astron.Astrophys. 17, 189
Fort B, Mellier Y, Picat JP, Rio Y, Lelièvre G, 1986. Proc SPIE 627, 321
Freedman WL, 1986. In Lum.stars and assoc.in gals.(IAU Sy.116),p.61,Reidel
French HB, 1980. Ap J 240, 41
Frenk CS, White SDM, 1980. MNRAS 193, 295

Gaposchkin SI, 1955. Peremennye Zvezdy 10, 337
Gilmore GF, Reid IN, 1983. MNRAS 202, 1025
Graham JA, 1984. In Struc.and Ev.of the Mag.Clouds, p.207, Reidel
Greenstein JL, Schmidt M, 1964. Ap J 140, 1
Griffin R, 1967. Ap J 148, 465
Grotrian W, 1939. Naturwissenschaften 27, 214

Hanes DA, 1980. In Globular Clusters (Eds. Hanes, Madore) Ch. 12,Cambridge
Hanes DA, Madore BF, (eds.) 1980. Globular Clusters, Cambridge
Haro G, 1952. Ap J 115, 572
Haro G, 1968. In Neb. and Interst.Matter (ed.Middlehurst,Aller), Chicago
Haro G, 1976. Boletin del Instituto de Tonantzintla Vol 2 No 6
Harris WE, Racine R, 1979. Ann.Rev.Astron.Astrophys. 17,241
Hartmann JF, 1904. Ap J 19, 268
Hartwick FDA, Barlow DJ, Hesser JE, 1981. AJ 86, 1044
Hawkins MRS, 1984. MNRAS 206, 433
Hawkins MRS, 1986. MNRAS 223, 845
Heacox WD, 1986. AJ 92, 219
Heckman TM, 1980. Astron.Astrophys. 87, 152
Herbig GH, 1951. Ap J 113, 697
Hertzsprung E, 1905. Zeit. fur wissen. Phot. 3, 429
Hidayat B, Supelli K, v d Hucht KA, 1982. In Wolf Rayet Stars,p 27, Reidel
Hill J, AngelJRP,LindleyD,ScottJ,HintzenP,1980. Opt/IR tels for 1990s,T'son
Hodge PW, Wright FW, 1967. The Large Magellanic Cloud, Smithsonian
Hubble EP, 1922. Ap J 56, 400
Hubble EP, 1929. Proc. Nat. Acad. Sciences 15, 168
Huchra J, 1977. Ap J Supp 35, 171
Huchra J, Davis M, Latham D, Tonry J, 1983. Ap J Supp 52, 89
Huchra J, Sargent WLW, 1973. Ap J 186, 433
Huggins W, 1868. Phil.Trans. 158, 529
Huggins W, 1872. MNRAS 32, 361
Humason ML, Mayall NU, Sandage AR, 1956. AJ 61, 97

Illingworth GD, 1986. Modern Instrumentation conference, Herstmonceux

Jarvis JF, Tyson JA, 1981. AJ 86, 476
Johnson HL, Morgan WW, 1953. Ap J 117, 313
Joy AH, 1945. Ap J 102, 168

Karachentsev ID, 1980. In Obj. of High Redshift (IAU Sym. 92), p.17, Reidel
Keel WC, 1983. Ap J Supp 52, 229
Kerr FJ, Lynden-Bell D, 1986. MNRAS 221, 1023
Kibblewhite EJ, et al., 1975. In Image Proc.Techs.in Astr., p.245, Reidel

King HC, 1955. The History of the Telescope, Griffin, London
King IR, 1980. In Globular Clusters (ed Hanes, Madore), Ch 13, Cambridge
Kinman TD, 1959. MNRAS 119, 559
Kinman TD, Wirtanen CA, Janes KA, 1966. Ap J Supp 13, 379
Kitchen CR, 1984. Astrophysical Techniques, Hilger
Koo DC, 1986. Observational Cosmology, Beijing
Kraft RP, 1965. In Gal.Struct. (Ed. Blaauw, Schmidt) p 157, Chicago
Kukarkin BV, et al., 1969. Gen.Cat.of Var.Stars, 3rd Ed., Moscow

Lelièvre G, 1983. Proc SPIE 445 (Inst.in Astr.V), p.151
Lindblad B, 1925. Arkiv for matem. astr. och fys. 19A No 21, 1
Longair MS, 1982. In Space Tel.Observatory, NASA CP-2244, p.121
Longair MS, 1984. Nature 310, 13
Longair MS, 1985. Observatory 105, 171
Luyten WJ, 1968. MNRAS 139, 221
Lynden-Bell D, Cannon RD, Godwin PJ, 1983. MNRAS 204, 87P

Macgillivray HT, Stobie RS, 1984. Vistas Astr. 27, 433
Mackay CD, 1986. Ann.Rev.Astron.Astrophys. 24, 255
Madore B, 1980. In Globular Clusters (ed Hanes, Madore), Ch 2, Cambridge
Margon B, et al., 1979. Ap J 230, L41
McCuskey SW, 1965. In Gal. Struc. (Ed.Blaauw, Schmidt)p 12, Chicago
Meaburn J, 1976. Detection and Spectrometry of Faint Light. Reidel
Mihalas D, Binney J, 1981. "Galactic Astronomy", Freeman
Minkowski R, 1941. PASP 53, 224
Minnaert M, Mulders G, 1930. Zeit. fur Astrophysik 1, 192
Mirzoyan LV, 1984. Vistas Astr. 27, 77
Morgan DH, 1984. MNRAS 208, 633
Morgan DH, Good AR, 1985. MNRAS 213, 491
Morgan WW, Keenan PC, Kellman E, 1943. Atlas of Stellar Spectra, Chicago

Nort H, 1950. BAN 11, 181

Oort JH, 1927. BAN 3, 275
Opik E, 1922. Ap J 55, 406
Osterbrock DE, Mathews WG, 1986. Ann.Rev.Astron.Astrophys. 24, 171
Ovenden MW, Byl J, 1976. Ap J 206, 57

Parry IR, 1986. PhD Thesis, University of Durham
Payne CH, 1925. Stellar Atmosph. Chap 13, Harvard Univ Press
Peacock JA, 1985. MNRAS 217, 601
Peebles PJE, 1980. In Sci.Res.with the Space Tel.(IAU Col.54) NASA CP-2111
Perek L, Kohoutek L, 1967. Cat. of Galactic Planetary Nebulae, Prague
Peterson BA, et al., 1979. Ap J 233, L109
Pettersson B, 1986. Astron.Astrophys., in press
Plaut L, 1966. BAN Supp. 1, 105
Plaut L, 1968. BAN Supp. 2, 293
Plaut L, 1971. Astron. Astrophys. Supp. 4, 75
Porcas RW, 1985. In Active Galactic Nuclei (ed.Dyson) p.20, Manchester
Preston GW, 1959. Ap J 130, 507

Reid IN, Gilmore GF, 1982. MNRAS 201, 73
Rodgers AW, 1977. Ap J 212, 117
Rousseau J, et al., 1978. Astron.Astrophys.Supp. 31, 243

Russell HN, 1914. Popular Astron. 22, 275

Sandage A, 1961a. ApJ 133, 355
Sandage A, 1961b. The Hubble Atlas of Galaxies, Carnegie, Washington
Sanduleak N, 1976. AJ 81,350
Sanduleak N, 1984. In Struc.and Ev.of the Mag.Clouds, p.231, Reidel
Sargent WLW, Kowal ST, Hartwick FDA, van den Bergh S, 1977. AJ 82, 947
Sargent WLW, Young PJ, Boksenberg A, Tytler D, 1980. ApJ Supp 42 41
Savage A, et al., 1985. The UKST Objective Prisms, ROE
Sawyer-Hogg H, 1973. Pub.David Dunlap Obs. 3 No 6
Schechter P, 1976. Ap J 203, 297
Schmidt M, 1963. Nature 197, 1040
Secchi A, 1867. Compt.Rend. 64, 774
Seitter WC, 1970. Atlas for Objective Prism Spectra I, Bonn
Seyfert CK, 1943. Ap J 97, 28
Shajn GA, Struve O, 1929. MNRAS 89, 222
Shanks T, BeanAJ,EfstathiouG,EllisRS,FongR,PetersonBA,1983. Ap J 274, 529
Shanks T, Stevenson PRF, Fong R, MacGillivray HT, 1984. MNRAS 206,767
Shapley H, Cannon AJ, 1924. Harvard Reprint No 6
Slipher VM, 1909. Lowell Obs. Bull. No 42
Slipher VM, 1916. Lowell Obs. Bull. 2, No 75, 155
Slipher VM, 1917. Proc. Am. Philosphical Soc. 56, 403
Stobie RS, Bishop IS, King DL, 1986. MNRAS 222, 473
Stothers RB, 1983. ApJ 274, 20
Struve O, Elvey CT, 1939. Ap J 89, 119

Taylor K, 1983. Low-disp. survey spectr. (AAT instrument proposal)
Taylor K, Atherton PD, 1980. MNRAS 191, 675
Taylor K, Ellis R, 1986. AAO Newsletter No 38
Tritton SB, et al., 1983. UKSTU Handbook, ROE
Trumpler RJ, 1930. Lick Obs. Bull. 14, No 420, 154
Tyson JA, Jarvis JF, 1979. Ap J 230, L153

Vogel HC, 1874. Astr.Nach. 84, 113

Walsh D, Carswell RF, Weymann RJ, 1979. Nature 279, 381
Warren SJ, et al., 1987. Nature 325, 131
Watson FG, 1980a. Phys Educ 15, 206
Watson FG, 1980b. Observatory 100, 39
Webster BL, Murdin P, 1972. Nature 235, 37
Weedman DW, 1977. Ann.Rev.Astr.Astrophys. 15, 69
Whittet DCB, KirraneTM,KilkennyD,OatesAP,WatsonFG,KingDJ, 1987. MN 224,497
Willstrop RV, 1984. MNRAS 210, 597
Willstrop RV, 1985. MNRAS 216, 411
Willstrop RV, 1987. MNRAS 225, 187
Wilson RE, 1953. Carnegie Inst. Wash. Pub. No 601

Zinn R, 1980. In Globular Clusters (eds. Hanes, Madore), Ch.11 Cambridge
Zinnecker H, CannonRD,HawardenTG,MacGillivrayHT,1985. In Virgo Clust.p.135
Zwicky F, 1937. Ap J 86, 217

CHAPTER 2

Optical fibre feeds

2.1 Optical waveguides

Although the phenomenon of light propagation along transparent cylinders by repeated total internal reflection was probably known to glassblowers in ancient times, the first recorded scientific demonstration was by John Tyndall (1854) in a popular lecture at the Royal Institution. Tyndall drained water from a horizontal pipe at the bottom of an illuminated vessel, and showed that light was constrained to follow the parabolic arc of the water. Some years later, a patent was awarded to W Wheeler (1881) of Concord, Mass, for his delightful "Apparatus for Lighting Dwellings or Other Structures" using total internal reflection in a network of hollow rods, illuminated by a single central arc lamp. It was C V Boys (1887) who succeeded in drawing the first quartz fibres, not for the propagation of light, but for use as mechanical suspensions in sensitive measuring instruments. The use of fibres in modern times dates back to patents by Baird (1927) and Hansell (1930) for image transfer devices in television systems using silica fibres, and to Lamm (1930), who attempted to use flexible fibre bundles for image transmission in gastroscopy. All these devices

used uncoated fibres and so had poor transmission, and it was not until the work of van Heel (1954), Hopkins and Kapany (1954) and Hirschowitz et al. (1958) that high-quality bundles of fibres individually coated with a sheath of lower refractive-index material were demonstrated for image transfer. The 1950s and 60s saw considerable further development of coherent (ie, image-transmitting) and incoherent (ie, scrambled) fibre bundles, together with the introduction of other devices such as fibre-optics faceplates for cathode-ray tubes, and optical-fibre lasers (see, eg, Kapany, 1967, Chap. 1; Allan, 1973, Chap. 1).

As we shall see, coherent fibre bundles - which are better described as imageguides - have a role in fibre-coupled multi-object spectroscopy, so we digress briefly to consider some of their properties. In Kapany's (1967) time, they were made by winding a single fibre many times around a drum, so that when the bundle was removed, secured at one point with cement and then cut, the ends would form the matching input and output faces. This technique produced bundles of a few thousand fibres a few metres long, which would, in use, have a gradually-increasing number of "dead" fibres due to breakage; by improved techniques (eg, drawing fused bundles of rods), flexible imageguides can now be made with tens of thousands of cores, tens of metres long, and with no lost fibres (eg, Fujikura, 1982). The general optical properties of fibres are discussed in Section 2.2, but there are some that are peculiar to imageguides; these include the packing fraction, p (the ratio of the total light-transmitting (ie, core) area to the total endface area), and the resolution. The former is maximized when hexagonal fibres are fused together to produce hexagonal packing. (See Morokuma, 1979, for a complete description of the properties of imageguides.)

In the late 1960s, a major change occurred in the thrust of research on optical fibres. The attenuation, A (in dB), of a fibre is defined by the normal power-loss formula

$$A = -10 \log (P_o/P_i) \qquad (2.1)$$

(where P_i and P_o are, respectively, the input and output optical power), and, in the mid-1960s, a unit-length attenuation (A') of 1000 dB/km (ie, 50 percent loss in a three-metre fibre) would have been somewhat better than typical. This was not a serious problem for the applications in which fibres were then being employed, but in 1966 it was demonstrated by C K Kao that fused silica fibres with very much lower attenuation were theoretically possible (Kao and Hockham, 1966; see also Kao, 1979). Together with the recently-invented laser, this could open the way to optical communications with an enormously high bandwidth provided by the optical carrier frequency. Thus, a strong stimulus was provided for reducing the attenuation of fibres and, by 1970, the first 20 dB/km fibre had been produced by Corning Glass Works at Corning, NY (see, eg, Giallorenzi, 1978). The key to low attenuation was high purity of the basic materials, and subsequent improvements in this area have now led to fibres with an attenuation of ~0.1 dB/km, with the promise of yet further improvements in the infrared region. The communications industry is currently the main user of single optical fibres, but there is growing interest in their use as remote sensors for pressure, temperature, velocity, acceleration, electrical current, etc. (see, eg, Dakin, 1983).

The low-loss fibres available today fall into the basic categories of

multi-mode fibres, which comprise step-index and graded-index types, and single-mode fibres. These are illustrated schematically in Figure 2.1. When considered as a dielectric waveguide, a fibre will only support a certain number of discrete modes of propagation, defined by the solution of Maxwell's field equations subject to the cylindrical boundary conditions of the fibre (see, eg, Kapany, 1967, Chap. 3; Allan, 1973, Chap. 9; Giallorenzi, 1978). If the fibre diameter is large compared with the wavelength of light, a very large number of modes will be supported, and the behaviour of the fibre can be described in terms of geometrical optics. This is the situation encountered in multi-mode fibres. Smaller fibres propagate fewer modes and, below a certain critical fibre diameter (which also depends on the refractive indices of the core and cladding), only one mode will be supported for a given wavelength. This lowest-order mode is termed the HE_{11} mode, and is propagated in single-mode fibres. Certain types of single-mode fibre will preserve the polarization state of light passing through them (see, eg, the review by Rashleigh, 1983) but, in general (and invariably, for multi-mode fibres), the effects of multiple reflections, residual stresses and scattering conspire to destroy the polarization.

As will be seen from Figure 2.1, step-index fibres transmit light by total internal reflection, whereas the light is guided by refraction in the core of graded-index fibres. The refractive-index profile of these latter fibres is axially symmetric, so that the fibre acts as a series of lenses, repeatedly focusing the beam. (Graded refractive-index lenses (or GRIN lenses) similar to short lengths of fibre are, in fact, commercially available.) The rays depicted in Figure 2.1(a) and (b) are meridional rays (ie,

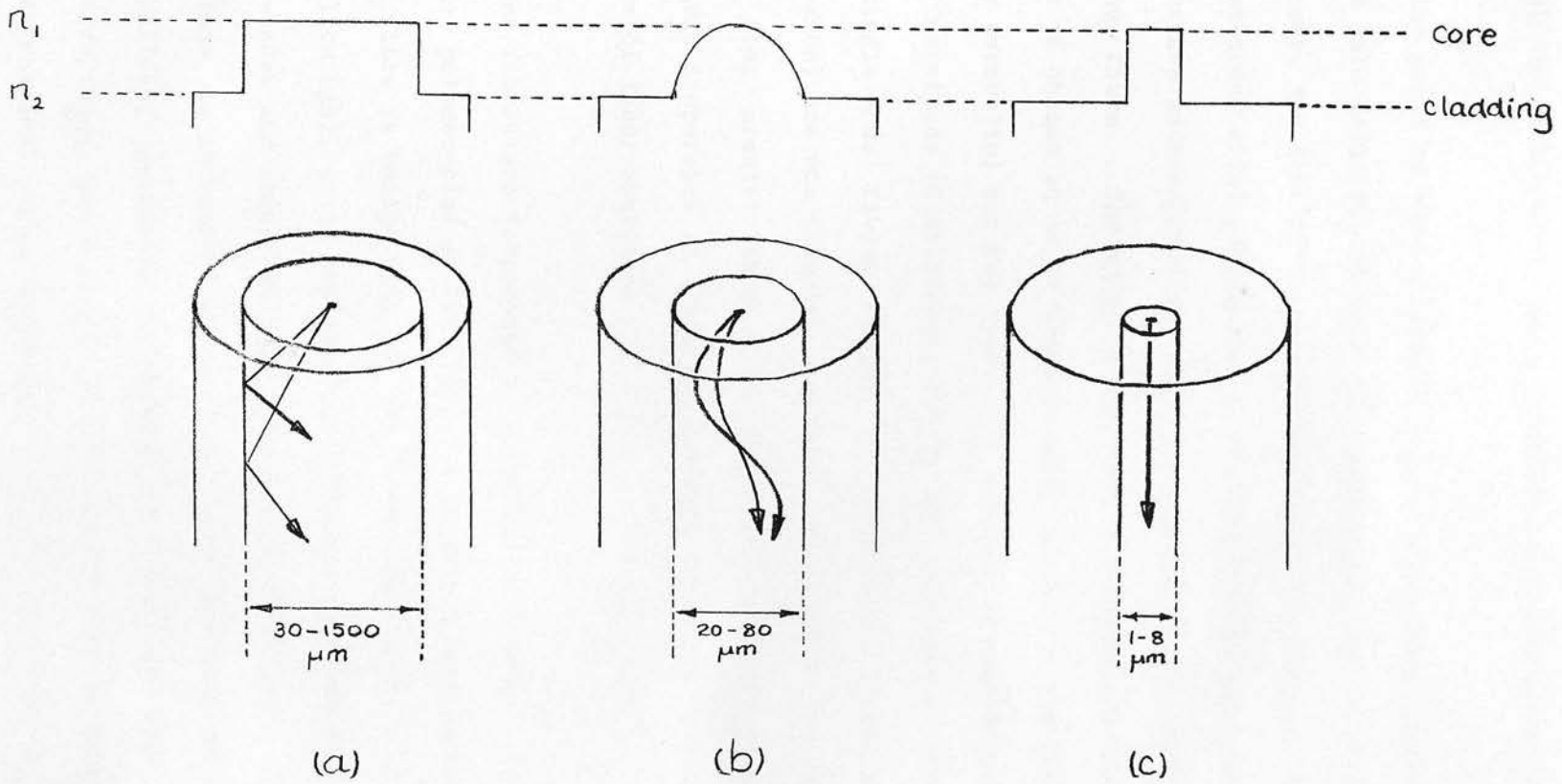

Figure 2.1 Schematic illustration of the three main types of optical fibre, together with their propagation modes and refractive-index profiles. (a) Step-index multi-mode fibre; (b) graded-index multi-mode fibre; (c) single-mode fibre.

those passing through the axis of the fibre); skew rays do not pass through the axis, but follow a pseudo-helical path along the fibre.

From the point of view of communications engineering, step-index multi-mode fibres are deficient in that they suffer from high modal dispersion; that is to say, the time difference at the output end between the lowest- and highest-order modes propagated is relatively large (typically a few ns/km). This causes pulse-spreading, and limits the bandwidth that can be carried by the fibre. The shape of the refractive-index profile of graded-index fibres is chosen so as to minimise modal dispersion (in fact, it is very nearly parabolic) and may produce an increase in capacity of up to two orders of magnitude (Giallorenzi, 1978). For this reason, graded-index fibres and single-mode fibres (which, by definition, do not suffer from modal dispersion) are now industry standards, particularly for long-haul applications (ie, greater than a few km). Bandwidths are primarily limited by chromatic dispersion in the fibre material (which is clearly minimised by the use of laser sources).

Low-loss fibres are fabricated by a variety of methods. Step-index fibres may be polymer-clad silica (PCS), in which a single strand of high-purity quartz fibre is coated with a low refractive-index silicone resin, or all-silica (AS), which has superior transmission characteristics. Low-loss graded-index and single-mode fibres are also of the AS type. Here, the variations in refractive index are produced by doping the pure silica with metal halides; germanium and phosphorous dopants are used to increase the refractive index, while boron and fluorine are used to lower it. A process known as chemical vapour deposition (CVD), or vapour-phase oxidation (VPO),

is employed to fabricate the AS fibre. The technique has several variants, but consists basically of the deposition of a soot of glass spheres (~0.1 μm in diameter) - formed by burning the glass-forming vapours in oxygen - onto a substrate, which may be a rod (outside CVD), tube (inside CVD) or flat rotating surface (axial CVD). The relative proportions of the dopants can be varied during deposition to build up (~ 1000) layers of soot particles with differing refractive indices; the process is usually carried out under computer control. (In the axial-deposition technique, the refractive-index profile is often produced by creating a deposition-temperature gradient for silica with a single dopant; see, eg, Chida et al., 1983.) Sometimes helium is added to the flow gas to speed up the deposition process. Once the soot preform is complete, it is sintered under heat to form a solid glass preform, with the desired refractive-index profile, which can then be drawn (again under heat) into a fibre. Depending on the exact fabrication method, the substrate may become part of the resulting fibre (as does the (pure silica) tube in the inside CVD process) or may be removed prior to sintering or drawing (as in the outside CVD process). Details of these techniques may be found in papers by Giallorenzi (1978), Schultz (1979), Blankenship and Deneka (1982), Inada (1982) and Miya, Nakahara and Inagaki (1983).

Fibres are usually jacketed during the drawing process with a protective outer coating. This performs the multiple role of protecting the bare fibre surface from scratches and other damage (which could lead to fracture), providing additional tensile strength, and rendering the fibre easier to handle by increasing its outside diameter. It is important that the jacket does not exert compressional forces on the fibre since these

will lead to increased attenuation (probably because of the occurrence of microbends due to localized pressure); other considerations are the matching of temperature coefficients of the fibre and jacket, their mutual adhesion, etc. Thus, a typical jacket might consist of a silicone rubber buffer layer, with a harder thermoplastic, UV-cured resin or nylon outer layer. An unjacketed fibre can withstand axial tensile stresses of many tens of kg mm^{-2} (eg, Chesler and Dabby, 1976; Allan, 1973, Chap. 3) and jacketing can increase this by more than a factor of two. The weight of jacketed fibre clearly depends on its diameter; a typical small-core (<100 μm) fibre in a 0.9 mm polyamide jacket weighs ~0.7 kg/km (Fujikura, 1982). The requirements for fibre jacketing and cabling are discussed in detail by Wolf (1979). Yoshizawa et al. (1981) present some experimental results on the compression of jacketed fibres.

In order for light to enter and leave a fibre, its end faces must be flat and perpendicular to its axis. Two techniques are commonly used to achieve this, namely cleaving and polishing; both have been extensively used by the writer in the preparation of optical fibre feeds. The method of cleaving gives surprisingly good results, and relies on the controlled fracture of the bared fibre from an incision scribed with a sapphire or diamond edge. Numerous variations in technique have been described (eg, by Gloge et al., 1973; Chesler and Dabby, 1976), compared interferometrically (Gordon, Rawson and Nafarrate, 1977) and recompared with torsional variations (Saunders, 1979); all give reasonably similar results once the basic skill has been acquired. Commercially-made fibre-cleaving tools are also available. While the method of cleaving gives satisfactory results for the rapid end-preparation of test-fibres, it has been found by most workers in

the area of astronomical fibre optics to be inferior to polishing when the highest-quality surfaces with perfectly repeatable characteristics are required. In this method, the bared fibre is encased in a ferrule of metal or other hard material using epoxy cement, and the end face ground (by hand or machine) with successively finer abrasives until the required surface is achieved. The abrasives are typically supplied as coatings on Mylar sheets, and are used on a hard flat slab with the fibre supported above in a chuck to maintain perpendicularity and prevent any tendency towards sphericity in the fibre end. Optically flat surfaces can be achieved rapidly with this method, and the use of 0.3 μm abrasive to finish produces a high degree of polish. This method is the only one suitable for the production of coplanar arrays of fibre ends, as in the "slit" of a multi-fibre spectrograph, for example.

There is a frequent requirement in the communications industry for fibres to be joined in series, either permanently by means of a splice, or temporarily with a connector. Optical losses in such joints are incurred by angular or transverse misalignment of the fibres, non-perpendicularity or non-flatness of their ends and Fresnel (ie, reflection) losses (see, eg, Esposito, 1979; Otten, 1981; Opielka and Rittich, 1983). Fibres are commonly spliced by thermal fusing (eg Bisbee, 1971) or with UV-cured optical cements, incurring losses of typically ~0.1 dB (Giallorenzi, 1978). Optical connectors must withstand repeated insertions (often in conditions that may introduce dirt or grit) in such a way that the exact mechanical alignment of the fibres is always preserved. Several types of optical connector have been developed, ranging from those that simply butt the fibres together (sometimes with an index-matching fluid to reduce Fresnel losses)

to expanded-beam devices using miniature collimating lenses to render the beam parallel between the fibres (eg, Nicia, 1981; Challans, 1983). Losses in these devices are typically up to 2 dB, but further improvements are likely. For example, Khoe, van Leest and Luijendijk (1982) have described a single-mode butted fibre connector (requiring a mechanical tolerance of considerably less than 1 μm) which has an average connection loss of 0.32 dB without index-matching. While fibre splicing is likely to be applied to astronomical fibre-optics systems only in unusual circumstances (eg, fibre breakage), it is possible that multiple connectors may offer advantages for proposed systems with large numbers of fibres ($j \sim 1000$), if the losses can be made small enough.

2.2 Characteristics of step-index fibres

It is the low optical loss of communications-type fibres that makes them attractive for astronomical use and, in that respect, the aims of the communications industry and the astronomical community are alike. Unfortunately, that is almost the total extent of the common ground, and beyond it, their respective needs are increasingly divergent. In particular, as we have seen, the multi-mode step-index fibre is no longer favoured by the communications sector for anything other than short-haul applications (eg, local area networks, avionics, etc.), because its modal dispersion leads to unsatisfactory (~10 ns/km) pulse-spreading. For the astronomer, whose "pulses" (ie, exposure times) may be thousands of seconds long, this is clearly of no consequence; of much greater interest are the image-scrambling properties of fibres, which will influence the uniformity of illumination of spectrograph optics in the presence of guiding or posi-

tioning errors and variable seeing. In this respect, step-index fibres are superior to the graded-index type, where the repeated focusing may preserve some memory of the image structure on the input face (1). Step-index fibres have thus found universal favour among workers in the field of astronomical fibre optics, and it has been necessary to examine the products of a wide range of manufacturers to find suitable fibres, particularly in view of the additional trend in the communications sector towards longer wavelength standardization (from 850 nm to the current 1.3 μm, with 1.55 μm likely in the near future and up to 4 μm possible with new materials; see, eg, Aggarwal, 1982; Mack and Tebo, 1986). Fortunately, the fibre-optics industry as a whole is sufficiently buoyant that manufacturers can be found whose products match astronomical requirements tolerably well. Indeed, there is some prospect of fibres being "tailor-made" for particular astronomical applications if sufficient quantities are required, and if procurement budgets will allow it.

Considering now the characteristics of step-index fibres, we begin with the bulk attenuation, which is a property of the fibre material itself (so that the discussion here applies equally to all fibre types). The losses within the fibre are due to material absorption and scattering and, in Figure 2.2, the characteristic wavelengths of the principal loss mechanisms are illustrated. In the UV, losses are due to Rayleigh scattering (proportional to λ^{-4}) by small-scale ($<\lambda$) fluctuations in concentration and composition, and

---

(1) Single-mode fibres are not suitable for astronomical applications because of their very restricted light-acceptance characteristics.

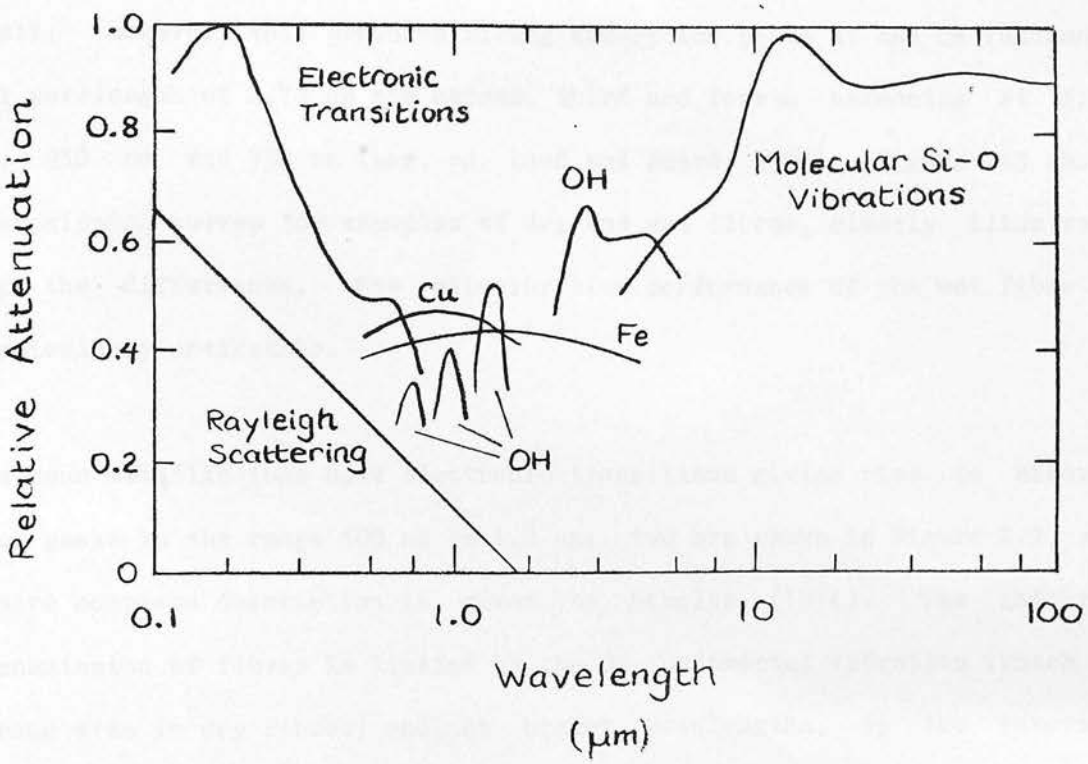

Figure 2.2 Principal sources of optical attenuation in fibres (from Wolf, 1979).

by electronic transition absorption by impurity ions of dopants and trace contaminant metals. The introduction of hydroxyl (OH) radicals into the silica (to produce so-called "wet" fibres) can substantially improve performance in the UV and allow the transmission to approach the Rayleigh limit; however, this produces strong absorption peaks at the OH fundamental wavelength of 2.73 μm and second, third and fourth harmonics at 1.37 μm, 950 nm and 730 nm (see, eg, Lund and Enard, 1983). Figure 2.3 shows transmission curves for examples of dry and wet fibres, clearly illustrating the differences. The superior blue performance of the wet fibre is particularly noticeable.

Numerous metallic ions have electronic transitions giving rise to absorption peaks in the range 400 nm to 1.8 μm; two are shown in Figure 2.2, and a more complete description is given by Schultz (1974). The infrared transmission of fibres is limited by the OH fundamental vibration (which is strong even in dry fibres) and, at higher wavelengths, by the internal vibrational transitions of the SiO_2 molecule. In addition to all these mechanisms, some fibres exhibit an absorption peak at 633 nm attributable to defects induced by the drawing process. Fibre loss mechanisms in general are reviewed in detail by Barnoski and Personick (1978), and they are described with particular reference to astronomical applications by Lund and Enard (1983), Gray (1986) and Heacox (1986).

The numerical aperture of a step-index fibre is defined, in common with that of other optical elements, as

$$NA = n_o \sin \theta_o, \qquad (2.2)$$

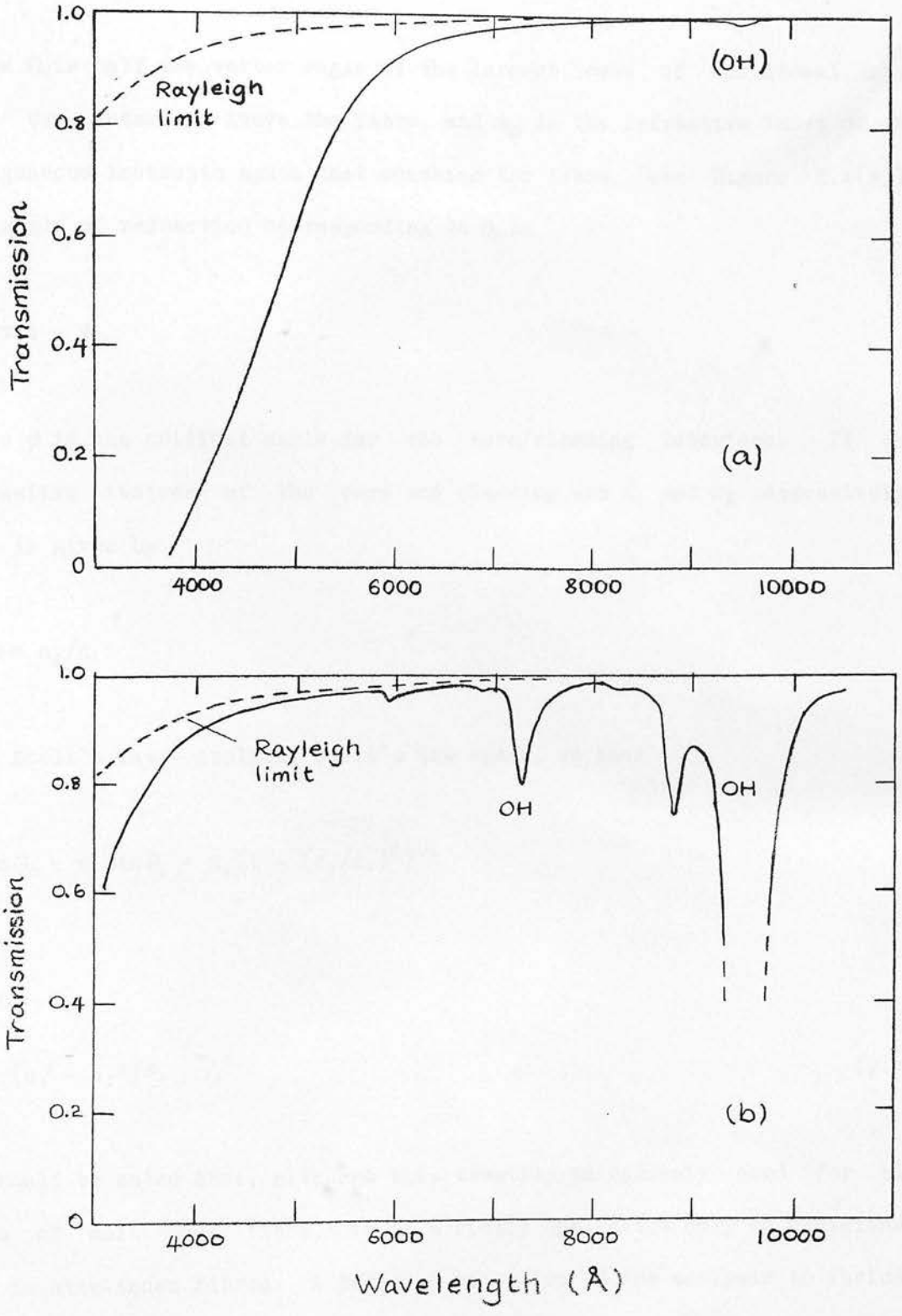

Figure 2.3 Spectral transmission of 10-metre samples of two different fibre types: (a) AWA-SD with 40 μm core, (b) Polymicro-FHP with 320 μm core (measured by Peter Gray). The diagrams show the characteristic differences between "dry" (a) and "wet" (b) fibres (see text). Some of the high UV attenuation of the dry fibre may also be due to its smaller core diameter (see Lund and Enard, 1983).

where θ_o is half the vertex angle of the largest cone of meridional rays that can enter or leave the fibre, and n_o is the refractive index of the homogeneous isotropic space that contains the fibre (see Figure 2.4(a)). The angle of refraction corresponding to θ_o is

$$\theta_1 = \pi/2 - \phi,$$

where ϕ is the critical angle for the core/cladding interface. If the refractive indices of the core and cladding are n_1 and n_2 respectively, this is given by

$$\sin\phi = n_2/n_1$$

from Snell's law. Applying Snell's law again, we have

$$n_o \sin\theta_o = n_1 \sin\theta_1 = n_1(1 - (n_2/n_1)^2)^{1/2}.$$

Thus

$$NA = (n_1^2 - n_2^2)^{1/2}. \qquad (2.3)$$

It should be noted that, although this identity is commonly used for all types of multi-mode fibre, it is strictly applicable only to meridional rays in step-index fibres. A detailed extension of the analysis to include skew rays and graded-index fibres has been given by Gallawa (1982).

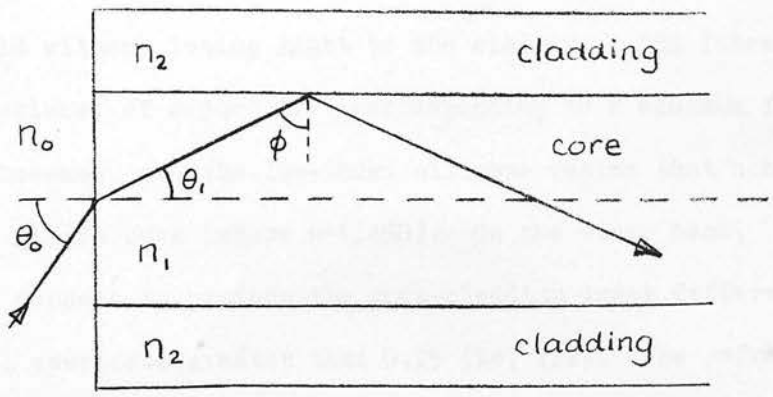

(a)

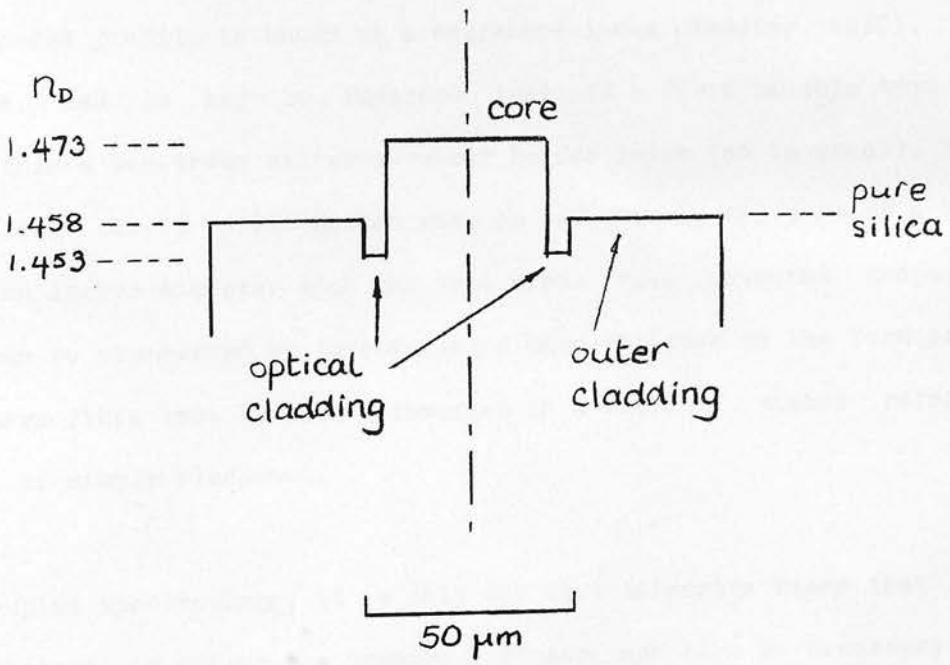

(b)

Figure 2.4 (a) Geometry of step-index fibre NA. (b) Refractive-index profile of AWA-SD 40-μm core fibre. The outer-cladding diameter is 125 μm.

The numerical aperture is clearly indicative of the fastest beam that the fibre can hold without losing light to the cladding. PCS fibres typically have high NA values, of around 0.4 (corresponding to a minimum focal ratio of f/1.1), because of the low-index silicone resins that can be used to coat the pure silica core (where n=1.458). On the other hand, AS fibres, which rely on dopants to produce the core-cladding index difference, seldom have numerical apertures greater than 0.25 (ie, f/2). The refractive-index profile of a typical small-core (40 μm) AS fibre is shown in Figure 2.4(b); it is, in fact, the same dry-type fibre whose transmission curve appears in Figure 2.3(a). It will be seen to have a numerical aperture of 0.242. This fibre was produced by the inside CVD process, and the original substrate tube now appears as the pure silica outer cladding. Such a refractive-index profile is known as a depressed-index cladding (DIC), or "W" profile, and it may be remarked that if a fibre of this type is enclosed within a low-index silicone-rubber buffer layer (as is usual), the outer cladding itself will become what is effectively the core of a PCS fibre of much larger diameter than the true core. This unwanted propagation mode can be suppressed by introducing a mode-stripper in the form of a length of bare fibre that is either immersed in a fluid of higher refractive index, or simply blackened.

In fibre-coupled spectroscopy, it is only for fast telescope beams that the fibre NA becomes a matter for concern. It may then also be necessary to consider the behaviour of the NA in curved fibres. By some rather tedious geometrical optics, it can be shown that for a fibre of core diameter 2r containing a bend of radius R (where R>>r), the numerical aperture becomes

$$NA = [n_1^2 - (1+2r/R)n_2^2]^{1/2} \qquad (2.4)$$

(see, eg, Allan, 1973, Chap. 2), so that light may be lost to the cladding on bends. (This analysis considers only rays in the meridional plane, of which there can only be one in a curved fibre; the behaviour of curved fibres in practice is therefore dominated by skew rays.) Finally, it may be mentioned that the treatment of fibre NA in the presence of angled end faces is also given by Allan (1973, Chap. 2), and that the NA for tapered fibres is given by Kapany (1967, Chap. 2). The first of these cases may result from fibre polishing errors, and will produce an overall effective reduction in NA; the second has been suggested as a way of increasing the focal ratio of very fast telescope beams (Lynden-Bell, 1986), and will change the NA by the ratio of the output to the input diameter of the fibre (which is assumed to be straight).

In the same way that the nuclear hardening of fibres, or their insusceptibility to tapping, holds no interest for astronomers, communications engineers have had no need for involvement with some of the properties of fibres that concern us here (2). Uppermost among these is <u>focal-ratio</u>

---

(2) There is growing interest in the communications industry in multiplexing techniques for increasing the effective bandwidth of fibres. Currently, the most popular of these is wavelength-division multiplexing, where separate carrier beams of different wavelengths are propagated simultaneously; however, Herskowitz, Kobrinski and Levy (1983) have suggested the use of angular-division multiplexing, where fibres with low modal coupling

degradation (FRD) or beamspreading, the decrease in focal ratio exhibited by a light beam after its passage through a fibre. Since the onset of interest in optical fibres for astronomy, this phenomenon has been the subject of a large number of experimental investigations, to the extent that a substantially complete bibliography requires a page of its own (Table 2.1). Most of these investigations were designed to identify specific fibre types with minimal FRD characteristics.

The effects of focal-ratio degradation are illustrated schematically in Figure 2.5. It will be seen that the beamspreading is more pronounced for slower focal ratios, so that in a typical fibre, an f/8 input beam will emerge with a much lower effective focal ratio, perhaps as low as f/4. This has serious consequences for telescope-spectrograph coupling, as will be discussed in the next section. The energy distribution in the emergent beam is, in fact, of a pseudo-Gaussian form, and the FRD properties of fibres are better described by diagrams such as that shown in Figure 2.6(a). Here, the absolute transmission of the fibre is plotted for a range of output focal ratios accepted by the detector, and this is done for several fibre input focal ratios. The resulting family of curves clearly illustrates the extent to which the light is contained within a given output beam. For very fast input beams, FRD may spread light beyond the fibre

---

permit the simultaneous propagation of separate carrier beams with different launch angles (ie, entrance angles of incidence). The implementation of this technique could lead to the development of fibres with very low focal-ratio degradation.

Table 2.1 Experimental investigations of focal-ratio degradation

(see text)

Angel et al. 1977	University of Arizona (Steward Observatory)
Heacox 1980	University of Arizona (Lunar and Planetary Laboratory)
Barden Ramsey and Truax 1981	Pennsylvania State University
Gray 1982	Anglo-Australian Observatory
Evans 1983	Australian National University (MSSSO)
Gray 1983a	Anglo-Australian Observatory
Lund and Enard 1983	European Southern Observatory
Powell 1983	Royal Greenwich Observatory
Schiffer 1983	Heidelberg (Landessternwarte Königstuhl)
Gray and Sharples 1985	Anglo-Australian Observatory
Gray 1986	Anglo-Australian Observatory
Ramsay and Huenemoerder 1986	Pennsylvania State University
Heacox 1986	University of Hawaii

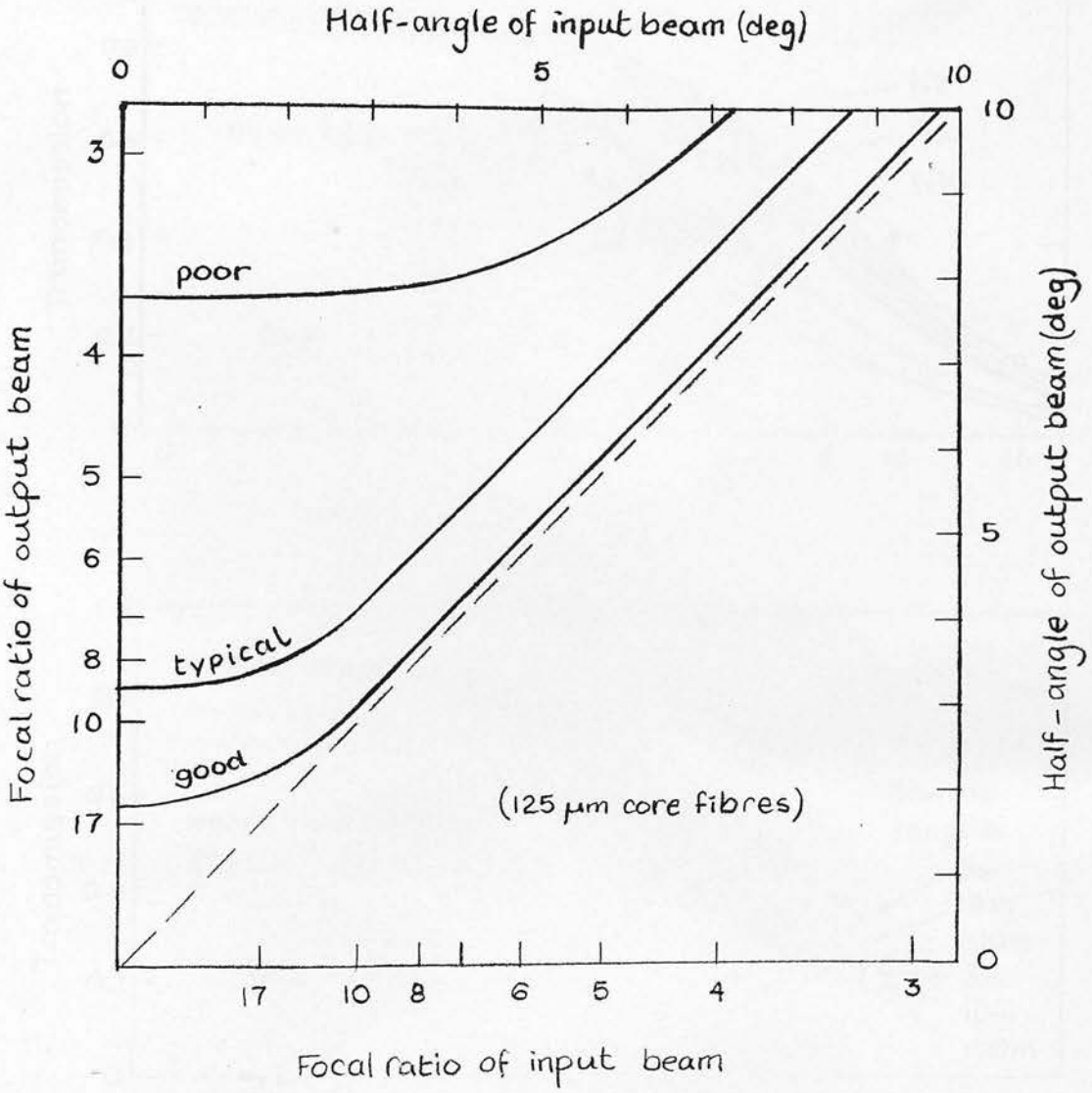

Figure 2.5 Schematic plot of output focal ratio against input focal ratio for fibres with good, typical and poor focal-ratio degradation characteristics. For the better fibre types, the degradation at low focal ratios amounts to a constant angular difference between the incident and emergent cones; in the limit, this will be equal to the diffraction-broadening of a circular aperture equal to the fibre diameter. (After Heacox, 1980; Barden, Ramsay and Truax, 1981.)

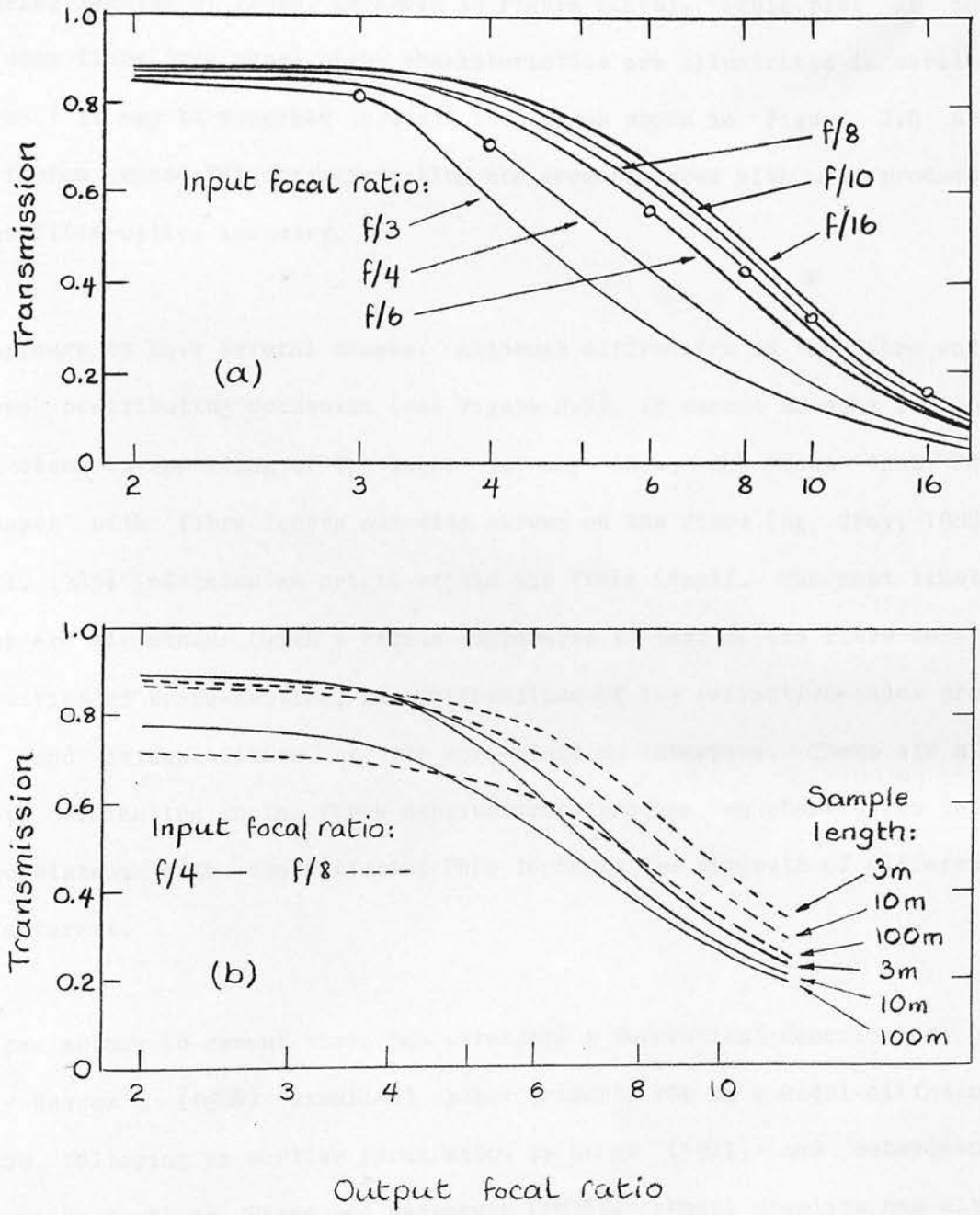

Figure 2.6 Focal-ratio degradation (FRD) curves for specific fibre types. The fraction of the fibre input flux to emerge within a particular focal ratio is plotted against that focal ratio. (a) The FRD curve for a 5-metre length of Fibropsil QSF-400ASW (400 μm core) fibre, plotted for various input focal ratios. The circles indicate the fibre transmission where input and output focal ratios are equal (from Powell, 1983). (b) The FRD curve for AWA-SD (40 μm core) fibre plotted for f/4 and f/8 input focal ratios, and for various lengths (measured by Peter Gray).

NA, causing loss to the cladding. The measurements can be extended to differing lengths of fibre, as shown in Figure 2.6(b). (This plot is for the same fibre type whose other characteristics are illustrated in earlier figures.) It may be remarked that all the curves shown in Figure 2.6 are for fibres whose FRD characteristics are good compared with most products of the fibre-optics industry.

FRD appears to have several causes. Although diffraction at the fibre ends is one contributing mechanism (see Figure 2.5), it cannot account for the total observed spreading of the beam; in any case, the fact that FRD increases with fibre length and with stress on the fibre (eg, Gray, 1982; Powell, 1983) indicates an origin within the fibre itself. The most likely causes are microbends (with a radius comparable to that of the fibre core), deformities of cross-section, non-uniformities of the refractive-index profile, and irregularities at the core-cladding interface. These are all defects originating in the fibre manufacturing process, an observation that is consistent with the differing FRDs found in the products of different manufacturers.

Only one author in recent times has attempted a theoretical description of FRD; Heacox's (1986) excellent paper presents FRD as a modal-diffusion process, following an earlier formulation by Gloge (1972) and subsequent analysis by Gambling, Payne and Matsumura (1975). (Modal coupling has also been discussed by Jeunhomme and Pocholle, 1975.) Heacox introduces a characteristic modal-diffusion length, l_D, approximately equivalent to the fibre length for which the internal FRD processes produce as much beamspreading as does diffraction.

It is Heacox (1986) who has also done the most thorough work on the last property of fibres that we shall consider here, that of image scrambling. The ideal fibre in this regard would be one that had a uniformly-illuminated output face, irrespective of the positioning of a point image (ie, a star) on the input face. Considering the polar coordinates of radius and azimuth on the fibre end-face, step-index fibres are extremely efficient at azimuthal scrambling by virtue of the pseudo-helical propagation of skew rays. Their scrambling properties in the radial direction are, to some extent, related to their beamspreading properties; however, Heacox (1986) has shown that even for a perfect cylindrical waveguide, there is substantial radial scrambling (see Figure 2.7). It may be remarked that some of the flux distributions in Figure 2.7 have been observed in practice during the FLAIR multi-object photometry experiments described in Chapter 7; here, large-core (200 μm) fibres with extremely good FRD characteristics are used to transmit small (~25 μm) stellar images, and positioning errors may give rise to a variety of image locations on the fibre input face.

We conclude this account of the properties of step-index fibres by listing in Table 2.2 some specific fibre-types that have been shown to have suitable characteristics for astronomical use. Among them are a few that show outstanding properties, notably the Fujikura fibre tested by Heacox (1986), which has exceptional FRD characteristics, and the new fibres tested by Gray (1986), which have very good UV transmission. Many of the fibres listed in Table 2.2 are embodied in the spectroscopy systems described in Chapters 4 and 6.

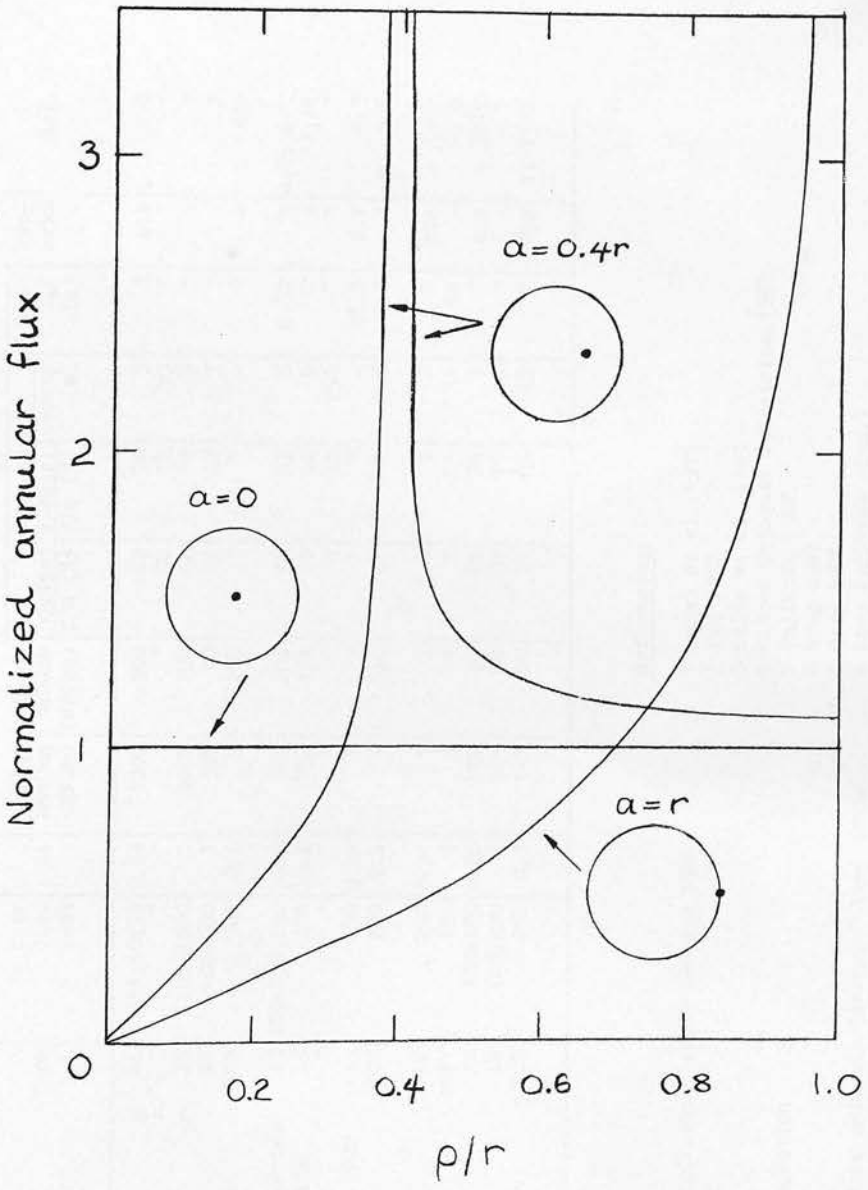

Figure 2.7 Normalized annular flux distributions on the output face of an idealized optical fibre, for point sources imaged (1) at the centre of the input face, (2) offset from the centre by 40 percent of the core radius, and (3) at the edge of the core on the input face. The fibre core radius is r, the radial coordinate on the input end of the fibre is a, and that on the output end is ρ (from Heacox, 1986).

Table 2.2 Properties of some commercially-available step-index fibres

Fibre	Type	Core dia. (μm)	NA	Blue atten. @350nm (dB/km)	Blue atten. @400nm (dB/km)	FRD: f/8 beam in Output f/8 (%)	FRD: f/8 beam in within: f/6 (%)	FRD: Length (m)	FRD: f/6 in l_D* (m)	Remarks	Ref.
AWA-SD	AS	33;40;50	0.24	~3000	900	62	78	3	?	a;b	2;8
"	"	"	"	"	"	54	72	10	"	"	"
EBI-HCS	AS	100-1000	?	2000	100	66	79	3	?	-	7
Fiberguide-G	AS	100;200	?	320	90	63	82	3	?	-	7
Fibropsil QSF-300A	PCS	300	0.4	?	~200	?	?	-	?	e	4;6
Fibropsil QSF-AS series	AS	100;135;200	≥0.2	900	200	65	83	3	0.52	b	4;7;9;11
Fibropsil QSF-400ASW	AS	400	≥0.2	330	114	43	61	5	?	c	4;11
"	"	"	"	"	"	28	33	250	"	"	"
Fujikura S.50/125.3000	AS	50	0.20	?	?	?	?	-	25.0	d;f	5;9
Galite 4000-LC-P	PCS	200	0.4	?	140	45	?	2.5	?	a	3;6
Maxlight KSC 200A	PCS	200	0.34	?	?	?	?	-	?	a;e	6
Pirelli SC 125 C1	PCS?	125	?	?	?	?	?	-	0.04	-	9
Polymicro-FH	AS	100-400	0.22	180	80	64	78	3	?	c;g	7;10
Spectran-SG	AS	105;200	?	361	89	60	77	3	?	-	7
Valtec-PC10	PCS	250	0.3	143	99	51	65	20	?	a;g	1;11;12

Notes:

* Measured modal-diffusion length (Heacox 1986)

Remarks:

a No longer in production
b Dry fibre
c Wet fibre
d Manufacturer's data indicate "average" blue trans.
e Test data at f/5 (length 2m) show reasonable FRD
f Exceptional FRD performance
g Exceptional blue transmission

References:

1 Angel et al. 1977
2 AWA 1982
3 Ellis et al. 1983
4 Fibres Optiques Industries 1983
5 Fujikura 1982
6 Gray 1982
7 Gray 1986
8 Gray (private comm.)
9 Heacox 1986
10 Polymicro Technologies 1986
11 Powell 1983
12 Barden Ramsay and Truax 1981

2.3 Considerations in fibre-feed design: general

As we have seen, the function of the fibre feed in multi-object spectroscopy is two-fold: image transfer (from telescope focus to collimator focus) and image reformatting (from a random pattern to a linear array). The transfer distance clearly determines the length of the fibre feed, and it may range from a few centimetres (when the telescope and spectrograph are merely separated by spacers to permit the fibre reformatting) to many tens of metres, if fibres are being brought from the prime focus of a large telescope to a spectrograph on the dome floor. (A 40-metre (single) fibre link of this kind has been successfully used at the ESO 3.6-metre telescope by Lund and Enard, 1983.)

Optical loss is clearly the most fundamental parameter dependent on fibre length, and it has two components. First, the bulk attenuation of the fibre material will combine with the Fresnel losses (3) at the fibre ends, given by

---

(3) (a) These losses could be reduced almost to zero by the addition of wide-band multi-layer coatings on the fibre ends. To date, only Heacox (1986) has reported the use of anti-reflection coatings, on fused-silica plates coupled with index-matching material to the ends of a single-fibre link. (b) Note that Equation 2.5 is strictly applicable only in the case of normal incidence, but that it is a very good approximation for beams even as fast as f/1 (see, eg, Allen, 1973, Chap. 3).

$$R_F = (n_1-n_o)^2/(n_1+n_o)^2, \qquad (2.5)$$

and with a scattering loss S, caused by imperfect polishing of the fibre end faces (4), to give the fibre transmission

$$T = (1-R_F)^2(1-S)^2 10^{-A'l/10} \qquad (2.6)$$

from Equation 2.1, where A' is the unit-length attenuation of the fibre and l its length. All three terms in this expression are clearly wavelength-dependent, the last most strongly so.

The second component of length-dependent loss is due to focal-ratio degradation, which may spread light outside the cone accepted by the spectrograph collimator. We will denote the value of this loss by D. Figure 2.8(a) is a schematic illustration of the input and output beam-profiles of a spectrograph fibre-feed, for the two cases of slight and severe FRD. For spectrograph optics that are matched directly to the focal ratio of the telescope (by far the most common situation facing the designers of fibre feeds), it will be seen that not only is the beam degraded beyond the periphery of the collimator mirror or lens, but that the shadow of the telescope central obstruction is partially or wholly filled in. Many spectrographs have a central obstruction within the shadow

---

(4) Gray and Sharples (1985) quote 0.03 as a typical value of S, with 0.02 as a minimum value for good-quality end-faces.

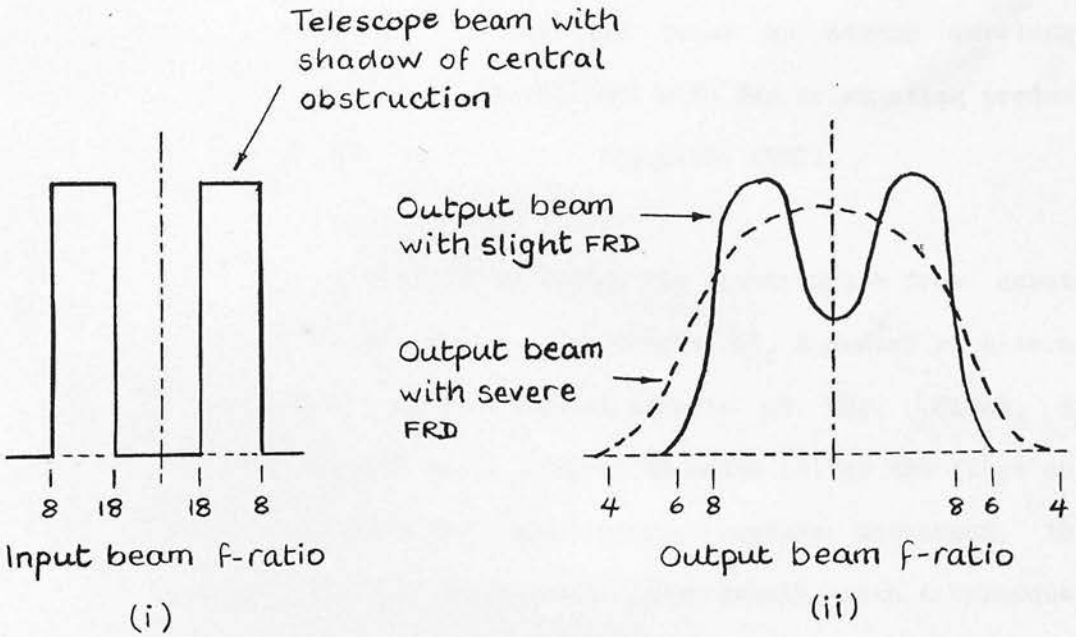

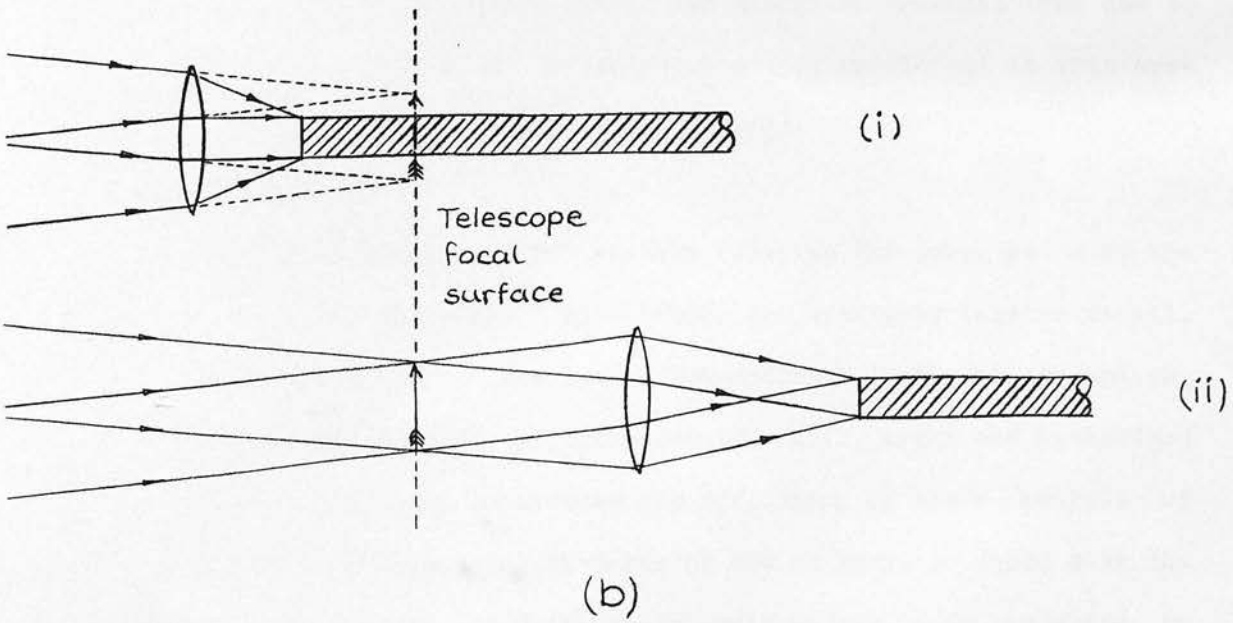

Figure 2.8 (a) Intensity profile of an f/8 telescope beam (i) before, and (ii) after its passage through an optical fibre, showing the effect of focal-ratio degradation (after Gray, 1983a). (b) Two schemes for using microlenses to decrease the focal ratio of a telescope beam before its passage through a fibre. (i) Re-imaging onto the fibre face; (ii) pupil imaging onto the fibre face (see text). (From Hill, Angel and Richardson, 1983.)

of that of the telescope, and this can be the cause of considerable additional loss. It may be noted that Gray has found no strong wavelength dependence of FRD, an observation consistent with FRD originating predominantly in reflection mechanisms (Gray and Sharples, 1985).

In the absence of complete freedom to design the spectrograph from scratch (a luxury that is not always denied - see Chapter 6), a number of alternatives are open for reducing the detrimental effects of FRD. First, the focal ratio of the collimator can be reduced to match better the fibre output beam. If the remainder of the spectrograph remains unchanged, this implies a reduction of the collimator focal length, with a consequent decrease in spectral resolution at the detector. This method has been employed at the AAT (Gray, 1983b; 1986), where an f/8 collimator mirror is replaced by one of f/6 for fibres work. The estimated residual loss due to FRD (collimator overfilling and central-obstruction infilling) in this system is D~15-20 percent (Gray and Sharples, 1985).

The other methods of minimising FRD involve reducing the focal ratio of the beam before it enters the fibre. Hill (1984) has discussed this in detail, and notes two basic methods: the use of conventional focal-reducer optics, and the use of microlenses at the fibre inputs. Hill, Angel and Richardson (1983) and Hill (1984) have considered the efficiency of these methods of telescope-spectrograph coupling in terms of the $A\Omega$ product, where A is the area of an optical element and Ω the solid angle of the beam accepted by the detector (see, eg, Meaburn, 1976, Chap. 1). In a perfect optical system, this product is invariant and equal to $A_t\Omega_s$, where A_t is the area of the telescope primary, and Ω_s the solid angle on the sky of light accepted

by the spectrograph. The effect of a fibre is to increase the $A\Omega$ product of the emergent beam, since A (now the fibre core area) will be larger than a point image on the input end, and Ω (the solid angle of the emergent beam) will be increased by FRD. A well-matched fibre coupler will reduce the $A\Omega$ product as nearly as possible to its limiting minimum value of $A_t\Omega_s$, and it can be shown (Hill, 1984) that the lens-coupling methods mentioned above are effective in this respect.

The use of a large-scale focal reducer has the disadvantage that it can cover only a limited field of view, so microlenses are preferred. There are, again, two possible methods, and these are illustrated in Figure 2.8(b), where the same microlens is used to increase the speed of an f/5 beam before its entry to a fibre. In method (i), the lens is used simply to re-image a very small portion of the focal surface onto the entrance-face of the fibre at a more compact plate-scale (by a factor of two), producing a reduction in focal ratio to f/1.25. In method (ii), devised by Angel and Richardson (see Hill, 1984), the lens images the telescope entrance pupil onto the fibre, thus acting in the manner of a Fabry lens, and producing a stationary image on the fibre in the presence of motion due to seeing, etc. The effective focal ratio of the beam carried by the fibre now depends on the image size (ie, the diameter of the seeing disc) and, if a similar optical arrangement is used at the output end, the seeing disc can, in principle, be restored, though its diameter will be increased by the effects of FRD. Non-centring of the input image on the lens/fibre axis will also conspire to increase the diameter of the final image. (A disadvantage of this method, pointed out by Powell (1986), is that, in the absence of a field stop in front of each microlens, much

unwanted sky light will be transmitted by the fibre.) Microlenses for these techniques can be miniature conventional lenses, ball lenses, rod lenses (glass cylinders with one end hemispherical) or GRIN lenses; their properties and relative merits are discussed by Nicia (1981) and Hill (1984).

Although microlens coupling (particularly with pupil-imaging) offers a neat solution to some of the problems resulting from FRD, it does appear that the identification of fibres having good FRD properties, reported in the previous section, has substantially reduced the need for this additional complication (see also Heacox, 1986). Indeed, the University of Arizona's MX Spectrometer, for which most of the foregoing ideas were developed, has now been deployed without microlenses (Hill and Lesser, 1986). There is no question but that the expense and difficulty of installing these components, particularly where large numbers of fibres are involved, is better avoided unless major optical-matching considerations dictate their use. One such case is the multi-object system built by Powell (1986) to couple the f/3.3 prime focus of the INT to its f/15 Cassegrain spectrograph. Here, 40 rod-lenses 1.0 mm in diameter are cemented onto the fibre output array, in the configuration shown in Figure 2.8(b)(ii), to slow the emerging beam to the required f/15.

We end this section by mentioning some of the less fundamental general considerations related to fibre-feed design. Fibre cost is a length-related parameter that may become extremely important if high-quality, highly-multiplexed fibre-optics systems for "new generation" large telescopes are envisaged. The 1986 price of good-quality (ie, having acceptable blue transmission and FRD) 100 μm core fibre is approximately

$A 1 per metre, scaling with the fibre core radius as ~$r^2/2$. A multi-object system for a 10-metre telescope, having j=1000 fibre feeds 400 μm in diameter and 20 metres long, could therefore be expected to cost ~$A 160,000 for fibre alone.

Protection and support of the fibres is usually achieved by enclosing them loosely in a single sleeve to form an optical cable. As we have seen, the fibres are not heavy, and can endure reasonable tensile stress, so the requirements on the protective sleeve are not stringent (in comparison with those used in the communications industry). Although expandable electrical sleeving, offering minimal protection, has been used successfully for fibre cabling (in the prototype FLAIR fibre feed described in Chapter 6), a more substantial environment is desirable, and the use of 2 cm flexible electrical conduit is now becoming widespread. It is important that the fibres are restrained independently of the sleeve, so that they will float loosely within it, even when the cable itself is pulled tight. Consideration should be given to the fibre route (avoiding sharp bends), to the convenience of the feed in use, and to its storage when not in use. The UKST's FLAIR system provides a good example of some of these considerations, since they are largely determined by the telescope's plate-loading environment, within which the system must work. Another example is the multi-object system of Baruch et al. (1986), designed to be used on many different telescopes, and which incorporates a "slack box" in its optical cable.

2.4 Considerations in fibre feed design: the telescope interface

The first consideration at the fibre input end is the matching of the fibre

diameter to the telescope plate-scale. We shall assume that the fibres are used with direct input (ie, without microlenses), and we shall denote by s the angular radius (in arcsec) of the fibre core projected onto the sky. The quotient s/r (where r is the physical radius of the fibre core) is simply the plate-scale, Π, of the telescope.

On a telescope of any reasonable size, the Airy disc is very much smaller than the random effects of refraction due to atmospheric turbulence. Thus the final image of a point source can be regarded as a probability distribution; in fact, its profile is very nearly Gaussian, so that the total intensity in the image is

$$I = k\int_0^\infty \exp(-z^2/2)\ z\ dz, \qquad (2.7)$$

where k is a constant of proportionality and z is radial distance from the image centre, here discussed in units of the distribution standard deviation, σ. The full-width at half-maximum (FWHM), equal to 2.354σ, is the diameter of the seeing disc, which encloses some 54 percent of the energy in the image. Clearly, the seeing disc is variable, and does not fix the fibre diameter, so that it may be desirable to have more than one size of fibre available for use in different seeing conditions (a feature of the AAT fibre system). Even the assumption of constant seeing does not completely constrain the fibre diameter, since the inclusion of background sky can be tolerated to a greater extent for brighter objects than for fainter ones, ie, fainter objects demand smaller fibres. Yet another consideration is the type of object to be observed, and there may be different requirements for galaxies, or other extended objects. For example, it may be

desirable to increase the fibre radius s so as to maximize the apparent magnitude, m, integrated over the fibre area, given by

$$m = \mu - 2.5 \log \pi s^2, \qquad (2.8)$$

where μ is the apparent surface brightness in magnitudes arcsec^{-2}. Against this may be a requirement to keep s within some characteristic isophotal radius for the object in question.

Clearly, in selecting fibre diameters, a compromise has to be arrived at. From consideration of existing systems, it appears that the optimum fibre radius is approximately equal to the 2σ radius of a Gaussian profile whose FWHM is defined by the average seeing diameter (5). If we define the entrance coupling efficiency, E, to be the fraction of the light in the Gaussian image that is intercepted by the fibre, then such a fibre will have E=0.88. Thus, for typical seeing of 1.5 arcsec, the optimum fibre diameter will be 2.5 arcsec; for seeing of 0.75 arcsec, the fibre diameter should be 1.3 arcsec. These values are very close to the minimum and maximum fibre diameters available on the AAT. For work on bright objects, particularly nearby galaxies, it may be desirable to increase the fibre radius to 3σ, resulting in a value of E of 0.99. Poor seeing will effec-

---

(5) This is somewhat more generous than the optimum fibre diameter arrived at theoretically by Heacox (1986). However, Heacox's calculations specifically included the effect of re-imaging the fibre output face onto a slit to limit the amount of light entering the spectrograph.

tively result in a mismatch between the image and fibre diameters; for example, if the fibre radius is reduced to 1σ (eg, by a 3 arcsec seeing disc falling on a 2.5 arcsec fibre), then E falls to 0.42.

A second consideration in telescope/fibre-feed matching is that the acceptance focal ratio defined by the NA of the fibre should not be numerically greater than that of the telescope. As we have seen, the NA of AS fibres is usually high enough to hold beams as fast as f/2 (although it may be noted that some of the AS fibres in Table 2.2 have an NA equivalent only to f/2.45). By analogy with the entrance coupling efficiency, we define the beam coupling efficiency, B, to be the fraction of the light in the incoming covergent beam that is within the acceptance focal ratio of the fibre, where the latter is defined by the fibre NA, diminished to include the effects of bends and FRD loss to the cladding. Clearly, for relatively slow beams (eg, at Cassegrain foci), we will have B=1.0. However, beams that almost fill the fibre (ie, that are close to the nominal fibre NA) may indeed lose light to the cladding on bends or by FRD, as discussed earlier, and the value of B will be reduced. Misalignment of the fibre input (considered below) may also result in light-loss.

There is a difficulty in this regard with the use of fibres in the proposed Willstrop telescope (Willstrop, 1984). The currently-favoured version of this design has a focal ratio of f/1.6, faster than the beam-holding capacity of any currently-available AS fibre. (A typical AS fibre with an effective NA of 0.20 would have a coupling efficiency, B, of only 0.43 in this telescope.) A number of options are open for circumventing this problem. One is to use PCS fibres, which have inherently high NA, and which

may still have some way to go in terms of the improvement of their transmission properties (Boucher, 1983). Another is to use microlenses on the fibre inputs to increase the focal ratio of the beam (the inverse problem of that discussed in the previous section), and Willstrop (1987) has produced a very neat design for a moulded aspheric microlens, which simultaneously slows the beam to f/3.2 and corrects the chromatic aberration introduced by an atmospheric dispersion compensator (see Chapter 3). However, it is possible that the long lead-time for this telescope ($\gtrsim$5 years?) will see the introduction of AS fibres with sufficiently high NA - or, at least, the means to manufacture them. Given that fibres would play a key role in the operation of the instrument, there may well be a case for making a substantial financial investment in the fabrication of an optimum fibre.

Returning to the present, we next consider the effects of misalignment of a fibre input in the telescope focal surface. The misalignment may be axial (defocusing), lateral (positioning error) or angular. Figure 2.9(a) shows the effect of defocusing on the entrance coupling efficiency, E. In this approximation, the Gaussian image is simply broadened with the geometrical beamwidth away from the best focus position, so that no account is taken of the changing beam-profile. In particular, the effect of the telescope central obstruction (which will serve to increase further the steepness of the fall-off in E) is ignored. However, it is clear that the entrance coupling efficiency is critically dependent on focus, particularly at lower focal ratios. For example, on the UK Schmidt telescope with 2σ radius fibres (eg, 40 μm diameter in 1.6 arcsec seeing), a focus error of 100 μm will reduce E by more than 50 percent. Clearly, the problem here lies not in

Figure 2.9 (overleaf) Effect of positioning errors at the fibre input.

The entrance coupling efficiency, E, is plotted against (a) focusing error, and (b) lateral alignment error. These curves are general; their application to specific telescopes is typified by the following data:

AAT (f/8; Π =6.7 arcsec/mm)

400 μm diameter fibres have 1σ radius when seeing is 3.1 arcsec;
" " " " " 2σ " " " " 1.6 " ;
" " " " " 3σ " " " " 1.0 " .

200 μm diameter fibres have 1σ radius when seeing is 1.6 arcsec;
" " " " " 2σ " " " " 0.8 " ;
" " " " " 3σ " " " " 0.5 " .

UKST (f/2.5; Π =67 arcsec/mm)

40 μm diameter fibres have 1σ radius when seeing is 3.1 arcsec;
" " " " " 2σ " " " " 1.6 " ;
" " " " " 3σ " " " " 1.0 " .

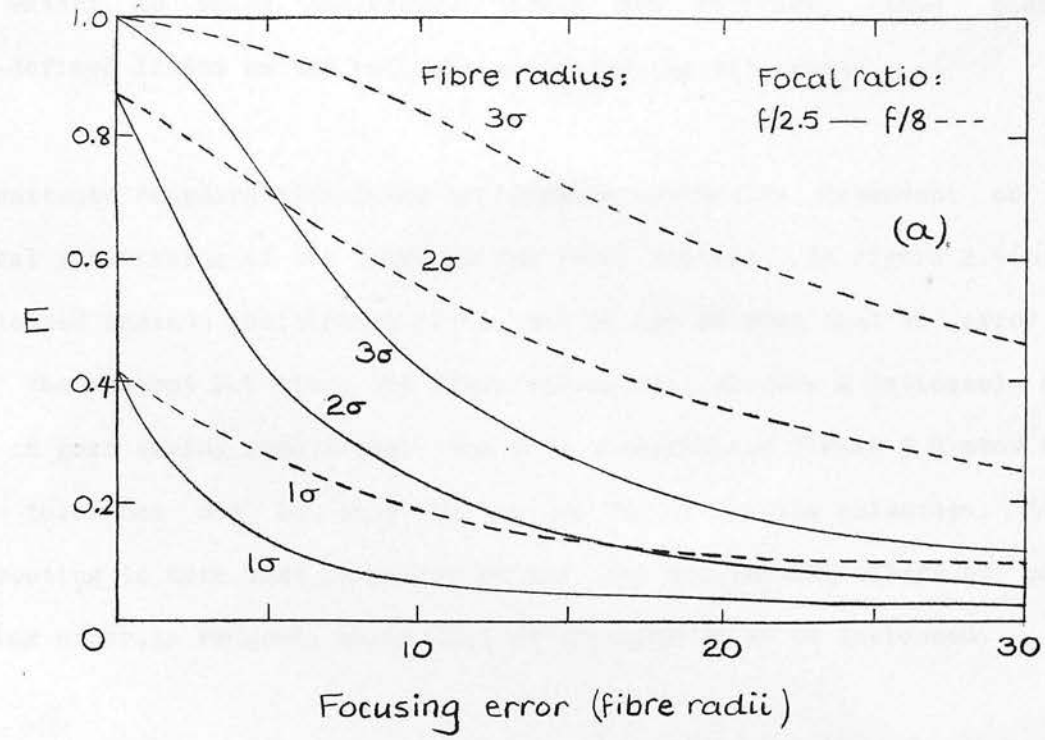
1.0
0.8
0.6
0.4
0.2
0
E
Fibre radius:
Focal ratio:
f/2.5 — f/8 ---
3σ
2σ
1σ
3σ
2σ
1σ
(a)
10
20
30
Focusing error (fibre radii)

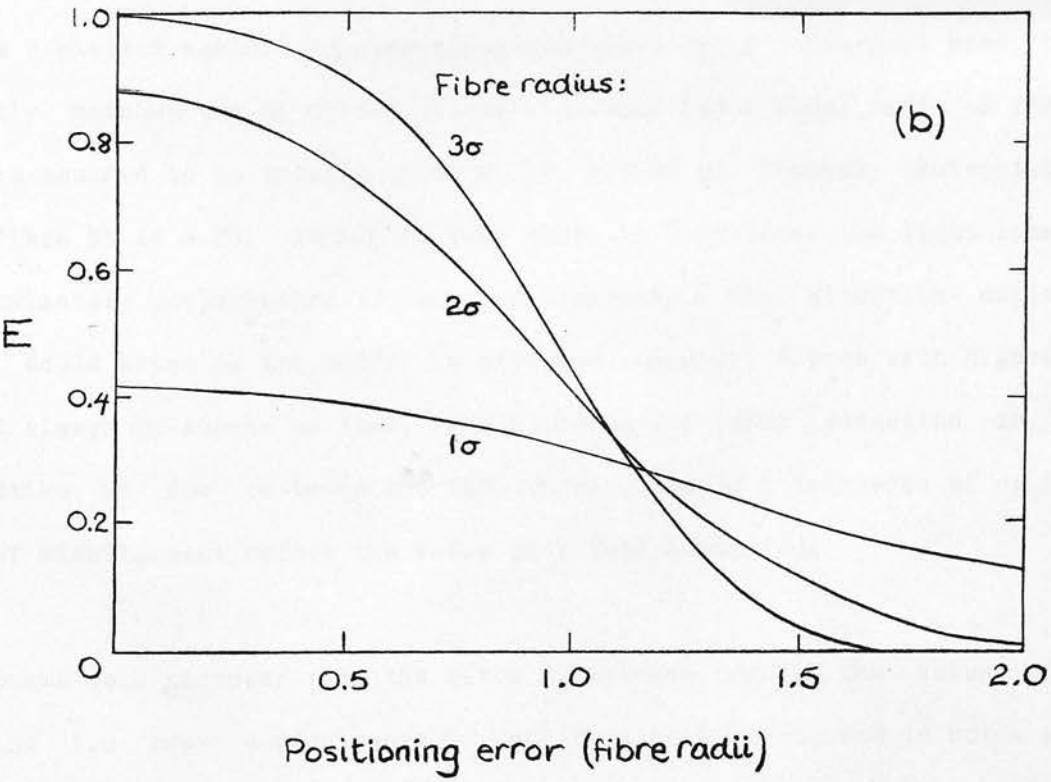
1.0
0.8
0.6
0.4
0.2
0
E
Fibre radius:
3σ
2σ
1σ
(b)
0.5
1.0
1.5
2.0
Positioning error (fibre radii)

focusing the array of fibre inputs, since this is always adjustable, but in the extent to which individual fibres are confocal, thus placing well-defined limits on the relevant manufacturing tolerances.

The entrance coupling efficiency is likewise critically dependent on the lateral positioning of the fibre in the focal surface. In Figure 2.9(b), E is plotted against positioning error, and it can be seen that an error of more than about 0.5 times the fibre radius will produce a noticeable drop in E in good seeing conditions. The data accompanying Figure 2.9 show that this tolerance may be only 10 μm on the UK Schmidt telescope. It is interesting to note that in poorer seeing, the detrimental effect of positioning error is reduced, while that of focusing error is increased.

The effect of angular misalignment may be described in terms of the beam coupling efficiency, B, for beams close to the fibre NA. Figure 2.10(a) shows B plotted against angular alignment error for a convergent beam that exactly matches the NA of the fibre. The beam has a focal ratio of f/2.5, and is assumed to be totally uniform (ie, having no central obstruction); the fibre NA is 0.20. It may be seen that, in this case, the light loss is approximately proportional to the misalignment. The situation depicted here could arise on the UKST; in practice, however, fibres with higher NA would always be chosen so that, even allowing for some reduction in the effective NA due to bends and FRD, there would be a tolerance of up to 3 deg of misalignment before the value of B fell below 1.0.

For beams much narrower than the fibre acceptance cone, the value of B remains 1.0 over a wide range of angular misalignment, and is not a good

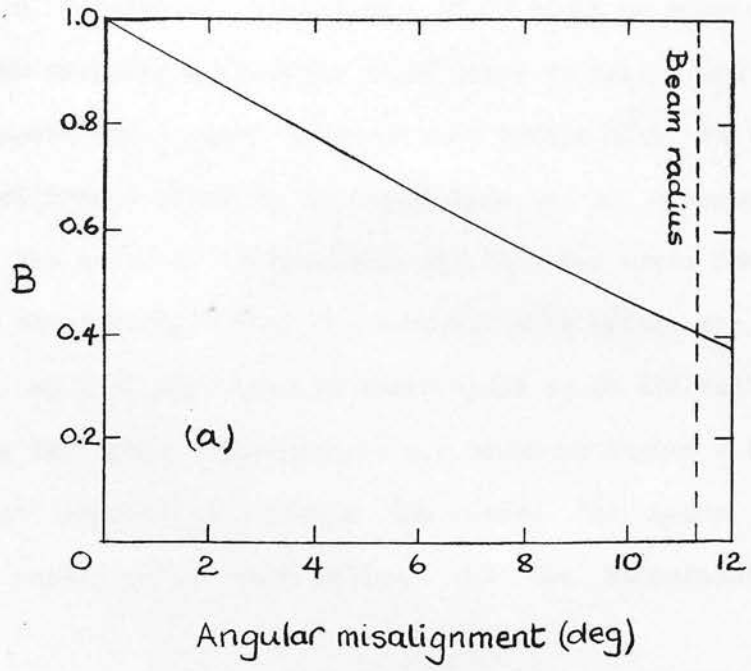

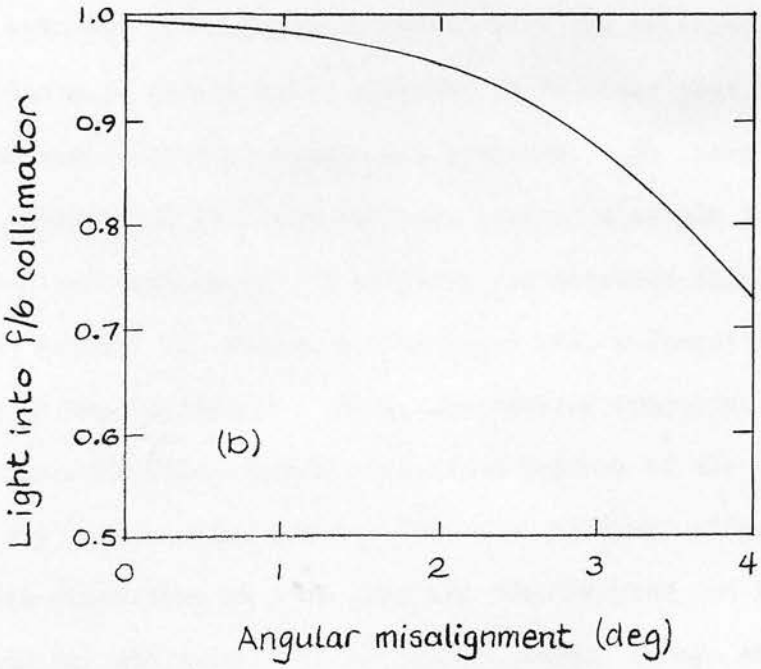

Figure 2.10 Effect of angular misalignment of the fibre input. (a) Beam coupling efficiency, B, plotted against alignment error for an f/2.5 beam entering a perfectly-matched fibre (ie, with NA=0.20). (b) Measured effect, on light intercepted by the collimator, of fibre angular misalignment for an input beam much narrower (f/8) than the fibre acceptance cone, showing the effect of collimator overfilling due to beamspreading (from Gray and Sharples, 1985). The geometrical value of B for the input beam is 1.0 over this range of misalignments.

indicator of the true coupling efficiency. For example, an f/8 beam entering the fibre considered in Figure 2.10(a) could be inclined by 7.7 deg before the beam coupling efficiency would begin to fall, and other, more significant losses would start to occur well before this limit. One of the effects of inclining a fibre to the input beam is to broaden the output beam by twice the angle of inclination, and this may cause immediate losses by collimator overfilling. Gray has measured this effect for the AAT fibre feeds, where an f/8 input beam is intercepted by an f/6 collimator on its emergence from the fibre. The results are shown in Figure 2.10(b), and it is clear that significant losses can occur for quite small angular misalignment, again with implications for the mechanical tolerances involved.

Although we are here principally concerned with the matching of fibres to the seeing discs of single point sources, it is clear that there are other possibilities when extended objects are observed. We have already mentioned the integration of light over the area of a single fibre; however, spatially-resolved spectra may be obtained for extended objects by using a close-packed matrix of fibres at the input end, reformatted to the usual linear array at the collimator. Here, the packing fraction, p, mentioned earlier in connection with imageguides, is a measure of the completeness of coverage of the target object rather than the optical efficiency of the system. Image dissection of this kind has been carried out at the AAT with both short (50 mm) and long (2.5 m) fibre feeds (Gray et al., 1982). (Gray, 1986, has also described a 290-element circle-to-line fibre image-slicer, for use with stellar images in poor (>2.5 arcsec) seeing. In this case, p reverts to being an indicator of optical efficiency.) Image

dissection over a wider area can be carried out using single fibres, and differs little from the normal mode of multi-fibre observation; a notable example of the use of this technique is the spectroscopy of Comet Halley obtained with the ESO 3.6-metre telescope (Lund and Surdej, 1986). It is possible to envisage a multi-object system for compact extended objects that would use several ($j \sim 10$) small matrices of perhaps 3, 7 or 14 (hexagonally-packed) fibres. Such a device may have applications in the spectroscopy of clusters of bright galaxies, for example.

Returning, in conclusion, to single fibres, the input ends are usually encased in ferrules that serve a variety of functions: facilitating the polishing of the fibre end, protecting its surface from damage during handling, permitting the mounting of the fibre in the focal surface, and so on. The detailed design of the ferrule is of some importance, as it determines (a) the minimum separation of fibres in the telescope field, (b) the extent (if any) to which the fibre is pinched at its input end (which would generate stress-induced FRD) and, often, (c) the extent to which tolerances in focus, lateral positioning and angular alignment are maintained.

The foregoing discussion of design considerations for the telescope/fibre-feed interface has been concerned with the details of light entry into individual elements in the fibre array. A number of other important considerations exist, related to the properties of the telescope focal surface itself; these are discussed in the first section of the next chapter. Details of fibre ferrules and of the actual mechanical arrangements for supporting fibres in the focal surface are given in Chapters 4 and 6.

2.5 Considerations in fibre-feed design: the spectrograph interface

As we have seen, the primary constraint in selecting the core radius, r, of fibre for use in multi-fibre feeds is its matching to the seeing disc imaged by the telescope. In general, the spectrograph must then be matched to the fibre radius and to the focal ratio of the output beam, either in its design *ab initio*, or in modifications to an existing instrument. This differs from matching to a slit in the common focus of telescope and collimator by the fact that the emergent beam from the fibre may be broadened by FRD; we have already discussed means of accommodating this, eg, by reducing the collimator focal ratio at the expense of spectral resolution. The beam coupling efficiency, B, introduced in the previous section, may be applied to the matching of fibre output and collimator input beams; it will clearly be 1.0 when the collimator focal ratio is less than that of the fibre output beam. Another noteworthy difference between direct-slit and fibre-coupled spectroscopy is that in the former, the image in the collimator focus retains its Gaussian profile, with most of the energy concentrated at the centre, whereas the illumination of the fibre face is much more nearly uniform, due to image scrambling. It is this property of fibre-coupled spectrographs that makes them attractive for accurate radial-velocity work. It may be noted that both these differences from direct-slit work (FRD broadening and image-scrambling) are reduced when pupil-imaging microlenses are used at each end of the fibre; this technique thus has a strong resemblance to the direct-slit technique in some of its characteristics.

Fibres may be used to couple telescopes and spectrographs with very dif-

ferent focal ratios, and here, additional optical elements must be used. The output-end microlenses employed by Powell (1986) to couple an f/3.3 telescope beam to an f/15 spectrograph have already been mentioned; Heacox (1986) gives a thorough account of the design considerations for a fibre coupler that incorporates a lens to re-image the fibre output onto the slit of a spectrograph. This is designed for single-fibre use (principally to capitalize on the scrambling properties of the fibre), but could be adapted to a multi-fibre environment. Heacox has built a system to couple an f/10 telescope beam to an f/33 spectrograph; it also incorporates pre-fibre optics to reduce the beam focal-ratio to f/4 before transmission by the fibre to the coudé position.

The relationship between fibre-core radius and spectral resolution is a property of the spectrograph optical system and the detector, and is discussed in the next chapter. We note, however, that spectral resolution need not be totally constrained by the fixed fibre-core radius, and that limiting slits can be used at the expense of some light-loss. The use of a limiting slit in the collimator focus is fundamental to the above-mentioned design considerations by Heacox; Gray and Sharples (1985) have described the use of a slit-mask placed in contact with the linear fibre output array on the AAT fibre-optics system, to improve spectral resolution when a long focal-length spectrograph camera is used. The light-loss incurred by placing a slit of width 2h symmetrically over a uniformly-illuminated fibre of radius r is

$$J = 2(r^2\cos^{-1}(h/r) - h(r^2-h^2)^{1/2})/\pi r^2. \qquad (2.9)$$

It may be further remarked that for an unmasked, uniformly-illuminated fibre, the equivalent slit-width (analagous to the equivalent-width of a spectral line) is $\pi r/2$.

The effects of misalignment considered at the fibre input have their counterparts in the fibre output. Axial misalignment (defocusing) is likely to be extremely small, since the fabrication of fibre output arrays involves the simultaneous polishing of all the fibres, so that their output faces will be coplanar with a very high degree of precision (6). If it did occur, defocusing would lead to degraded spectral resolution and image-spreading in the detector y-direction, so that while there would be no actual light-loss, there would be some reduction in efficiency. Lateral misalignment (positioning error) is not a problem in fibre output arrays. While it will certainly occur, in the sense that fibres will be positioned in the required array with some characteristic error, it will merely lead to a displacement of the fibre image in the detector plane, whose effect can be removed by calibration.

Angular misalignment is potentially the most serious of the three. Invariably, the fibre output beam will be closely matched to the collimator

---

(6) It may be noted that this simultaneous polishing incurs a disadvantage, in that control of the surface quality of individual fibres is much more difficult to maintain than when they are polished singly. Output faces are thus likely to have a higher value of the scattering loss, S, referred to in Section 2.3, than their input counterparts.

focal ratio, so the effect of misalignment is well-described by the beam coupling efficiency, B. The behaviour of B with alignment error for a perfectly-uniform f/2.5 emergent beam feeding an f/2.5 collimator would thus be as shown in Figure 2.10(a). In practice, the beam is made non-uniform by its passage through the fibre, and its profile is likely to resemble one of those shown in Figure 2.8(a), so that the actual fall-off in B with angular misalignment will be non-linear. Gray has measured the effect of output-end misalignment for the AAT fibre feeds when used with the f/6 collimator, and his results are plotted in Figure 2.11(a). In the same diagram we have plotted B for a uniform f/6 beam feeding the f/6 collimator; the line will be seen to lie beneath the measured points, indicating that, in practice, there is still some overfilling of the f/6 collimator by the degraded fibre output beam.

Gray has also measured the actual misalignments of individual fibres in his feed bundles (Gray and Sharples, 1985) to quantify the overall losses due to output misalignment. The results for one such fibre feed are shown in Figure 2.11(b), where deviations from the mean fibre alignment are plotted as a scatter diagram. (A fibre in the centre of the scatter is used when the array is aligned with the spectrograph optics.) Since the fabrication of fibre output arrays is, in general, carried out by the same method (viz, the location of fibres in a groove whose width is only slightly larger than the sum of their diameters, so that they self-align without the imposition of undue stress), this scatter can be regarded as typical. It may be noted that the points plotted in Figure 2.11(b) are deviations from parallelism in the output array, so that the fibres are intended to be aligned with the optical axis of the collimator rather than with its optical centre. In the

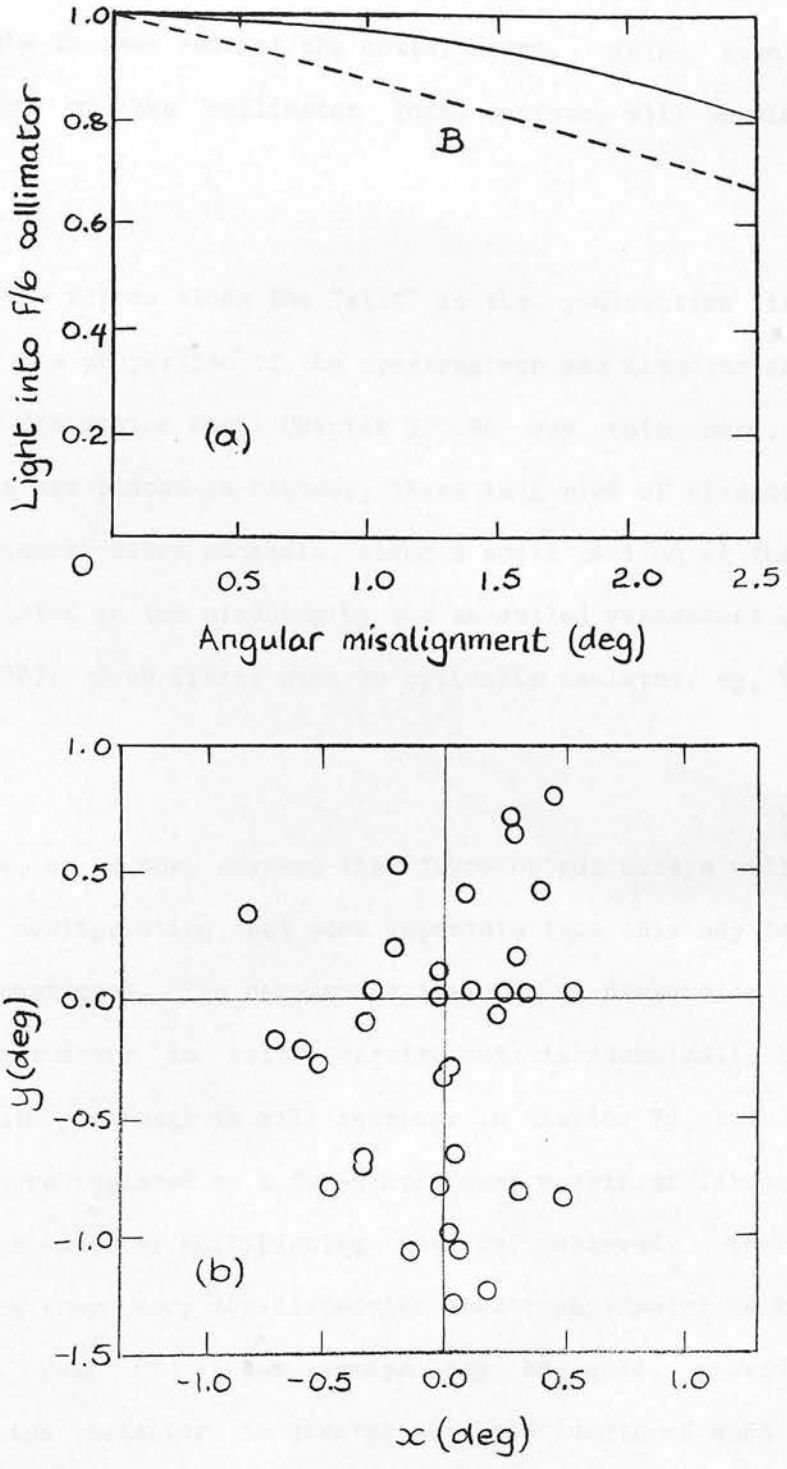

Figure 2.11 Effect of angular misalignment of the fibre output. (a) Measured effect, on light intercepted by an f/6 collimator, of angular misalignment of the fibre output (from Gray and Sharples, 1985). The geometrical beam coupling efficiency, B, for an f/6 beam is also plotted (see text). (b) Distribution of fibre output alignment in a typical fibre feed (from Gray and Sharples, 1985).

absence of a field lens, this may introduce vignetting of the beams from the fibres at the extreme ends of the output array. This, together with other properties of the collimator focal surface, will be discussed in Chapter 3.

The spacing of the fibres along the "slit" in the y-direction is largely determined by the properties of the spectrograph and detector and, again, is deferred for discussion until Chapter 3. We may note here, however, that if fibres are placed in contact, there is a risk of crosstalk occurring between adjacent fibre channels, since a small portion of the optical signal is propagated in the cladding by the so-called evanescent wave (see, eg, Gallowa, 1982). Such fibres must be optically isolated, eg, by opaque coatings.

Finally, we have, up to now, assumed that fibre output arrays will have a simple linear configuration, but some departure from this may be possible in special circumstances. The case where there is no dispersion (so that multi-object photometry is being carried out) is technically beyond the bounds of this study (though it will reappear in Chapter 7), but here the linear array can be replaced by a two-dimensional matrix of fibres, so that an extremely high order of multiplexing may be achieved. There is an intermediate case where very low-dispersion spectrophotometry is being carried out; here, rows of linear arrays may be used, provided their separation at the detector is greater than the length of each spectrum. Such an arrangement, consisting of two rows of fibres, has been described by Baruch et al. (1986).

References for Chapter 2

Aggarwal ID, 1982. Laser Focus, Nov issue, p.115
Allan WB, 1973. Fibre optics, theory and practice. Plenum Press, London
Angel JRP, Adams MT, Boroson TA, Moore RL, 1977. Ap J 218, 776
AWA (Amalagamated Wireless of Australia), 1982. Data sheets

Baird JL, 1927. Brit. Patent No 285738
Barden SC, Ramsay LW Truax RJ, 1981. PASP 93, 154
Barnoski MK, Personick SD, 1978. Proc IEEE 66, 429
Baruch JEF et al., 1986. Internal report, University of Leeds
Bisbee DL, 1971. Bell System Tech Jour, 50, 3153
Blankenship MG, Deneka CW, 1982. IEEE Trans, MTT-30, 1406
Boucher D, 1983. Proc SPIE 374 (Fibre Optics '83), p.2
Boys CV, 1887. The Philosophical Magazine, June issue

Challans JC, 1983. Proc SPIE 374 (Fibre Optics '83), p.58
Chesler RB, Dabby FW, 1976. Electronics, 5 Aug issue, p.90
Chida K, Nakahara M, Sudo S, Inagaki N, 1983. J Lightwave Tech LT-1, 56

Dakin JP, 1983. Proc SPIE 374 (Fibre Optics '83), p.172

Ellis RS, Gray PM, Carter D, Godwin J, 1983. MNRAS 206, 285
Esposito JJ, 1979. In Handbook of fiber optics (ed Wolf) Ch 5, Garland STPM
Evans I, 1983. Optical fibre measurements (Internal rep, MSSSO)

Fibres Optiques Industries (formerly Quartz et Silice), 1983. Data sheets
Fujikura Ltd, 1982. Optical fibre catalogue, Tokyo

Gallowa RL, 1982. Electro-optical Systems Design, April issue, p.46
Gambling WA, Payne DN, Matsumura H, 1975. Applied Optics 14, 1538
Giallorenzi TG, 1978. Proc IEEE 66, 744
Gloge D Smith PW Bisbee DL Chinnock EL, 1973. Bell System Tech J 52, 1579
Gloge D, 1972. Bell System Tech Jour 51, 1767
Gordon KS, Rawson EG, Nafarrate AB, 1977. Applied Optics 16, 818
Gray P, 1982. Beam scans (Internal report of AAO)
Gray P, 1986. AAO Newsletter No 39
Gray P, Sharples R, 1985. AAO fibre system user guide/tech manual
Gray PM, 1983a. Proc SPIE 374 (Fibre Optics '83) p.160
Gray PM, 1983b. Proc SPIE 445 (Instr in Astr V), p.57
Gray PM, 1986. Proc SPIE 627 (Instr in Astr VI), p.96
Gray PM, Phillips MM, Turtle AJ, Ellis RS, 1982. Proc ASA 4, 477

Hansell CW, 1930. US Patent No 1751584
Heacox WD, 1980. Proc KPNO conf on opt, IR tels for 1990s, p.702, Tucson
Heacox WD, 1986. AJ 92, 219

Herskowitz GJ, Kobrinski H, Levy U, 1983. Laser Focus, Feb issue, p.83
Hill JM, 1984. PhD Thesis, University of Arizona
Hill JM, Angel JRP, Richardson EH, 1983. Proc SPIE 445 (Instr.Ast V) p.85
Hill JM, Lesser MP, 1986. Proc SPIE 627 (Instr in Astr VI), p.303
HirschowitzBI CurtissLE PetersCW PollardHM 1958. Gastroenterology 35, 50
Hopkins HH, Kapany NS, 1954. Nature 173, 39

Inada K, 1982. IEEE Trans, MTT-30, 1412

Jeunhomme L, Pocholle JP, 1975. Electronics Letters 11, 425

Kao CK, 1979. Telephony, 12 Nov issue, p.28
Kao CK, Hockham GA, 1966. Proc Inst Elec Eng 113, 1151
Kapany NS, 1967. Fiber Optics. Academic Press, NY
Khoe G-D, van Leest JHFM, Luijendijk JA, 1982. IEEE Trans, MTT-30, 1561

Lamm H, 1930. Z. Instrumentenkd 50, 579
Lund G, Enard E, 1983. Proc SPIE 445 (Instr in Astr V), p.65
Lund G, Surdej J, 1986. ESO Messenger No 43, p.1
Lynden-Bell D, 1986. Willstrop telescope workshop, Cambridge

Mack R, Tebo A, 1986. Laser Focus/Electro-optics, Oct issue, p.104
Meaburn J, 1976. Detection and spectrometry of faint light, Reidel
Miya T, Nakahara M, Inagaki N, 1983. J Lightwave Tech LT-1, 14
Morokuma T, 1979. In Handbook of fiber optics (ed Wolf), Ch10, Garland STPM

Nicia A, 1981. Applied Optics 20, 3136

Opielka D, Rittich D, 1983. Applied Optics 22, 991
Otten HJM, 1981. Electronic components and applications 3, No 2, 87

Polymicro Technologies, 1986. Data sheets
Powell JR, 1983. Proc SPIE 445 (Instr in Astr V) p.77
Powell JR, 1986. Proc SPIE 627 (Instr in Astr VI), p.125

Ramsay LW, Huenemoerder DP, 1986. Proc SPIE 627 (Instr in Astr VI) p.282
Rashleigh SC, 1983. Jour Lightwave Tech LT-1, 312

Saunders MJ, 1979. Applied Optics 18, 1480
Schiffer JGV, 1983. Proc SPIE 445 (Instr in Astr V) p.52
Schultz PC, 1974. J Am Ceram Soc 57, 309
Schultz PC, 1979. Applied Optics 18, 3684

Tyndall J, 1854. Proc Roy Instn 1, 446

van Heel ACS, 1954. Nature 173, 39

Wheeler W, 1881. US Patent No 247229
Willstrop RV, 1984. MNRAS 210, 597
Willstrop RV, 1987. MNRAS 225, 187
Wolf HF, 1979. In Handbook of fiber optics (ed Wolf) Chap 2, Garland STPM

Yoshizawa N Tetsurou Y Nobuya K Negishi Y, 1981. Applied Optics 20, 3146

CHAPTER 3

Instrumentation for multi-fibre spectroscopy

3.1 Telescopes

3.1.1 In a classic paper on optical arrays, Disney (1972) investigated the cost-effectiveness of astronomical observation, and concluded that an array of telescopes capable of being combined so as to observe the same object simultaneously would produce more astronomy per unit cost than a single large telescope. The use of many telescopes to look at one object is clearly an inverse of the arrangement that concerns us here, where a single telescope simultaneously observes many objects. The enormous potential of mutliplexing within the field of view was neglected by Disney, even though it had already been highlighted in the context of the efficiency of observing systems by Fellgett (1970). Other investigations of the merits of array telescopes, up to and including the extremely thorough study by Humphries et al. (1984), have also neglected the possibility of multi-object observing, since the primary aim has always been to seek the most cost-effective way of achieving large apertures. The importance of spatial multiplexing has been formalized in Chapter 1 of this thesis in terms of effective aperture, α, and it is clear that, other things being equal,

overall cost-effectiveness will increase monotonically with the multiplex advantage, j, embodied in α. Thus, were Disney's paper to be written now, additional considerations related to telescopic field would need to be included, and it is possible that the same conclusions would not be reached. It is interesting to note that the first suggested use for optical fibres in astronomy was to link the elements of an array telescope (Angel et al., 1977), and there appears to be no reason why a fibre-coupled multi-object array telescope could not be built, if it could be shown to offer significant advantages.

In the present discussion, we shall concern ourselves with those properties of single telescopes that are related to multi-fibre work. Some of these have been considered already, and we may mention in recapitulation that the area of field, F, determines the lowest number-density for which multi-object observations may be carried out, the plate-scale, Π, determines the optimum fibre diameter, and the focal ratio determines the minimum fibre NA that may be used. The effect of aperture, a, on limiting magnitude will be discussed in the last section of this chapter. In the present section, we shall frequently cite as examples the f/8 Ritchey-Chrétien focus of the Anglo-Australian telescope (Chrétien, 1922; see also Bowen, 1967), the UK Schmidt telescope (Schmidt, 1932) and the proposed 5-metre Willstrop telescope (Willstrop, 1984). The optical arrangement of this latter instrument is shown in Figure 3.1.

One property of a telescope that has not been mentioned is its optical efficiency, Q_T. This is simply the product of the transmittance, τ, or reflectance, ρ, of all surfaces in the optical system. For uncoated

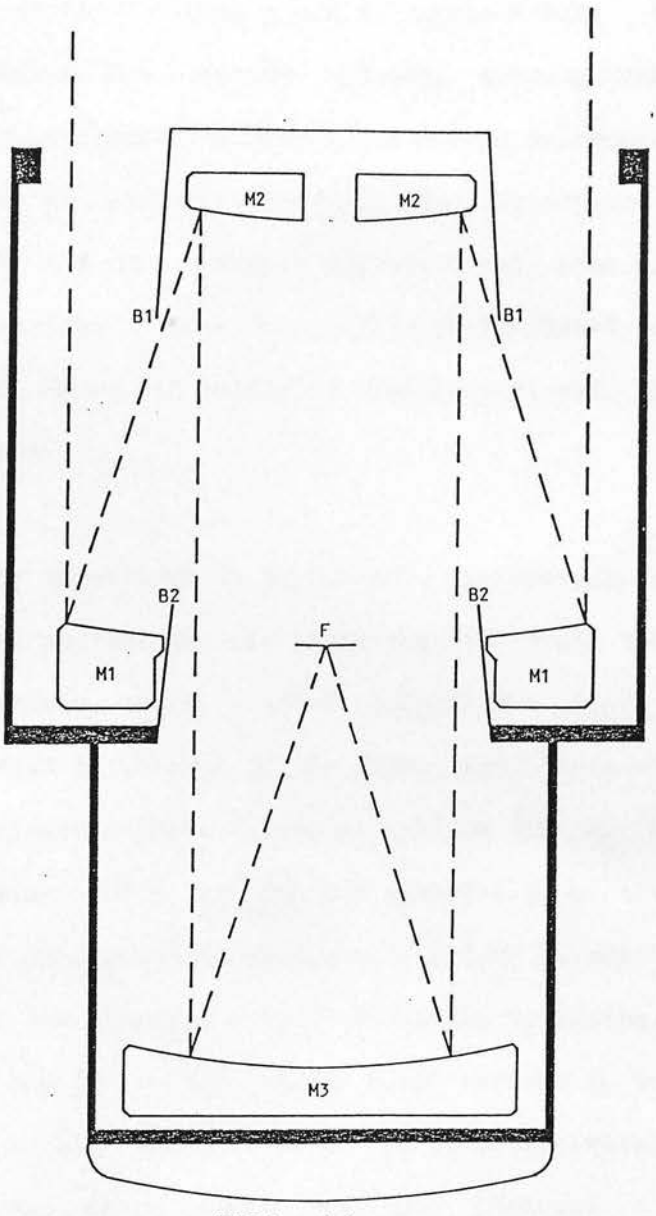

Willstrop telescope.

M1, M2 and M3 are the primary, secondary and tertiary mirrors.
B1 and B2 are the upper and lower sky fog baffles.
F is the curved focal surface; radius of curvature = focal length.

Figure 3.1 Optical arrangement of the Willstrop telescope. (From Willstrop, private communication.)

refracting surfaces, it is usual to assume that τ is equal to $(1-R_F)$, where R_F is the Fresnel reflection loss given by Equation 2.5; bulk losses in refracting components are usually ignored, although the attenuation in glass can become significant for even quite modest thicknesses (see Eastman Kodak, 1973, for an extreme example). The reflectance of an aluminium coating varies with its age, and will typically fall from 0.9 to 0.8 within a year of deposition. This degradation is inhibited to some degree in Schmidt telescopes, where the mirror is totally enclosed. Both τ and ρ are wavelength-dependent.

3.1.2 Of particular importance in multi-fibre spectroscopy are the properties of the focal surface and the image that is formed there. For fields wider than a few arcmin, there is often significant field curvature (of radius R) that must be matched by the fibre input faces within the tolerances implied by Figure 2.9(a). Examples include the 40 arcmin diameter f/8 Ritchey-Chrétien focus of the AAT with R=4.37 m, the 6.5 deg square f/2.5 focus of the UK Schmidt telescope with R=3.07 m, and the 5 deg diameter f/1.6 focus of the proposed 5-metre Willstrop telescope, with R=8.00 m. This last example has by far the largest focal surface in terms of its physical dimensions; its diameter of 700 mm is approximately twice that of the other two. Willstrop (1985) has also produced a design for a flat-field version of his three-mirror telescope, but its slower focal ratio (f/2.6) and smaller field of view (3 deg) combine with other drawbacks to make it a less attractive option than the curved-field version.

A property of the focal surface that is unimportant in other field-imaging applications may be referred to as beam inclination, b, and is the angular

deviation of the axis of symmetry of the converging beam from the normal to the focal surface. This arises when the centre of curvature of the focal surface and the centre of the telescope exit pupil do not coincide. Classical Schmidt telescopes have a virtual exit pupil at the centre of curvature of the mirror; it is thus concentric with the focal surface, and b is everywhere zero. Both the other designs that we are here citing as examples suffer from beam inclination; the 5-metre Willstrop telescope has a virtual exit pupil 2.67 m behind the focal surface (Willstrop, 1987) and in the AAT's f/8 Ritchey-Chrétien design, the exit pupil is 30.78 m in front of the focus. (Note that the focal surface here is concave towards the incident light.) Thus, at the edge of the AAT's 40 arcmin field, a fibre feed positioned normal to the focal surface will have b=2 deg, resulting in a light-loss at the collimator of 5 percent (from Figure 2.10(b)). (Of the AAT's fibre systems described in Chapter 4, FOCAP will suffer more from this loss than AUTOFIB, in which some compensation is achieved by the use of a stepped focal-surface plate, so that the fibres are positioned in an approximation to the surface of best focus, while pointing towards an approximation to the centre of the exit pupil.)

Most telescopes with an appreciable field of view suffer from a vignetting loss. In Schmidt telescopes, this is mainly caused by failure of the mirror to intercept all the incoming beam above a certain off-axis angle. For the UK Schmidt, this angle is 2.7 deg; the vignetting function itself is shown in Figure 3.2 in terms of both the varying efficiency over the field, V, and the resulting magnitude loss. The UKST vignetting function is discussed in detail by Dawe (1984). In the Willstrop telescope, vignetting is caused by the secondary mirror and primary perforation, and amounts to a

$$V(\alpha) = \frac{I(\alpha)}{I(0)}$$

$$\Delta m(\alpha) = -2.5 \log \frac{I(\alpha)}{I(0)}$$

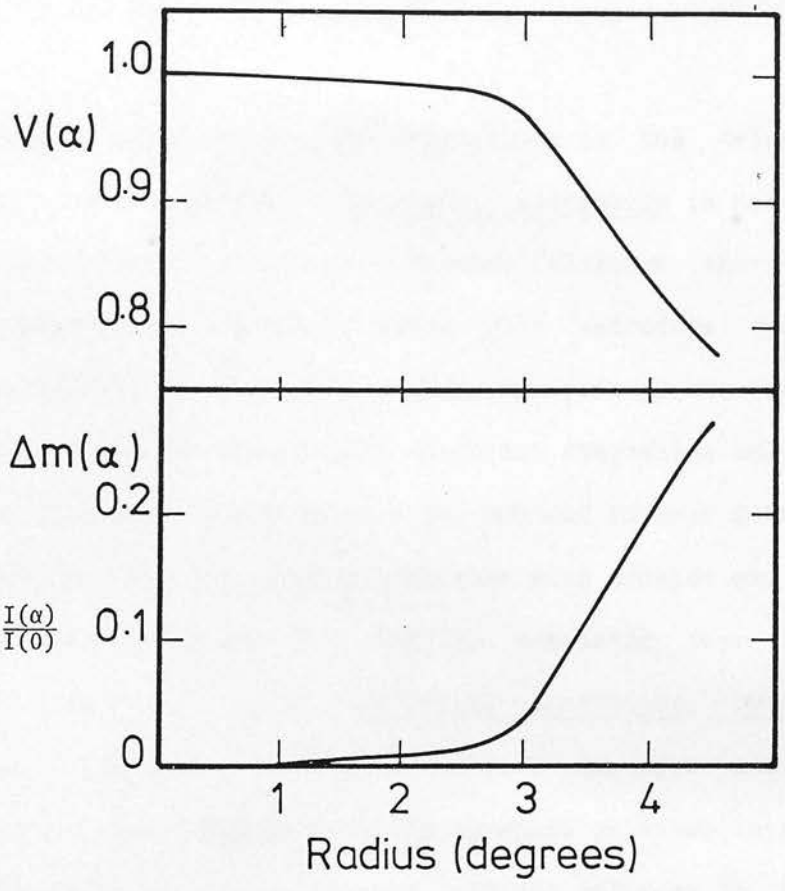

Figure 3.2 Vignetting function of the UK Schmidt telescope. The optical efficiency, V, and magnitude loss, Δm, are plotted against distance from the field centre, α. (From Tritton et al., 1983.)

loss of 22 percent at the edge of the 5 deg field (Willstrop, 1987); the central 2-deg diameter area is unvignetted. There is no vignetting over the 40 arcmin field of the AAT's f/8 Ritchey-Chrétien focus.

As with all field-imaging applications, the aberrations in the telescopic image are important considerations. Chromatic aberration is naturally absent in the Ritchey-Chrétien and Willstrop designs (although the atmospheric-dispersion compensator discussed below will introduce residual effects), but may be introduced to a small extent by prime-focus correctors. Large Schmidt telescopes suffer from chromatic aberration unless an achromatic corrector is used; in common with the ESO and Palomar Schmidts, the UKST is thus equipped, and its imaging qualities with singlet and doublet correctors are compared in Figure 3.3. Of the remaining four Seidel aberrations (after field curvature), spherical aberration, coma and astigmatism are, like chromatic aberration, subject to more stringent tolerances for conventional imaging with photographic or other detectors than are required for multi-fibre spectroscopy, and are unlikely to be of concern. Spot diagrams for the Willstrop telescope are given in Willstrop (1984; 1987), those for the AAT are given in Morton et al. (1976), while the images produced by Schmidt telescopes are discussed by Brown, Dunlop and Major (1984). These latter images are, of course, coma-free, and should have minimal residual spherical aberration (Schmidt, 1932).

Distortion may be a particularly important consideration for multi-fibre work when fibres must be accurately located at positions in the focal surface derived from the celestial coordinates of target objects. The evaluation of distortion for this purpose (together with exact plate-scale)

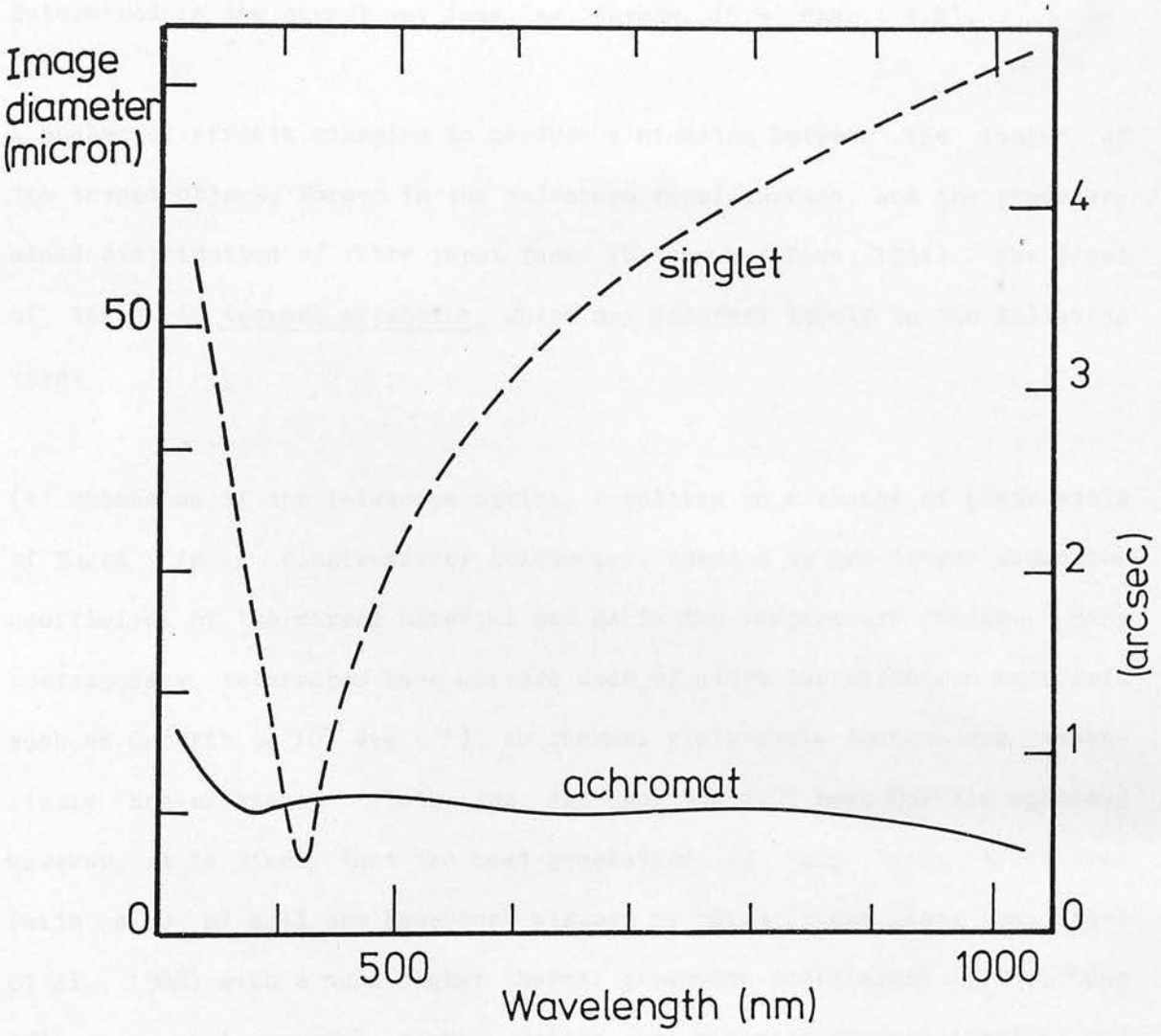

Figure 3.3 Wavelength dependence of FWHM image diameter for the UK Schmidt telescope equipped with single-element and doublet (achromatic) correctors. The former was used until April, 1977 (plate no. 3148); the latter has been in use since. (From Tritton et al., 1983.)

is commonly achieved by photographic astrometry, with plate-constants being determined in the normal way (see, eg, Watson, 1975, Chap. 1.2).

A number of effects conspire to produce a mismatch between the images of the target objects formed in the telescope focal surface, and the predetermined distribution of fibre input faces (Watson and Dawe, 1984). The first of these is thermal expansion, which may manifest itself in the following ways:

(a) Expansion of the telescope optics, resulting in a change of plate-scale of $\pi\alpha\Delta t$ (in a single-mirror telescope), where α is the linear expansion coefficient of the mirror material and Δt is the temperature change. Many contemporary telescopes have mirrors made of ultra low-expansion materials such as Cer-Vit ($\alpha \sim 10^{-7}$ deg C^{-1}), so thermal plate-scale changes are essentially non-existent. (Both the AAT and the UKST have Cer-Vit optics.) However, it is likely that the next generation of very large telescopes (with $a \sim 10$ m) will use honeycomb mirrors of borosilicate glass (eg, Angel et al., 1982) with a much higher thermal expansion coefficient (3×10^{-6} deg C^{-1}), so that careful mirror design (to mimimise thermal inertia) and strict thermal control in use will be necessary.

(b) Expansion of the telescope structure, resulting in defocusing that will cause light-loss at the fibre entry unless it is duly corrected.

(c) Expansion of the plate or other structure supporting the fibre input faces. This is peculiar to multi-fibre spectroscopy, and is potentially the most serious of the three. For example, a fibre supported by a hole

near the corner of a 356 mm square brass plate (as might be utilized in the UKST), which was drilled at 20 deg C and used in the telescope at 0 deg C, would move by nearly 100 μm relative to the plate centre (since, for brass, $\alpha = 18.9 \times 10^{-6}$ deg C^{-1}). At the plate-scale of the UKST, this corresponds to 6.5 arcsec, or more than two typical fibre diameters; it would clearly be disastrous. (At the AAT's coarser plate-scale, the larger fibre diameter would render the situation less critical, but considerable light-loss would still ensue.) In the fibre-positioning method actually adopted for the UKST's FLAIR system (direct cementing to a glass positive copy plate - see Chapter 6), the important temperature difference is that between the exposure of the original master plate and the use of the resulting copy plate in the telescope (since the expansion coefficient for both plates is identical). This difference will usually be small ($\lesssim 5$ deg C), since both types of observation are made at roughly the same time of year. That, coupled with the lower coefficient of expansion of the glass (8.1×10^{-6} deg C^{-1}; Eastman Kodak, 1973) results in an inherently more thermally-stable system. (It may be noted that Argyll and Standen (1985), in seeking to determine an accurate value for the UKST's plate-scale, also inadvertently measured the linear expansion coefficient of Kodak plates.) Fibre positioning techniques that use remotely-controlled actuators may permit some degree of real-time compensation for thermal expansion.

The remaining field effects that result in a mismatch of the fibres with the target images originate not in the telescope, but in the Earth's atmosphere; however, they may be conveniently discussed here. The first is due to differential atmospheric refraction across the field of the telescope. This has been investigated for Schmidt telescopes (which have the largest

field presently being considered, and therefore represent the worst case) by Bowen (1967) and by Wallace and Tritton (1979), with reference to photographic imaging near the meridian. However, a full investigation of the problem in relation to multi-fibre spectroscopy over the whole sky has been carried out by the author (Watson, 1984), and the results of that will be summarized here.

Any image in the field of a telescope is subjected to a refraction-induced trail that will have two components: (a) trail due to an overall rotation of the field, and (b) trail due to a distortion of the field within the rotating frame. The rates of these trails in terms of hour-angle and declination (h,δ) on the sky may be derived from analytical formulae such as those given by Smart (1971, p. 73) or obtained by numerical differentiation; however, Hinks (1898) has developed the expressions required in terms of the standard coordinates (ξ,η). These expressions are quoted in full by Watson (1984). It was Hinks (1898) who first suggested offsetting the instrumental pole from the true pole to compensate for the rotational component of atmospheric refraction, and this is routinely carried out at the UKST by means of motorized jacks. The effect of this compensation is shown in Figure 3.4, where contours of equal trail rate, computed from Hinks' formulae, are plotted over the southern sky for a telescope at the latitude of the UKST. The trail-rates are those that would be experienced by a star at the NE corner of a 6-deg square centred on the guide star (and are thus extreme values); the position-angles of the instantaneous trail vectors are also shown. In Figure 3.4(a), the trail-rates caused by refraction-induced field rotation alone are given, together with the result (Figure 3.4(b)) of applying the declination-dependent polar-axis offset to

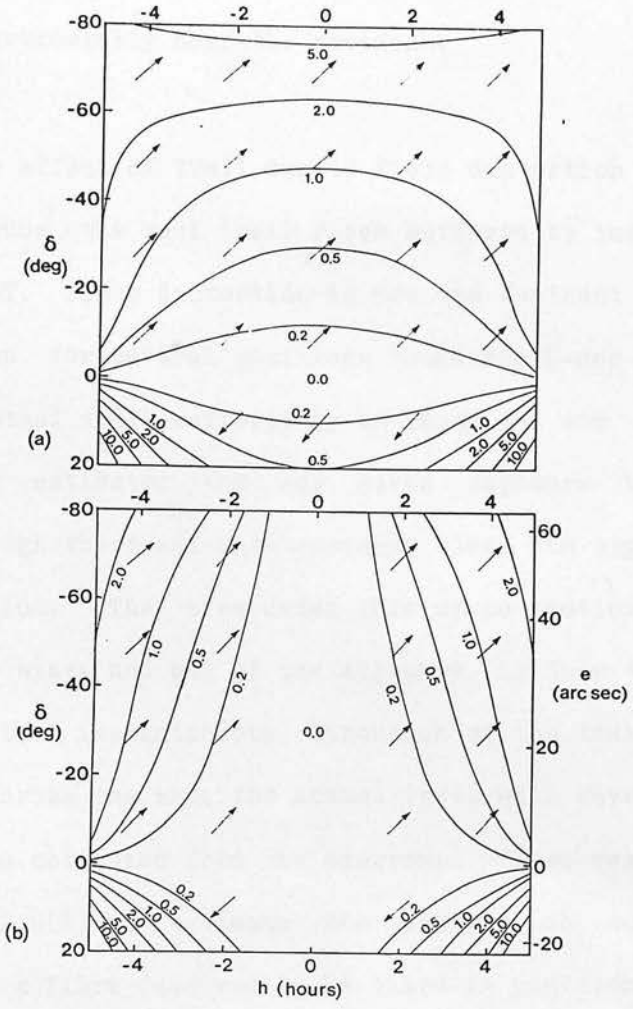

Figure 3.4 Contours of equal trail rate (in arcsec/hr) over the southern sky, showing the correction of field rotation due to atmospheric refraction, by elevation of the polar axis. The diagrams show the rates and instantaneous position angles (arrows) of the trail suffered by an image in one position in the field of the UK Schmidt telescope; they are plotted for $(\xi,\eta)=(3^\circ,3^\circ)$, the NE corner of the field. (a) Trail rates due to rotational component of refraction alone. (b) Resulting trail rates when the polar axis is elevated by an amount e (a function of declination) to produce the appropriate counter-rotation. (From Watson, 1984.)

provide the appropriate counter-rotation. Clearly, the compensation is very effective, particularly near the meridian.

In Figure 3.5, the effect of trail due to field distortion is added to Figure 3.4(b) to show the real trail rates suffered by images in the focal surface of the UKST. Since distortion is now the dominant effect, diagrams have to be given for several positions round the 6-deg square; in this case four. The actual trail suffered by an image in one of these field positions can be estimated for any given exposure by considering a cross-section through the trail-rate contours along the appropriate line of constant declination. The area under this cross-section, bounded by the hour angles at the start and end of the exposure, is then the total image trail. Because the instantaneous direction of the trail changes as the field is tracked across the sky, the actual trail will have some curvature; this, too, can be estimated from the diagrams. These results may be compared with Figure 2.9(b) to estimate the changes in entrance coupling efficiency, E, for a fibre (assumed to be fixed in position) over the duration of an observation. It will be seen that, even at the E and W edges of the field where the trail is worst (because of the relatively low latitude of the telescope), integrations of about 4 hours duration are possible on point sources in good seeing over much of the sky (1). This figure increases to 6 hours for the E and W edges of a 4-deg square field.

---

(1) These figures refer to 3σ radius fibres in 1 arcsec seeing (see Section 2.4). For fibres that are smaller relative to the seeing disc, the situation will be less favourable.

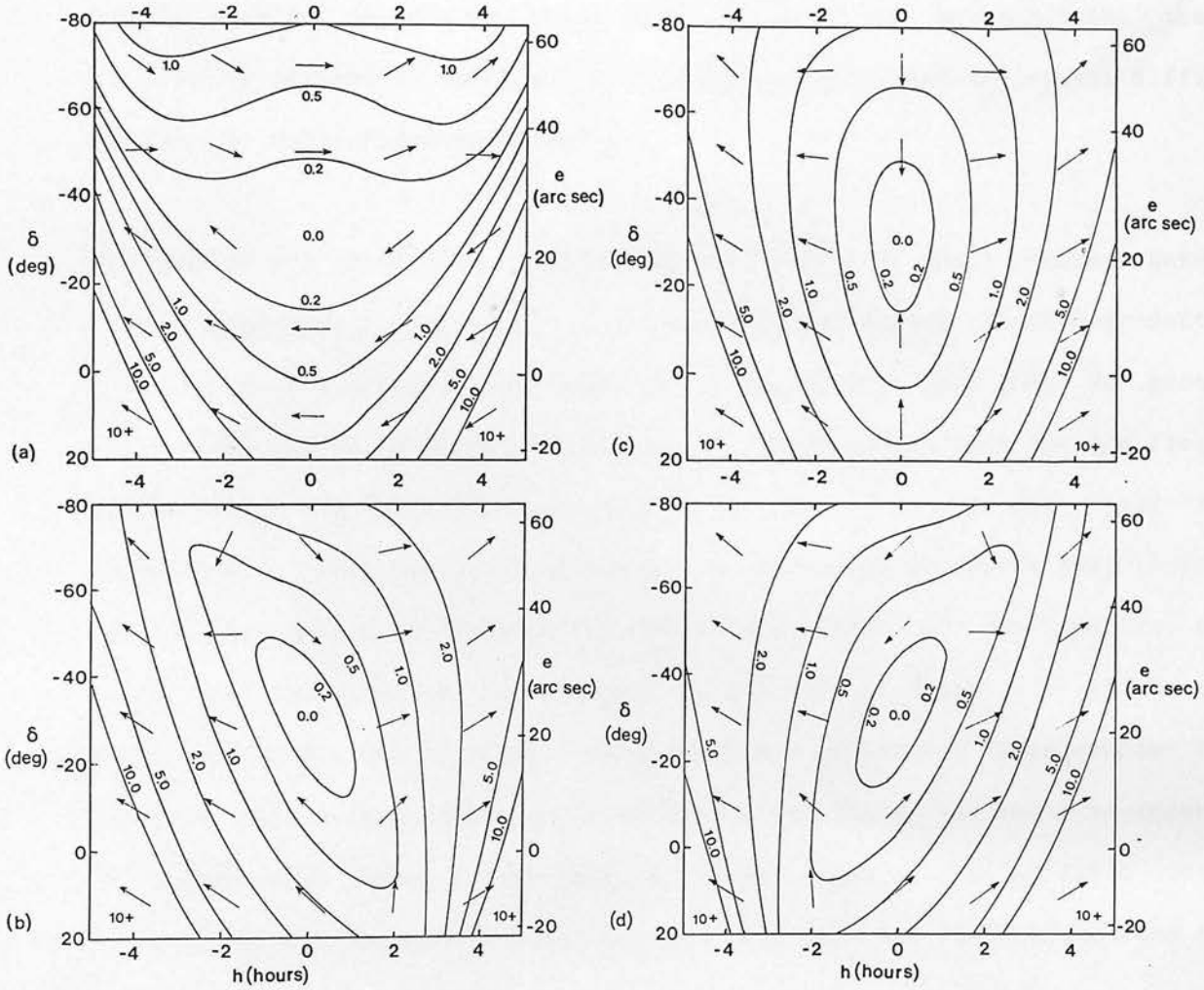

Figure 3.5 Trail-rate contours when field distortion due to atmospheric refraction is added to the residual field rotation shown in Figure 3.4(b). The contours are plotted for four positions in the field: (a) $(\xi,\eta)=(0°,3°)$, N edge mid-point; (b) $(\xi,\eta)=(3°,3°)$, NE corner; (c) $(\xi,\eta)=(3°,0°)$, E edge mid-point; (d) $(\xi,\eta)=(3°,-3°)$, SE corner. Over much of the sky, the trail rates are greatest along the E (and W) edges of the field (b-d); they are not in simple proportion to off-axis distance. The position angles indicate that the nature of the distortion varies across the sky. Near the meridian, it is a diagonal shear. (From Watson, 1984.)

Clearly, these tolerances are even further relaxed when the seeing is poor, or when extended objects are being observed, so it may be concluded that atmospheric refraction is unlikely to present significant additional difficulties for multi-fibre spectroscopy.

The same is not necessarily true of the last effect we shall consider here, that of atmospheric dispersion. Although this is, indeed, field-dependent, that aspect is a second-order variation of an effect that may be gross everywhere, and it is normal to attempt any compensation only for the field centre, since its differential extension to all parts of the field is impractical. Atmospheric dispersion is discussed by van de Kamp (1962) and, in more detail, by Willstrop (1987); the extent of the problem at higher zenith-distances is revealed by the data in Table 3.1. (At lower zenith-distances, the effects of dispersion are comparable with those of seeing.) The differences between alternate entries in the table represent the differential effect at the upper and lower edges of a 5-deg field such as that of the Willstrop telescope, and show that the field effect can be considerable.

The need for atmospheric dispersion compensation was appreciated as long ago as the 1860s, and a delightful early example is afforded by Airy's (1870) compensating eyepiece, in which the hemispherical eye-lens could be rotated in a cup-mount about the centre of curvature of its convex surface, to produce an inclination of the outer plane surface. Since that time, several atmospheric dispersion compensators (ADCs) have been described, usually consisting of a pair of zero-deviation (ie, doublet) prisms that can be rotated with respect to one another to produce continuously-variable

Table 3.1 Atmospheric refraction and dispersion.

Zenith Distance (degrees)	Standard Refraction r_o arcsec	Atmospheric dispersion (arc sec) Sea level (365 nm to 1014 nm)	La Palma	Mauna Kea
45.0	57.018	2.232	1.766	1.453
47.5	62.210	2.436	1.927	1.586
50.0	67.917	2.659	2.104	1.731
52.5	74.245	2.907	2.300	1.892
55.0	81.330	3.184	2.519	2.073
57.5	89.347	3.498	2.768	2.277
60.0	98.526	3.857	3.052	2.511
62.5	109.187	4.275	3.382	2.783
65.0	121.764	4.767	3.772	3.103
67.5	136.883	5.359	4.240	3.489
70.0	155.471	6.087	4.816	3.963
72.5	178.962	7.006	5.543	4.561
75.0	209.681	8.209	6.495	5.344
77.5	251.669	9.853	7.796	6.414
Relative pressure		1.000	0.75	0.59
Temperature C.		15.0	0.0	-12.0
Relative dispersion		1.000	0.7912	0.6510

(From Willstrop, 1987)

dispersion. Certainly the most ambitious of these is the ADC designed by Willstrop (1987) for his three-mirror telescope; it comprises a pair of zero-deviation prisms of meniscus form, over 1 m in diameter and with 4.96 m radius of curvature. These are placed 0.47 m in front of the focal surface, and will produce a maximum separation between images at 365 and 1014 nm of 4.776 arcsec. (They also introduce 0.96 mm of longitudinal chromatic aberration between these images that may be corrected by the fibre microlenses referred to in Section 2.4.) The greatest zenith-distance for which compensation can be achieved may then be ascertained from Table 3.1 to be 65 deg, 70 deg and 73 deg for telescopes at sea-level, at La Palma (Roque de Los Muchachos) and Hawaii (Mauna Kea) respectively. These zenith-distances will be increased if some image-spread other than zero is permitted, but it may be seen from the table that the field-dependent effect mentioned earlier will, in fact, reduce the maximum zenith-distances to 51 deg, 57.5 deg and 61 deg respectively for the three sites quoted, if all the spectral range must be imaged within 0.5 arcsec over the full 5-deg field of the telescope.

This small (0.5 arcsec) image diameter arises because we are here discussing a relatively large (5-metre) telescope that will be intended to observe fainter objects, so that it is important to use small (~1 arcsec) fibres to exclude as much sky light as possible (see Section 2.4). With a telescope of more modest aperture, such as the UKST, it is likely that generally brighter objects will be observed, and larger fibres may be used (2.7 arcsec on the prototype FLAIR system). If a limited spectral range is observed, and restrictions are placed on zenith-distance for optimum performance, then it is possible to carry out successful observation without

the use of an ADC. This also applies (to a lesser extent) to the AAT and, indeed, neither of these telescopes is thus equipped. It is, however, important that the tracking of the telescope on a guide star should be carried out in the same waveband as that of the spectra being observed. It may be noted for comparison with the data in Table 3.1 that, at the altitude of the UKST and AAT (Siding Spring Mountain), the relative pressure is 0.88.

There are some practical considerations related to the focal surface and its adaptability to fibres work that may be briefly discussed here. Size has already been mentioned; another is accessibility, and it will be seen that, in this respect, the Ritchey-Chrétien design is far superior to both the Schmidt and Willstrop designs, where the large focal surface is within the incoming beam. This also has serious drawbacks where equipment (eg, for remote fibre-positioning) needs to be mounted around the focal surface. Prime-focus use of fibres is likewise inconvenient, although the field here is generally smaller relative to the incoming beam. There may be mechanical obstructions to consider; for example, the space behind the UKST's focal surface is limited to only 55 mm by the plateholder support and focusing mechanism. Other usage of the focal surface may have to be taken into account; again, the normal photographic operation of the UKST places strong constraints on the modifications permissible for multi-fibre observation.

3.1.3 The requirements for the mounting of telescopes used for multi-fibre spectroscopy remain the same as those for any field-imaging technique, ie, that the focal surface should be kept in registration with the sky (involv-

ing tracking in translation and position angle) with the required precision for the duration of the exposure. This ability is not, of course, restricted to equatorial mountings, and a number of other alternatives are available (see Bingham, 1977, for an unusual example). Of these, the altazimuth is likely to be the most widely used due to its relative engineering simplicity.

The optical altazimuth telescope has three drives, viz. azimuth, altitude and field rotation, and the behaviour of these as objects are tracked across the sky has again been investigated in detail by the author, with particular reference to the zenithal region (Watson, 1978). The results of this investigation show that there is a blind spot at the zenith through which objects cannot be tracked at the sidereal rate, due to the large drive velocities and accelerations that would be required. The blind spot for a particular telescope is, in fact, the envelope of eight subsidiary blind spots, produced by a combination of the maximum velocities and accelerations attainable by each of the three drives in tracking and slewing modes. Equations for these blind spots are derived by Watson (1978). The blind spot of the 4.2-metre William Herschel telescope at La Palma was determined in this paper, and found to have dimensions of 0.66 deg x 0.42 deg (E-W x N-S), clearly a very small area of sky. It may be remarked that a multi-fibre spectroscopy system is being developed for this telescope.

New large telescopes that are currently being planned or are under construction will undoubtedly take the prospect of multi-fibre spectroscopy into account in their design (eg, Angel, 1984). This is a distinctly different situation from the adaptation of the technique to existing

telescopes and, in the case of a telescope to be used exclusively for fibres work, could result in a relaxation of the normal tolerances on image quality (eg, as in the NOAO's planned Multiple Object Spectroscopic Telescope; Barden et al., 1986). The paramount considerations of aperture and field size will, of course, remain. Some proposed telescopes that incorporate fibres into their planning are Caltech's 10-metre Keck telescope, already under construction (see, eg, Chown, 1985), the 4 x 7.5-metre National New Technology Telescope (NOAO, 1985), ESO's Very Large Telescope (Enard, 1986) and, perhaps further downstream, a large fibre-coupled transit telescope (Angel, 1982) and, of course, the Willstrop telescope. One other design that might be mentioned is a proposal by Dawe in collaboration with the author; it is a 2.4-metre classical Schmidt telescope (with a multi-fibre option) that takes advantage of the generous alignment tolerances of the Schmidt corrector by mounting it independently of the other optical components under servo control (Dawe and Watson, 1985). A sketch of this telescope is shown in Figure 3.6.

3.2 Spectrographs

3.2.1 The characterization of the various types of spectrograph used in astronomy is given in full by Meaburn (1976). We here restrict ourselves to an account of the properties of spectrographs employing plane diffraction gratings, as being the most widely-used type for multi-fibre observations; we may, however, note in passing the writer's previous involvement with a rather unusual Fourier-transform spectrometer (see Boggett, 1977). The bulk of the work described in this thesis involves the use of blazed plane reflectance gratings, and a number of formulae useful

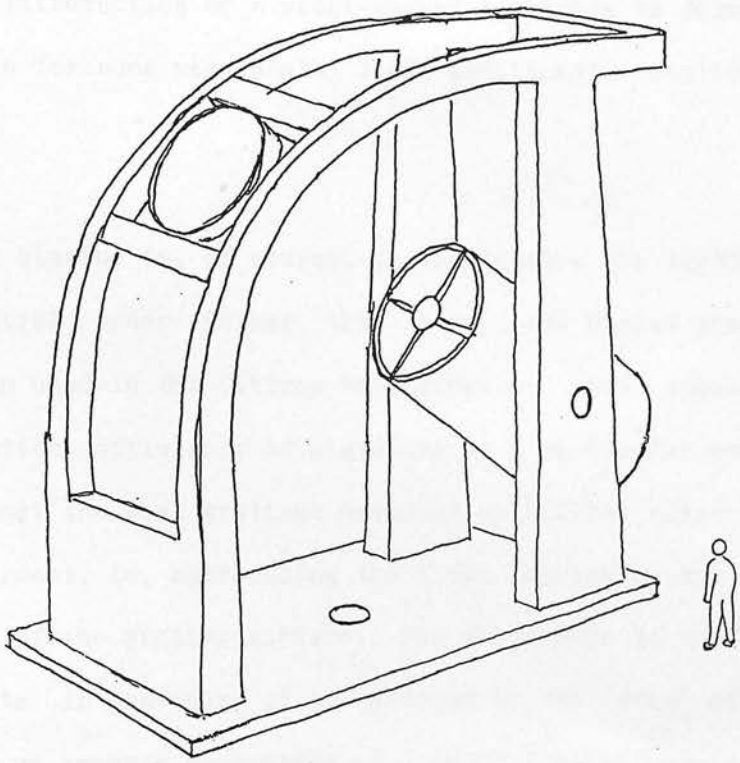

Figure 3.6 Sketch of a large altazimuth Schmidt telescope proposed by Dawe and Watson (1985). The classical Schmidt optical system has a 2.4-metre corrector, which, because of its relatively large alignment tolerances, can be mounted independently of the rest of the telescope, thereby improving stability and reducing cost.

for describing the behaviour of such gratings are derived from elementary considerations in an appendix to the present chapter. Similar formulae apply to transmission gratings, with the added ingredient of Snell's law; the further introduction of a wedge-shaped substrate to form a grism (with zero deviation for some wavelength) lends additional complication to the derivation.

The effect of blazing is, of course, to concentrate the light into a particular spectral order (other than zero), and blazed gratings are most efficient when used in the Littrow configuration (see Appendix). If we denote the optical efficiency of a grating at a particular wavelength by G, we may note that the best gratings measured at Littrow blaze wavelength can have G~85 percent, ie, approaching the limit imposed by the reflectance or transmittance of the grating surface. The adaptation to the Ebert configuration results in shadowing of the grooves by the "step" of the blaze, so that there is an inverse dependence of G on collimator/camera separation ϕ. The use of gratings at wavelengths other than the blaze wavelength for a particular order also reduces efficiency, with a fall-off that is generally more rapid toward the blue than toward the red. Transmission gratings tend to be more efficient than reflection gratings for inverse spacings of up to 600 grooves/mm, simply because the reflectance, ρ, of an aluminized surface is lower than the transmittance, τ^2, of two refracting surfaces (which can also be further improved by coating). At higher inverse spacings, however, the transmission of the ruled surface becomes progressively poorer, so that reflection gratings are superior. Blazed gratings are replicated from masters that are either ruled in the traditional manner, or produced holographically by interference in photoresist material (eg, Wilson, 1983).

The principal advantage of the latter type is that they eliminate the ghosts that may be formed by periodic errors in ruled gratings (2). Experimentation is just beginning in the use of holographic gratings for astronomy (eg, Hickson, 1986).

Turning to the properties of spectrographs that use plane gratings, the optical efficiency, Q_S, is defined in the same way as that for a telescope; it specifically does not include G, the grating efficiency. Meaburn (1976, Chap. 1), following Jacquinot (1954; 1960), defined a luminosity, L, for spectrographs; for fibre-coupled grating instruments, this will be given by

$$L = Q_S G \, A\Omega , \qquad (3.1)$$

where the $A\Omega$ product now refers to the illuminated area of the grating and the solid angle subtended at the collimator pupil by the fibre exit face (compare Section 2.3). Jacquinot demonstrated that the product LR of spectrograph luminosity and resolution (which is not necessarily the grating resolution derived in the Appendix) is constant for spectrographs of the

---

(2) These are distinct from the geometrical ghosts that may be produced in spectrographs by reflections between the detector surface and the slit surround; spectrographs fed by multiple fibres are particularly susceptible to these because of the method of polishing the fibre faces within the surround, which itself becomes polished. They may be reduced by embedding the fibre ends in an epoxy resin containing a black dye prior to polishing.

same type, a result that might be expected intuitively. This product was included by Meaburn (1976) in a figure of merit, Z, for the intercomparison of spectrographs of different type; for our purposes, however, the spectrograph's contribution to the overall optical efficiency in the determination of signal-to-noise is a parameter of more immediate relevance, and is discussed in the last section of the present chapter.

3.2.2 The ab initio design of classical grating spectrographs for use with multiple optical fibres is largely determined by the radius, r, of the fibre, the focal ratio, f, of the beam emerging from it, and the geometrical properties of the detector: viz, its physical dimensions, (x',y'), and the size, z, of the minimum resolution element or pixel, here assumed to be square. We define the magnification, M, of the spectrograph to be the ratio of image and object scales in the conjugate detector and fibre "slit" planes; it is thus simply the ratio of focal lengths f_{cam}/f_{coll}. The equivalent width at the detector (in terms of wavelength) of a fibre output face projected through the system may now be written; it is

$$d\lambda_f = M(\pi r/2)(d\beta/d\alpha)(d\lambda/dx), \qquad (3.2)$$

where $d\beta/d\alpha$ and $d\lambda/dx$ are the slit projection factor and reciprocal linear dispersion respectively (see Appendix), and $\pi r/2$ is the equivalent slit-width of the fibre (see Section 2.5). The quantity $d\lambda_f$ is clearly the minimum resolution-element of the spectrograph, or the width of its instrumental profile, and the spectrograph resolution, $\lambda/d\lambda_f$, will normally be smaller than the grating resolution, R, derived in the Appendix.

A related quantity is the detector pixel width in terms of wavelength; this is simply

$$d\lambda_p = z\, d\lambda/dx. \qquad (3.3)$$

The ratio $d\lambda_f/d\lambda_p$ is the sampling interval of the detector, and is usually chosen to lie between 1 and 2. Less than this (ie, undersampling) fails to make full use of the resolution of the spectrograph, and may introduce errors due to possible variations in sensitivity across a single pixel; more than this (ie, oversampling) does not make full use of the resolution of the detector. It is the sampling interval, $d\lambda_f/d\lambda_p$, that determines the magnification, M, of the spectrograph, since $d\beta/d\alpha$ will be fixed by the grating angle, and $d\lambda/dx$ cancels out. For most spectrographs, the relative sizes of slit and detector pixel result in $M<1$, but if particularly small fibres are being matched to a detector (as in the spectrograph for the UKST FLAIR system, for example), then $M>1$ may be necessary.

Once the spectrograph magnification is fixed, then the maximum number of fibre channels, j, that may be used is determined, because

$$M = y'/j\sigma, \qquad (3.4)$$

where σ is the separation of the fibre centres along the slit. The value of σ should be chosen so that at least two rows of empty pixels fall between adjacent spectra at the detector, ie,

$$\sigma \geqslant 2z/M + 2r. \qquad (3.5)$$

Thus, the situation where fibres are placed in contact along the slit ($\sigma \sim 2r$) is not acceptable, unless there is a large-diameter non-propagating outer glass cladding such as that shown in Figure 2.4(b). (This is the case for the fibres used in the prototype FLAIR system, which are, indeed, placed in contact along the slit, and it may be noted that the outer cladding here performs the additional role of isolating the optical claddings of adjacent fibres.)

Consider now the focal ratio, f, of the beam emerging from each fibre. We have already discussed the matching of this to the collimator focal ratio in Section 2.5; we must have

$$f \geqslant f_{coll} / D_{coll} ,$$

where D_{coll} is the collimator pupil diameter. The required angular field of the collimator, 2δ, is given by

$$2\delta = j\sigma / f_{coll} , \qquad (3.6)$$

and economics dictates that this will be the total extent of the well-corrected (and preferably flat) field of the collimator optical system. Thus, the minimum collimator pupil diameter is now determined because, by combining Equation 3.6 with the previous inequality, we find

$$D_{coll} \geqslant j\sigma / 2\delta f \qquad (3.7)$$

for all the light to be collected from the fibres.

There is an implicit assumption in Condition 3.7 that each fibre in the linear array is directed towards the centre of the collimator pupil and, as we have seen in Section 2.5, this will not normally be true, since fibre output ends are almost invariably aligned parallel with the collimator axis. Clearly, this will result in vignetting of the output beam from fibres near the ends of the "slit" by the edge of the collimator pupil. The problem may be remedied either by placing a field lens of focal length f_{coll} over the slit, or by increasing the minimum permissible diameter of the collimator, D_{coll}, to $f_{coll}/f + j\sigma$, thus reducing its focal ratio to $(f^{-1} + j\sigma/f_{coll})^{-1}$. This is, in fact, the situation found in the collimator of the simple Ebert spectrograph designed and built by the writer for use with FLAIR; here, the focal ratio of a collimator lens with f_{coll} = 50 mm is reduced to f/1.7 so that the lens will intercept all the f/2 beams from a fibre "slit" 5 mm long.

The possibility of vignetting by the camera pupil also needs to be considered, and this may be investigated using the geometrical constructions shown in Figure 3.7. Here, a schematic linear spectrograph is depicted, and it will be seen that the geometry of camera-pupil vignetting differs in the x- and y-planes. For brevity, we do not derive analytical expressions giving the conditions for no vignetting; however, we may note that the collimator and camera distances from the grating, d_{coll} and d_{cam}, are of considerable importance, and, in general, require to be minimised. In Ebert spectrographs, these minimum distances are determined by the physical diameters of the collimator and camera, and their angular separation, ϕ, so

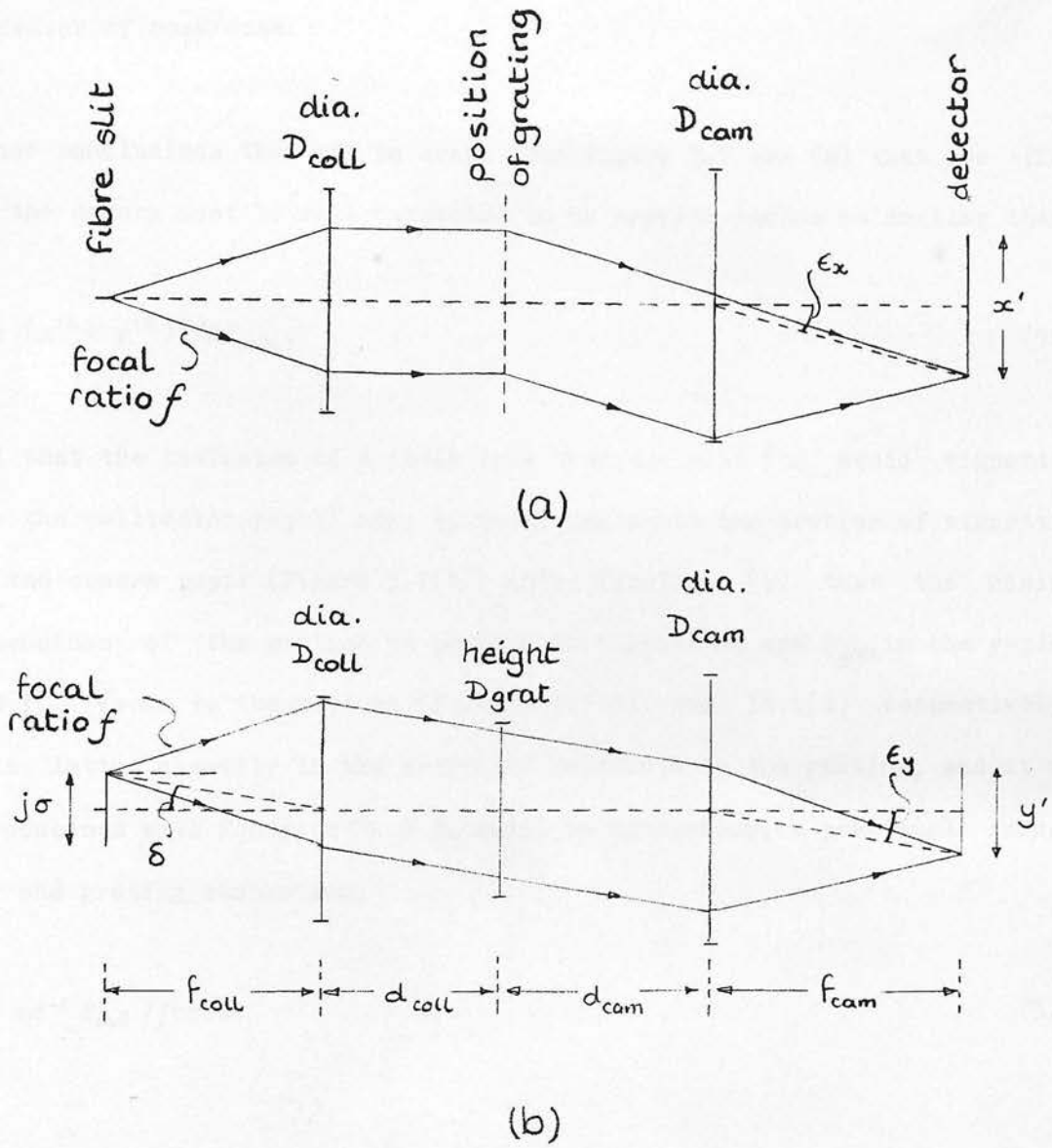

Figure 3.7 Geometry of pupil vignetting in a fibre-coupled spectrograph; (a) x-plane, (b) y-plane (see text).

that d_{coll} and d_{cam} may be relatively large. We also note, from consideration of Figure 3A.1(d), that the grating changes the beamwidth in the x-plane by a factor of $\cos\beta/\cos\alpha$.

Other conclusions that may be drawn from Figure 3.7 are (a) that the field of the camera must be well-corrected to an angular radius no smaller than

$$\epsilon = (x'^2 + y'^2)^{1/2}/2f_{cam}, \qquad (3.8)$$

(b) that the inclusion of a field lens over the slit (to avoid vignetting by the collimator pupil) may, in fact, aggravate the problem of vignetting by the camera pupil (Figure 3.7(b)) and, finally, (c) that the minimum dimensions of the grating to produce no vignetting are D_{grat} in the y-plane and $f_{coll}/f\cos\alpha$ in the x-plane (Figures 3.7(b) and 3A.1(d) respectively). This latter quantity is the projected beamwidth on the grating, and it may be combined with Equation 3A.8 to give, in conclusion, a practical formula for the grating resolution,

$$R = md^{-1} f_{coll}/f\cos\alpha. \qquad (3.9)$$

In the foregoing discussion, we have demonstrated the steps necessary for the optical design of fibre-coupled spectrographs, and shown that the entire system is determined from a relatively small number of initial parameters (r, f, x', y', z). However, within the design guidelines, considerable variation is possible. For example, the foregoing applies equally to reflecting or refracting optics, to Ebert or Littrow spectrographs, and to reflection

or transmission gratings. We have already alluded several times to the spectrograph built for FLAIR, and will give a more detailed account of it in Chapter 6. By the standards of conventional spectroscopy, the requirements for this instrument are unusual: it must have a very fast collimator to accept an f/2 beam from all the fibres (allowing for degradation of the f/2.5 telescope beam to the NA limit of the fibre) and, at the same time, must accept a sufficiently wide field of view to permit the use of a satisfactory number of fibres. These requirements will become increasingly more common if some of the telescopes mentioned at the end of the previous section are built. The solution chosen for the prototype FLAIR spectrograph was to limit the number of fibres to 40, producing a slit length of only 5 mm and thus allowing the use of ordinary 35 mm SLR camera lenses for the optics, with correspondingly small (52 mm square) diffraction gratings - an altogether inexpensive solution. Other designs are possible, though, and a particularly attractive scheme for increasing the number of fibres would be the use of a Schmidt-type collimator, perhaps in an autocollimating (Littrow) configuration with the grating replicated onto a figured substrate to produce a reflective corrector. Numerous other options are open for producing fast, fibre-coupled spectrographs, and this promises to be a fruitful area for optical designers.

3.2.3 The basic problem in the mechanical design of astronomical spectrographs is the elimination of flexure, and the traditional way of achieving this has been to incorporate great rigidity into the structure. These considerations remain the same for multi-object spectrographs coupled with short fibres for image-reformatting alone, since the spectrograph will still be mounted on the telescope (as is, for example, the Royal Greenwich

Observatory (RGO) spectrograph on the AAT). However, the use of extended fibre feeds to stationary spectrographs permits much greater freedom in mechanical design, since gravity always acts in the same direction relative to the instrument. Such freedom has long been the prerogative of designers of coudé spectrographs, who have traditionally used massive supports for what are often very large optical elements, isolating them from vibration in the same way as a telescope pier.

We here propose an alternative solution for the support of more modest (low to medium-high dispersion) fibre-coupled spectrographs in stationary positions. This is to follow the conventional methods used in optical laboratories, where the optical components are set up on individual lightweight mountings bolted to a rigid flat plate, which is itself supported on an active vibration-isolation system incorporating both horizontal and vertical isolation. A fibre-coupled spectrograph built on such an optical table can be simply placed on the floor of the dome, or in a nearby laboratory. It will be immune to the vibrations of the floor due to movement of the dome, wind gusts, exhaust-fan motors and personnel movement; its components are easily accessible on the table surface for adjustment or reconfiguration, and the whole assembly can be moved around at will, if retractable wheels are fitted.

This technique was adopted for the UKST-FLAIR spectrograph, using the smallest vibrationally-isolated optical table produced by the Newport Corporation (USA) together with the same company's optical component mountings. The table top is of laminated stainless steel/aluminium honeycomb construction, 914 mm x 1219 mm x 109 mm, which is flat to within 75 μm over

the entire surface, and which has a static load deflection of less than 0.01 arcsec/kg (Newport, 1983). The air-mount isolation system is effective for frequencies above 0.9 Hz (vertical) or 2 Hz (horizontal) with a maximum loading of ~700 kg; it is supported by a chassis with retractable castors, fabricated in Australia by Quentron Ltd. This table has been outstandingly successful in use, enabling the theoretical resolution of the spectrograph to be maintained over exposures in excess of 6 hours. A similar, non-moveable system has recently been deployed for a single-fibre high-resolution spectrograph on the 1.6-metre telescope of Pennsylvania State University (Ramsay and Huenemoerder, 1986). Since vibrationally-isolated optical tables are commercially available in a wide range of sizes capable of carrying loads of up to several tonnes, it is suggested that they are an obvious choice for the mechanical support of stationary fibre-coupled spectrographs for existing and future large telescopes.

3.3 Detectors

3.3.1 The properties required of two-dimensional detectors for fibre-coupled multi-object spectroscopy are identical with those for most astronomical imaging applications, and so the same types of low light-level detector systems are used. Detailed accounts of astronomical detectors and their properties abound in the literature (eg, Eastman Kodak, 1973; Meaburn, 1976, Chap. 2; Ford, 1979; Eccles, Sim and Tritton, 1983; Kitchen, 1984, Chaps. 1 and 2; Mackay, 1986) and we here restrict ourselves to an outline of the most important characteristics of detectors, together with a brief survey of the various types, with some emphasis on

detectors that figure in later chapters of this thesis.

We begin with the quantum efficiency, q, which is defined as the ratio of the number of photons detected to the number of incident photons, for a given wavelength. More precisely, it is the fraction of incident photons that produce one measureable event; it is sometimes referred to as the responsive quantum efficiency. Because (a) q does not allow for photons that may be recorded and then lost at a later stage in the detection process, (b) the measured events may be given unequal statistical weight in that subsequent detection process, and, (c) the subsequent process may itself introduce so-called receiver noise, it is usual to consider a parameter for the whole detection system, referred to as the detective quantum efficiency, q_D. This is defined as

$$q_D = (S_o/N_o)^2/(S_i/N_i)^2 \qquad (3.10)$$

(Rose, 1946; Fellgett, 1958; Jones, 1958; see also Eastman Kodak, 1973) where S_i/N_i, S_o/N_o are the signal-to-noise ratios of the input and output signals respectively. Thus, in an ideal detector, where none of (a)-(c) above apply, and for an input signal subject to Poisson noise only, we will have

$$q_D = (S_o^{1/2})^2/(S_i^{1/2})^2 = q.$$

Detective quantum efficiency (DQE) is therefore a measure of the efficiency of a real system relative to that of an ideal detector, and we will always have $q_D \leq q$. It might be added that it is always necessary to specify exact-

ly what is meant by S_o/N_o, since there may be abiguity as to what is the output signal (eg, in photography, where the photographic image may be subsequently digitized by ancillary equipment).

The linearity of response of a detector is an important parameter related to its quantum efficiency; it is simply the extent to which the output and input signals follow a linear relationship. Nonlinearity may be regarded as a variation of responsive quantum efficiency, q, with the total number of events that have already been recorded in a single detection process. Dynamic range is the ratio of the largest and smallest output signals, or numbers of events, that can be detected. The human eye is remarkable in this respect, being able to operate satisfactorily in light levels differing by more than 10^9, compared with a dynamic range of $\sim 10^4$ for charge-coupled devices (CCDs) and perhaps 100 or so for the IPCS (image photon counting system), described below. The wavelength range is that within which the quantum efficiency is above some specified value (eg, zero, or 1 percent of its peak value); it is bounded by the cut-off wavelength(s). As might be expected, the peak wavelength is that for which the quantum efficiency is a maximum.

The linear resolution of a detector is usually specified as the number of line-pairs/mm that it can resolve. It is more precisely defined in terms of the modulation transfer function (MTF), commonly used for comparing the performance of optical imaging systems. An image consisting of a sinusoidal intensity pattern

$$I = a + b \sin 2\pi\nu x$$

with spatial frequency ν, has a modulation defined to be

$$M = (I_{max} - I_{min})/(I_{max} + I_{min}). \qquad (3.11)$$

When this image falls on the detector, the output signal will also be modulated, and the modulation transfer, defined as M_{out}/M_{in}, will be a decreasing function (ie, the MTF) of spatial frequency, ν. Thus, the value of ν at which the MTF falls to some specified value will define the linear resolution of the detector. We have already referred, in Section 3.2, to a pixel as the minimum resolution element of a detector; for those detectors consisting of arrays of independent photo-sensitive cells (eg, CCDs), the pixel size, z, is a well-defined entity, but for others, such as photographic emulsions, it may be regarded as the reciprocal of the linear resolution. Finally, the linear dimensions, (x',y'), of a 2-d detector may, as we have seen in the previous section, have a strong influence on the design of the instrument in which the detector is being used.

3.3.2 Turning now to the properties of particular types of detectors, photographic emulsions operate by the conversion of silver halide crystals (usually AgBr or AgCl) into particles of metallic silver by the action of incident photons. (These are the measureable events referred to earlier.) The development of the emulsion is a chemical amplification of the original signal, and the subsequent chemical processing removes the unused light-sensitive material to leave a permanent image, which may then be digitised, if necessary, by means of a scanning densitometer of some type.

The original signal is recorded in the presence of receiver noise, which takes the form of chemical fog, and is present even without exposure to light; the density D (Section 1.4) of the chemical fog varies with emulsion type, age, storage and operating temperatures, developer type, development time and temperature, and the effects of pre-exposure hypersensitization techniques. The detective quantum efficiency of photographic emulsions is low, and this constitutes their principal disadvantage. An often-quoted peak DQE measured for the best photographic emulsions is ~4 percent at 4500 Å, but it is much lower at higher wavelengths. The spectral response of photographic emulsions is usually presented in terms of sensitivity, ie, the reciprocal of the exposure required to produce a given density above the chemical fog. Such sensitivity curves for some Kodak emulsions with differing spectral response are shown in Figure 3.8(a). Photographic emulsions have a natural, or unmodified, response similar to that of the 103-0 type in Figure 3.8(a); it is sensitive to blue light only, and the extension to higher wavelengths requires the modification of the emulsion by the inclusion of sensitizing dyes during manufacture. The effect of these is seen in the other curves.

The non-linearity of photographic emulsions is expressed in characteristic curves of the kind shown in Figure 3.8(b). Here, the density of the processed emulsion is plotted against exposure (ie, the amount of incident light), and it can be seen that the curve has a toe (which lies above the chemical fog level), a useful portion that is approximately linear, and a shoulder, where the emulsion is saturated. The slope of the linear portion is referred to as the contrast, γ, of the emulsion, and the range of densities over which it is linear is the dynamic range. Two classes of

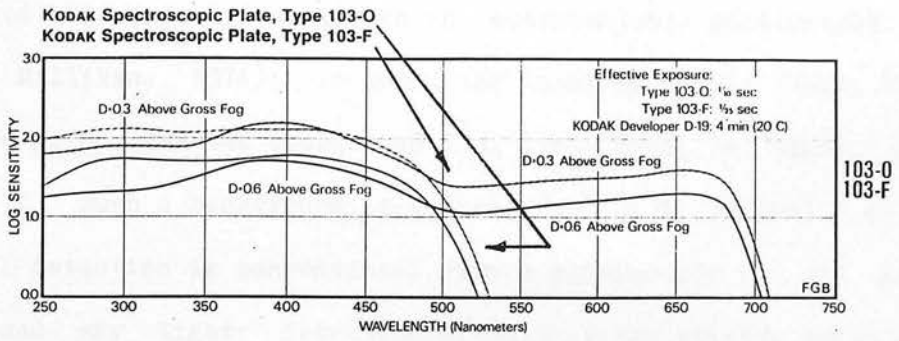

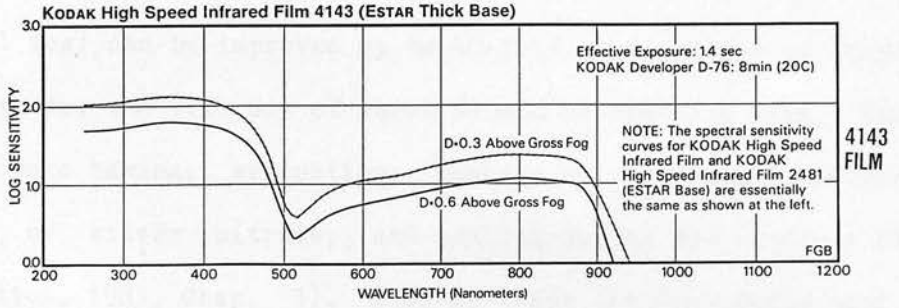

(a)

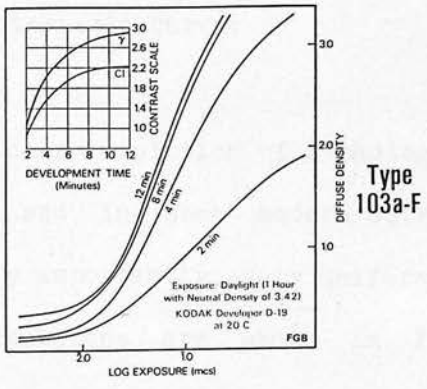

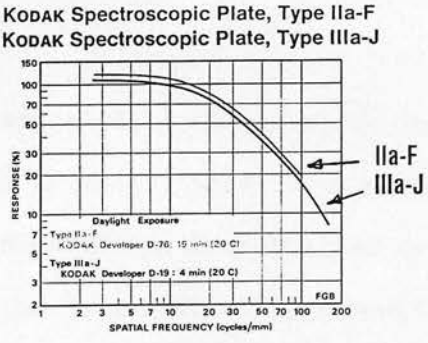

(b)

(C)

Figure 3.8 (a) Spectral sensitivity of some Kodak emulsions. (b) Characteristic curves of Kodak 103a-F emulsion. (c) Modulation transfer functions of some Kodak emulsions. (From Eastman Kodak, 1973.)

detection are commonly recognised in astronomical photography (Marchant, 1964; Millikan, 1974); in both, the input signal is faint, but in Class I, there is no unwanted background flux (ie, S_i/N_i is high), whereas in Class II, such a background is present (ie, S_i/N_i is low). An example of Class II detection is conventional direct photography in the presence of background sky light; detection of multi-fibre spectra would normally be Class I, however. In both these classes of detection, the speed of the emulsion (ie, the exposure required to attain a specified density above chemical fog) can be improved up to 50-fold by a variety of hypersensitizing methods, the efficacy of which depend on emulsion type. These include pre-exposure baking; evacuation; soaking in nitrogen, hydrogen, water, ammonia or silver nitrate; and cooling during the exposure (Eccles, Sim and Tritton, 1983, Chap. 3). Some of these are frequently used in combination. In addition, Class I detection may be further improved by preflashing to raise the minimum density above the insensitive toe of the characteristic curve.

The linear resolution of a photographic emulsion is dependent on the grain size, and in some modern astronomical emulsions this is very small and, equally importantly, very uniform. The MTFs of two fine-grained astronomical emulsions are shown in Figure 3.8(c), and it will be seen that the resolution approaches 200 cycles/mm, with an implied pixel size of 5 μm. From the point of view of general astronomical detection, high resolution is just one of the advantages of photography. The others may be summarized as almost unlimited linear dimensions; enormous information storage capacity; high dimensional stability; wide spectral coverage; well-established technology and continuity with earlier-epoch observations;

low cost. Against these, we have the disadvantages: low DQE; non-linearity; difficulty of correcting for non-uniformity of response over the detector area; need for advance preparation by hypersensitizing; need for additional processing to digitize the data; limited dynamic range. (For a full discussion of these and all other aspects of astronomical photography, see the excellent account by Eccles, Sim and Tritton, 1983, Chaps. 2 and 3.)

In multi-fibre spectroscopy, some of the above are of reduced importance and, in particular, perhaps the biggest single advantage of photography (ie, large detector size) is of relatively little consequence. Nevertheless, photographic detection has been used to advantage in the FLAIR system, as described in Chapters 6 and 7. The emulsions used most successfully have had the "F" response shown in Figure 3.8(a) and, of these, the most useful results have come from Kodak Technical Pan type 2415. This fine-grained emulsion has similar resolution characteristics to IIIa-J (Figure 3.8(c)), and responds extremely well to hydrogen hypersensitization with pre-baking in nitrogen, with the surprising proviso that it must be on a film substrate rather than on glass (see also Everhart, 1980; Marling, 1980; Ogura and Liller, 1985; and compare Waller, 1980). The emulsion is always used in FLAIR with additional pre-flashing. Occasional use has also been made of Kodak High-Speed Infrared film, whose sensitivity curve is also shown in Figure 3.8(a). Although this emulsion does respond to silver-nitrate hypersensitization (Armstrong, 1980), it has been merely pre-flashed when used in FLAIR. Finally, it goes without saying that the FLAIR fibre-positioning technique relies heavily on the merits of the photographic method.

The poor quantum efficiency of photographic emulsions may be improved by the use of image intensifiers. Here, the initial image is formed on a photocathode, and the resulting electron flux is focused (electrostatically or magnetically) and accelerated to form an electron image on a target that may be an output phosphor (single-stage intensifier), a phosphor/photocathode interface (multi-stage intensifier), or an electron-sensitive emulsion (electronographic camera). Image intensifiers, as such, are more convenient in use than electronographic cameras, but lack the high degree of linearity found in the latter (eg, Meaburn, 1976, Chap. 2; Hawkins, 1983). The important characteristics of image-intensifier tubes are the spectral response of the photocathode (of which a typical example - that of the S-20 type - is shown in Figure 3.9), the spectral emission profile of the output phosphor, the extent to which linear resolution is preserved and image distortion is avoided, and the amount of dark noise (analagous to chemical fog) present.

Image intensifiers may have photocathode diameters in excess of 50 mm, and a typical resolution at the phosphor would be ~80 line-pairs/mm. The output image is transferred from the phosphor to the photographic emulsion by such means as lens-coupling (which is extremely inefficient, due to the quasi-isotropic nature of the phosphor emission) or the use of a fibre-optics faceplate, both of which tend to degrade the resolution.

The responsive quantum efficiency of image intensifier photocathodes is high (up to 20 percent) and their response intrinsically linear; the overall gain in radiant power may also be very high (up to ~10^7). However, a major source of noise that tends to reduce the DQE and impair the overall

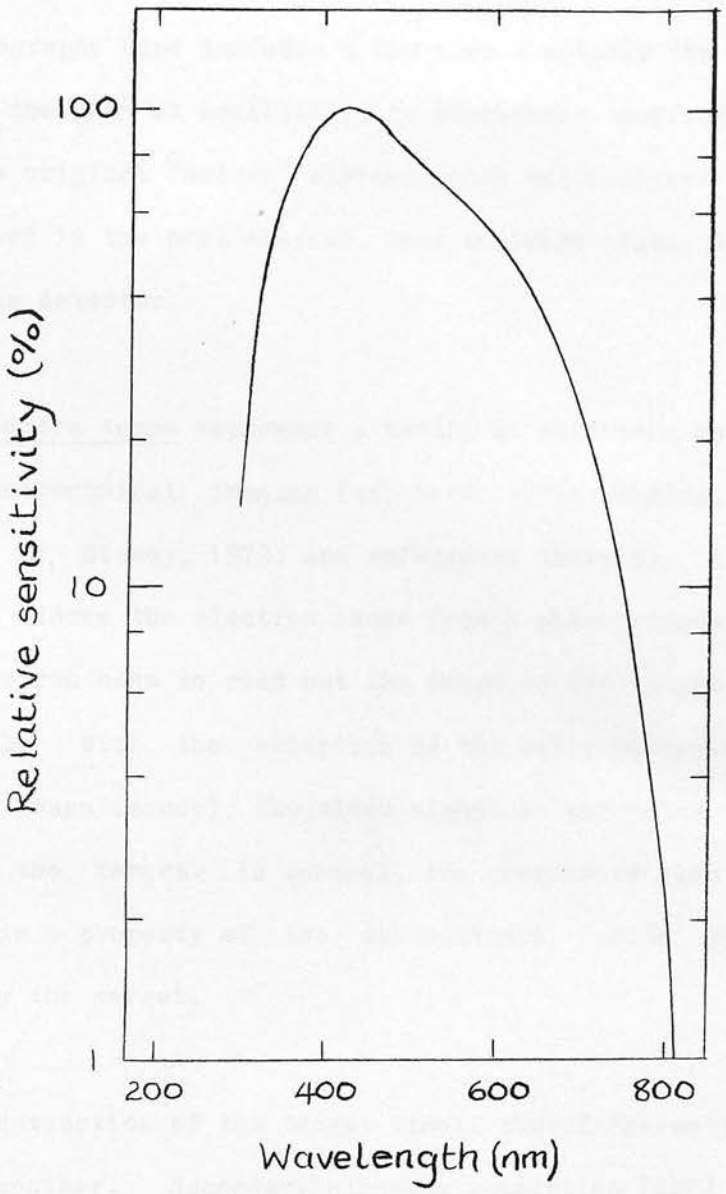

Figure 3.9 Spectral response of an S-20 photocathode (after RCA, 1970).

linearity in some intensifiers is a variation in the size of the final photographic image produced by a single incident photon. In fact, the photographic use of image intensifiers also shares most of the drawbacks of direct photography (and includes a few more - notably the distortion of the image), but the gain in sensitivity is frequently sufficient to outweigh these. The original "Medusa" fibre-coupled multi-object spectroscopy system, described in the next chapter, used an image tube with photographic plates as its detector.

Television camera tubes represent a family of detectors that have applications in astronomical imaging (eg, Ford, 1979; Eccles, Sim and Tritton, 1983, Chap. 7; Disney, 1972, and references therein). All consist of a target that stores the electron image from a photocathode, together with a scanning electron beam to read out the image on the target as a sequential video signal. With the exception of the early return-beam tubes (image orthicon and image isocon), the video signal is extracted as the current flowing in the target. In general, the responsive quantum efficiency of these tubes is a property of the photocathode, while the linearity is determined by the target.

It is the construction of the target itself that differentiates one type of tube from another. Secondary electron conduction (SEC) tube targets are usually composed of low-density potassium chloride, and have a very low dark current, permitting long integrations on the target without cooling. These tubes also have relatively high resolution (~40 line-pairs/mm). Vidicon tubes, of which the lead-oxide vidicon (eg, Philips Plumbicon) is a common type, have a photoconductive target that both creates and stores the

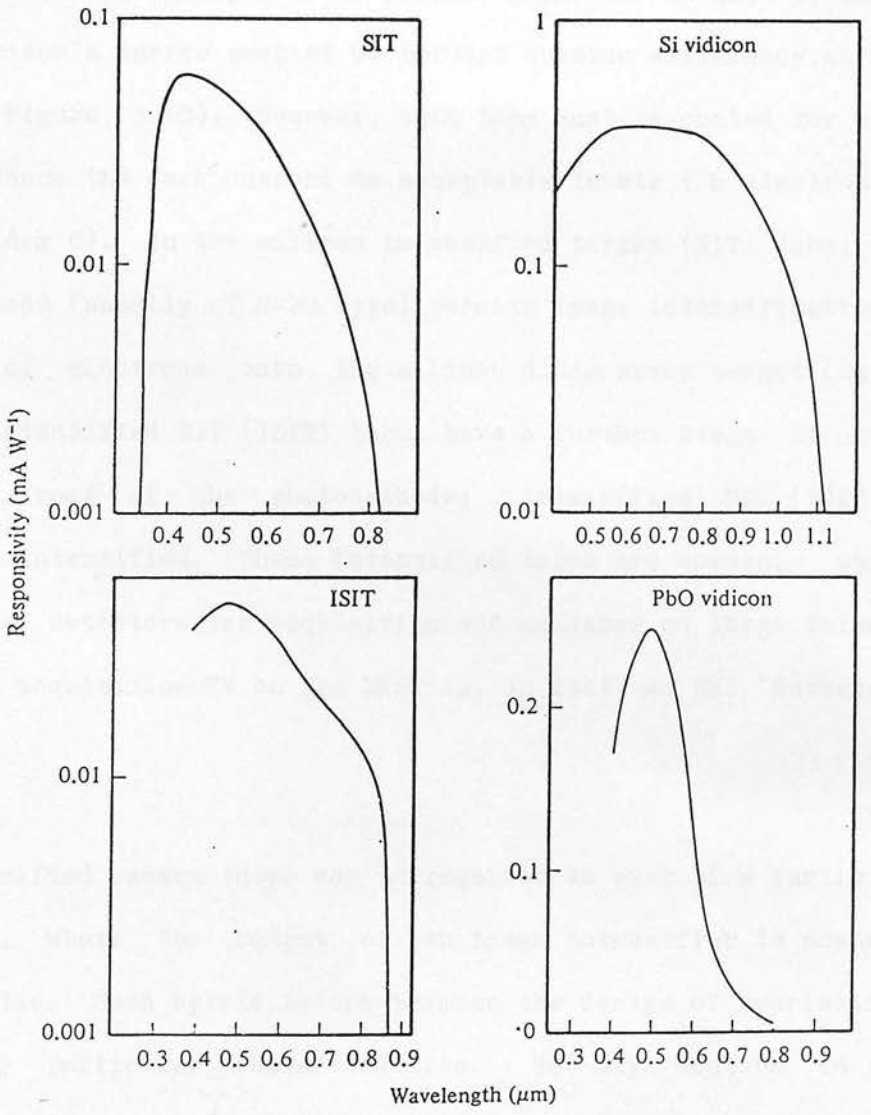

Figure 3.10 Spectral response characteristics of four types of TV camera tube. (From Eccles, Sim and Tritton, 1983.)

charge image, dispensing with the separate photocathode. The silicon target vidicon's diode array structure produces a much-extended red response, with quantum efficiency over 50 percent from 4000 to 8000 Å, compared with the Plumbicon's narrow peak of 50 percent quantum efficiency at around 5000 Å (see Figure 3.10). However, this tube must be cooled for astronomical use to reduce the dark current to acceptable levels (~6 electrons/pixel/sec at -78 deg C). In the silicon intensified target (SIT) tube, a separated photocathode (usually of S-20 type) permits image intensification by acceleration of electrons onto the silicon diode array target (eg, Robinson, 1977). Intensified SIT (ISIT) tubes have a further stage of intensification in front of the photocathode; intensified SEC (ISEC) tubes are similarly intensified. These intensified tubes are commonly used as low light-level detectors for acquisition and guidance on large telescopes, and the FLAIR acquisition TV on the UKST is, in fact, an EMI "Surveyor II" ISIT camera.

The intensified camera tubes may be regarded as part of a family of hybrid detectors, where the output of an image intensifier is scanned by some other device. Such hybridization permits the design of specialized detectors with particular characteristics. We may mention in passing the photon-counting array of the Australian National University (Dopita, private communication), which uses a micro-channel plate image intensifier (see, eg, Eccles, Sim and Tritton, 1983, Chap. 6) coupled to a CCD detector. However, the most important of these in the present context is the University College, London, image photon-counting system (IPCS) (Boksenberg, 1972; Jorden, 1977), since this is the principal detector used with the AAT multi-fibre systems.

In the IPCS, a magnetically-focused four-stage EMI intensifier (achieving a gain in radiant power of 10^7 with 40 kV applied over the four stages) is lens-coupled to a Plumbicon TV camera tube. The choice of lens-coupling (with only 1 percent efficiency) rather than a fibre-optics faceplate, and the choice of a lead-oxide vidicon rather than a silicon target vidicon (with a diode array) is specifically to avoid structure in the image planes. The quantum efficiency of the Plumbicon is very high, particularly in the blue (see Figure 3.10), and is matched to the output of the (P-11 type) phosphor of the image tube. The Plumbicon's dark current is also very low.

The enormous gain of the intensifier is sufficient to ensure that single photon events can be recorded easily and unequivocally by the camera when operating at room temperature. As we have seen, the variation in size of the recorded images of these photon events is a major contributor to reducing DQE, and the great strength of the IPCS lies in the complete elimination of this effect by the subsequent electronic processing of the video signal. This is the so-called event-centring logic, which ensures that each output pulse from the phosphor is given equal statistical weight, whatever its size. Discrimination of ion events is also provided for, and the system noise is negligible. Successive event-centred output frames may then be added in the on-line computer to form a digital image.

Because of its true photon-counting properties, this detector has $q_D \tilde{} q$, where q is the responsive quantum efficiency of the (S-20 type) first photocathode of the intensifier, which is about 15 percent. The response is linear, but there is a disadvantage in the relatively low dynamic range,

caused partly by the decay time of the intensifier output phosphor and partly by the time required for the electronic signal processing. The effective linear resolution of the detector is about 60 line-pairs/mm, and its useful area is about 30 mm. There are considerable advantages in the digital format of the output image: subsequent processing becomes straightforward, and such necessary chores as the division by a flat field image to remove non-uniformities in detector sensitivity, or the subtraction of the sky signal, can be carried out almost immediately. With the IPCS, the astronomer also enjoys the considerable luxury of being able to see the photon counts accumulating, via a monitor screen, as the integration proceeds.

Finally, we come to solid-state imaging detectors, of which the most important for our purposes is the charge-coupled device (CCD) (see Mackay, 1986). These devices are simply large-scale integrated circuits, consisting of a rectangular array of electrodes which, by means of a bias voltage, creates potential wells in the silicon substrate that will collect photoelectrons when the device is exposed to light. The electron image is extracted from the CCD by the application of suitably phased voltages to groups of electrodes (commonly three, in a three-phase CCD), so that the charge is transferred from one potential well to the next. The exact manner in which this is done depends on the architecture of the particular CCD; most devices used in astronomy have frame-transfer architecture, in which the "rows" (or scan-lines) of the image are progressively stepped along to a serial output register at the edge of the imaging area. Each row is then read out sequentially, via an integrated output amplifier.

CCDs exhibit very high responsive quantum efficiencies. The wavelength-dependence of q is typically as shown in Figure 3.11, where the data for GEC P8600 series devices similar to those used in the Durham University CCD system for FLAIR are illustrated. It will be seen that the red response is good, but that the sensitivity falls steeply below ~700 nm, and has reached zero by 400 nm (broken lines). This poor blue response is one of the drawbacks of CCDs, and a number of means have been implemented to attempt to improve it. One method is to overcoat the CCD with a thin layer of a dye that will absorb blue photons and re-emit them in the red (eg, Cullum et al., 1985), and the effect of this is also shown in Figure 3.11 (solid lines). There is clearly a marked improvement in blue quantum efficiency, despite the quasi-isotropic nature of the re-emission by the dye. Another method relies on the fact that the intrinsic blue quantum efficiency of silicon itself is high (perhaps 60 percent at 400 nm), and it is attenuation by the electrodes that results in poor blue performance; the device is therefore thinned, and illuminated from the back. This technique has proved successful for some RCA CCDs, although the full potential is not realized, apparently due to surface charge effects (Mackay, 1986). An undesirable side-effect of this procedure is the generation of interference fringes in the thinned substrate.

Although they are analogue devices requiring additional circuitry to produce a digital signal, CCDs are highly linear; their large dynamic range has already been noted. Thermal effects give rise to a dark current, i, given by the diode law

$$i = a \exp(-b/kt) \qquad (3.12)$$

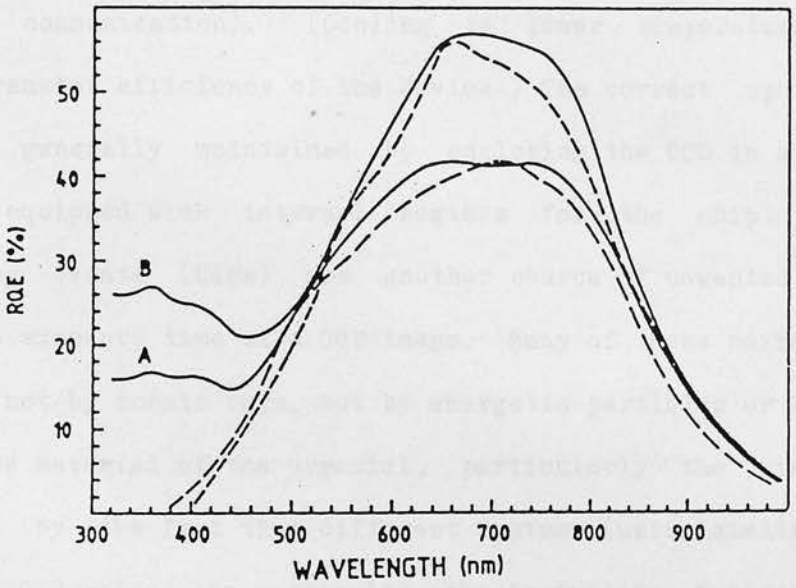

Figure 3.11 Responsive quantum efficiencies of two GEC CCDs before (broken lines) and after (solid lines) the application of a dye coating. (From Cullum et al., 1985.)

(Mackay, 1986), where a, b are constants, k is Boltzmann's constant, and t is device temperature. To minimise this, CCDs are cooled, typically to ~150 K, where the dark current will be ~0.04 electrons/pixel/sec (McLean, private communication). (Cooling to lower temperatures impairs the charge-transfer efficiency of the device.) The correct operating temperature is generally maintained by enclosing the CCD in a liquid nitrogen cryostat equipped with internal heaters for the chip. The so-called cosmic-ray events (CREs) are another source of unwanted noise that will limit the exposure time of a CCD image. Many of these noise spikes may be caused, not by cosmic rays, but by energetic particles or X-rays originating in the material of the cryostat, particularly the window. This is supported by the fact that different systems (using similar CCDs) display different CRE rates; in particular, the Australian National University's CCD system (MSSSO, 1986) showed less than half the Durham University system's CRE rate (which is rather high at ~5 events/min) when used with FLAIR. The final source of instrumental noise is generated by the output transistor and is intrinsic to the chip itself; this readout noise, r, may vary from ~70 electrons/pixel (RCA chip, no longer in production) to $\lesssim$8 electrons/pixel (GEC P8600 series chips).

The pixel size of a CCD is clearly determined by the electrode structure, and is 22 μm square for the P8600 series device. This CCD has a detecting area amounting to almost a quarter of a million pixels, arranged in 576 rows and 385 columns, all of which are adjoining. The technique of on-chip binning permits the addition of rows on the chip to provide the option of reducing the readout noise (relative to the signal) at the expense of reso-

lution. We have seen, in the previous section, how the number of channels in a multi-fibre spectrograph is limited by the detector area, and we remark that the rectangular CCD format gives a choice between maximising the number of fibre channels and maximising the spectral coverage. The availability of large-format CCDs with up to 2048 x 2048 pixels (eg, Tektronix, 1985) is eagerly anticipated.

3.4 Overall performance of the complete system

We end our survey of the instrumental requirements for multi-object spectroscopy, conducted in this and the previous chapter, by attempting to assess the overall performance of real fibre-coupled multi-object spectroscopy systems (compare Hill et al., 1982; Watson and Dawe, 1985). We shall do this in terms of signal-to-noise ratios, S/N, in the output spectra (eg, Meaburn, 1976, Chap. 11). First, however, it is necessary to write down the overall optical efficiency of a single channel of a multi-fibre spectroscopy system having j fibre channels, and we also take the opportunity to indicate the more important functional dependences of the various sources of loss. Here, in addition to those symbols already defined, ζ denotes the angular radius of a target object (which may include the effects of seeing), e denotes a fibre positioning or alignment error, a gothic $\mathfrak{T}$ denotes time in a long-term process (eg, the ageing of an aluminised surface), t denotes temperature, f_T denotes telescope beam focal ratio, and f_C denotes collimator focal ratio.

The overall efficiency, $\mathbb{E}$, is given by

$$\mathbb{E} = \mathbb{A}\,\mathbb{T}\,\mathbb{F}\,\mathbb{S}, \qquad (3.13)$$

where

$\mathbb{A} = \mathbb{A}(\lambda,(h,\delta))$ is atmospheric transmission (Figure 1.1; Allen, 1973, p.125);

$\mathbb{T} = Q_T\ V$ is the telescope transmission, where

$Q_T = Q_T(\lambda, \mathfrak{T})$ is the telescope optical efficiency (Section 3.1.1);

$V = V(\xi,\eta)$ is the telescope vignetting function (eg, Figure 3.2);

$\mathbb{F} = E\ B_i\ T\ (1-D)\ B_o$ is the overall efficiency of the fibre feed, assumed to be used without microlenses, where

$E = E(\zeta,s,e,t,(h,\delta),\lambda)$ is the entrance coupling efficiency (Section 2.4; Figure 2.9; Section 3.1.2);

$B_i = B_i(f_T, NA(\lambda), e, b)$ is the input beam coupling efficiency (Section 2.4; Figure 2.10; Section 3.1.2);

$T = T(\lambda,l)$ is the fibre transmission (Equation 2.6);

$D = D(l, f, NA(\lambda), f_c)$ is the FRD loss, including that due to collimator overfilling and shadow infilling (Section 2.3);

$B_o = B_o(e)$ is the output beam coupling efficiency, normalized to exclude the FRD loss (Figure 2.11);

$\mathbb{S} = (1-J)\ Q_S\ G$ is the transmission of the spectrograph, which is assumed to have no field vignetting effects, and to be in perfect adjustment, where

$J = J(h)$ is the loss due to a slit of width 2h (Equation 2.9);

$Q_S = Q_S(\lambda, \mathfrak{T})$ is the spectrograph optical efficiency;

$G = G(\phi, \lambda, \mathfrak{T})$ is the grating efficiency (Section 3.2.1).

Placing some estimated values on these quantities, we have $\mathbb{A}$=0.80 (at 5000 Å) for unit air-mass; $\mathbb{T}$=0.72 for the AAT at f/8, and $\mathbb{T}$=0.78V for the UKST (assuming ρ=0.85). For the fibre efficiency, there are two cases to consider:

(a) Point source targets. Gray and Sharples (1985) estimate $\mathbb{F}$=0.70T for the AAT fibre system, adopting reasonable positioning and alignment errors, and assuming typical (1.5 arcsec) seeing. For FLAIR, we will have (1-D)~1.00 (much higher than for the AAT), while B_i, B_o will be similar (~0.96). However, because of the vastly smaller plate-scale and the f/2.5 telescope beam, the fibre input positioning and alignment tolerances are far more stringent. Thus, despite FLAIR's more accurate positioning method, the value of E will be lower than that for the AAT system. A reasonable estimate for average conditions (1.5 arcsec seeing) is E~0.55, giving $\mathbb{F}$~0.51T. Inserting the appropriate values for T (eg, Gray and Sharples, 1985) gives approximate values of $\mathbb{F}$ at 4000, 5000 and 6000 Å of 0.43, 0.59 and 0.62 for the AAT; 0.31, 0.43 and 0.45 for FLAIR, assuming that the same fibre attenuation applies, and that there are no additional losses at the cemented input face (see Chapter 6). In fact, the prototype FLAIR system uses the AWA-SD fibre, whose spectral transmission is shown in Figure 2.3(a), and the corresponding values for $\mathbb{F}$ are 0.06, 0.28 and 0.41.

(b) Extended targets, with ζ>>s. In this case, we will always have E=1.00, giving $\mathbb{F}$=0.78T=0.66 at 5000 A for the AAT system, and $\mathbb{F}$=0.92T=0.77 at 5000 A for FLAIR, with efficiencies for the other wavelengths scaling as above. Here, the superior performance of the UKST system is due to the lower FRD loss. For the FLAIR prototype, $\mathbb{F}$=0.51 at 5000 Å.

Finally, the RGO spectrograph at the AAT with the 25 cm camera is estimated to have $\mathbb{S}$=0.56G, with a vignetting function that depends on grating angle (Robinson, 1985, after Hanes, Gillingham and Morton, 1982), while the UKST spectrograph for FLAIR has a remarkable $\mathbb{S}$=0.96G over a wide range of wavelengths (Asahi, 1985). Grating efficiencies for the AAT (3) are given by Robinson (1985), while those for FLAIR are given in Chapter 6; all values quoted are relative to an aluminised surface and are for near-Littrow configuration (Bausch and Lomb, 1974), whereas both spectrographs under consideration have ϕ=45 deg. We here adopt G=0.65 (for a quoted efficiency of 0.80) as a typical value.

Thus, for observations carried out near the zenith at ~5000 Å, and for fibres near the field centre, we will have $\mathbb{E}$=0.12 (point sources) or $\mathbb{E}$=0.14 (extended objects) for the AAT, and $\mathbb{E}$=0.17 (point sources) or $\mathbb{E}$=0.30 (extended objects) for the UKST (assuming the same fibre transmission, T, as for the AAT system). For the UKST with the prototype FLAIR system, these figures fall to $\mathbb{E}$=0.11 (point sources) or $\mathbb{E}$=0.20 (extended objects), and there may be an additional scattering loss at the fibre input (Equation 2.6) due to the positive-copy positioning method (see Section 6.3).

Consider now the signal received from a target object. If F is the flux density of a discrete source in photons sec^{-1} nm^{-1} m^{-2} at the top of the Earth's atmosphere, then

---

(3) These have recently been accurately measured by Johnston et al. (1986).

$$F = 10^{8 - m/2.5} \qquad (3.14a)$$

approximately, where m is the apparent magnitude of the source in some waveband (Disney, 1972; Eccles, Sim and Tritton, 1983, Chap. 1). Similarly, if I is the brightness, or intensity, of an extended source in photons $sec^{-1}\,nm^{-1}\,m^{-2}arcsec^{-2}$ at the top of the Earth's atmosphere, then we will have

$$I = 10^{8 - \mu/2.5} \qquad (3.14b)$$

approximately, where μ is the apparent surface brightness of the source in magnitudes $arcsec^{-2}$ in some waveband. Thus, the flux received at the detector is

$$\Phi_p = A \mathbb{E} \Delta\lambda F \qquad (3.15a)$$

photons/sec for point sources, or

$$\Phi_e = A\Omega \mathbb{E} \Delta\lambda I \qquad (3.15b)$$

photons/sec for extended objects, where A is now the area of the telescope aperture (excluding that of the central obstruction), $\Omega = \pi s^2$ is the solid angle on the sky subtended by the fibre entrance face, and $\Delta\lambda$ is the wavelength resolution of the observation.

We wish to consider the signal in the presence of noise from a number of

sources, including Poisson noise on the object signal and on the signal from the background sky, and receiver noise, which may be incorporated in the DQE, q_D, of the detector (4). The noise from these sources will add in quadrature, so that the total noise will be the square root of the sum of the variances (see, eg, the note by Longair, 1981, Chap. 14). Thus, the signal-to-noise ratio in a spectral resolution element for an exposure lasting t seconds will be

$$S/N = S_o/(S_o + S_s)^{1/2}, \qquad (3.16)$$

where

$$S_o = \Phi_o q_D t$$

is the signal at the detector produced by the integrated object flux (from Equations 3.15a or 3.15b), and

$$S_s = \Phi_s q_D t$$

is the signal at the detector produced by the integrated sky flux (from Equation 3.15b).

In faint-object spectroscopy, it is usual to subtract the background sky

---

(4) It may be remarked for comparison with the functional dependences referred to earlier that, in general, $q = q(\lambda,(x,y),t,\mathcal{T})$.

spectrum from that of the object, and the noise resulting from this can be substantially reduced if the mean of a number of samples of the local sky signal is obtained (Parry, 1986). Thus, if S_S is the mean signal obtained from k fibres each directed at empty sky and sampling an area of Ω arcsec^2, then the signal-to-noise ratio in the sky-subtracted signal will be

$$S/N = S_o/(S_o + (1+1/k)S_S)^{1/2}. \qquad (3.17a)$$

Clearly, it is advantageous to maximise k. However, Parry (1986) has noted three possible difficulties with this for limiting faint-object spectroscopy: first, the sky-subtraction process gets noisier as the distance separating the object and sky fibres increases; second, the correction of fibre-to-fibre variations in transmission, T, by uniformly illuminating the telescope field and normalizing to the resulting observed transmission, is an inherently noisy process, and third, noise may be introduced by variations in spectral transmission from one fibre to another. Of these, the first two are likely to be the most important, particularly for large fields and long exposures, and we here introduce a noise term, σ_f, due to fibre sky subtraction, so that Equation 3.17a becomes

$$S/N = S_o/(S_o + (1+1/k)S_S + \sigma_f^2)^{1/2}. \qquad (3.17b)$$

It is not possible to determine σ_f from a priori considerations, and further experimental work is necessary. However, we may be sure that it will be substantially less than the contribution from Poisson sky noise.

Equations 3.17 represent the sky-subtracted signal-to-noise ratio that will

be obtained with detectors such as photographic emulsions, image intensifiers and the IPCS, where the receiver noise contribution is incorporated in the DQE. For CCDs, it is possible to evaluate the receiver noise explicitly, so that the signal-to-noise ratio in the sky-subtracted signal from a single spectral resolution element will be

$$S/N = S_o/(S_o + (1+1/k)S_s + \sigma_f^2 + (2it+nr^2)p)^{1/2}, \qquad (3.18)$$

where the signal is now given by

$$S = \Phi q t,$$

i is the dark current (assumed to have been removed by the subtraction of a dark exposure of the same length) given by Equation 3.12, r is the readout noise per pixel, n is the number of times the image is read out in the total integration, and

$$p = (d\lambda_f/d\lambda_p)(2rM/z)$$

(Section 3.2.2) is the area of the fibre output face projected through the spectrograph, in CCD pixels. This last term indicates that additional noise is introduced when the width of each spectrum covers more pixels than are necessary, and there is therefore a case for arranging the dispersion to be along the rows, so that adjacent rows can be binned on readout. This will reduce the readout noise, although the dark current will be unaffected.

We end by considering a single example, that of the prototype FLAIR system used with the UKST spectrograph and the GEC CCD detector whose properties were described in the previous section. Assuming that a signal-to-noise ratio of 20 is sufficient to give useful data at 7 Å resolution on the absorption lines in star and galaxy spectra in the V band, and that, of the j=39 fibres 40 μm in diameter, k=3 are used on the sky (ignoring σ_f), we find, by iterative solution of Equation 3.18, that the required signal-to-noise can be attained for a 16th magnitude star in ~1200 seconds. The noise signal here is dominated by Poisson noise on the star signal and the readout noise of the CCD. For an extended object such as a galaxy, with a surface brightness of 19 magnitudes arcsec^{-2}, a signal-to-noise of 20 should be attained in about 2400 seconds, assuming a sky brightness of μ_V=21.5 magnitudes arcsec^{-2}. The sky is now a more important noise source.

These estimates are rather better than those actually achieved in the observations described in Chapter 7, particularly for galaxies. This may be due to a variety of causes, such as the presence of scattered light in the spectrograph, the existence of losses in the system not accounted for here, or the galaxies having a lower surface brightness than assumed. It should also be noted that the calculation here is for the signal-to-noise in a spectral resolution element, so that the signal is assumed to be summed over more than one pixel in the wavelength direction.

Finally, we remark that although it would be impractical to use the UKST for direct slit spectroscopy, such use under the conditions described above would give the required S/N for stars ~1.2 magnitudes fainter, and for extended objects ~0.7 magnitudes arcsec^{-2} fainter. This, then, is the price

paid (in the prototype FLAIR system, at least) for the multiplex advantage provided by the fibres. It would appear to be very good value.

References for Chapter 3

Airy GB, 1870. MNRAS 30, 57
Allen CW, 1973. Astrophysical Quantities, 3rd Ed, Athlone, London
Angel JRP, 1982. In Inst.for Astr.with large Opt.Tels., p.117, Reidel
Angel JRP, 1984. In Astronomy with Schmidt-type tels, p.549, Reidel
Angel JRP, Adams MT, Boroson TA, Moore RL, 1977. Ap J 218, 776
Angel JRP, et al., 1982. In Inst.for Ast.with Large Opt.Tels, p.33, Reidel
Argyll RW, Standen PR, 1985. Occ.Rep.Royal Obs.Edin. No 16, p.9
Armstrong EB, 1980. AAS Photo-Bulletin No 25, p.3
Asahi Optical Co Ltd, 1985. Pentax Lenses and Accessories, Tokyo

Barden S, et al., 1986. NOAO Newsletter No 8 p.4
Bausch and Lomb, 1974. Catalogue of diffraction gratings
Bingham RG, 1977. In Optical telescopes for the future, p.335, Geneva
Boggett H, 1977. Observatory 97, 8P
Boksenberg A, 1972. In Proc.ESO/CERN Conf.on aux.inst., p.295, Geneva
Bowen IS, 1967. QJRAS 8, 9
Brown DS, Dunlop CN, Major JV, 1984. In Ast with Sch-type tels,p.185,R'del

Chown M, 1985. New Scientist, 14 March issue, p.24
Chrétien MH, 1922. Rev Optique 1 No 13, 49
Cullum M, Deiries S, D'Odorico S, Reiß R, 1985. Astron.Astrophys. 153, L1

Dawe JA, 1984. In Astr with Schmidt-type telescopes, p.193, Reidel
Dawe JA, Watson FG, 1985. Occ.Rep.Royal Obs.Edin. No 16 p.15
Disney MJ, 1972. MNRAS 160, 213

Eastman Kodak Co, 1973. Plates/Films for Sci. Phot (Kodak pub P-315)
Eccles MJ, Sim ME, Tritton KP, 1983. Low light-level det in astr, Camb.
Enard D, 1986. Proc SPIE 628 (Advanced Tech. Optical Tels. III)
Everhart E, 1980. AAS Photo-Bulletin No 24, p.3

Fellgett PB, 1958. MNRAS 118, 224
Fellgett PB, 1970. In Optical Insts and Techniques, p.475, Oriel
Ford WK, 1979. Ann Rev Astron Astrophys 17, 189

Gray P, Sharples R, 1985. AAO fibre system user guide/tech.man.,AAO

Hanes DA, Gillingham PR, Morton DC, 1982. The effic. of s/graphs, AAO
Hawkins MRS, 1983. In Low light-level det.in astr., Chap.4, Cambridge
Hickson P, 1986. PASP 98, 696
Hill JM, Angel JRP,Scott JS,Lindley D,Hintzen P, 1982. Proc SPIE 331, 279
Hinks AR, 1898. MNRAS 58, 428
Humphries CM, et al., 1984. Optical/IR telescope arrays, SERC publication

Jacquinot P, 1954. J Opt Soc Am 44, 761
Jacquinot P, 1960. Rep Prog Phys 24, 267
Johnston H, Gray P, Stathakis R, Robinson R, 1986. Effic.of AAO gratings
Jones RC, 1958. Phot Sci Eng 2, 57
Jorden A, 1977. IPCS Operating Manual, 1st Edition, AAO

Kitchen CR, 1984. Astrophysical techniques, Hilger

Longair MS, 1981. High energy astrophysics, Cambridge

Mackay CD, 1986. Ann Rev Astron Astrophys 24, 255
Marchant JC, 1964. J Opt Soc Amer 54, 789
Marling JB, 1980. AAS Photo-Bulletin No 24, p.9
Meaburn J, 1976. Detection and spectrometry of faint light, Reidel
Millikan AG, 1974. In Res.progs.for the new large tels., ESO/SRC/CERN
Morton DC, et al., 1976. AAT Observer's Guide, 2nd Edition, AAO
MSSSO (Mt Stromlo and Siding Spring Obs'ies), 1986. Newsletter Vol 2 No 1

Newport Corporation, 1983. Table systems catalogue
NOAO (Nat.Opt.Astr.Obs'ies), 1985. NNTT Advanced Development Program

Ogura K, Liller W, 1985. AAS Photo-Bulletin No 40, p.11

Parry IR, 1986. PhD Thesis, University of Durham

Ramsay LW, Huenemoerder DP, 1986. Proc SPIE 627 (Instr in Astr VI), p.282
RCA (Radio Corp.of America), 1970. Tech.inf.on C33063 ser.image tubes
Robinson GA, 1977. Jour.Soc.Mot.Pic.TV Engineers 86, 414
Robinson RD, 1985. RGO Spectrograph user manual, 2nd Ed, AAO
Rose A, 1946. J Soc Mot Pic TV Engineers 47, 273

Schmidt B, 1932. Mitt. Hamburger Sternwarte in Bergedorf 7, No 36, 15
Smart WM, 1971. Text-book on Spherical Astronomy, 5th Edition, Cambridge

Tektronix Inc, 1985. Technical specifications of CCD imagers
Tritton SB, et al., 1983. UKSTU Handbook, Royal Obs. Edin.

van de Kamp P, 1962. In Astronomical Techniques, p.487, Chicago

Walker PE, 1980. AAS Photo-Bulletin No 24, p.7
Wallace PT, Tritton KP, 1979. MNRAS 189, 115
Watson FG, 1975. MSc Thesis, University of St Andrews
Watson FG, 1978. MNRAS 183, 277
Watson FG, 1984. MNRAS 206, 661
Watson FG, Dawe JA, 1984. Proc ASA 5, 579
Watson FG, Dawe JA, 1985. Occ.Rep.Royal Obs.Edin., No 16, p.1
Willstrop RV, 1984. MNRAS 210, 597
Willstrop RV, 1985. MNRAS 216, 411
Willstrop RV, 1987. MNRAS 225, 187
Wilson IJ, 1983. In CSIRO Div of Chem Phys Biennial Report, p.17, CSIRO

Appendix to Chapter 3

Formulae for plane reflectance gratings

(a) The grating equation

Consider the situation shown in Figure 3A.1(a), where coherent parallel light is incident at angle α on a series of plane reflectors separated by d; then for constructive interference at an angle of diffraction β, the path difference AB+BC must be equal to an integral number of wavelengths, or

$$m\lambda = d\,(\sin\alpha + \sin\beta)\,. \qquad (3A.1a)$$

Clearly, β becomes negative if incident and diffracted rays are on opposite sides of the grating normal, and the order of diffraction, m, becomes negative if incident and diffracted rays are on opposite sides of zero order.

If d^{-1} is the reciprocal spacing in grooves/mm, then

$$\lambda = \frac{10^7}{m d^{-1}}(\sin\alpha + \sin\beta) \qquad \text{Ångstroms.} \qquad (3A.1b)$$

(b) Littrow blaze wavelength

In Figure 3A.1(b), parallel light is normally incident on the groove faces of a blazed plane reflectance grating, with blaze angle θ; the diffracted rays follow the same path as the incident rays. This is the Littrow configuration, and for constructive interference we must have

$$\lambda_L = 2d \sin\theta\,, \qquad (3A.2a)$$

where λ_L is the first-order Littrow blaze wavelength. Obviously, this may also be obtained from Equation 3A.1a by setting $\alpha=\beta=\theta$, and m=1. Again,

$$\lambda_L = \frac{2\times10^7}{d^{-1}} \sin\theta \qquad \text{Ångstroms,} \qquad (3A.2b)$$

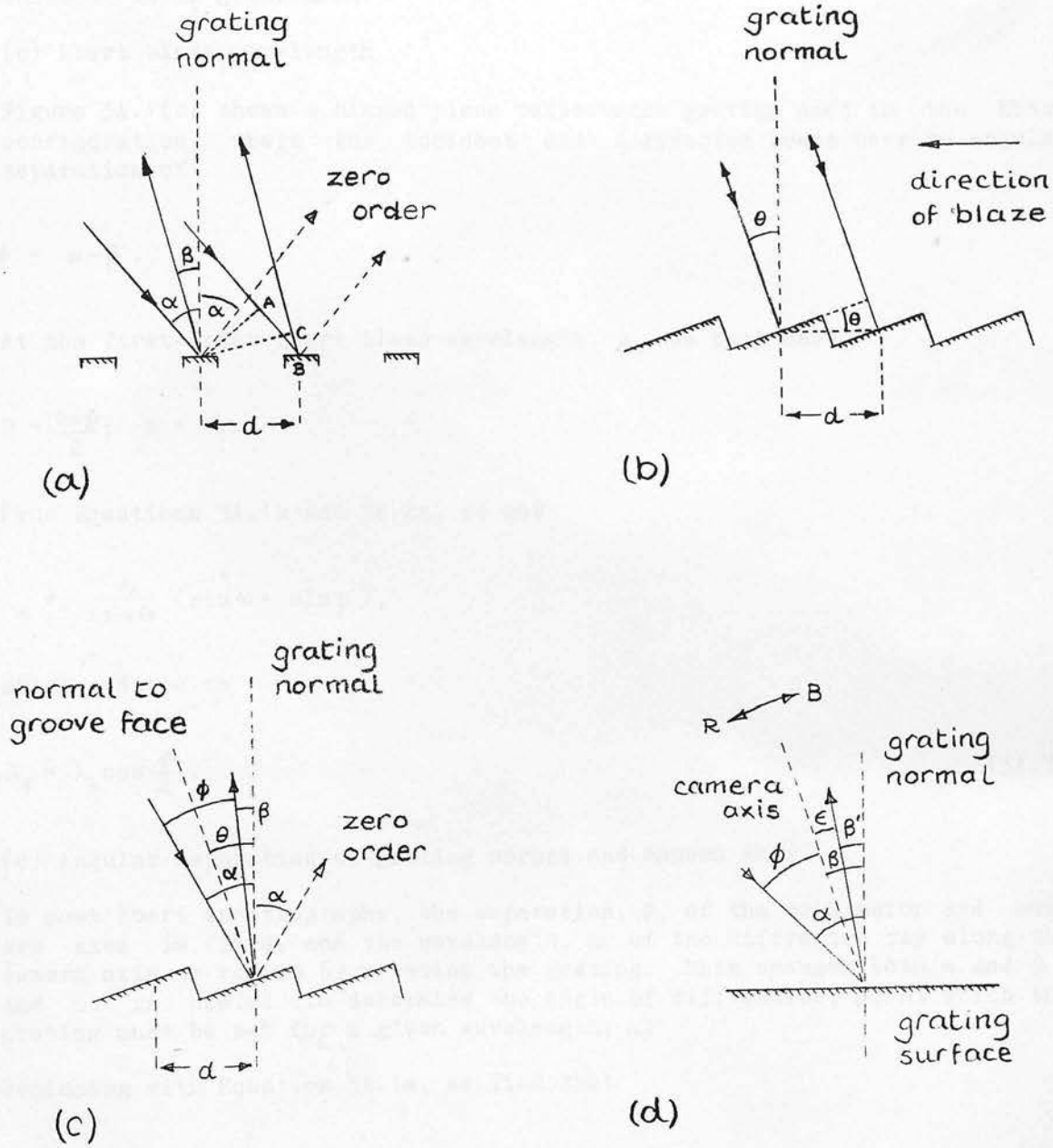

Figure 3A.1 (a)-(d) Geometry of plane reflectance gratings (see text).

where d^{-1} is in grooves/mm.

(c) Ebert blaze wavelength

Figure 3A.1(c) shows a blazed plane reflectance grating used in the Ebert configuration, where the incident and diffracted beams have an angular separation of

$$\phi = \alpha - \beta .$$

At the first-order Ebert blaze wavelength, λ_E, we must have

$$\theta = \frac{\alpha+\beta}{2}; \quad m = 1.$$

From Equations 3A.1a and 3A.2a, we get

$$\lambda_E = \frac{\lambda_L}{2\sin\theta} (\sin\alpha + \sin\beta),$$

which reduces to

$$\lambda_E = \lambda_L \cos\frac{\phi}{2} . \qquad (3A.3)$$

(d) Angular separation of grating normal and camera axis

In most Ebert spectrographs, the separation, ϕ, of the collimator and camera axes is fixed, and the wavelength, λ, of the diffracted ray along the camera axis is varied by rotating the grating. This changes both α and β, and it is useful to determine the angle of diffraction, β, at which the grating must be set for a given wavelength, λ.

Beginning with Equation 3A.1a, we find that

$$m\lambda = 2d \sin\left(\frac{\phi+2\beta}{2}\right)\cos\frac{\phi}{2} .$$

Thus

$$\beta = \arcsin\left(\frac{m\lambda}{2d\cos\frac{\phi}{2}}\right) - \frac{\phi}{2} , \qquad (3A.4a)$$

or

$$\beta = \arcsin\left(\frac{m\lambda d^{-1}}{2\times10^{7}\cos\frac{\phi}{2}}\right) - \frac{\phi}{2}, \qquad (3A.4b)$$

where d^{-1} is in grooves/mm and λ is in Ångstroms.

(e) Wavelength at edges of camera field

The image formed in the camera of an Ebert spectrograph will, in its horizontal (ie, x) direction, encompass a range of values of β, so that a spectrum will be formed there. If the angular field of the camera is 2ϵ, then the angle of diffraction at the edges of the field will be

$$\beta' = \beta \pm \epsilon$$

(see Figure 3A.1(d)). If λ' are the wavelengths at the edges of the camera field then, from Equation 3A.1a,

$$\lambda' = \frac{d}{m}(\sin(\phi+\beta) + \sin\beta'), \qquad (3A.5a)$$

or

$$\lambda' = \frac{10^{7}}{md^{-1}}(\sin(\phi+\beta) + \sin(\beta\pm\epsilon)) \quad \text{Ångstroms}, \qquad (3A.5b)$$

where d^{-1} is in grooves/mm.

(f) Reciprocal linear dispersion

Differentiating Equation 3A.1a with respect to λ gives the angular dispersion

$$\frac{d\beta}{d\lambda} = \frac{m}{d\cos\beta}. \qquad (3A.6a)$$

If f_{cam} is the focal length of the spectrograph camera in mm, then the reciprocal linear dispersion is

$$\frac{d\lambda}{dx} = \frac{10^{7}\cos\beta}{m\,d^{-1}\,f_{cam}} \quad \text{Å/mm}. \qquad (3A.6b)$$

(g) Slit projection factor

Differentiating Equation 3A.1a with respect to α gives the slit projection factor,

$$\frac{d\beta}{d\alpha} = \frac{-\cos\alpha}{\cos\beta} \,. \qquad (3A.7)$$

(h) Grating resolution

It can be shown (eg, Kitchen, 1984, Chap. 4) that the intensity distribution produced by a series of N plane reflectors such as those depicted in Figure 3A.1(a) will fall to zero when

$$\frac{m'\lambda}{N} = d\,(\sin\alpha + \sin\beta\,),$$

where $m' \neq mN$ is an integer (compare Equation 3A.1a). Differentiating with respect to m' gives

$$\frac{d\beta}{dm'} = \frac{\lambda}{Nd\cos\beta} \,,$$

the angular separation of the minima, or the full-intensity half-width of the maxima (when $m' = mN$). By the Rayleigh criterion, this is also the minimum resolvable separation, $d\beta$, of two maxima, so that the resolving power, R, of the grating is

$$R = \frac{\lambda}{d\lambda} = \frac{\lambda}{d\beta}\frac{d\beta}{d\lambda} = Nd\cos\beta\,\frac{d\beta}{d\lambda} \,.$$

By Equation 3A.6a, this is simply

$$R = mN. \qquad (3A.8)$$

CHAPTER 4

Implementation of the multi-fibre technique

4.1 General remarks

It is now more than seven years since the first multi-object spectra were obtained using an array of optical fibres. As we have seen in Chapter 1, the technique is well-suited to a variety of astronomical problems, and offers very substantial gains in observing efficiency. Yet, it is in regular use at only a handful of observatories throughout the world, and the technical requirements for its implementation are sufficiently diffuse that it is still expedient to devote two lengthy chapters of a doctoral thesis to them. It is possible that herein lies the reason for the current limited deployment of multi-fibre spectroscopy: despite its conceptual simplicity, its proper implementation may demand resources in manpower and equipment that are not available. This is particularly true when existing telescopes and spectrographs need to be modified for multi-fibre work, and at least two institutions have actually abandoned their development programmes on multi-fibre spectroscopy, apparently for this reason. As we have already seen, the new generation of telescopes will incorporate fibres into their design from the start, and it can be expected that the technique

will then become more firmly established.

In this chapter, we present what is thought to be a substantially complete survey of progress in multi-fibre instrumentation at various observatories throughout the world, paying particular attention to the methods adopted for positioning the fibres in the telescope focal surface. Some of this work has already been described in an earlier review (Watson, 1983). We begin with a brief account of the related technique of fibre-coupled single-object spectroscopy.

4.2 Single-fibre systems

As a result of Angel's initial investigations into fibre properties for the proposed fibre-linked optical array telescope (FLOAT; Angel et al., 1977; Angel, 1978), an experiment was set up at the Steward Observatory (University of Arizona) 0.9-metre telescope to bring light from an image at the prime focus to a stationary spectrograph in a laboratory below the observing floor, using a single-fibre link (Hubbard, Angel and Gresham, 1979). The fibre was a 20 m length of the Valtec PCS-type highlighted in Table 2.2 for its exceptional blue transmission, and its 125 μm diameter core subtended 5 arcsec in the telescope focus. A novel acquisition system was incorporated into the experiment, the fibre input end being mounted in a plexiglass plate behind which were the acquisition TV camera optics, so that the target image would appear in the TV field only when it was not perfectly aligned with the fibre. Several objects as faint as magnitude 15 were observed with this system, using the image-tube Cassegrain spectrograph from Steward's 2.3-metre telescope; as recounted by Hill (1984), it was

the success of this demonstration that led Angel's group to develop the multi-object "Medusa" spectrograph for the 2.3-metre itself.

At about this time, Serkowski et al. (1979) at the Lunar and Planetary Laboratory, University of Arizona, were constructing a Fabry-Perot spectrometer for the measurement of stellar radial velocities with a precision of ~10 m/s, with a view to searching for extra-solar planets. In addressing the problem of image scrambling to provide invariant illumination of the spectrograph optics, Serkowski et al. were advised by Angel and P Connes to investigate the possibility of using a single fused-silica fibre. This they did, and a 3-m long, 125 μm diameter fibre coupler was built by Heacox (1980) to link the radial-velocity spectrometer to the Mt. Lemmon 1.5-metre and other telescopes. This coupler incorporated a refined input lens system (similar in principle to that shown in Figure 2.8(b)(i)) to reduce the focal ratio of the beam, and an output pupil imaging lens analagous to that in Figure 2.8(b)(ii), thus foreshadowing the suggestion of input-pupil imaging by Angel and Richardson (Section 2.3).

Heacox later moved to Hawaii, where he constructed a single-fibre coupler for the University of Hawaii's 2.2-metre telescope at Mauna Kea (Heacox, 1986). This device uses a 14-m length of Fujikura 50 μm core fibre, and has a multi-purpose Cassegrain adaptor at its input end to permit the acquisition of the target image, allow the injection of light from a calibration lamp, and reduce the beam focal ratio to f/4. At its output end is an interchangeable spectrograph adaptor (mounted on an optical rail at the coudé position), which contains a transfer lens acting as a focal enlarger to match the beam to the collimator focal ratio. As we have already

remarked, this fibre feed is unique in having anti-reflection coatings on its ends. The system is being used in a programme of spectroscopy to obtain stellar radial velocities with a very high degree of precision.

At the European Southern Observatory (ESO), Enard and Lund (1983; Lund and Enard, 1983) have experimented with optical fibres approximately 40 m long to couple the prime focus of the 3.6-metre telescope to its coudé echelle spectrograph (CES). Here, because of the f/3 telescope beam, no pre-fibre optics are required to decrease the focal ratio (although a rather complex prime-focus adaptor unit has been built to permit image acquisition and light input from calibration lamps). At the fibre output, a transfer lens is used to slow the beam to f/30 for input to the CES collimator, in the same way as in Heacox's system at Mauna Kea. Because of the resulting 10x magnification of the fibre end, it is desirable to use an image slicer (eg, Richardson, 1972) to maximise the light entering the CES slit. A range of fibre diameters has been used in the experiments by Lund and Enard, and useful high-resolution (160 mÅ) stellar spectra have been obtained.

A single-object fibre-linked spectrograph for use with telescopes of less than 1 m aperture has been built by Schiffer (1983) at Heidelberg. This instrument has interchangeable fibres, spectrograph cameras, and detectors, for use at different telescopes, and is capable of reciprocal dispersions ranging from 27 to 370 Å/mm. The fibres are used in pairs to provide one channel for the target object and one for background sky, sampled 2 mm from the object in the telescope focal surface, and at any desired position angle. Thus, the system is not limited to high-resolution spectroscopy of bright objects, where sky subtraction is of reduced importance. The acqui-

sition system is similar to that devised by Hubbard, Angel and Gresham (1979), using a transparent mounting plate for the fibre, so that the surrounding field is accessible to the TV camera. Schiffer's spectrograph has provided useful data on stellar targets, and it is interesting to note that it has been used north of the arctic circle to permit long-duration monitoring of T Tauri and flare stars (Appenzeller et al., 1983).

A number of other single-object spectroscopy systems, with features similar to those described above, have been built or are planned. Ramsey and Huenemoerder (1986) have described a fibre-coupled medium/high resolution CCD/echelle spectrograph used with the 1.6-metre telescope of Pennsylvania State University for spectroscopy of active stars. Wayte (unpublished) used a single fibre to couple a Michelson interferometer to the 3.8-metre UK Infrared telescope (UKIRT) some years ago, while, at the other end of the aperture scale, fibres will be used to couple the seven 0.37-metre elements of the Preston Multi-Aperture telescope (MAT) to a stationary spectrograph (Grainger, 1981; Robson and Grainger, 1983; Oates, 1987). An optical-fibre link is in use at the Cerro-Tololo Inter-American Observatory (CTIO) to couple the 1.5-metre telescope to the 4-metre telescope's echelle spectrograph (Weller and Ingerson, 1986). Finally, mention must be made of a remarkable 0.67-metre telescope and fibre-coupled spectrometer built by an amateur astronomer in New Mexico (Flint, 1984). Again, the motivation for the instrument is the search for extra-solar planets.

4.3 The Steward Observatory multi-fibre systems

In the wake of Angel's success with the single-fibre spectroscopy experi-

ment at the Steward Observatory 0.9-metre came the development of "Medusa", the world's first fibre-coupled multi-object spectroscopy system. As Hill (1984, p. 49) recalls:

"At that point, I (JMH) came along looking for a graduate research project and John Scott came along looking for the "missing mass" in clusters of galaxies. Roger Angel had then collected the key ingredients for a successful instrumental collaboration: a scientific problem, clever new ideas, cheap graduate student labor, and cash. In December 1979, Hill, Angel, Scott, Lindley and Hintzen (1980a,b) used 20 fibers mounted in an aluminum aperture plate to make the first simultaneous multiple-object spectroscopic exposure on the cluster Abell 754. This aperture-plate prototype was named the Medusa spectrograph, and has been taking scientific data continuously since then."

Medusa was deployed on the Steward Observatory 2.3-metre telescope at its Ritchey-Chrétien focus, where π=9.8 arcsec/mm. The novel feature of the system was the interchangeable aperture-plate box (later referred to as the fibre "nucleus"), in which the fibres reformatted the target images from a 30 arcmin (18.4 cm) square portion of the telescope field to a 3 cm long slot in the collimator focus of the Boller and Chivens spectrograph. This aperture-plate box, shown schematically in Figure 4.1, could be inserted into, and removed from the gap between the telescope focal surface and the spectrograph (created by a 22 cm spacer) without disturbing the rest of the system.

The details of Medusa have undergone some evolution since its inception. Its history is recorded in Hill et al. (1980a,b), Hill et al. (1982; the most detailed account), Hill, Angel and Scott (1983), Hill (1984; containing similar material to the previous reference), and its demise is heralded in Hill and Lesser (1986). PCS fibres of 300 μm diameter (2.9 arcsec) have been used throughout (Galite in the early days, QSF 300A later

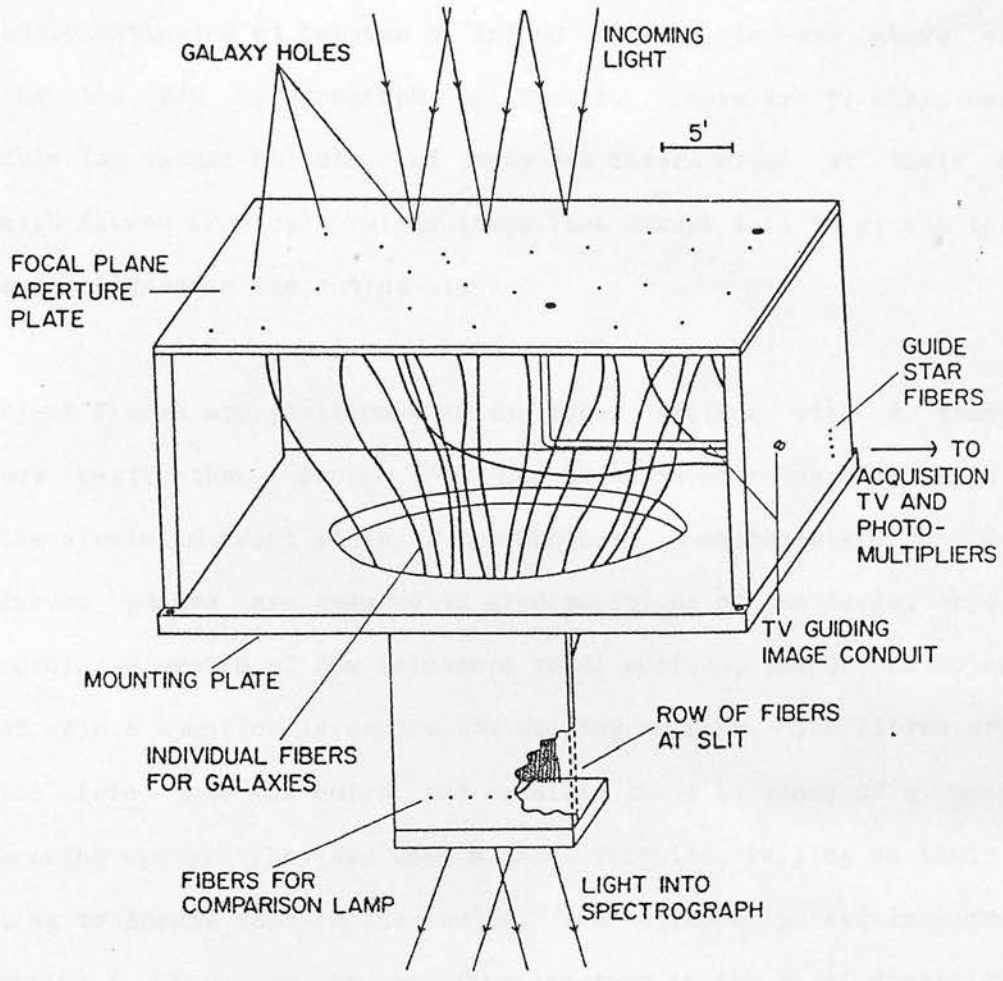

Figure 4.1 Medusa aperture-plate box (from Hill et al., 1982).

- see Table 2.2) in lengths of 20 cm. By far the biggest loss encountered is due to FRD of the f/9 telescope beam, with only a fraction of the light (variously estimated at between 35 and 60 percent in the above papers) entering the f/9 spectrograph collimator. There are 37 fibre channels available for target objects, and these are interspersed at their output ends with fibres from calibration lamps (see Figure 4.1) to give a total of 44 fibres aligned in the output slot.

The object fibres are positioned in the focal surface with a transverse accuracy better than 1 arcsec (~100 μm) by means of holes drilled in the 3 mm thick aluminium front plate of the nucleus. Measurements from Palomar Sky Survey plates are reduced to give positions of the target objects in the coordinate system of the telescope focal surface, and 0.7 mm holes are drilled with a numerically-controlled milling machine. The fibres are then "stuffed" (sic) into the holes, and retained there by means of a smear of rapid-curing epoxy. They are used without ferrules, relying on their outer jacketing to locate them in the holes, and apparently require frequent repolishing. There is no positive location in the axial direction and, indeed, the flat aperture plate ignores the 1.6-m radius of curvature of the focal surface. The relatively slow telescope beam will help in this regard, however (Figure 2.9(a)). Field acquisition is carried out by means of two 3 mm diameter image conduits (rigid imageguides) coupled via a transfer lens to an intensified TV camera. In addition, four fiducial-star fibres (identical to the object fibres) lead to two photomultiplier tubes, providing a signal that can be maximized while guiding on the field.

In the early days of Medusa, the spectra were detected using hypersensi-

tized (nitrogen baked) IIIa-J plates with a Carnegie image intensifier (RCA C33063 series tube; see Section 3.3) at the focus of the Boller and Chivens spectrograph. Later, however (December, 1981), the plates were replaced by a front-illuminated, liquid-nitrogen cooled RCA CCD, with similar lens-coupling to the image intensifier. With this detector, the spectra are recorded as a series of 20-minute exposures to allow intercomparison of frames for the removal of CREs. Calibration spectra from the conmparison lamp fibres are added at the beginning and end of each exposure; full frames of comparison spectra are also obtained at intervals by illuminating a diffuser screen above the aperture plate with a calibration lamp. With the CCD detector, typically three fields of galaxies can be observed in a night, requiring the preparation (or "stuffing") of three aperture-plate boxes during the previous day. The changeover from one field to the next is reported to take only 15 minutes (Hill, 1984).

Medusa was conceived with the aim of gathering medium-precision (100 km/s) redshift data on large numbers of moderately bright ($V \lesssim 18$) galaxies occurring in clusters. (Inspection of Figure 1.3 shows that the mean number density of galaxies to this limit is itself insufficient to allow all 37 fibre channels to be used in the 0.25 deg^2 field of the telescope.) The principal interest lay in gathering statistically-significant samples to study the relationships between the dynamical properties of the clusters and such other attributes as their X-ray emission, subclustering, and the possibility of hidden matter. In this respect, the system has evidently been successful, having gathered some 800 galaxy spectra as at February, 1983 (Hill, 1984). Some results have been published in Hill et al. (1980b), Hintzen et al. (1982) and Hill (1984).

Without question, Medusa was a pioneering device, and it is with some justification that Hill and Lesser (1986) suggest that multi-fibre systems using aperture plates might be referred to as Medusa-class instruments. We will use that nomenclature here.

The possibility of a second-generation multi-object system with remotely-controlled fibre positioners was raised as long ago as 1980 (Hill et al., 1980b). In the event, this proposal has taken nearly half-a-dozen years to materialize, but the instrument has now been commissoned on the Steward 2.3-metre telescope. Known as the "MX" spectrometer, it is described at various stages of its development by Hill et al. (1982); Hill, Angel and Scott (1983); Hill (1984), and its deployment is recounted in Hill and Lesser (1986). A data-reduction software package is also presented (Hill, Eisenhamer and Silva, 1986). Some of these papers give rather whimsical accounts of the origins of the name of the device; to this author, however, it appears to be as self-evident as that of its predecessor!

MX was designed to eliminate the need to prepare aperture plates before an observing run, to improve observing efficiency by making more rapid field changes possible (90 seconds), to allow the observer to respond to changes in observing conditions, and to minimise the handling of the fibre ends, which can thus be finished with surfaces of the highest quality. All this appears to have been achieved, at a total cost of about a quarter of a million US dollars (Hill and Lesser, 1986).

Hill (1984; Hill and Lesser, 1986) defines three classes of

computer-controlled remote fibre positioners. In the first, specific areas of the field of view are alloted to single fibres, which are not permitted to venture elsewhere in the field. This system cannot cope with strongly non-uniform distributions of target objects. In the second, the patrol areas of the fibre positioners overlap, allowing much more flexibility in the distribution of fibre inputs. Anti-collision software is required in the control programs, preferably backed up with fail-safe limiting devices. In the third, which is an automated version of the Medusa technique, a single positioner can move the fibres anywhere in the field; once positioned, they are held in place by some other means. Again, intelligent control software is required. The MX spectrometer falls into the second of these categories; examples of the other two are described later in this chapter. MX consists of 32 fibre positioning arms, with (r,θ) movement, in the so-called "fishermen round the pond" configuration (see Figure 4.2(a)). Each arm has access to 20 percent of the focal surface. (It will be noted immediately that the system is clearly unsuitable for instruments like the UKST and the Willstrop telescope, where the focal surface is within the incoming beam.)

The portion of the 2.3-metre telescope's Ritchey-Chrétien focus accessed by MX is 45 arcmin in diameter, and some correction for curvature has been incorporated by inclining every other positioner to be tangent to the outer portion of the focal surface (as shown in Figure 4.2(b)), the remainder being tangent to the field centre (axial focal plane). The design goal for positioning accuracy is 0.25 arcsec (25 μm), and this is to be achieved using open-loop stepping motors (rather than DC motors under servo control from absolute encoders) to save cost. At the time of the most recent

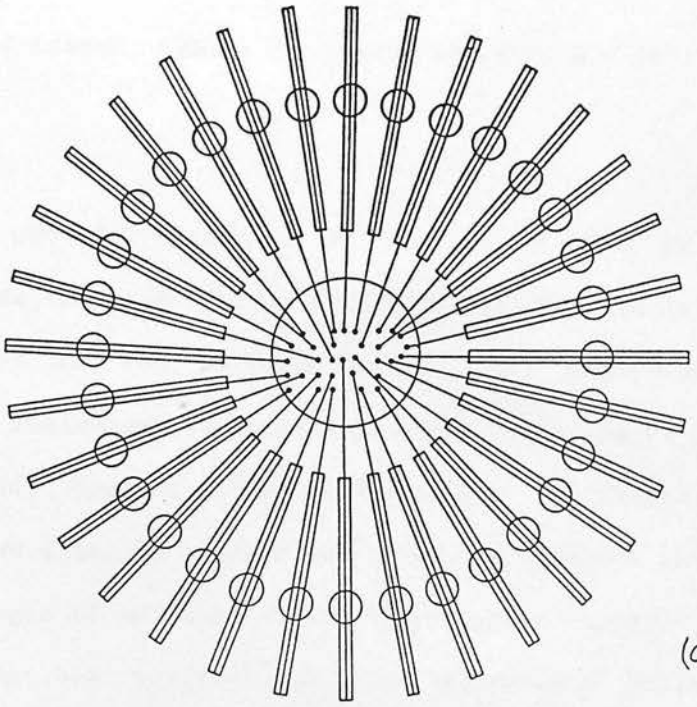

(a)

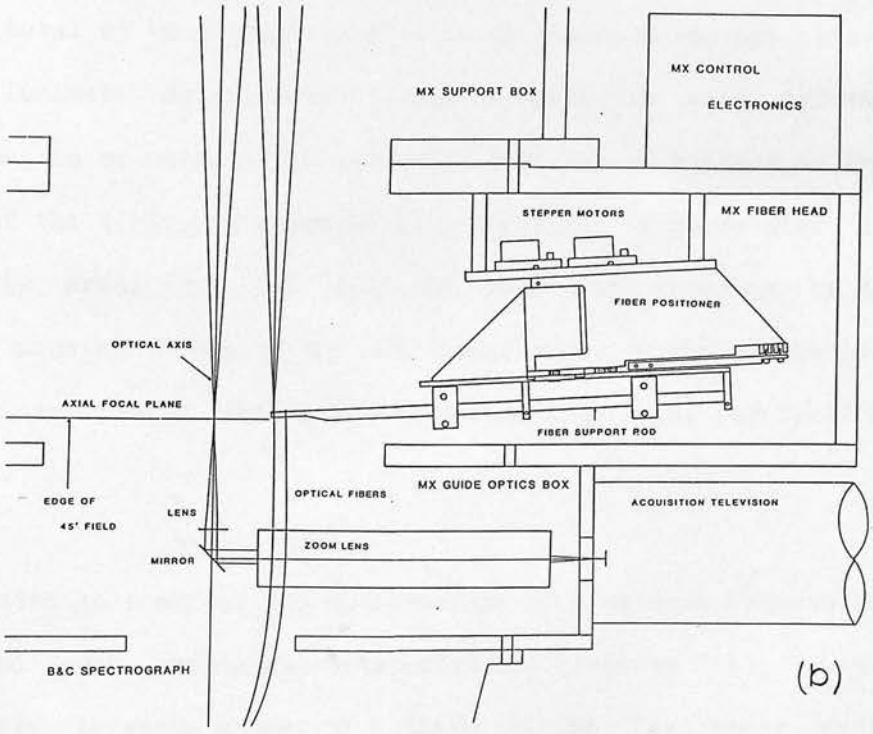

(b)

Figure 4.2 MX fibre-positioning system. (a) Schematic axial view of fibre positioners set up on a "random" distribution of target objects within the field of the telescope (central circle). (From Hill et al., 1982.) (b) Cross-section of telescope focal surface showing one of the 32 fibre positioners, with object and sky fibres attached. The spectrograph "slit" is located just off the bottom of the diagram. (From Hill, 1984.)

report (Hill and Lesser, 1986), the system was within a factor of four of this precision.

The lightguides used for MX are 30 cm lengths of 200 μm diameter QSF 200/300 AS fibre (compare Table 2.2), whose FRD characteristics are sufficiently good that they can be used without the microlenses originally planned for the instrument (Hill et al., 1982; Hill, Angel and Richardson, 1983; Hill, 1984; Section 2.3 of this thesis). The fibres are used in pairs, with two attached to each positioner as depicted in Figure 4.2(b), to provide a sample of adjacent sky for each target object. As with Medusa, the spectra are recorded on the telescope's Boller and Chivens spectrograph, now equipped with a cooled 800x800 pixel Texas Instruments CCD. A total of 66 fibres are aligned on the spectrograph slit, of which six are illuminated by calibration lamps, again as with Medusa. Field acquisition is by means of an intensified TV camera looking at the central 1 arcmin of the field, as shown in Figure 4.2(b). A guide star is chosen within this area; it can also be used for focusing by means of a knife-edge mounted on one of the positioner tips. Eight of the positioners have additional fibres leading to two photomultipliers, for field alignment or guiding.

MX is intended to continue the spectroscopy of clustered objects begun with Medusa, and some sample galaxy spectra are given by Hill, Eisenhamer and Silva (1986). It would appear from these that MX has every prospect of proving a worthy successor to its venerable forerunner. It is pleasing to note that Hill's work on Medusa and MX has recently earned him the Trumpler Award of the Astronomical Society of the Pacific (Wolff and Fraknoi, 1986).

4.4 Multi-fibre spectroscopy at ESO, RGO and elsewhere

Concurrently with their experiments on long, single-fibre links, Lund and Enard (1983) built a prototype fibre-coupled multi-object system for the Cassegrain focus of the ESO 3.6-metre telescope. Again, there is evidence of a certain amount of whimsy in the naming of this device; it was originally called Fibre Optopus, but is now invariably referred to simply as OPTOPUS. (If this is meant to be an acronym, its significance is even more elusive than that of TAURUS - see list of abbreviations!) It would appear that the upper and lower case characters are, in fact, used to distinguish the different versions of the system.

After undergoing a period of testing (Lund and Enard, 1983), the prototype Optopus was replaced with a second-generation system, which is now available as a common-user instrument at ESO (ESO Optical Instrumentation Group, 1985; Lund and Surdej, 1986). It is mainly this version that will be described here, and it is illustrated in Figure 4.3. OPTOPUS is a Medusa-class system, incorporating a fairly high degree of sophistication. It uses 274 mm diameter circular aperture plates (referred to as "star-plates") to cover the 33 arcmin field of the telescope (Π=7.14 arcsec/mm); these are thick discs of aluminium prepared in advance from astrometric data on a high-precision programmable milling machine at the ESO headquarters in Garching bei München. Compensation for field curvature is achieved by hole-depth adjustment in the milling-machine program; this is a very satisfactory approach, since the resulting alignment of the fibres parallel to the optical axis is a good approximation to the correct alignment with the exit pupil 28.89 m away, thus minimising the beam inclination, b.

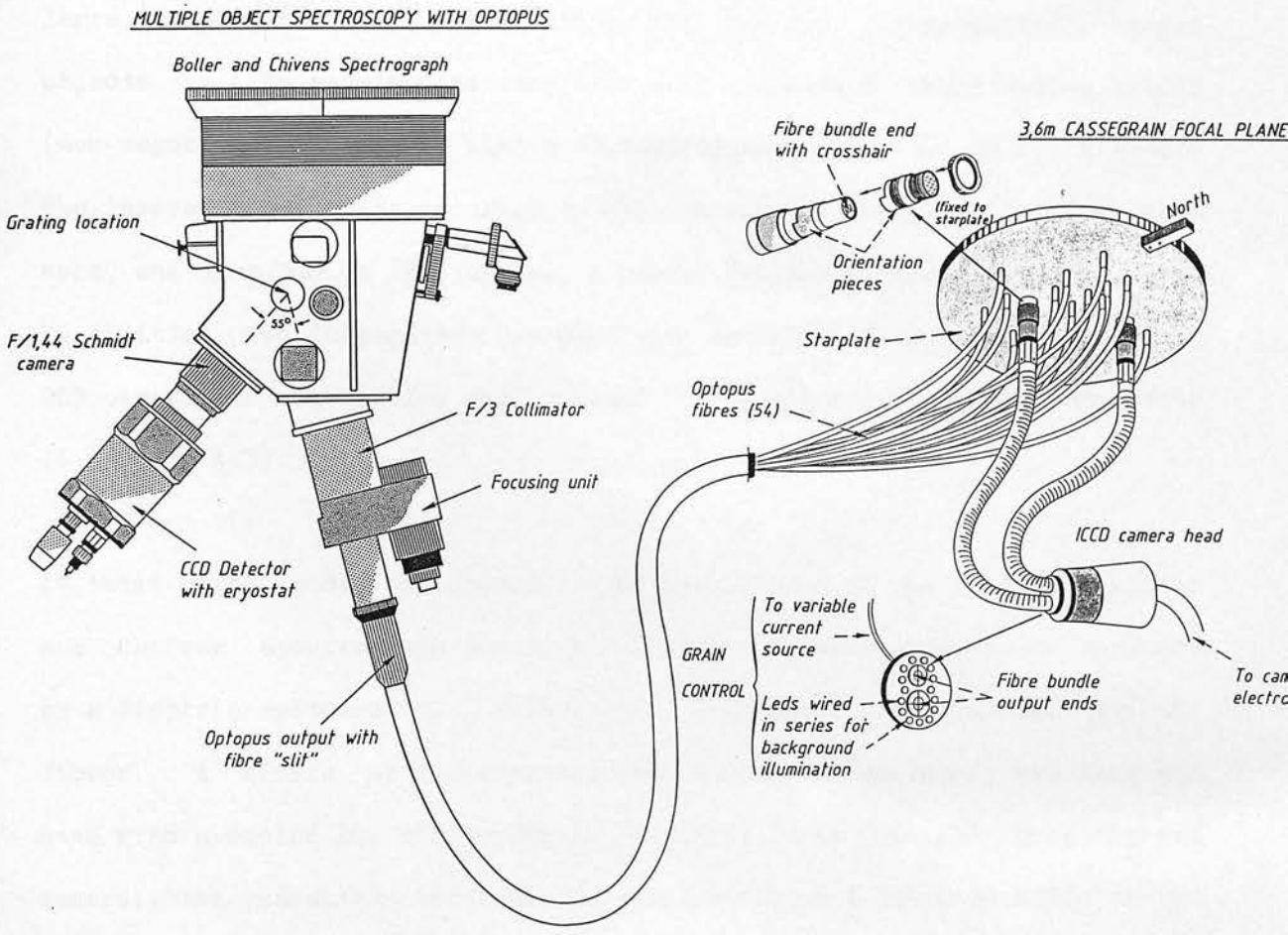

Figure 4.3 Schematic representation of the OPTOPUS multi-object spectroscopy system at the ESO 3.6-metre telescope (from Lund and Surdej, 1986).

In the original Optopus, the fibres were retained in a steel aperture plate by means of magnetic ferrules. These had the disadvantage of relatively large diameter (10 mm), restricting the minimum separation of target objects to 1.25 arcmin, and they have been replaced by positively-locating (non-magnetic) connectors, with a minimum separation of 3.4 mm (25 arcsec). The lateral positioning accuracy is 0.2 arcsec. OPTOPUS has 54 fibre channels, and uses 360 μm (2.6 arcsec) diameter fibres in lengths of about 2 m. In addition, two imageguides are used with an intensified (non-integrating) CCD camera for acquisition and guidance, using stars as faint as magnitude 16 (Figure 4.3).

At their output ends, the object fibres are aligned in the slit of a Boller and Chivens spectrograph with its f/8 off-axis collimator mirror replaced by a dioptric system of f/3, evidently to compensate for large FRD in the fibres. A choice of two spectrograph cameras is available, and they are used with a cooled RCA CCD detector. With the usual (f/1.44) spectrograph camera, the sampling interval is 2.2 pixels, and the separation of the edges of the spectra is 4 pixels. This appears to have eliminated the difficulties with CCD charge-transfer crosstalk experienced earlier with Optopus (Lund and Enard, 1983). Unlike Medusa, where the spectrograph was simply spaced back from the telescope focal surface to accommodate the fibres, the ESO spectrograph is laterally displaced from its usual position, and bolted onto the back of the mirror cell. Facilities no longer in the beam, such as order-sorting filters and the shutter, are duplicated in the new collimator.

The fibres are cabled together in an armoured flexible conduit to form a

single link between the starplate and the displaced spectrograph, as shown in the diagram. Changing fields involves removal of the fibres and image-guides from the old starplate, and reinsertion into the new, an operation that requires access to the telescope's Cassegrain cage. Calibration frames are obtained by introducing a diffusing screen above the Cassegrain focal surface and illuminating it with light from calibration lamps, so that the light path through the fibres mimics that of the target images. The quoted performance of the system is such that a spectrum with a signal-to-noise of 10 or more at 170 Å/mm can be obtained in one hour for an object with V=18 (ESO Optical Instrumentation Group, 1985). There is a sharp cut-off in efficiency at wavelengths below 3900 Å, due partly to the fibre transmission, and partly to the CCD response.

OPTOPUS is a general-purpose device, and has already been used for observing SMC HII regions and planetary nebulae, Fornax carbon stars, clusters of galaxies, and quasar candidates, with most of these objects lying in the magnitude range 17 to 19 (compare Section 1.3). In addition, area spectroscopy of a diffuse optical jet in a starburst galaxy, and the spectacular observations of Comet Halley, referred to in Section 2.4, have also been carried out (Lund and Surdej, 1986). There appears to be every prospect of OPTOPUS going on to make a significant contribution to the spectroscopic data on southern hemisphere clustered objects.

Development work on optical fibre spectroscopy at the Royal Greenwich Observatory (RGO) has been reported by Powell (1983a,b,c; 1986). The last of these papers describes the fabrication of fibre-coupled multi-object systems for the 2.5-metre Isaac Newton telescope (INT) and the 4.2-metre

William Herschel telescope (WHT) at the La Palma observatory (see, eg, Boksenberg, 1984; RGO, 1985). The INT multi-fibre system is, again, a Medusa-class instrument, but it is of particular interest because of the disparate focal ratios of the input and output beams, as mentioned in Chapter 2. The system is designed to accept the f/3.3 beam of the telescope's primary mirror, and transfer the light to the Cassegrain position, where it can be fed to the f/15 collimator of the intermediate-dispersion spectrograph.

For a number of reasons, not least of which was the already fast focal ratio of the telescope beam, Powell (1986) elected to use direct input to the fibres, but did choose an array of microlenses as the optimum method of matching the output beams to the spectrograph collimator. Again, for a number of reasons, mainly connected with freedom of design, rod lenses were preferred over the other types of microlens mentioned in Section 2.3. The INT prime focus has a plate-scale of 24.7 arcsec/mm, with its three-element corrector (modified from Wynne, 1974), and 100 μm (2.5 arcsec) diameter fibres were chosen as optimum. They are used with 1.5 mm focal-length rod-lenses (whose physical lengths (2.33 mm) are equal to their focal length in glass), and the lenses are cemented direct to the fibre output ends to produce the f/15 beam, in an arrangement analagous to that depicted in Figure 2.8(b)(ii). Thus, the output focal ratio is defined by the geometry of the fibre/microlens system, and any FRD results not in a loss of efficiency, but in a degradation of the spectrograph resolution (1).

---

(1) This can, if necessary, be recovered at the expense of some light loss

The diameter of the microlenses was chosen to be 1.0 mm, larger than that required to accept a beam degraded to the NA of the fibre so that there will be no risk of loss due to vignetting. The microlens diameter limits the number of fibres that can be aligned on the 44 mm long spectrograph slit and, in the prototype system, 40 fibres are used with their output lenses in contact. A special alignment jig was constructed to facilitate the assembly of the output array with the required precision. Powell (1986) notes that the effects of aberrations in the microlenses are minimal, and only a very small amount of chromatic aberration is detectable in the output beam profile.

In the selection of fibre type for this system, greater weight had to be given to transmission properties (because of the length) than to FRD properties (because of the microlenses), and Spectran 820 105/125 was chosen. At their input ends, the fibres are fitted with ferrules, which are a near-interference fit in the focal plane aperture plate, and incorporate a shoulder to provide positive axial location. This is a very similar arrangement to that developed by Gray for the AAT (described in the next section). The flat aperture plates are 160 mm square, giving a field coverage of 1.1 deg on a side, of which the central 40 arcmin diameter portion is unvignetted. It is understood that, although Powell has now left RGO, this system has been deployed on the INT and is undergoing trials.

---

by means of a slit or aperture at the collimator focus, ie, in the position analagous to that of the image in Figure 2.8(b)(ii). (Compare Serkowski et al., 1979; Heacox, 1980; Powell, 1983c.)

The planned multi-fibre system for the WHT differs from that just described in that it is simply an image-reformatter, using telescope and spectrograph beams that are matched for normal direct coupling (Powell, 1986). However, since their common focal ratio of f/11 would not be preserved in the fibres, the same microlens technique has been adopted to define the output focal ratio. Here, 200 μm and 400 μm diameter fibres (subtending 0.89 and 1.78 arcsec, since Π=4.45 arcsec/mm) will be used with rod lenses of length 3.3 and 6.7 mm respectively. In fact, the difficulty of manufacturing lenses of this length and only 1 mm or so in diameter may dictate the use of shorter lenses spaced from the fibre ends by a single flat silica plate. The fibres need to be only 2 m long to reach from the Cassegrain acquisition and guidance box to the ISIS triple spectrograph (Boksenberg, 1985; RGO, 1985). Because of the large bandwidth of the spectrograph, the transmission properties of the fibres are again important, and the selected types are Fiberguide's Superguide G 200-UV and Polymicro Technologies' 400/480-UV. Development work on this major fibre-optics system is clearly still at an early stage, but is expected to progress rapidly once the telescope is operational.

We end this section by mentioning a few other fibre-coupled multi-object spectroscopy systems that are in various stages of development. An MX-type system is being developed for the prime-focus of the CTIO 4-metre telescope (Ingerson, 1986). The 50 arcmin field will be accessed by 2x24 fibre channels (paired for object and sky) with the surprisingly large diameter of 4 arcsec (200 μm). Long fibres will be used, feeding a stationary spectrograph in a controlled environment near the coudé focus. The system is expected to be completed early in 1988.

A paper by Tubbs, Goss and Cohen (1982) is the only published account of a remotely-positioned 20-channel fibre feed for the prime-focus spectrograph of the 5-metre Hale telescope at Palomar. Development of this system now appears to have been abandoned. The design was an example of the first class of fibre positioning systems described in Section 4.3, except that areas of the field of view were allocated to pairs of fibres rather than single ones. The 76 mm (15.8 arcmin) square field of the telescope was divided into 10 strips, each of which was patrolled by two fibre inputs capable of moving anywhere within the strip (except past one another) under computer control. This was achieved by fibre carriages with (x,y) motion driven by stepper motors. An additional degree of freedom in target allocation could be achieved with a field-rotation system. In their paper, Tubbs, Goss and Cohen (1982) discussed the merits of the various remote positioning schemes, and described tests with a prototype system.

Following a visit to Siding Spring Observatory, and examination of the UKST's FLAIR multi-object spectroscopy system, Pettersson (private communication) et al. have embarked on the development of a similar system for the 1.0-metre Kvistaberg Schmidt telescope of Uppsala University. The photographic performance of this instrument suffers because of poor sky conditions, and multi-fibre spectroscopy is seen as a promising alternative. The system under development has detail differences from FLAIR (in particular, in the 90-deg prisms terminating the input ends, so that they can be cemented to the front of a glass plate rather than the back), but the use of an inexpensive off-telescope spectrograph is similar.

Another system whose early development was based on that of FLAIR is the

photometric/spectrometric instrument built at Leeds University (Baruch, private communication; Baruch et al., 1986). This device is intended for use on several different telescopes, and employs an identical fibre-positioning method to FLAIR (ie, positive copy plate). It is not clear, however, that this is always necessary, given that many of the telescopes on which the system might be used will have plate-scales large enough to permit Medusa-type positioning. For example, Baruch et al. (1986) describe acquisition experiments on the 1-metre Jacob Kapteyn telescope (JKT) at La Palma, whose f/8 plate scale is 25.6 arcsec/mm. The system is intended for multi-object photometry and very low-dispersion spectroscopy, using a cooled CCD camera as detector.

Finally, mention might be made of some other fibre-coupled photometry systems that have been developed, first by Caton and Pollock (1986) at Appalachian State University, second by Walker (1986) at RGO (a photometer designed specifically for amateur use), and last, the remarkable system recently described by Barwig, Schoembs and Buckenmayer (1987). While none of these is conventionally spectrometric, and all, at present, have very limited numbers of channels, they are interesting in the light of the FLAIR multi-object photometry experiment described in Chapter 7.

4.5 Fibre optics at the Anglo-Australian telescope

Although, as we have seen, the technique was not invented there, it is probably no exaggeration to say that the art of multi-object spectroscopy with optical fibres has been perfected at the Anglo-Australian telescope. Since the earliest experiments with fibres at the AAT in 1981, there has

been a steady development of the associated instrumentation in response to a steadily increasing demand from the British and Australian user communities, which has resulted in the quite spectacular rise in actual usage shown in Figure 4.4. An effective response to the requirements of users is characteristic of the service provided by the AAT (although, of course, it is never possible to please all the people all the time - see Griffin, 1983; Griffin and Griffin, 1984) but, in this case, much of the success is due to the individual efforts of Peter Gray, and the sustained interest of a succession of AAT staff astronomers. The AAT fibre-optics system has been used at various stages in its development by the writer, as reported in the next chapter, so a reasonably complete account of its history and current status is given here. As well as the references cited, the detailed development of the system can be traced through the pages of the AAO Newsletter.

A memorandum, dated 16.1.81 and simply entitled "Fibre optics" (Carter, 1981), appears to mark the beginning of interest in optical fibre spectroscopy at the AAT. The memo notes the developments in Arizona at Steward Observatory and the Lunar and Planetary Laboratory, records the interest of David Carter (AAO) and Richard Ellis (Durham) in a number of possible fibre-coupled instruments for the AAT, and suggests an investigation into the practical use of fibres, nominating Peter Gray as the project engineer. The Anglo-Australian Observatory (AAO) was, in fact, well-placed from the start to embark on fibre-coupled multi-object, or area spectroscopy, having a telescope with a relatively wide-field (40 arcmin) Ritchey-Chrétien focus, a fully-commissioned long-slit spectrograph (the RGO spectrograph) and an excellent two-dimensional detector system (the IPCS). Carter's

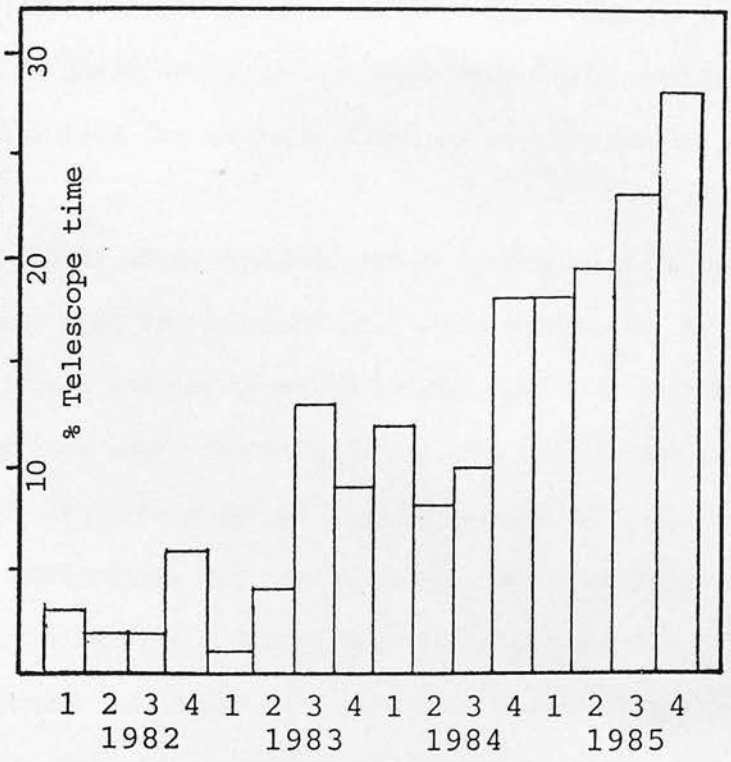

Figure 4.4 AAT fibre system usage 1982-85 (from Gray, 1986a).

(1981) memo quickly led to the fabrication of a short-coupled (50 mm) fibre image-converter (Gray et al., 1982; Gray, 1983b) for insertion in front of the RGO spectrograph slit; this had approximately one hundred 200 μm (1.3 arcsec) PCS fibres transforming a 17x22 arcsec rectangle into a 32 mm line at the slit. In spite of its relatively large (50-70 percent) losses, this was successfully used for area spectroscopy of galaxies in August, 1981.

The next step was to attempt multi-object spectroscopy using longer (2.5 m) fibres leading from the Cassegrain auxiliary focus of the telescope (a 12 arcmin square focal station accessed by the insertion of a 45-deg mirror in the converging beam above the main focus) directly to the focus of the collimator mirror. This arrangement had the considerable merit of leaving the spectrograph undisturbed on the telescope, and requiring only the retraction of the auxiliary focus mirror and the replacement of a Newtonian flat in the collimator to revert to direct slit spectroscopy. The system that was constructed for this was a Medusa-class instrument called FOCAP (fibre-optic coupled aperture plate), and it was first used on the telescope in December, 1981. It is fully described by Gray et al. (1982), Gray (1983b), Ellis et al. (1983), and in the review by Watson (1983).

The original FOCAP consisted of 25 lengths of 200 μm core diameter Galite 4000-LC-P PCS fibre, terminated at their input ends with ferrules consisting of lengths of 0.5 mm (outside) diameter steel microtubing with a shoulder formed by a 2.5 mm diameter brass bush. These ferrules were a characteristic feature of the system, and were designed to give positive lateral and axial fibre location in the 0.5 mm holes drilled in the (flat) aperture plate, itself made from 1.6 mm thick engraving brass. The fibre

bundle was 2.5 m long. Acquisition and guidance were carried out by means of two pseudo-imageguides, each consisting of a bundle of seven close-packed fibres feeding the acquisition TV camera; arc frames were obtained from calibration lamps placed in the central chimney (Cassegrain light-baffle) of the telescope. Shortly after the completion of FOCAP, a second image-dissector was made with 53 fibres 2.5 m long, transferring a 12x15 arcsec rectangle in the Cassegrain auxiliary focus to a "slit" at the collimator focus in the same way as FOCAP (Gray, 1983b). Although this was used to obtain data at the telescope, the hoped-for gains in efficiency for area spectroscopy were not realized because of the relatively large optical losses, and the dissector was not used again.

FOCAP was very much a prototype system, but such was the demand for telescope time using the system that improvements quickly followed. In March, 1983, a new feed bundle (eventually designated 200A) was introduced, using 3 m lengths of 200 μm QSF 200/300-AS fibre, whose superior FRD characteristics were intended to improve the ~50 percent average transmission of the earlier bundle (Gray, 1983a,b). The new feed offered 50 fibre channels (although, as with all the FOCAP bundles, a few fibres suffered early breakages) and, shortly after its introduction, a new external fibre input to the RGO spectrograph was commissioned, allowing rapid feed-bundle changes, and the use of neutral density (ND) filters and a shutter. An interchangeable f/6 collimator mirror was introduced, further improving the FRD efficiency, (1-D), of the new bundle from 64 percent (into f/8) to 83 percent (into f/6), and improved arrangements for obtaining arc frames using a diffuser screen in the chimney were deployed. In order to improve the flexibility of the system, another new fibre bundle was introduced

(400A), using 400 μm core (2.7 arcsec) QSF 400/600-ASW wet fibre, but otherwise identical to 200A. A second 400 μm bundle was completed shortly afterwards.

In August, 1983, a new faint-object red spectrograph (FORS; Gillingham, 1983) was commissioned on the AAT. This instrument is a low-dispersion (450 Å/mm), high-efficiency collimatorless spectrograph using a cooled GEC CCD detector, and an optical-fibre input was fitted for use with the FOCAP system, thus providing a red-sensitive, low-resolution alternative to the RGO spectrograph for multi-object work. What was perhaps a more significant advance took place in February, 1984, when the full 40-arcmin field of the f/8 focus was opened up for multi-fibre spectroscopy by the commissioning of a new aperture plate mounting. A strong box-truss was constructed to lower the RGO spectrograph by 30 cm, allowing the insertion of 380-mm diameter circular brass aperture plates in specially-designed interchangeable plateholders. The aperture plates are deformed to an approximation of the focal surface by a central tensioning screw in a cantilever arm on the back of the plateholder; the resulting shape is not spherical, but does provide some compensation for beam inclination (Gray, 1986a). (Interestingly, the Cassegrain photographic plates that were taken for the astrometric determination of distortion prior to the commissioning of the 40 arcmin FOCAP system were among the very few that had been obtained in the telescope's ten-year history, despite the fact that the entire optical design was optimised for that purpose.) The use of interchangeable plateholders, together with the range of three available 50-fibre (nominal) feed bundles, meant that aperture plates could be set up while observing was taking place, and a minimum of down-time was needed to change fields. In

addition, the 12-arcmin square auxiliary focus was still available if required, adding further to the system's flexibility.

Other developments that took place during 1984 were the introduction of a new guide bundle providing coarse imaging of four fiducial stars rather than two, and the introduction of a separate high-resolution imageguide for aperture plate pre-alignment and focusing. Parallel with these were developments in the software associated with the system (eg, the APLATE program, providing positional data on target objects for the numerically-controlled milling machine used to manufacture the aperture plates; ALIGNX, a program to optimise the aperture-plate alignment in the telescope from the appearance of the fiducial-star images; and the various programs for extracting spectra from the final 2-d data frames). In addition, the most effective techniques for observing with FOCAP were evolved (some of which are described in the next chapter), and it was not long before 100 fibres were used simultaneously to feed images from a single aperture plate to both the RGO spectrograph and FORS. This situation is depicted schematically in Figure 4.5, which illustrates most of the features of the system.

The AAO fibre system had now reached a reasonably stable configuration and, in March, 1985, a substantial User Guide and Technical Manual (Gray and Sharples, 1985) was issued to steer observers and support staff through the complexities of setting the system up and making the best use of the large number of options available. Later in 1985, a second 200 μm fibre bundle was added to give a total of four available feeds (200A,B and 400A,B; Gray, 1986a). Two more bundles were commissioned in 1986 to take advantage

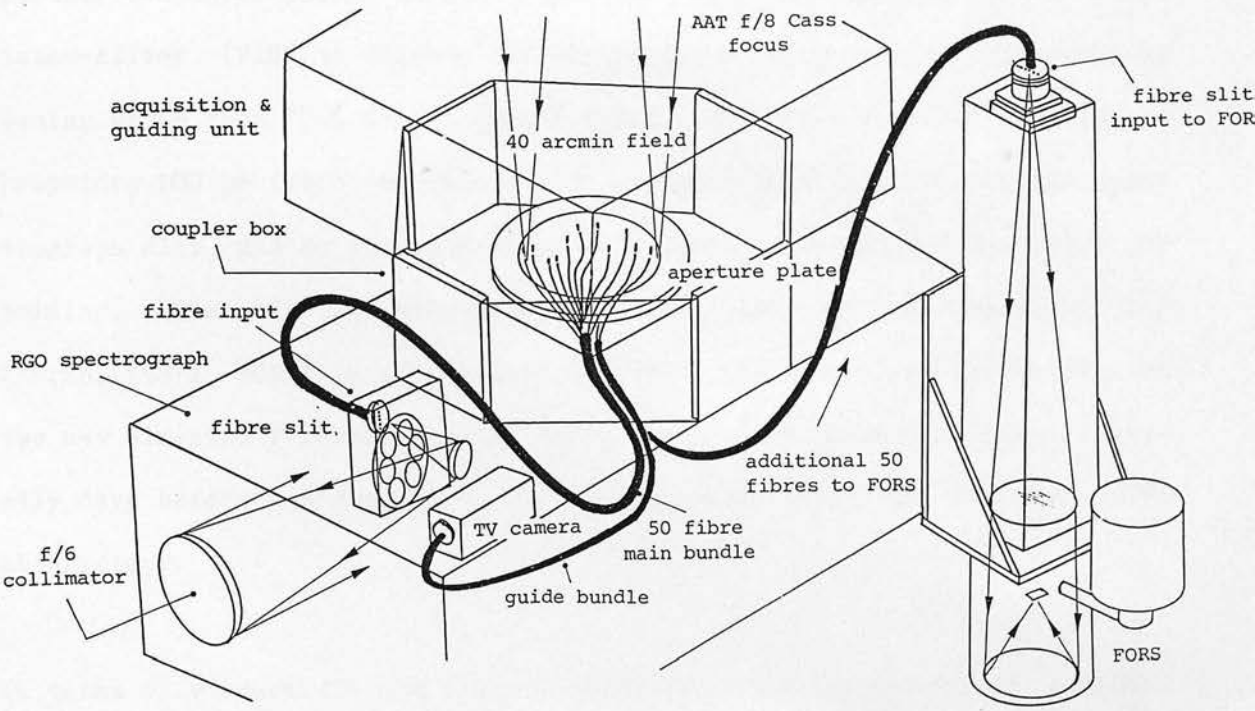

Figure 4.5 Principal components of the FOCAP multi-fibre system at the AAT (from Gray, 1986a).

of the good UV transmission of the recently-introduced Polymicro FHP fibre (Gray, 1986b,d); these bundles are designated 300A,B, and have 64 fibres of 320 μm core diameter. All six fibre bundles are interchangeable. Another new development during 1986 was the introduction of a fibre image-slicer (FIS) to improve the efficiency of single-object observing in seeing worse than ~2.5 arcsec (Gray, 1986b,c,d). This uses 290 lengths of Polymicro 100 μm fibre to convert a 13 arcsec circle to a line at the spectrograph slit, and is equipped with a separate imageguide to allow TV guiding. The FIS is interchangeable with FOCAP. At the time of writing (March, 1987), FOCAP is still being improved, and Peter Gray is working on two new six-star fiducial bundles using 200 μm core Polymicro fibre, literally days before his departure for a two-year visit to the La Palma observatory.

In terms of versatility and optical efficiency, the current FOCAP undoubtedly represents the pinnacle of development of the Medusa-class system. In terms of astronomical results, FOCAP has achieved much in its five-year history, with successful research programmes including quasar surveys, studies of distant and nearby clusters of galaxies, globular cluster systems of external galaxies, rotation of dwarf galaxies, cepheids in the Magellanic Clouds, globular cluster metal abundances and velocity dispersions, stellar dynamics and population gradients within the Galaxy, and time-resolved spectroscopy of RR Lyraes and flare stars (Gray, 1986a). It is clearly a success story that has not yet ended.

The possibility of building a remote fibre positioning system to supplement and eventually replace FOCAP has been discussed for some time. The motiva-

tion for such a system is similar to that described for MX in Section 4.3; there are, however, some additional considerations, of which perhaps the most important is the high cost (~$A 12,000 per year) of manufacturing aperture plates for a system as much in demand as FOCAP (Parry, 1986; Parry and Gray, 1986). A proposal developed by Ian Parry and others at the University of Durham (Ellis and Parry, 1983; Parry, Ellis and Breare, 1984; Parry et al., 1984) to build an automated optical fibre coupler for the AAT was accepted as a joint Durham/AAO venture (Parry, Ellis and Gray, 1986) and, at the time of writing, the device is undergoing final commissioning at the telescope.

The instrument is called AUTOFIB, and is fully described by Parry (1986), and Parry and Gray (1986). It is an archetypal example of the third class of fibre positioning systems described in Section 4.3, using a single manipulator mounted on a high-speed, precision (x,y) carriage to position the fibres in a sequential fashion. The general arrangement is illustrated schematically in Figure 4.6(a). Each fibre is terminated with a probe tip unit (or "button"), containing a 90-deg prism and a powerful rare-earth magnet, as shown in Figure 4.6(b); these are affixed magnetically to a steel field-plate situated just behind the telescope's 40-arcmin Ritchey-Chrétien focal surface, so that the target images fall on the fibre entrance faces. As we have already noted in Section 3.1, the field plate is stepped to give a coarse match to the focal curvature.

The first 30 cm of each fibre is encased in a fine steel tube to prevent it from bending within the field area; these tubes, or probes, are free to slide through a pivot at the edge of the field. The entire fibre module

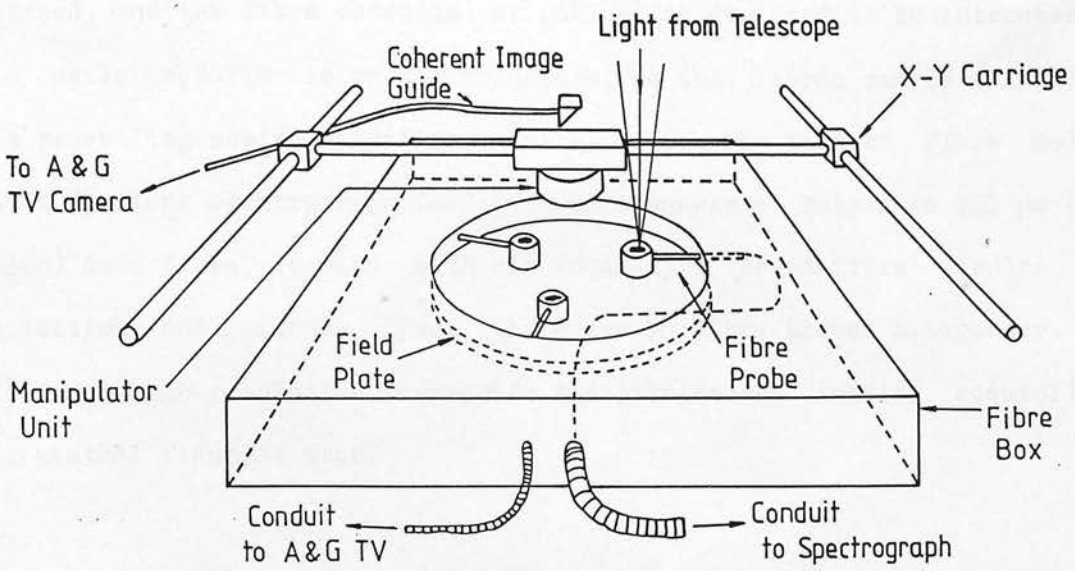

(a)

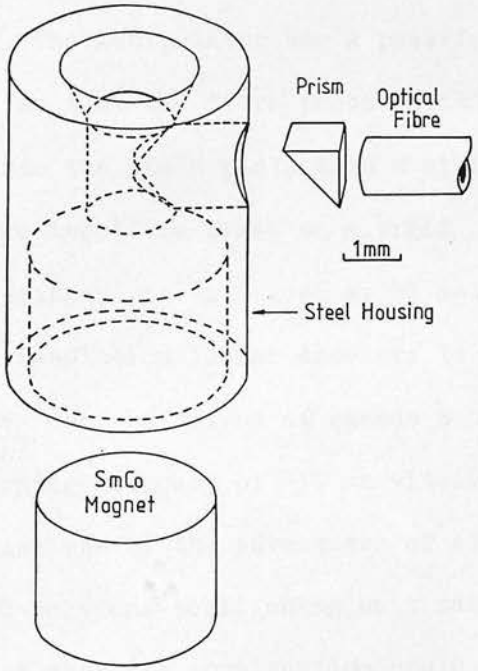

(b)

Figure 4.6 AUTOFIB fibre-positioning system. (a) Schematic view showing general arrangement. (b) Detail of fibre probe tip (from Parry, 1986).

(comprising the field plate, the surrounding fibre-box with the probes attached, and the fibre conduits, or cables) is designed to be interchangeable while AUTOFIB is on the telescope, so that fibres can be changed to suit prevailing seeing conditions, for example. The initial fibre module has a 3 m long spectrograph feed with 64 channels of Polymicro 320 μm (2.1 arcsec) core fibre, together with six FOCAP-type seven-fibre bundles for acquisition and guidance. Thus, there are 70 fibre probes altogether. An additional high-resolution imageguide facilitates the initial acquisition of a central fiducial star.

The rest of AUTOFIB comprises the truss structure to support the RGO spetrograph, and the positioner itself, which consists of a manipulator moving on the (x,y) carriage. This can also be moved in a direction normal to the field plate. The manipulator has a powerful electromagnet tipped with a conical spigot, so that the fibre probe units can be picked up from, and released back onto the field plate with a minimal lateral error (~10 μm). The (x,y) carriage itself is based on a rigid frame and uses very high-quality linear bearings; it is driven by DC motors under microprocessor control, with 2 μm resolution linear encoders to close the servo loops. Thus, the manipulator can be moved at speeds exceeding 200 mm/sec, and still achieve a positioning accuracy of ~10 μm within its 380 mm square patrol area. Herein lies one of the advantages of AUTOFIB over the MX system; the need to build only one positioning unit rather than one for each fibre channel has meant that its construction could be of the very highest quality, while remaining within a reasonable budget (~£20,000, far less than that of MX). The penalty for this is, of course, a reconfiguration time for a 64-fibre field of ~10 min, compared with ~90 seconds for MX.

AUTOFIB is operated by a dedicated microprocessor, which ensures that the positioning of fibres will proceed without any risk of mechanical conflict. It also provides information for a mimic display in the telescope control room, showing the current configuration of the fibres. The microprocessor is interfaced to the AAT's VAX 11/780, through which the observer sets up and executes the allocation of fibres to target images. The execution will normally happen as the telescope is moved from one field to another, so the positioner has to be able to function while it is at a random, changing orientation with respect to gravity.

The first results from the current AUTOFIB commissioning runs appear to be promising, with positioning accuracy approaching the target of ~25 μm. The introduction of this instrument for routine work on the AAT is anticipated with great interest, and it appears certain that it will eventually rank among the world's most productive multi-fibre spectroscopy systems, a fitting note on which to end this survey.

References for Chapter 4

Angel JRP, 1978. In Opt.telescopes of the future, p.227, ESO/CERN, Geneva
Angel JRP, Adams MT, Boroson TA, Moore RL, 1977. Ap J 218, 776
Appenzeller I, OstreicherR,SchifferJG,EggeKE,PettersenBR,1983.AandA 118, 75

Baruch JEF et al., 1986. Internal report, University of Leeds
Barwig H, Schoembs R, Buckenmayer C, 1987. Astr.Astrophys. 175, 327
Boksenberg A, 1984. Telescope Making No 23, p.47
Boksenberg A, 1985. Vistas Astr. 28, 531

Carter D, 1981. Fibre Optics (Internal report of AAO)
Caton DB, Pollock JT, 1986. Proc SPIE 627 (Inst. in Astr. VI), p. 132

Ellis RS, Gray PM, Carter D, Godwin J, 1983. MNRAS 206, 285
Ellis RS, Parry IR, 1983. An automated fibre coupler (Univ. of Durham)
Enard D, Lund G, 1983. ESO Messenger No.31 p.1
ESO Optical Instrumentation Group, 1985. ESO Messenger No 41, p.25

Flint G, 1984. Sky and Telescope 67, 402

Gillingham PR, 1983. Proc SPIE 445 (Inst. in Astr. V), p.577
Grainger JF, 1981. Observatory 101, 140
Gray PM, 1983a. Proc SPIE 374 (Fibre Optics '83), p.160
Gray PM, 1983b. Proc SPIE 445 (Inst. in Astr. V), p.57
Gray PM, 1986a. Proc SPIE 627 (Inst.in Astr.VI), p.96
Gray PM, 1986b. AAO Newsletter No 38
Gray PM, 1986c. Australian Lasers and Optics 4 (No 2), p.4
Gray PM, 1986d. AAO Newsletter No 39
Gray PM, Phillips MM, Turtle AJ, Ellis RS, 1982. Proc ASA 4, 477
Gray PM, Sharples R, 1985. AAO fibre system user guide (Manual No 18)
Griffin R, 1983. AAO Newsletter No 24, p.1
Griffin R, Griffin R, 1984. JBAA 94, 282

Heacox WD, 1980. Proc KPNO conf.on opt/IR tels.for the 1990s,p.702,Tucson
Heacox WD, 1986. AJ 92, 219
Hill JM, 1984. PhD Thesis, University of Arizona
Hill JM, Angel JRP, Richardson EH, 1983. Proc SPIE 445 (Inst.in Astr.V)p.85
Hill JM, Angel JRP, Scott JS, 1983. Proc SPIE 380, 354
Hill JM, Angel JRP, Scott JS, Lindley D, Hintzen P, 1980a.Opt/IRtels..p.370
Hill JM, Angel JRP, Scott JS, Lindley D, Hintzen P, 1980b. Ap J 242, L69
Hill JM, Angel JRP, Scott JS, Lindley D, Hintzen P, 1982. Proc SPIE 331,279
Hill JM, Eisenhamer JD, Silva DR, 1986. Proc SPIE 627 (Inst.in Ast.VI)p.693
Hill JM, Lesser MP, 1986. Proc SPIE 627 (Inst. in Astr. VI), p.303
Hintzen P, Hill JM, Lindley D, Scott JS, Angel JRP, 1982. AJ 87, 1656
Hubbard EN, Angel JRP, Gresham MS, 1979. Ap J 229, 1074

Ingerson T, 1986. NOAO Newsletter No 8 p.32

Lund G, Enard D, 1983. Proc SPIE 445 (Inst.in Ast. V), p.65
Lund G, Surdej J, 1986. ESO Messenger No 43, p.1

Oates AP, 1987. PhD Thesis, Lancashire Polytechnic

Parry IR, 1986. PhD Thesis, University of Durham
Parry IR, Ellis RS, Breare JM, 1984. ACIAAT submission
Parry IR, Ellis RS, Breare JM, Gray PM, 1984. ACIAAT submission
Parry IR, Ellis RS, Gray PM, 1986. New Scientist, 17 April issue, p.36
Parry IR, Gray PM, 1986. Proc SPIE 627 (Inst.in Astr.VI), p.118
Powell JR, 1983a. Fibre optic preliminary report, RGO
Powell JR, 1983b. Proc SPIE 445 (Inst. in Astr. V), p.77
Powell JR, 1983c. 2nd progress report on optical fibre investigations, RGO
Powell JR, 1986. Proc SPIE 627 (Inst. in Astr. VI), p.125

Ramsey LW, Huenemoerder DP, 1986. Proc SPIE 627 (Inst.in Astr. VI),p.282
RGO (Royal Greenwich Obs), 1985. Telescopes, Instruments, Res.and Services
Richardson H, 1972. In Proc.ESO/CERN conf.on aux.inst.,p.275,Geneva
Robson EI, Grainger JF, 1983. JBAA 93, 75

Schiffer JGV, 1983. Proc SPIE 445 (Inst.in Astr. V), p.52
Serkowski K, Frecker JE, Heacox WD, Roland EH, 1979. Proc SPIE 172, 130

Tubbs EF, Goss WC, Cohen JG, 1982. Proc SPIE 331 (Inst.in Astr. IV),p.289

Walker EN, 1986. JBAA 97, 30
Watson FG, 1983. JBAA 93, 193
Weller WG, Ingerson T, 1986. NOAO Newsletter No.8 p.31
Wolff S, Fraknoi A, 1986. Mercury 15, 139
Wynne CG, 1974. MNRAS 167, 189

CHAPTER 5

Multi-fibre spectroscopy of RR Lyrae stars with the AAT

Prefatory remarks

This chapter presents a progress report on a long-term programme of spectroscopy of RR Lyrae and other variables in the nuclear bulge of the Galaxy. The programme aims to investigate the kinematics and chemical history of the bulge, and to provide a direct measurement of any radial motion of the local standard of rest (LSR) in the Galaxy. It was initiated more than a decade ago by Victor Clube (Oxford; formerly ROE), who remains the senior collaborator in the project. The writer's role in this study has been quite clear-cut: viz, to be responsible for all facets of securing and reducing the observational data, and these aspects are given the main emphasis here. Some contribution has also been made to the interpretation of the results.

The work is included in this thesis because it provides an excellent example of the practical application of multi-fibre spectroscopy, and demonstrates the use of the AAT's FOCAP system, described in the previous chapter. It clearly illustrates the gains in observing efficiency that can

be achieved thereby, and, to highlight this aspect, the early results from the programme (which were obtained before the advent of the multi-fibre technique) are also included. Some of these have been presented in an earlier report (Watson, Murdin and Clube, 1979). Spectra from the most recent (and most productive) observing run in 1984 are not yet fully reduced, mainly because of competing demands for time incurred by the development and implementation of FLAIR. However, these, together with the other data given here, will be published in a forthcoming paper that will also include a full discussion of the results. This chapter, therefore, represents an interim report on the progress of the study.

5.1 Introduction

Ever since Baade's (1963) classic determination of the value of the galactocentric distance of the Sun, R_o, the RR Lyrae variables in the low-absorption windows towards the galactic nucleus have been recognised as uniquely suited to the detailed study of a representative sample of the galactic bulge population. Photometric data (eg, Gaposchkin, 1956; Clube, 1965; Plaut, 1966, 1968, 1971) have been used to determine the structure of the inner galactic halo (Oort and Plaut, 1975; Clube and Watson, 1978), while more recent photometry (Hartwick, Hesser and Hill, 1972; Blanco, 1984) and low-dispersion spectroscopy (Butler, Carbon and Kraft, 1976) have enabled assessments to be made of the metallicities of the bulge RR Lyraes.

These data, comprising light-curves and values of the metallicity index, ΔS (Preston, 1959), indicate RR Lyraes very like most of those we observe in the solar neighbourhood, and provide evidence that we are dealing with a

stellar population in the nuclear region that is similar to the (relatively not very dense) metal-weak, slowly-rotating halo to which many of the more widely-distributed globular clusters belong (1). There is evidence for a small, old disc population of RR Lyraes as well, in the solar neighbourhood, comprising some ten percent of all such stars (Clube and Dawe, 1983), but no definite counterparts of this somewhat brighter, metal-rich population have, as yet, been found in the nuclear bulge. A nuclear bulge component that is less metal weak than the halo is, nevertheless, generally assumed to exist, so it would appear on this account to be dominated by relatively youthful stars that are not associated with the RR Lyrae phase of evolution. There are grounds, therefore, for expecting the kinematics of the RR Lyraes in the nuclear bulge to reflect a dynamical and evolutionary history that differs from the bulge as a whole. The ability to measure accurate velocities for these stars in order to explore the kinematic properties of the nuclear bulge has, until recently, been denied to investigators for all but the nearest of them (Rodgers, 1977; Clube and Watson, 1978) by their faintness ($15<B<20$) and the very crowded nature of the fields, particularly those closest to the galactic centre.

---

(1) It may be noted, however, that recent studies of the globular cluster systems of giant elliptical galaxies suggest that these systems may have properties that are fundamentally different from those of the stellar halos, because the radial decline in globular cluster number density is considerably shallower than the galaxy luminosity profile in the same region (Lauer and Kormendy, 1986; Grillmair, Pritchet and van den Bergh, 1986; Harris, 1986).

In recent years, there has been an accumulation of other evidence, suggesting that these observations may be at least as important for our understanding of the dynamics of the Galaxy as a whole as they are for what they will tell us about motions within the bulge. Since Kerr's (1962) initial postulation of an outward motion of the LSR in the Galaxy, a variety of optical, infrared and radio data (eg, Clube, 1973, 1978 (and references therein), 1986; Gatley, Geballe and Wade, 1987) has indicated the possibility that the galactic radial velocity of the LSR, Π_o, may, indeed, have a positive value significantly different from zero. The discovery of expanding motions in the inner region of the galactic globular cluster system (Clube and Watson 1979, Frenk and White 1980) and the emergence of systematic radial drifts among early-type stars (Watson and Clube, 1981) reinforce the suggestion that the Galaxy may not be in a simple, steady dynamical state. In particular, there is an implication that an important error was made in the 1920s when Kapteyn's two-stream model of local stellar motions was abandoned in favour of Schwarzchild's velocity ellipsoid (Clube 1982). In a recent assessment of our understanding of activity in galactic nuclei (Balick and Heckmann 1982), the ~ 50 km/s mean motion of ionized gas at the galactic centre (Wollman et al., 1977) is highlighted as a continuing problem. Of course, the view can also be taken that these apparent inconsistencies in the present picture are chance effects and are not of fundamental importance. Thus, it has been suggested by Oort (1977, 1982) and Feast, Robertson and Black (1980) that the galactic radial motion of the LSR is not sensibly different from zero, but it is by no means certain that galactic-centre populations like the planetaries and the long-period variables, on which this conclusion is based, can be clearly equated with the nuclear bulge, since their absolute magnitudes are consid-

erably more dispersed than is the case with RR Lyraes. Evidently, knowledge of the radial motion of the LSR is still an important requirement for dynamical theory.

Because the standard of rest defined by the bulge RR Lyraes is that of the Galaxy as a whole, measurement of the radial velocities of a sample of these stars does, in principle, provide the currently most accessible signature of any radial motion of the LSR. The closest low-obscuration window to the galactic centre in which RR Lyraes have been identified is Baade's NGC 6522 field (Baade, 1963; Gaposchkin, 1955), which contains ~100 RR Lyrae stars ($\bar{m}_{pg}$ =17.5) in ~0.25 deg^2. The magnitude distribution of these stars (2) shows that they are a representative sample of the bulge population (Baade, 1963); since they lie close to the galactic centre line of sight (l=1.0 deg, b=-3.9 deg) and are sufficiently large in number to provide a statistically significant sample, they offer the best possibility of a direct determination of the value of Π_o. In order to eliminate the effects of the non-zero rotation component on the velocities of these RR Lyraes, it is clearly desirable to have similar velocity measurements in other parts of the galactic nucleus. The field of NGC 6304 (l=356 deg, b=+5 deg), on the other side of the galactic centre direction from Baade's window, contains a number of RR Lyraes belonging to the nuclear bulge (Hartwick, Barlow and Hesser, 1981) with a mean blue magnitude of about 18. These stars are thus suitable candidates for additional velocity measurements to permit separation of the effects of galactic rotation and

---

(2) See Figure 5.3.

expansion.

In 1977, with the commissioning of the RGO spectrograph and image photon counting system (IPCS) on the 3.9 metre Anglo-Australian telescope (AAT), that instrument became capable of securing the velocities of the nuclear bulge RR Lyrae stars with sufficient accuracy (~20 km/s) to make the direct measurement of Π_o a realistic proposition. In the following year, we embarked on a long-term programme on the AAT to carry this out, and here present results from that work. Unfortunately, in its early stages, the project was bedevilled by almost unbelievably bad weather and progress was very slow. However, a substantial number of Baade's window RR Lyraes have now been observed, although the velocities in the NGC 6304 field are still sparse and would benefit from further work. As well as the RR Lyraes in these two fields, we have measured a number of the nearer variables in the higher latitude Palomar-Groningen fields surveyed by Plaut (1966, 1968, 1971) to establish whether the motions of these stars reflect those of the globular clusters in the inner halo (Clube and Watson, 1979); this work has formed a secondary programme for poor observing conditions. Many of the spectra we have obtained have sufficiently good signal-to-noise to allow reliable measurements of the metallicity parameter [Ca/H] to be made (Rodgers, 1974). Such measurements for a large enough sample (compare Butler, Carbon and Kraft, 1976) are clearly relevant to our understanding of the chemistry of the nuclear bulge, and these are being undertaken. As we have already noted, the measurements from the most recent (1984) observing season are not yet complete, but we here present such radial-velocity observations as are currently available (obtained 1979-83), together with a brief discussion of the provisional conclusions. The final results,

comprising a catalogue of ΔS values and radial velocities for $\gtrsim$100 bulge RR Lyraes, must await publication in due course when the programme is completed.

5.2 Techniques

In the early stages of the work, conventional slit spectroscopy was used to obtain the velocities of the RR Lyraes. Although the IPCS was operated in 2-dimensional mode, this was merely to facilitate sky subtraction, and the stars were observed sequentially. Sky subtraction was accomplished using the beamswitching method introduced in Chapter 1, and described further in the Appendix to the present chapter. The grating (1200B) and camera (25 cm) combination selected on the RGO spectrograph gave a reciprocal dispersion of 33 Å/mm, producing a wavelength increment of approximately 0.5 Å per IPCS channel. Given the relatively early spectral types of RR Lyrae stars, the spectral coverage was chosen so as to embrace as many as possible of the higher-order Balmer lines (from H_γ shortwards), together with the H and K lines of Ca II, and was typically 3600-4600 Å. To maximize accuracy in guiding, a blue filter was used in the slit-viewing TV optics. Calibration of the spectra was achieved by frequent Cu-Ar lamp exposures ("arcs"), and regular observations of standard velocity stars were made.

The high number density of RR Lyrae stars in the galactic centre windows, particularly Baade's field, rendered ours an ideal programme to be carried out with the AAT's FOCAP multi-fibre system when the prototype was introduced in 1981. All subsequent observations for the programme (with the exception of one night in 1984) were thus made using FOCAP. As recounted

in Section 4.5, the system has undergone almost continuous development since its introduction, so the RR Lyrae observations carried out in 1982, 1983 and 1984 were all made with different versions.

The prototype system, when used for the 1982 observations, had 20 available Galite 4000-LC-P fibres linking the 12 arcmin square Cassegrain auxiliary focus to the spectrograph. As we have seen, the FRD losses in this feed bundle reduced its transmission to only ~50 percent; moreover, there were significant fibre-to-fibre differences, possibly caused by differing stress conditions in the epoxy mounting at the output ends. An attempt was made to use these differences during observing to compensate for the differing mean magnitudes of the RR Lyraes in each field. A consequence of their existence, together with that of the limited number of fibre channels available, was the difficulty in obtaining satisfactory sky data. Complete frames of sky spectra were obtained by offsetting the telescope to a nearby star-free region (in fact, the heavily-obscured direction of the galactic centre itself) rather than using dedicated sky fibres for simultaneous sky-subtraction, as with the later work. However, poor weather conditions limited the integration times on the sky to less than half those on the RR Lyraes, and the sky spectrum was simply averaged over all the fibres and scaled to the correct intensity to allow sky subtraction. Although this averaging would help to reduce the noise in the sky-subtraction process, as described in Section 3.4, the noise introduced by the fibre-to-fibre transmission differences and the non-simultaneity of the sky observations would almost certainly outweigh the advantage.

The new FOCAP system, introduced in March 1983 to replace the pilot model

coupler, had QSF-AS fibres and the f/6 collimator mirror (commissioned during our 1983 observing run) to reduce the FRD loss. Up to 46 fibre channels were available during the 1983 run and, since the maximum RR Lyrae number density is such that no more than half that number could be allocated to programme stars in any one 12 arcmin square field, the allocations were made in pairs, each star having its own sky fibre in addition to the object fibre. The positioning of the sky fibres in Baade's window was a non-trivial task; the background star density is so high that it had to be surveyed for suitable clear spots near each programme star, and these measured astrometrically! Unfortunately, this meant that a proposed trial of the beamswitching method for sky subtraction (with the sky fibres all offset from the object fibres by the same distance and in the same direction so that they can be interchanged by a single movement of the telescope) could not be accomplished (3). In the event, the individual sky fibre signals were simply subtracted from the corresponding object fibre signals without averaging or scaling, so transmission differences between the star and sky fibres remain in the data; however, for the most part, the stars were sufficiently bright that this would have produced no

---

(3) It is possible that this could be the optimum method for multi-fibre spectroscopy. Referring to Equation 3.17b; although the 1/k term will increase to unity, the fibre noise term, σ_f, will be small since the sky is sampled very close to the object and, in good sky conditions, the effects of fibre transmission differences are much reduced (see Appendix to this chapter). There is clearly a trade-off here that may bear further investigation.

ill-effects.

By the time of the 1984 observing season, the 40 arcmin FOCAP system had been commissioned, and this was used for our observations in the NGC 6304 field, where the number density of the variables was relatively low. Only two fibres were used to monitor the sky, and separate offset-sky exposures were made to calibrate the fibre-to-fibre differences. Observations in the Baade field were made using the 12 arcmin field system as in the previous year.

The dispersion and spectral coverage chosen during the fibre runs were exactly as for the direct slit work, and a Cu-Ar lamp was again used for calibration. Arc exposures were made by illuminating a white diffuser screen from within the primary mirror central chimney so that the light path was not dissimilar to that followed by the starlight. Problems were experienced during the 1983 and 1984 observations (despite pleas for improvement) with severe UV loss in the arc spectra, apparently occurring at the diffuser screen, and the Cu-Ar arc had to be augmented with a helium lamp for some exposures. Standard star observations were made in the 1982 and 1983 seasons by aligning the star on a single fibre selected to be near the field centre (and also near the array centre at its output end) and relying on the arc frames to extend the calibration to the other fibres. (A check on the effectiveness of this was provided by the inclusion of known-velocity objects in the fibre fields.) Before the introduction of the external fibre input to the RGO spectrograph, with its inbuilt ND filters (1983 observations), the light from standard stars had to be attenuated by partially closing the primary mirror cover, a somewhat time-consuming

operation. (The need for such attenuation is, of course, a consequence of the small dynamic range of the IPCS, and the attendant risk of permanent damage to the image-tube by overexposure.) For the 1984 season, an improved method of standard star observation, using a highly defocused image of the star, was employed. This had the three-fold advantage of (i) allowing brighter stars (with better-known velocities) to be used, (ii) allowing light from the same star to be spread over several fibres to provide a check on the fibre-to-fibre wavelength calibration, and (iii) allowing the spectrograph to be used without ND filters, which, because of their position in the optical system, could lead to systematic velocity errors.

In poor conditions, spectra of single, bright RR Lyraes were obtained by aligning them with a selected fibre, as described for standard stars. One of the drawbacks of the early FOCAP system was, in fact, its relative inflexibility in variable conditions, as the effective slit width was fixed by the fibre core diameter of 200 μm. It was to help overcome this drawback that the new bundles of 400 μm core fibres were introduced; however, although one of these was available for our 1984 observations, we elected not to use it because of the loss in spectral resolution that would have occurred (made worse by the need to adopt a different IPCS data format). Fortunately, for the most part, the seeing was reasonably good during this run.

At their input ends, the 200 μm fibres subtend an angle of 1.3 arcsec on the sky, when used with the f/8 secondary. As we have seen, in the FOCAP system they are supported at the Cassegrain auxiliary or main focus by a Medusa-type aperture plate, which has been pre-drilled with holes cor-

responding to the positions of the target objects; the alignment of each hole needs to be accurate to ~0.3 arcsec, or 50 μm, if the system is to work at full efficiency (Figure 2.9(b)). Because the aperture plates are prepared automatically on a high-precision tape-controlled milling machine, the quality of the astrometry is the major contributor to the final alignment accuracy. Astrometry for the RR Lyrae runs was carried out using an excellent AAT prime-focus plate of Baade's window (taken for us early in the service photography programme) and a UK Schmidt telescope (UKST) Short Red Survey film copy of the region around NGC 6304 (field 454). These plates were measured by hand using a conventional two-coordinate measuring machine, although an attempt was made to use COSMOS data for the 1984 NGC 6304 observations. This proved unsatisfactory because of image merging, even though this field is the least crowded of all those observed in our fibre programme.

The astrometric reductions were carried out using Starlink* software, and this was also used extensively during the reduction of the spectra. The reduction of fibres data is a fairly substantial undertaking and, in the early days, was one to which the existing Starlink software was not altogether well-suited. For example, there was initially no Starlink-supported means of satisfactorily removing the residual S-distortion (introduced by the image-tube) from the 2-d IPCS data, and early programs for simultaneously straightening (by rebinning) and wavelength-calibrating the spectra using 2-dimensional polynomials derived from arc frames (see, eg, Ellis et al., 1983) were, in our experience, unreliable. In the event, this was not a serious drawback in the 1982 and 1983 runs as, in the usable portion of the spectra, the S-distortion ranged over a sufficiently small number of

---

* Starlink is the UK Science and Engineering Research Council's image and data processing facility, comprising a network of linked VAX 11/780 computers and associated software.

increments to allow a straightforward projection of each spectrum onto 1-d before wavelength calibration. The 1984 spectra were extracted using continuum-following routines written by John Lucey to run under DSCL in the Starlink environment.

The early slit spectra were wavelength-calibrated (with prior division by a flat field) using SDRSYS software at the AAT, but 2-dimensional wavelength-calibration for the spectra obtained with fibres was carried out using the ARC2 routine in the Starlink SPICA package. None of the spectra were flux-calibrated. Velocities were obtained by cross-correlating each sky-subtracted spectrum with that of a standard star, using the methods described by Peterson (1979), and Efstathiou, Ellis and Carter (1980). It may be noted that this method takes no account of the known velocity differences between the Balmer and metallic lines in the spectra of RR Lyrae stars. These differences are small compared with the desired velocity precision of ~20 km/s, and can therefore be neglected; however, they will contribute to the overall standard error in the results. The basic cross-correlation procedure involves continuum subtraction, logarithmic rebinning, apodization, Fourier filtering, and cross-correlation of the Fourier transforms (so as to reduce the convolution operation to a simple product). The early slit spectra were cross-correlated using SDRSYS software, while the 1982 and 1983 fibre data were cross-correlated by means of the XCORR routine in SPICA (a program with idiosyncrasies that were not fully understood, so that some care was needed in its use to obtain reliable velocities). All these results are given in the present chapter. The 1984 spectra are currently being cross-correlated using the DUSDERS software package.

5.3 Observations

The observations secured in the present work are summarized in Table 5.1. Some of the more depressing meteorological aspects of the programme have been recounted elsewhere (Watson, 1983); we merely remark here that the nights shown in the table were the only ones out of a total allocation of 23 nights on the AAT when observing was possible. The observations made in 1982, using the original FOCAP system, suffered particularly from poor working conditions with short and unpredictable clear spells, because the high effective attenuation of the fibres meant that normal integration times (~ 30 minutes) were totally inadequate to produce acceptable signal-to-noise ratios. This is reflected in the high rejection rate of the spectra (see later), only 35 percent of the stars attempted being included in the results presented here. By comparison, the corresponding figure for the 1983 data, obtained in similar conditions, is 91 percent. A naive estimate of the gain in efficiency produced by using fibres can be made by noting that on the most recent night for which the data are fully reduced (1983 Jun 7), a total of 28 measurable RR Lyrae spectra were obtained in two hours of integration (with, in addition, simultaneous observation of a standard-velocity object). Neglecting setting time, these two hours would have produced no more than four conventionally-observed spectra of similar RR Lyraes, so that the gain in efficiency is at least a factor of seven.

The contemporaneous photographic photometry referred to in Table 5.1 was carried out on the Australian National University (ANU) 1-metre telescope at Siding Spring with the aim of determining the phases of the stars when

Table 5.1 Journal of observations

UT Date	JD at 12h UT 2440000	Mode	IPCS format(a)	Stars observed	Velocities measured
1979 Jun 25	4050	slit	2040 x 12	14	18 (b)
26	4051	slit	1997 x 8	5	8 (b)
1980 Jul 20	4441	slit	2040 x 12	4	5
1982 Jun 14	5135	fibres (c)	2044 x 100	5	5
15	5136	fibres (c)	2044 x 100	11	11
1983 Jun 6	5492	fibres (d)	2044 x 232	17	26
7	5493	fibres (d)	2044 x 232	22	31
1984 Jun 1	5853	fibres (e)	2044 x 232	33 (f)	- (g)
2	5854	fibres (d)	2044 x 232	22 (f)	- (g)
3	5855	fibres (d)	2044 x 232	26 (f)	- (g)
4	5856	slit	2044 x 12	12	- (g)

Notes:

(a) Wavelength channels x spectrum increments.
(b) Supported by contemporaneous photographic photometry.
(c) 20 available fibre channels; 12 arcmin field.
(d) 46 available fibre channels; 12 arcmin field.
(e) 46 available fibre channels; 40 arcmin field.
(f) Time-resolved observations.
(g) Final reductions still in progress.

their spectra were obtained. A series of 12 B plates of Baade's window was taken over four nights in July 1979, and measurements of these with an iris photometer produced reliable phases for many of the stars observed that year. (Additional data points were provided by photographs taken with the AAT Cassegrain TV system immediately before the spectra were obtained.) As a result of this photometry, one of the stars (no. 27) was confirmed to be a short-period Population II Cepheid rather than an RR Lyrae star (Watson, 1980). The photometric phases obtained for the stars were not sufficiently accurate to be applied to more than the current year's observations, and an attempt to carry out similar photometry during 1980 was stopped by bad weather. One of the useful aspects of the photometry, which was less trivial than might be imagined, was that it did provide unequivocal confirmation of the correct identification of the Baade's window RR Lyraes. Almost every investigator who has worked in this field has remarked on the inadequacy of Gaposchkin's (1956) finding charts, given the extraordinarily crowded nature of the region, and locating the stars is, indeed, far from easy. This situation has recently been improved with the publication of new finding charts by Blanco (1984). (This paper also gives new photometric ephemerides, which we intend to use in the final analysis of our spectroscopic results.) No difficulties were experienced with the identification of the variables near NGC 6304 from the charts given by Hartwick, Barlow and Hesser (1981), and the Palomar-Groningen stars (Plaut, 1966, 1971) were bright enough to be immediately identifiable, given the AAT's setting accuracy.

The selection of the Baade field variables to be observed was, in the pre-fibre stage of the programme, based solely on apparent magnitude

(brightest first) so as to maximize the initial data collection rate. When the FOCAP system became available, the selection was determined by the stars' distribution on the sky and, in fact, three 12 arcmin square fields were chosen, which maximized the number observable with fibres. For the region around NGC 6304, a single 12 arcmin square field observed in 1982 was replaced with one of 40 arcmin diameter for the 1984 run. Since the RR Lyrae number density is here much less than in Baade's window, other types of variable were included among the FOCAP target objects, and the 1984 list included 10 suspected long-period variables, four variables of unknown type, and four anonymous objects, as well as 15 RR Lyraes and the globular cluster itself. Stars in the Plaut fields were always observed singly, either when conditions were too poor to observe the fainter variables in the other fields, or when those fields were passing through the notorious "flop zone" that resulted from a mechanical instability in the IPCS image-tube. The Plaut field stars were selected to have mean photographic magnitudes brighter than 16, and to have periods (in the range 0.45 to 0.65 days) and photographic amplitudes (in the range 0.6 to 2.0 magnitudes) that would characterize them as a-type RR Lyraes. On the last night of our 1984 run, we elected to dispense with the FOCAP system and use direct slit spectroscopy to observe RR Lyraes that were near the edges of the main fields, where the number density was too low to carry out multi-object spectroscopy. This was intended to improve our overall coverage of the RR Lyrae population.

Standard velocity stars were selected from the catalogue of fundamental data for southern stars (FDS) compiled at the Radcliffe Observatory (Evans, Menzies and Stoy, 1957, 1959; Evans et al., 1964). They are SAO 208819

(FDS 211), SAO 227680 (FDS 443), SAO 229216 (FDS 453), SAO 229335 (FDS 458) and SAO 210640 (FDS 757); all are fainter than V = 8.0 and lie within about 20 degrees of the galactic centre fields. As described in the previous section, use was made in 1984 of much brighter standard stars; these were τ Cen (BS 4802) and θ Sco (BS 6553). Most of the selected standard stars had A or F type spectra so that they would be suitable for use as cross-correlation templates for the RR Lyraes, and frequent observations of standards were made during each run as a check on overall stability. The resulting velocities show satisfactory interagreement, and seldom have standard deviations exceeding 5 km/s.

During the fibre-optics runs, the globular clusters NGC 6304, 6522 and 6528 were included in the target fields, and fibres were aligned on them so that they could be observed concurrently with the RR Lyraes. The intention was to use them as velocity standards to provide a check on the calibration of the spectra over the frame, an arrangement that leaves a little to be desired, since the observation will not yield an integrated velocity. The spectra of N6304 and N6528 were of comparable intensity to those of the programme stars. Four measurements (1983) of the velocities of N6522 and N6528 had a standard deviation for each cluster of 30 km/s, and gave mean values of -35 ± 15 and +172 ± 15 km/s respectively. A single measurement of the velocity of N6304 in 1982 gave -57 km/s. The most reliable recent compilation of globular cluster velocities is that given by Hesser, Shawl and Meyer (1986), and the velocities quoted by these authors are -11 ± 6 (N6522), +160 ± 6 (N6528) and -102 ± 15 km/s (N6304). Our values are clearly in reasonable agreement with these, given the somewhat unsatisfactory nature of the measurement technique.

In Table 5.2, we present the results of the observations so far as they are reduced. Velocities for 66 stars are given, 23 of which have multiple measurements. (The 1984 observations are expected to add a further 56 variables to the list, and provide additional velocities for 32 stars that appear already.) All the results are corrected for the Earth's radial velocity. For those observations with photometrically-determined phases, the estimated centre-of-mass velocities were arrived at using a pulsation correction based on the assumptions that the velocity and light curves are exactly in phase (mirror-imaged), and that their amplitudes are related by $\Delta v = \Delta m_{pg} \times 64$ km/s (Rodgers, 1960; Allen, 1973). A "standard" light-curve (Strohmeier, 1972) was adopted for the four Palomar-Groningen stars for which a pulsation correction (derived from Plaut, 1971) was attempted. One of the attractive possibilities of multi-object observations of RR Lyrae stars is that of obtaining series of time-resolved spectra over a substantial part of the pulsation cycles of the stars, thus allowing direct measurements of centre-of-mass velocities and velocity amplitudes. Of course, for the fainter stars, the data can simply be summed to improve signal-to-noise ratios, and yield reliable average velocities. Time-resolved spectroscopy was the main aim during the first three nights of our 1984 observing run, and data were obtained in two 12 arcmin fields in Baade's window, and the 40 arcmin field around N6304. For a few of the brighter RR Lyraes observed earlier with fibres, it was possible to estimate roughly the phase of each observation by combining the multiple velocity measurements with a velocity amplitude inferred from the known light amplitude. The centre-of-mass velocities thus determined are given in Table 5.2; they are relatively uncertain, but do illustrate the potential of time-resolved spectroscopy.

Table 5.2 Spectroscopy of RR Lyrae stars

Star	m_{pg}	Period (days)	Type	Epoch of spectrum JD 2440000	Dwell (sec)	Measured helioc. velocity (km/s)	Phase	Centre of mass velocity (km/s)	
				Baade's window (NGC 6522 field) (a)					
2	17.86	0.63862?	a	5492.015	6000	+17			(i)
12	17.48	0.47863		5136.285	3600	+39			(i)
13	17.51	0.52956		5136.285	3600	-17			(i)
16	17.43	0.26902	c	5134.992	7200	+42			(i)
				5492.015	6000	+140			
17	17.01	0.59084	a	4049.975	1200	+88	0.887	+69	(d,g)
				4049.994	1200	+44	0.919	+42	(d,g)
				5492.015	6000	+121			
19	17.54	?		5134.992	7200	+6			(i)
				5491.988	3000	+8			
				5492.043	3000	-27			
21	17.28	0.36900?	c	5134.992	7200	+4			(i)
				5491.988	3000	+75			
				5492.043	3000	+56			
22	16.98	0.42950	a	4049.928	1200	-84	0.152	-64	(d)
				4049.946	1200	-66	0.192	-50	(d)
				5491.988	3000	+27			
				5492.043	3000	+111			
26	17.24	0.77048	a	4051.031	1600	+201	0.913	+200	(d,g)
				4051.050	800	+235	0.937	+252	(d,g)
27	16.52	1.74797	cph	4051.132	1200	+62	0.062	+88	(d,e)
				5492.957	1800	-72	0.01)		(h)
				5492.984	1800	-54	0.03)	-30:	(h)
				5493.027	3600	-75	0.05)		(h)
34	17.35	0.42414	c	4441.182	1000	-49			
				4441.195	721	-74			
35	17.54	0.48284?	c	5492.999	7200	+9			
37	17.86	0.28682	c	5492.999	7200	-40			
43	17.36	?		5492.999	7200	-38			(i)
44	17.70	0.28870	c	5492.999	7200	-4			
45	17.09	0.44023		5492.999	7200	+45			
46	17.00	0.42767	a	4050.212	1600	+240	0.267	+217	(d)
				4050.231	1200	+258	0.311	+230	(d)
				5136.285	3600	-61			(i)
				5492.999	7200	-24			
49	17.62	0.57722	a	4050.263	1600	-56	0.054	-17	(d)
50	17.20	0.45423		5492.999	7200	+95			

Table 5.2 (continued)

Star	m_{pg}	Period (days)	Type	Epoch of spectrum JD 2440000	Dwell (sec)	Measured helioc. velocity (km/s)	Phase	Centre of mass velocity (km/s)	
51	17.38	0.45871		5492.970	3600	+19			
				5493.027	3600	+29			
52	17.77	0.32189?	c	5492.015	2400	+93			(i)
58	17.86	?	c?	5492.015	6000	+56			
59	17.50	0.52114		5491.988	3000	-4			(i)
61	16.57	uncertain	c?	4050.189	1600	-54	?	-39	(f)
				5491.974	1200	-52			
				5492.002	1800	-37			
				5492.043	3000	+33			
77	17.94	-		5134.992	7200	+22			(i)
				5492.015	6000	+95			
82	17.12	0.55452	a	4050.045	1600	+50	0.909	+43	(d,g)
83	17.51	0.23096	c	5492.999	7200	-24			(i)
84	17.47	0.35850?	c	5136.285	3600	-128			(i)
91	17.69	0.66693		5492.015	6000	+253			(i)
93	17.32	0.49710		5491.988	3000	+241			
				5492.043	3000	+139			
106	17.03	0.48968		5492.999	7200	-31			
113	17.26	0.57148		5492.970	3600	-47			
				5493.027	3600	-93			
118	17.10	0.55722		5136.285	3600	-206			(i)
122	17.18	0.49506	a	4050.949	1200	+82	0.125	+115	(d)
125	15.85	0.48546	c	4049.892	1200	+72	0.920	+105	(d)
127	17.62	0.29190	c	5492.015	6000	+156			
133	17.73	0.32491?		5492.970	3600	-28			
				5493.027	3600	-65			
144	17.36	0.55032	a	4050.980	1600	-85	0.238	-89	(d)
				4051.005	1600	-19	0.284	-28	(d)
155	17.29	0.59476		5492.999	7200	-93			
160	17.70	0.49761	c	5492.970	3600	+11			
				5493.027	3600	+4			
161	17.53	0.31004	c	5492.999	7200	+3			
162	17.78	0.32069	c	5492.999	7200	+48			(i)
164	17.41	0.27929?	c	5136.285	3600	-37			(i)
170	17.93	0.56385		5492.999	7200	+20			(i)
194	17.30	0.50710	a	4050.130	1600	+8	0.882	-11	(d,g)
				4050.151	1600	+12	0.923	+27	(d,g)
				5491.974	1200	+36	0.94)		(h)
				5492.002	1800	-9	0.00)	+35	(h)
				5492.043	3000	+28	0.08)		(h)

Table 5.2 (continued)

Star	m_{pg}	Period (days)	Type	Epoch of spectrum JD 2440000	Dwell (sec)	Measured helioc. velocity (km/s)	Phase	Centre of mass velocity (km/s)	
203	17.85	0.46722		5136.285	3600	-16			(i)
216	17.10	0.33436	c	4050.019	1600	-97	0.953	-73	(d)
221	16.25	uncertain	c	4049.910	1200	+94	?	+113	(f)
222	17.47	0.26996	c	5492.999	7200	+9			
232	17.03	0.29872	c	5492.970	3600	-116			
				5493.027	3600	-178			
235	17.26	-		5134.992	7200	-29			(i)
				5492.015	6000	+30			
241	17.52	0.36203		5491.988	3000	+201			
				5492.043	3000	+204			
247	18.00	0.23836	c	5492.999	7200	-244			(i)
258	17.15	uncertain	c?	4051.165	1600	-41	?	-56	(f)
				4051.189	600	-84	?	-99	(f)
				NGC 6304 field (b)					
5	17.49	0.21448		5135.888	6000	+9			(i)
8	17.61	0.60794		5135.888	6000	-12			(i)
67	17.23	0.46675		5135.888	6000	-55			(i)
72	18.70	?	LPV	5135.888	6000	-151			(i,j)
				Palomar-Groningen fields (c)					
1-32	14.78	0.51307	a	5493.097	900	-101	0.00	)	(h)
				5493.139	900	-77	0.08	) -50	(h)
				5493.159	900	-67	0.12	)	(h)
3-37	14.08	0.52444	a	4441.136	1000	-260			
3-235	14.18	0.49225	a	4441.164	1000	-113			
3-271	14.09	0.62675	a	4441.225	717	-39			
3-723	13.54	0.58174	a	4050.299	600	+13	0.555	-11	
3-1004	14.40	0.52119	a	4050.312	1000	-19	0.059	+1	
3-1015	14.49	0.52261	a	4050.330	800	+1	0.748	-32	
3-1450	14.40	0.47796	a	4050.287	1200	-106	0.726	-158	

(Notes to table appear on following page)

Notes to Table 5.2

(a) Star numbers and magnitudes from Gaposchkin (1955). Periods and types from Plaut (1973) unless otherwise indicated.

(b) Star numbers, B magnitudes, periods and types from Hartwick, Barlow Hesser (1981).

(c) Star numbers, magnitudes and periods from Plaut (1966,1971). Phases not otherwise accounted for derived from Plaut (1971), but uncertain because of large time interval.

(d) Type, and phase at spectrum determined by photographic photometry (present work).

(e) Period from present work (Watson, 1980).

(f) Plaut's (1973) period inconsistent with photographic photometry, and no alternative period found. Pulsation correction based on AAT Cass TV photograph - uncertain.

(g) Spectrum obtained on rising branch - pulsation correction uncertain.

(h) Phase estimated from velocities.

(i) Spectrum has fewer than 10 counts/channel (mean) above sky.

(j) Balmer lines in emission. Emission-line velocity given (standard error = 7 km/s).

A measure of the external error in the velocities given in Table 5.2 can be obtained from sets of independent values for the same stars. First, we note that there are three stars where the discrepancies between sets of values are significantly greater than the 100 km/s or so maximum that might be expected to occur because of pulsation; they are stars 22, 27 and 46, all in Baade's window. Star 46 shows the most serious discrepancies (although the 1982 and 1983 velocities are in reasonable agreement), and this star is excluded from the subsequent discussion of errors. For star 27, if the recent value for the centre-of-mass velocity is accepted, then it is almost certainly a member of NGC 6522 (compare Watson, 1980). No explanation for these discrepancies is, at present, forthcoming (although some suspicion might fall on XCORR); stars 22 (see later remarks) and 46 were both included in the 1984 observations, and the results are awaited with interest. It should be noted that the discrepancies do not appear to have been caused by inaccurate positioning of fibres, resulting in companion stars being observed; however, there are three stars (Baade's field nos. 35, 84 and 106) which do have equally-bright companions within 2 arcsec, and their velocities should therefore be treated with some caution.

For those stars with photometrically-determined pulsation corrections, the standard error in the centre-of-mass velocity is estimated from six pairs of velocities to be 21 km/s in a single observation, or 15 km/s in the mean of a pair. It is possible that a significant proportion of this error is contributed by the pulsation correction, particularly as five of the six stars used to determine it are a-type RR Lyraes with relatively large velocity amplitudes. Two of the Palomar-Groningen stars (3-723 and 3-1450) have been measured by Rodgers (1977) and differ from our values by -14 and

+11 km/s respectively, well within the error estimate. Of the 17 Baade's window RR Lyraes whose velocities have recently been measured by Gratton (1986), only three (nos. 22, 82 and 155) appear in Table 5.2 (although another three were observed by us in 1984). The velocities for stars 82 and 155 differ from our values by -2 and -25 km/s respectively, which are again consistent with the error estimate, given that our value for the latter star is not pulsation-corrected. However, it is very interesting to note that Gratton's value for star 22 is -233 km/s, adding yet another highly discrepant value to those noted above, and suggesting that there might be a more fundamental origin to the discrepancies than faulty cross-correlation.

The standard deviation (from the means) of 57 uncorrected velocity measurements for 22 stars is 36 km/s. More than half these stars appear to be c-types, so that an estimate of ~30 km/s for the contribution due to the absence of phase correction is probably appropriate, and this again leaves an intrinsic measurement uncertainty on the order of 20 km/s for a single observation. If the eight velocity values for stars 22 and 27 mentioned above are omitted, the overall standard deviation falls to 27 km/s, which is consistent with a 20 km/s measurement error combined with a lower (~20 km/s) pulsation uncertainty than before, both omitted stars being large-amplitude objects.

The data are insufficient to investigate the expected variation of standard error with signal-to-noise in the spectrum, although it may be noted that the omission of all spectra with mean intensities lower than 10 counts per wavelength channel above the sky produces no significant change in the

above results. (Spectra with mean intensities lower than this value are flagged in Table 5.2.) The cross-correlation technique is able to produce reliable velocities from absorption spectra with very small numbers of counts in the continuum. Unfortunately, the methods used to obtain the velocities presented in Table 5.2 do not give any formal indication of the significance of the results and, at some level of faintness, the effect of noise will dominate and the results will become meaningless. For typically strong-lined RR Lyrae spectra, it appears that this does not begin to occur until signal-to-noise ratios as low as ~ 2 are reached. A somewhat arbitrary "reliability test" was devised for faint spectra with mean counts/channel above sky of 5 or less: the spectra were cross-correlated against several templates whose spectral types encompassed the range expected for RR Lyraes, and were only accepted if the solutions agreed within the standard error of 20 km/s, when a mean of the resulting velocities was adopted. All other spectra were rejected.

The signal-to-noise ratios of the spectra obtained in 1984 were very much higher than those previously obtained with fibres in the present programme. Figure 5.1 shows some examples of unsmoothed, wavelength-calibrated spectra of stars in the field of NGC 6304, obtained simultaneously using the 40 arcmin FOCAP system on 1984 June 1. They are the results of summing seven time-resolved exposures with a total integration time of 13,000 seconds. Figure 5.1(a) presents the spectrum of star 8 (Hartwick, Barlow and Hesser, 1981), which is an RR Lyrae with $\bar{B}$ = 17.61; it shows the broad Balmer lines and narrow K line characteristic of an A5 star. A very similar (but slightly later) spectrum is shown in Figure 5.1(b); this is the spectrum of star 70 ($\bar{B}$ = 15.19; ΔB = 1.01), which is listed by Hartwick, Barlow and

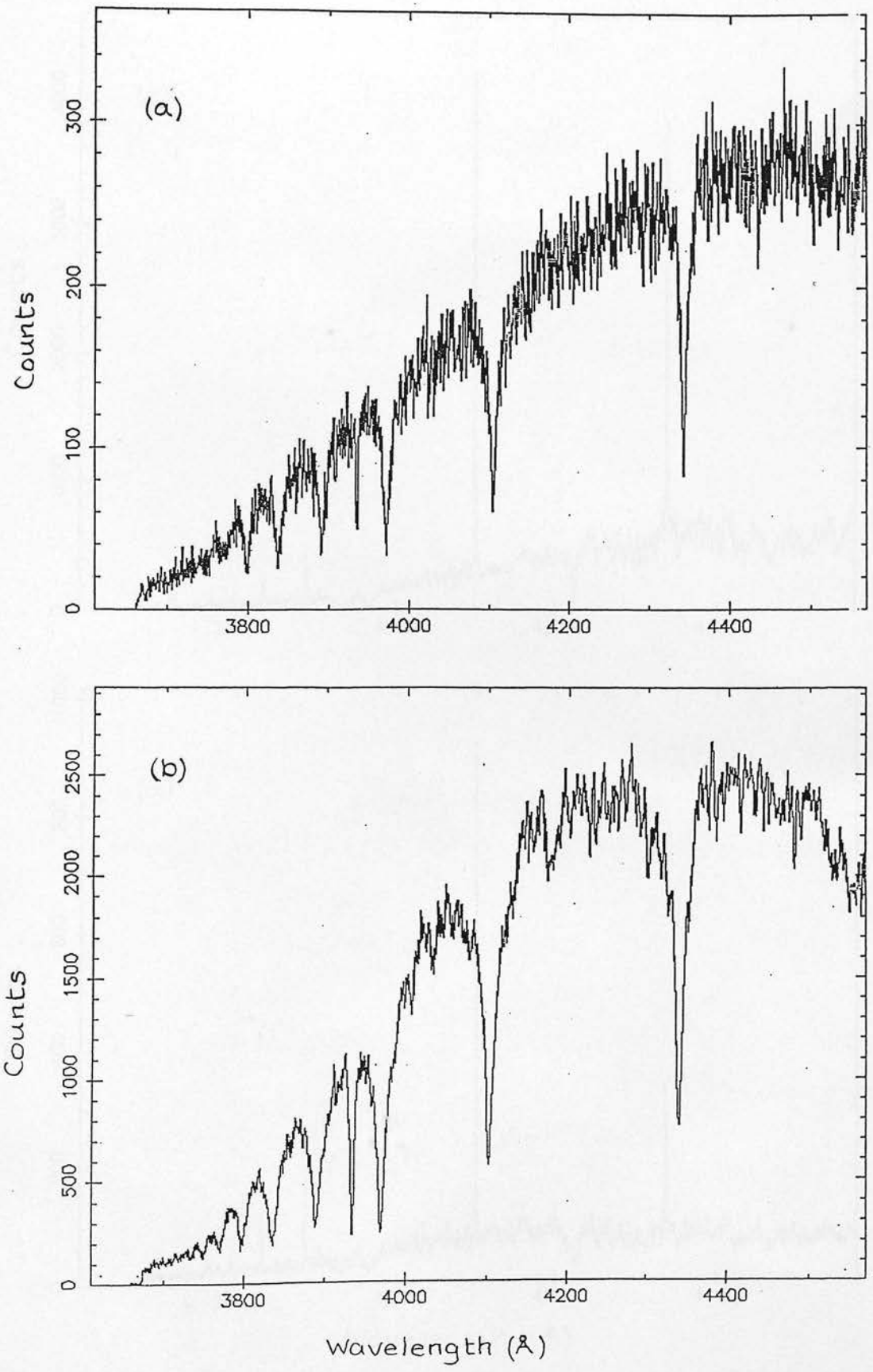

Figure 5.1(a),(b) Multi-fibre spectra of RR Lyrae stars in the field of NGC 6304 (see text).

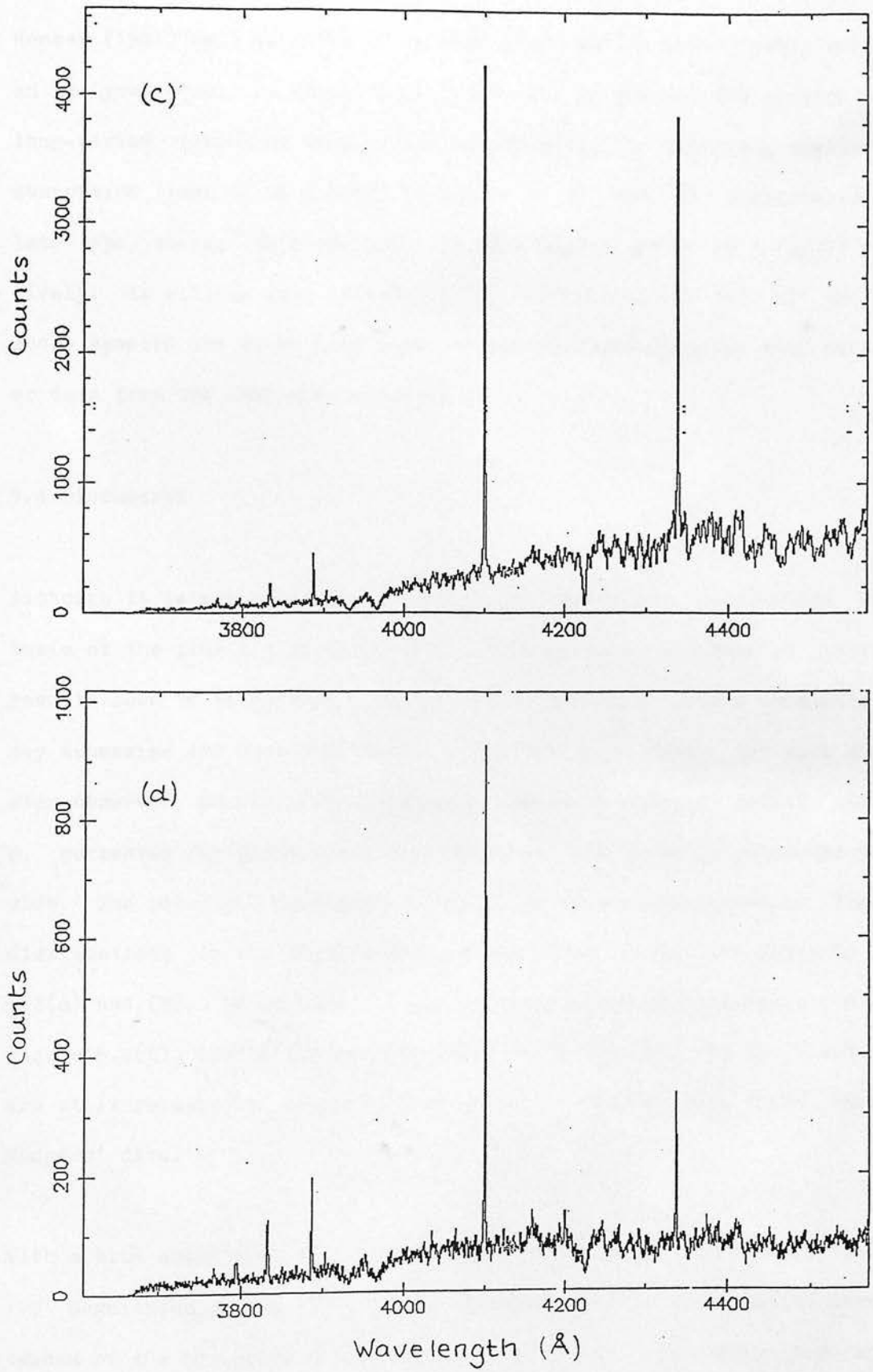

Figure 5.1(c),(d) Multi-fibre spectra of long-period variables in the field of NGC 6304 (see text).

Hesser (1981) as a variable of unknown type, but is here clearly seen to be an RR Lyrae star. In Figure 5.1(c) and (d), we present the spectra of two long-period variables showing the Balmer series in emission, together with absorption lines of Ca I (4227 Å) and Ca II (H and K) characteristic of late-type stars; they are nos. 72 ($\bar{B}$ = 18.70) and 91 ($\bar{B}$ = 19.00) respectively. As will be seen from Table 5.2, velocities for two of the stars whose spectra are given here (nos. 8 and 72) were obtained with much poorer data from the 1982 observing run.

5.4 Discussion

Although it is not possible to arrive at definitive conclusions on the basis of the provisional velocities presented here, a number of interesting results seem to be emerging, which justify some preliminary comments. We may summarize the data from Table 5.2 in histogram form: for each RR Lyrae star observed, we calculate a simple, unweighted average radial velocity, ρ, corrected for phase where available, and bin these in intervals 50 km/s wide. The resultant histograms, displaying the radial velocity frequency distributions in the Baade field and the Plaut fields, are shown in Figure 5.2(a) and (b). We include the set of stars observed by Rodgers (1977) in Figure 5.2(b), and it can be seen that, while our data for the Plaut fields are still relatively sparse, they appear to follow the trend shown by Rodgers' data.

With a blue absorption of 2.0 magnitudes in the Baade field (Arp, 1965) and 1.0 magnitudes in the Plaut fields (Rodgers, 1977), the relative mean distances of the RR Lyraes belonging to these fields (in Table 5.2 and in

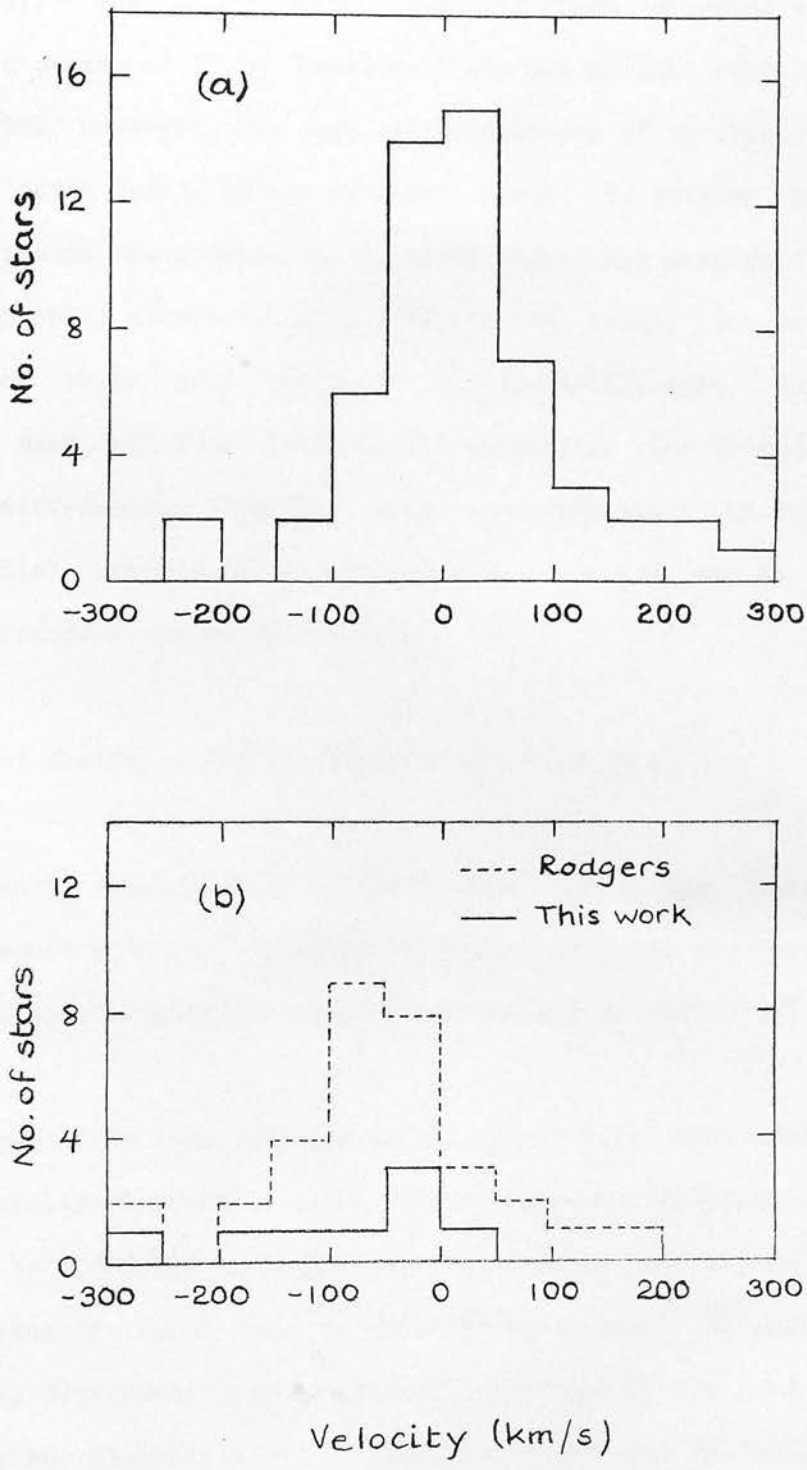

Figure 5.2 Distribution of velocities presented in Table 5.2. (a) RR Lyraes in Baade's window; (b) RR Lyraes in the Palomar-Groningen fields, with additional velocities measured by Rodgers (1977).

Rodgers, 1977) are in the ratio ~ 1.0:0.7. Thus, adopting a distance to the galactic centre of 10 kpc (compare Clube and Watson, 1978, 1979; Clube and Dawe, 1980, however), the mean radial distance of the Plaut field stars from the galactic centre is approximately 3 kpc. It follows that, although the Plaut fields are outside the galactic plane, any average line-of-sight velocity component attributable to rotation is likely to be relatively small, since their mean longitude is essentially zero. Any difference between the Baade and Plaut field radial velocities thus relates to peculiar-motion differences, together with any difference in their systemic galactic radial components, conventionally expected to be zero. The observed difference, based on Figure 5.2, is

$$\Delta\bar{\rho} = \bar{\rho}(\text{Plaut fields}) - \bar{\rho}(\text{Baade field}) = -67 \pm 20 \text{ km/s}, \qquad (5.1)$$

which is clearly significantly different from zero, and, remarkably, in broad agreement with the expanding inner halo inferred previously from the radial velocities of globular clusters (Clube and Watson 1979)*.

It would appear from this interesting and potentially far-reaching result that the radial velocities of the Palomar-Groningen field RR Lyrae stars, if gathered in sufficiently large numbers, could be used to investigate an assumed expanding inner halo in considerable detail. In particular, the nature of any dependence on galactocentric distance of the kind apparently displayed by the globular cluster velocities (Clube and Watson, 1979) would be extremely valuable data for our understanding of galactic dynamics. As we have seen in Section 1.3.2, the number densities of the RR Lyraes in these fields range from 1 to 20 deg^{-2}, and this, coupled with their

---

* If Rodgers' velocities are neglected on the grounds of possible zero-point differences, there remains a significant deviation at the 5 per cent level (Student's t-test) between $\bar{\rho}$(Plaut fields) and $\bar{\rho}$(Baade field).

brighter magnitudes resulting from lower absorption, makes them ideal targets for FLAIR. Indeed, FLAIR was originally conceived with these stars partly in mind. The existence of recent photographic photometry (Le Poole, private communication), together with the possibility of contemporaneous multi-object photometry with FLAIR itself (Chapter 7) means that reasonably accurate pulsation-corrected velocities could be obtained with the modest spectral resolution demanded by the telescope aperture (Section 3.4). It is intended that test observations for this programme will be carried out during the coming (1987) observing season.

Returning to Figure 5.2, the mean heliocentric velocity of the Baade's window stars given in Figure 5.2(a) is

$$\bar{\rho}(\text{Baade field})_{\text{Sun}} = +15 \pm 13 \text{ km/s}; \qquad (5.2)$$

and, correcting for the standard solar motion (eg, Mihalas and Binney, 1981, Chap. 6), this becomes

$$\bar{\rho}(\text{Baade field})_{\text{LSR}} = +25 \pm 13 \text{ km/s} \qquad (5.3)$$

relative to the local standard of rest. The line-of-sight velocity dispersion of the data given in Figure 5.2(a) is (±) 95 km/s; this clearly includes any velocity errors due to ignorance of phases, as well as instrumental errors, and, if we provisionally set this uncertainty at ± 30 km/s (see previous section), a cosmic velocity dispersion of

$$\sigma(\text{Baade field}) = 90 \text{ km/s} \qquad (5.4)$$

is implied. Results 5.3 and 5.4 may be compared with those obtained from the velocities of 17 Baade's window RR Lyraes by Gratton (1986); they are $\bar{\rho}_{LSR}$= +11 ± 34 km/s, a value clearly in broad agreement with ours, and σ = 133 ± 25 km/s, which is more in accordance with that found for other components of the bulge (Gratton, 1986, and references therein) than our rather low value.

It would be premature to interpret our value of $\bar{\rho}_{LSR}$ (Result 5.3) as a measurement of Π_o. In Figure 5.3, we plot a number-magnitude diagram for the RR Lyraes in Baade's window, showing also the distribution of those stars in the field whose velocities appear in Table 5.2, and it is apparent that we have so far sampled predominantly the brighter end of the distribution, thereby preferentially selecting too many stars between us and the galactic centre. Furthermore, the data currently available in the NGC 6304 field are too sparse to make a relatively model-free separation of rotation and radial motion. Nevertheless, our value of $\bar{\rho}_{LSR}$ is tantalizingly in accordance with the discoveries mentioned at the outset; it remains to be seen whether the addition of results from the data obtained in 1984 will consolidate or dispel this value.

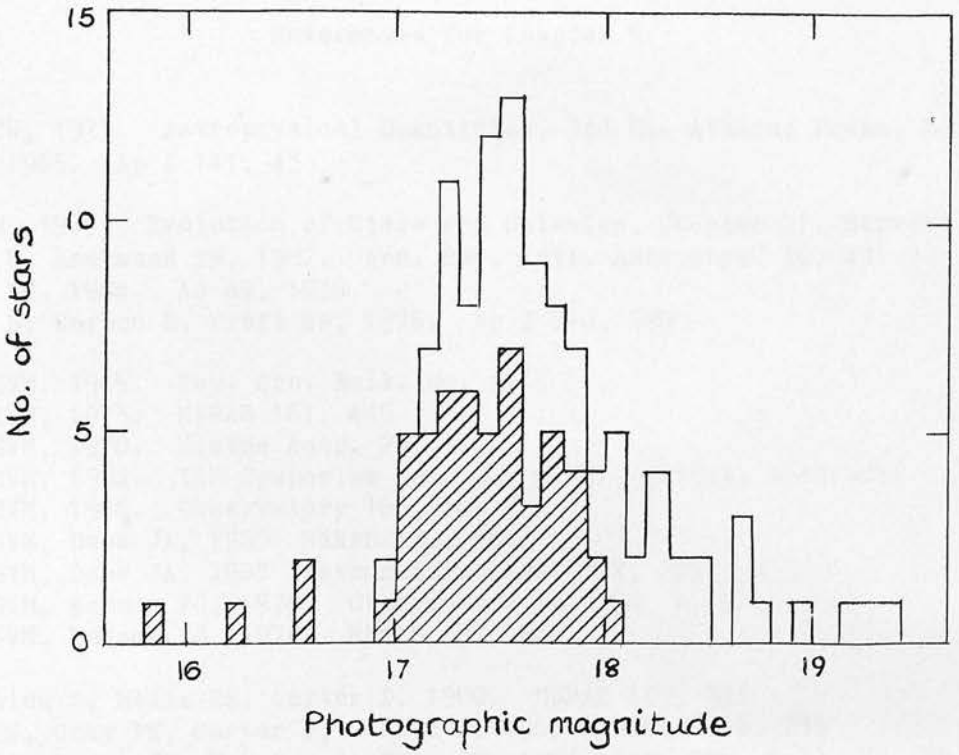

Figure 5.3 Magnitude distribution of RR Lyrae stars in Baade's window (data from Gaposchkin, 1955). The hatched area shows the distribution of stars whose velocities are given in the present work (Table 5.2).

References for Chapter 5

Allen CW, 1973. Astrophysical Quantities, 3rd Ed. Athlone Press, London
Arp H, 1965. Ap J 141, 43

Baade W, 1963. Evolution of Stars and Galaxies, Chapter 21, Harvard
Balick B, Heckmann TM, 1982. Ann. Rev. Astr. Astrophys. 20, 431
Blanco BM, 1984. AJ 89, 1836
Butler D, Carbon D, Kraft RP, 1976. Ap J 210, 120

Clube SVM, 1965. Roy. Obs. Bull. No. 95
Clube SVM, 1973. MNRAS 161, 445
Clube SVM, 1978. Vistas Astr. 22, 77
Clube SVM, 1982. IAU Symposium No. 100, p.161, Reidel, Dordrecht
Clube SVM, 1986. Observatory 106, 166
Clube SVM, Dawe JA, 1980 MNRAS 190, 591
Clube SVM, Dawe JA, 1983 Astron.Astrophys. 122, 255
Clube SVM, Watson FG, 1978. Observatory 98, 124
Clube SVM, Watson FG, 1979. MNRAS 187, 863

Efstathiou G, Ellis RS, Carter D, 1980. MNRAS 193, 931
Ellis RS, Gray PM, Carter D, Godwin J, 1983. MNRAS 206, 285
Evans DS, Laing JD, Menzies A, Stoy RH, 1964. Roy. Obs. Bull. No. 85
Evans DS, Menzies A, Stoy RH, 1957. MNRAS 117, 534
Evans DS, Menzies A, Stoy RH, 1959. MNRAS 119, 638

Feast MW, Robertson BSC, Black C, 1980. MNRAS 190, 227
Frenk CS, White SDM, 1980. MNRAS 193, 295

Gaposchkin SI, 1955. Peremennye Zvezdy 10, 337
Gaposchkin SI, 1956. Peremennye Zvezdy 11, 268
Gatley I, Geballe TR, Wade R, 1987. In preparation.
Gratton RG, 1986. Monte Porzio Preprint No.8 (submitted to MNRAS)
Grillmair C, Pritchet C, van den Bergh S, 1986. AJ 91, 1328

Harris WE, 1986. AJ 91, 822
Hartwick FDA, Barlow DJ, Hesser JE, 1981. A J 86, 1044
Hartwick FDA, Hesser JE, Hill G, 1972. Ap J 174, 573
Hesser JE, Shawl SJ, Meyer JE, 1986. PASP 98, 403

Kerr FJ, 1962. MNRAS 123, 327

Lauer TR, Kormendy J, 1986. Ap J 303, L1

Mihalas D, Binney J, 1981. Galactic Astronomy, Freeman, San Fransisco

Oort JH, 1977. Ann.Rev.Astron.Asrophys. 15, 295
Oort JH, 1982. In The Galactic Center (ed.Riegler,Blandford)p.180,Caltech
Oort JH, Plaut L, 1975. Astr.Astrophys. 41, 71

Peterson BA, 1979. Cross-correlation rad.vel.meas.using SDRSYS (AAO)
Plaut L, 1966. B.A.N. Suppl. 1, 105
Plaut L, 1968. B.A.N. Suppl. 2, 293
Plaut L, 1971. Astr.Astrophys.Suppl. 4, 75
Plaut L, 1973. Astr.Astrophys. 26, 317
Preston GW, 1959. Ap J 130, 507

Rodgers AW, 1960. Observatory 80, 220
Rodgers AW, 1974. Ap J 191, 433
Rodgers AW, 1977. Ap J 212, 117

Strohmeier W, 1972. Variable Stars, p. 124, Pergamon, Oxford

Watson FG, 1980. Observatory 100, 39
Watson FG, 1983. In 1984 Yearbook of Astronomy, p.179, Sidgwick Jackson
Watson FG, Clube SVM, 1981. The kinematics of O,B stars (ROE int. rep.)
Watson FG, Murdin PG, Clube SVM, 1979. Spect'y of RR Lyrae stars ... (ROE)
Wollman ER, Geballe TR, Lacy JH, Townes CH, 1977. Ap J 218, L103

Appendix to Chapter 5

Sky subtraction by beamswitching

Consider a detection system with two spatial channels, denoted A and B. These may be areas defined on a spectrograph slit, or separate fibre feed inputs; they are assumed to have efficiencies E_A, E_B (here taken to include optical transmission, detector efficiency, and solid angle subtended on the sky) that may differ. They are also assumed to be sufficiently close together that there are no spatial variations in the sky background signal, S_S. Let the object signal be S_O.

Suppose, now, that the object is switched between the two apertures so that it spends exactly half its time in each. Then, for one half of the exposure, the total signals in channels A and B are

$$A_1 = E_A(S_{O1} + S_{S1}) \qquad (5A.1a)$$

and

$$B_1 = E_B S_{S1}, \qquad (5A.1b)$$

and for the other half of the exposure, they are

$$A_2 = E_A S_{S2} \qquad (5A.2a)$$

and

$$B_2 = E_B(S_{O2} + S_{S2}). \qquad (5A.2b)$$

The required signal, R, may now be obtained by forming the sum

$$R = A_1 + B_2 - (A_2 + B_1);$$

thus,

$$R = E_A(S_{O1} + S_{S1}) + E_B(S_{O2} + S_{S2}) - (E_A S_{S2} + E_B S_{S1}),$$

which can be rearranged as

$$R = E_A S_{O1} + E_B S_{O2} + (E_A - E_B)(S_{S1} - S_{S2}). \qquad (5A.3)$$

In perfectly stable sky conditions, we will have $S_{S1} = S_{S2}$, and for a perfectly uniform detection system, we will have $E_A = E_B$. Clearly, if either of these conditions applies, Equation 5A.3 becomes

$$R = E_A S_{O1} + E_B S_{O2}, \qquad (5A.4)$$

which is a function only of the object signal and the properties of the instrument, the sky signal having been eliminated.

CHAPTER 6

The FLAIR multi-object spectroscopy system

6.1 Fibre optics at the UK Schmidt telescope

The idea of developing a multi-fibre spectroscopy system for the 1.2-metre UK Schmidt telescope originated in a conversation between John Dawe (then Astronomer-in-charge of the telescope), Victor Clube and the writer during the June, 1982 RR Lyrae observing run at the AAT (see previous chapter). Dawe was quick to seize the potential of the suggestion, and within a few days, a Royal Observatory, Edinburgh (ROE) internal memorandum entitled "Proposal for a radical extension in the use of the UK Schmidt telescope" had been produced (Dawe and Watson, 1982). Shortly before the writer's transfer to the UKST in October, 1982, Dawe obtained a single ~50 m length of 50 μm core graded-index fibre from Amalgamated Wireless of Australia (AWA) and, with the input end mounted temporarily in a disused UKST plate-holder and the output end observed visually, managed (by the crudest means imagineable!) to acquire the star Vega low on the northern horizon. Thus began the development of fibre-coupled spectroscopy at the UKST.

Much of the early work was concerned with investigating the properties of

fibres with the help of Peter Gray (AAO). No major comparative study of different fibres (of the kind described in Section 2.2) was carried out, however, because the usual stumbling-block in selecting fibres for astronomical use (viz, FRD) was of much-reduced importance due to the low focal ratio of the telescope. During 1983, an experimental fibre plateholder was constructed for the UKST by Eric Coyte (whose mechanical skills were instrumental in the success of FLAIR), with the electronics for the rotation mechanism being made by Magnus Paterson. At this time, a straightforward Medusa-type positioning system for the fibres was envisaged (although the UKST's small plate-scale made this a very difficult proposition) and, while the idea of directly cementing the fibres to a positive copy plate had been discussed earlier, it was not until mid-1983 that the technique was given serious consideration (Dawe and Watson, 1984; Watson and Dawe 1984, 1985). Another proposal current in 1983 was that of using the spectrograph and CCD detector stages of the ROE Imaging Spectropolarimeter (ISP; McLean, 1983; McLean and Watson, 1983); this idea never came to fruition, although the ISP's ISIT acquisition TV camera did eventually find its way into the FLAIR prototype. 1983 also saw the formulation of some of the concepts on spectroscopy with multi-fibre systems presented in Section 1.5 of this thesis (Dawe and Watson, 1984), and various other considerations of a theoretical nature (Watson, 1984a; Watson and Dawe, 1985).

FLAIR (fibre-linked array-image reformatter) got its name early in 1984, and the first acquisition tests with cemented aperture plates were carried out at about the same time. As was expected, these were largely unsuccessful until the acquisition imageguide was procured, and test observations

with this device at the end of August, 1984, produced some remarkable fibre-coupled photographs of Jupiter and Saturn (Watson, 1984b). A significant milestone was passed on 1984 Oct 4/5, when five stars spread over the full 6.5 degrees-square field of the telescope were simultaneously acquired (visually) using 33 and 50 μm core fibre, thus demonstrating the viability of the entire positioning scheme. With assistance from a vacation student at the UKST, Colin Willcock, development work on the prototype 40-fibre feed bundle had been started earlier, and this continued (together with work on the acquisition system and spectrograph) into 1985. The ISIT TV camera system was the last externally-procured component of FLAIR to arrive (May, 1985) and, by early August, the entire spectroscopic system was ready to be tested with photographic detection.

The first observing run took place on the nights of 1985 Aug 11/12 and 12/13, and yielded five frames of spectra (on unhypersensitized 103a-F emulsion) of 37 stars ranging in magnitude from 7.2 to 12.5. The success of these observations led to further tests and, in Jan, 1986, to the first observing run specifically aimed at securing astronomical rather than instrumental data (for stars in the Chamaeleon dark cloud, as presented in Chapter 7). Further development of the system itself also continued and, in May, 1986, the University of Durham's cooled CCD camera (procured for use with FLAIR at the instigation of Tom Shanks (Durham)) arrived to replace the 35 mm camera body as the main detector. Problems with the implementation of the CCD meant that its commissioning (by Shanks, Paddy Oates (Durham) and the writer) was not properly started until Sept, 1986, but several successful observing runs since then have given a clear picture of the strengths and weaknesses of the FLAIR/CCD system, and have provided

some useful astronomical results. Again, some of these are reported in the next chapter.

At the time of writing (April, 1987), applications have just been invited by the UKST subcommittee of the Panel for the Allocation of Telescope Time (PATT) for the use of FLAIR by the general UK astronomical community. Despite its current limitations, FLAIR remains the only wide-field multi-object spectroscopy system operating anywhere in the world, and represents a new, effective and inexpensive way of exploiting simultaneously the extraordinarily wide field of the UKST and the sensitivity and linearity of modern 2-d electronic detectors. Thus, it is anticipated that FLAIR will now begin to make a real contribution to astronomy, and it is hoped that this will increase with the continuing development programme.

The remainder of this chapter is devoted to an account of the technical aspects of FLAIR. The system has been described several times (eg, Watson, 1986, 1987) and has been featured on national television in Australia ("Beyond 2000", October, 1986). The account given here is an updated version of the author's paper at the "Instrumentation in Astronomy VI" conference at Tucson in March, 1986 (Watson, 1986).

6.2 Design considerations

The general considerations for the design of fibre-coupled multi-object spectroscopy systems have been described at length in the second and third chapters of this thesis. Since FLAIR was there cited frequently as an example, it is, for the most part, only necessary to summarize the design

constraints here. They are:

(a) The focal surface is physically large (356 mm square plates are used); it is within the incoming beam, steeply curved (R=3.07 m) and there is very limited access (55 mm) behind it (Section 3.1.2; see also the cross-section given in Figure 6.1).

(b) The plate scale is very fine (Π=67 arcsec/mm), resulting in the need to use small (~50 μm diameter) fibres with correspondingly small positioning tolerances (Section 2.4; Figure 2.9(b)). (Fibres of this diameter have minimum bending radii of only a few mm, so that some of the constraints in (a) above are eased.)

(c) The telescope beam is fast (f/2.5), so that the axial positioning and angular alignment tolerances are small, and the fibre NA becomes an important consideration (Section 2.4; Figures 2.9(a), 2.10(a)). There is, however, no beam inclination (Section 3.1.2).

(d) There is substantial vignetting at the edges of the field (Figure 3.2). (In practice, there is little that can be done about this.)

(e) The field effects of thermal expansion and differential atmospheric refraction are are significant (Section 3.1.2; Figures 3.4, 3.5). The latter effect demands a small rotation capability (of order ten arcmin) in the structure supporting the fibres, because the routine elevation of the polar axis to compensate for refraction-induced field-rotation introduces an offset in position-angle at all telescope positions away from the meri-

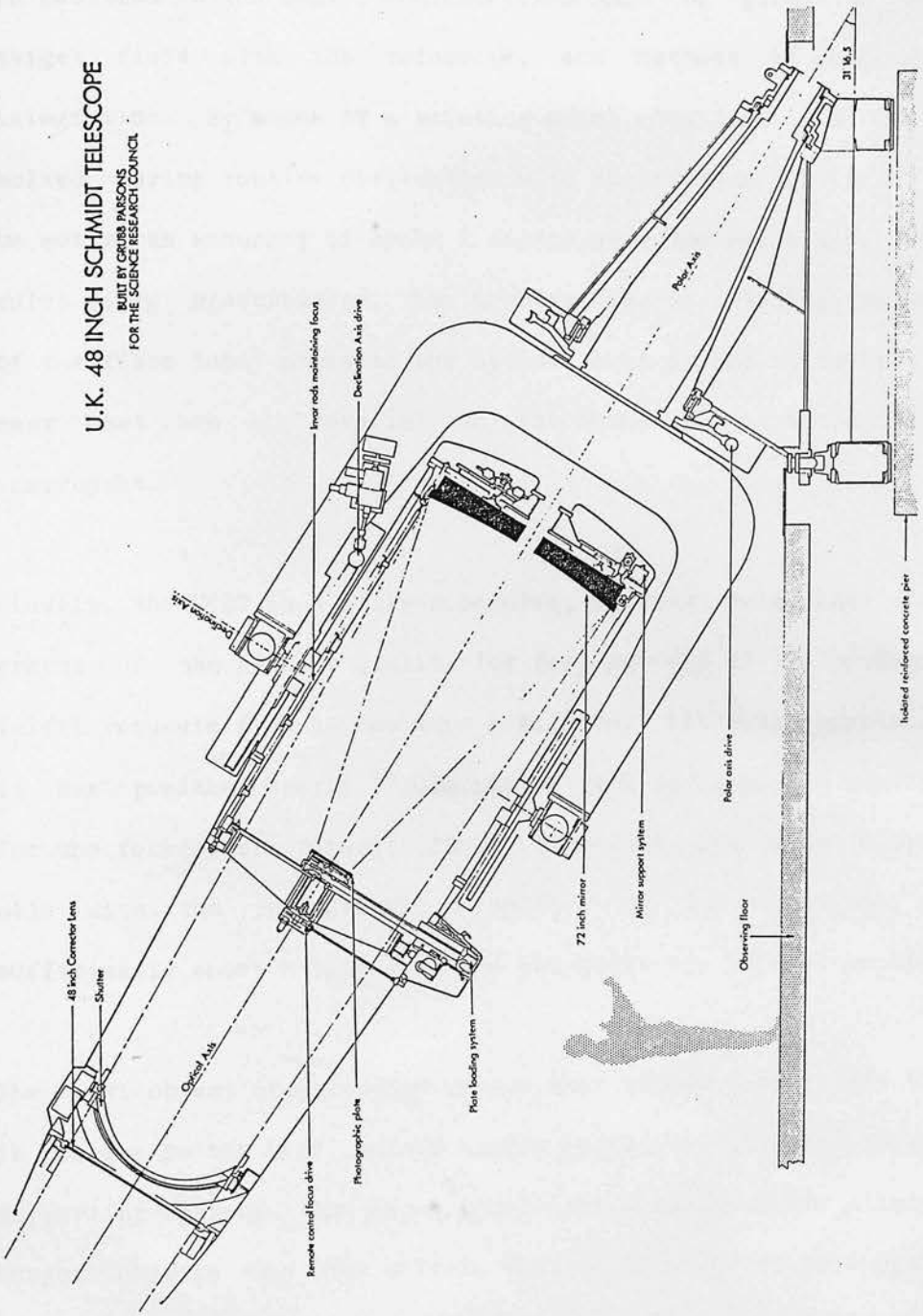

Figure 6.1 Cross-section of UK Schmidt telescope (Grubb-Parsons drawing).

dian (Watson, 1984a).

In addition to the above, consideration must be given to acquiring the target field with the telescope, and methods of guiding it during an integration. By means of a pointing model (Wallace and Tritton, 1979), solved during routine observation with an off-line PDP 11/24, the UKST can be set to an accuracy of about 6 arcsec over the whole sky. However, with multi-fibre spectroscopy, the problem lies in relating the exact position of the fibre input array to the optical axis of the telescope, a requirement that has no parallel in the normal photographic operation of the instrument.

Finally, the UKST is a fully-scheduled, working telescope, taking photographs of the highest quality for deep surveys of the southern sky and to fulfil requests from astronomers worldwide. Since its completion in 1973, it has produced nearly 12,000 plates, and is likely to continue this role for the foreseeable future; FLAIR, therefore, has to be fully interchangeable with the photographic operation of the telescope, preferably in sufficiently short a time that the two modes can be used on the same night.

The multi-object spectroscopy system that has evolved within this framework is unique to the UKST, and is highly integrated with the telescope and its supporting systems. The major problem of accurate fibre alignment with the target objects has been solved, for the first generation system at least, by making direct use of photographs taken with the telescope. Optical, rather than absolute mechanical methods are used, both for the alignment of the individual fibres relative to one another, and the alignment of the

resulting array of fibres with the target field in the sky. The UKST's separate autoguider can then be engaged to maintain this alignment. The fibres are supported in a rotateable plateholder that duplicates a standard UKST photographic plateholder in weight, external dimensions and location points, so that it can be loaded into the telescope using the normal plateholder elevator (Figure 6.1). With FLAIR on standby, it is possible to change between normal photography and multi-object spectroscopy in less than 40 minutes and, when more than one plateholder is fully commissioned, it will be possible to switch target fields in about the same time. This has been accomplished with an absolute minimum of modification to the telescope itself, so that the implementation of FLAIR has not resulted in any down-time.

Like most new instrumentation for astronomy, FLAIR was developed with one other major constraint in mind, namely cost. Because much of the development work on the system was experimental in nature, its cost had to be absorbed within the already tightly-streched budget of the UK Schmidt Telescope Unit (UKSTU), which itself competes for funds from the UK Science and Engineering Research Council (SERC). In fact, the FLAIR system as it was originally configured (with photographic detection) cost considerably less than £10,000 for materials and equipment, and a substantial fraction of that amount was due to two major capital items (the vibrationally-isolated table for the spectrograph, and the high-resolution imageguide for the acquisition system). The Durham University CCD camera was built with separate SERC funding. Without being unduly pious, it may be remarked that the UKSTU has always sought to produce astronomical data of the highest quality in the most cost-effective way, and it is appropriate that the Unit

does seem to have embarked on its new venture with at least one element of that tradition intact.

6.3 FLAIR - technical description

Fibre plateholder and positioning technique. As we have seen already, the method of positioning the fibres in alignment with the target objects is based on the inherently simple idea of cementing the fibres directly to the images on a positive copy of a UKST plate. The fibres are illuminated from what is normally the output end; since it is their illuminated cores that are aligned with the images on the plate, errors due to non-concentricity of the core, cladding, mounting ferrule, etc, (all of which would be present in a Medusa-type system) are eliminated. The required positioning accuracy of about 10 μm (Figure 2.9(b)) is then reasonably easy to achieve.

The positive is a vacuum contact copy of a telescope plate of the target field (which will usually exist already) made on 1 mm thick glass so that it can be deformed to match the spherical focal surface of the telescope. This is brought about in exactly the same way as with normal photographic plates, by clamping it onto a curved mandrel; in this case, however, the mandrel is cut away to a thin skeleton in order to allow the fibres to pass through. The mandrel causes some restriction of access to the field, but substantially complete coverage of a given area of sky can always be obtained in two observations if plates with different field centres are used.

The plateholder itself (Figure 6.2(a)) consists of an open square frame

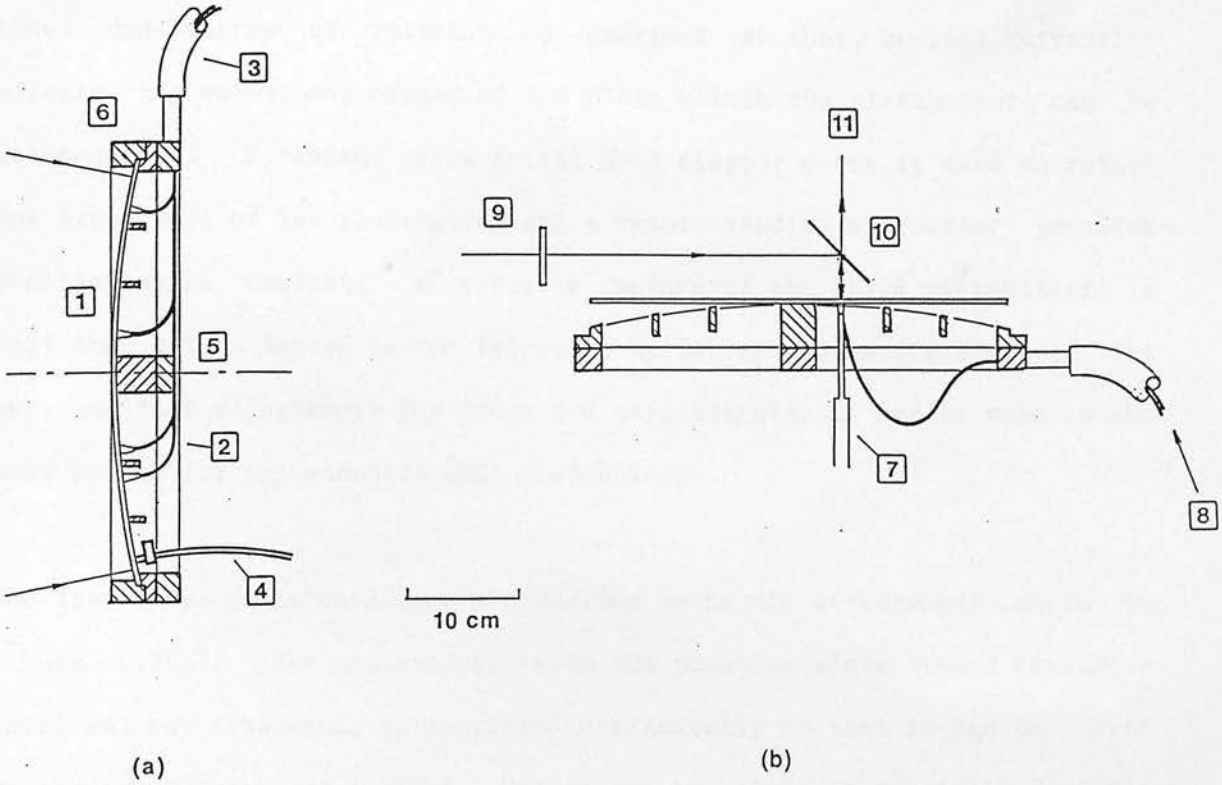

Figure 6.2 Sectional view of FLAIR plateholder (a) in use in the telescope, and (b) during setting-up. (1) Positive copy plate deformed by skeleton mandrel. (2) Fibres attached to plate. (3) Fibre cable. (4) Acquisition imageguide in adjustable socket. (5) Centre bearing. (6) Plate clamp. (7) Fibre chuck. (8) Fibre illumination. (9) UV lamp and shutter. (10) 45-deg beamsplitter. (11) Viewing microscope. (From Watson, 1986.)

with cross-struts supporting a central bearing, on which the mandrel/copy plate assembly rotates to permit the adjustment in position angle (1). About one degree of rotation is provided so that, besides refraction effects, any rotational offset of the plate within the plateholder can be accommodated. A tangent screw driven by a stepper motor is used to rotate the front part of the plateholder and a remote-reading micrometer provides position-angle readout. A valuable feature of the FLAIR plateholders is that they can be tested in the telescope by taking ordinary plates of the sky, so that adjustments for focus and perpendicularity can be made in the same way as for the standard UKST plateholders.

The fibres are positioned before observing using the arrangement shown in Figure 6.2(b). The plateholder, with the positive plate loaded (emulsion down) but not tensioned, is supported horizontally so that it can be moved freely in the horizontal plane. Underneath the plate, a specially-designed fibre-chuck with fine motions in (x,y) allows each fibre to be positioned in alignment with the target image, as viewed in the microscope above. The chuck can be withdrawn vertically to facilitate the insertion of the fibres. The fibres themselves have their input ends enclosed in ferrules (Figure 6.3), which (a) artificially increase the end diameter (to about 5 mm) for good adhesion to the plate, and (b) ensure that the fibre is exact-

---

(1) Only the prototype FLAIR plateholder (designated 14/5) has the centre bearing; in 14/6 and subsequent plateholders it is replaced with high-precision pins moving in short arcs at the four corners of the plateholder, to provide improved access to the field centre.

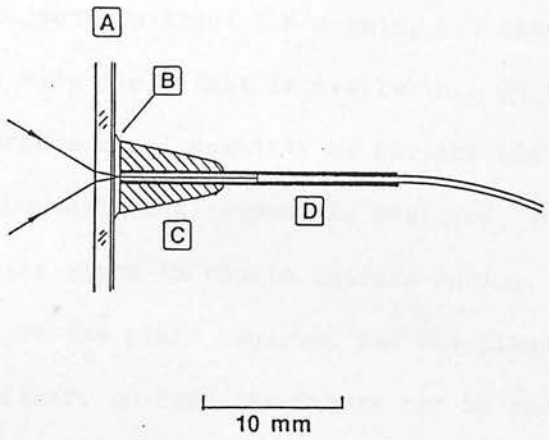

Figure 6.3 Fibre input. (A) 1 mm thick glass positive copy plate. (B) Cement interlayer bonding fibre ferrule to emulsion. (C) Plastic fillet. (D) Stainless-steel microtube with fibre (stripped of its protective jacket) epoxied in. (From Watson, 1986.)

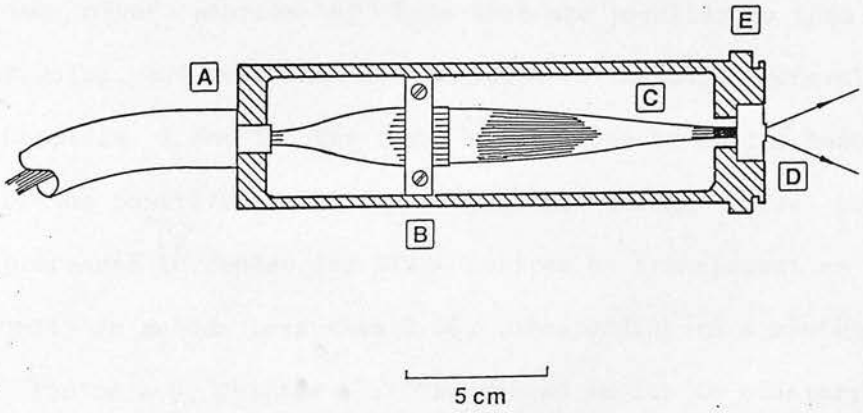

Figure 6.4 Sectional view of 40-fibre slit unit. (A) Cable restraint. (B) Fibre clamp. (C) Mode-strippers (blackened bare fibres). (D) Slit-block with fibres aligned on slit. (E) Camera-type bayonet mount. (From Watson, 1986.)

ly perpendicular to the plate. (The large ferrules limit the minimum separation of target objects to about 5.6 arcmin, but this is not usually a problem given the very wide field that is available.) On the polished end of each ferrule is placed a small quantity of Norland NOA 81 UV-cured optical cement and, when the desired alignment is achieved, this is hardened by irradiation through the plate to ensure uniform curing. The cement cures quickly and bonds well to the plate emulsion and the plastic ferrule, but not permanently to either, so that the fibres can be easily removed after use and the cement interlayer discarded, before recementing to the next copy plate. Repolishing is not necessary.

When the copy plate is in the telescope, the glass, emulsion and cement all form part of the optical train. Their D-line refractive indices are 1.516, 1.52 and 1.56 respectively (Eastman Kodak, 1973; Norland, 1983), tolerably well-matched to that of the fibre core (1.458), so that the principal Fresnel loss takes place at the first (air-glass) surface. There are, however, two other sources of loss that are peculiar to this method of fibre positioning, and were thus not included in the more general discussion in Chapters 2 and 3. The first arises because of the base chemical fog level of the positive plate, and occurs even though these plates are specially processed to render the image centres as transparent as possible. The fog density is seldom less than 0.06, coresponding to a minimum loss of 0.13 (see Footnote 5, Chapter 1). The second is due to scattering caused by occasional crystallization of the cement on curing. The cause of this phenomenon is not yet understood, and it may currently affect as many as one in four cemented joints. The loss is again estimated to be about 0.13, so the result of these two is a total "FLAIR loss", $\mathcal{F}$, that could be as

much as ~0.25. This will introduce an additional factor of $(1-\mathcal{F})$ in Equation 2.6.

Although the copy plate is an exact positive replica of the original, there are several effects that degrade the perfect matching of the images on it with the images formed in the telescope. Atmospheric refraction and thermal expansion have already been mentioned, and we have seen in Section 3.1.2 how the effects of the latter are reduced by the positive copy-plate technique. An occasional mismatch is caused by stellar proper motions (see Chapter 7); the risk of this can obviously be reduced by using recent plates to produce the copies. Perhaps the most important effect arises because the emulsion side of the copy plate has the opposite curvature in the telescope to that of the original. It is shown in the Appendix to the present chapter that the result of this is an apparent increase in the scale of the image formed in the telescope over that of the copy plate. The mismatch may amount to 55 μm at the corners of the plate - more than the core diameter of a fibre. However, the effect can be corrected when cementing by offsetting each fibre from the image centre by the appropriate amount, using a calibrated graticule in the microscope eyepiece.

It will be evident from the foregoing that the setting-up procedure in this first-generation FLAIR system is very labour-intensive (although, in practice, it is little different from the conventional astrometric measurement of a photographic plate). Because of this, a new fibre-positioning table has recently been built at the UKST, incorporating vastly improved mechanical arrangements, and TV viewing of the fibre and plate. It is expected that, in the hands of a skilled operator, this will bring the setting-up

time per fibre down from the current four minutes or so, to around 90 seconds.

Fibre feed. The prototype feed bundle (designated 39/40R) consists of 39 all-silica (DIC) fibres 10 m long, with 40 μm (2.7 arcsec) core diameter and a numerical aperture of 0.24 (2). The fibres are of the AWA-SD type, frequently cited as an example in Chapter 2, so that many of their properties are to be found there (including spectral transmission (Figure 2.3(a)), refractive-index profile (Figure 2.4(b)) and focal-ratio degradation (Figure 2.6(b))). Although they perform reasonably well in most respects, they have the poor blue transmission characteristic of dry fibres, and it is expected that subsequent feeds will make use of the wet type.

The fibres have an outer silica cladding diameter of 125 μm, and are protected by a silicone buffer encased in a 0.5 mm diameter UV-cured resin jacket. At their input ends, they are terminated with the ferrules described previously (Figure 6.3), and cemented to the target images on the copy plate. Some 70 cms further along, they are gathered together into a single protective cable, which is anchored to the plateholder, although the fibres themselves can float freely within it (see Section 2.3). Because of this arrangement, no fibres have yet been broken in operational use,

---

(2) The FLAIR fibre feed design has a nominal 40 fibre channels (Section 3.2.2); however, in the prototype feed, one fibre fell victim to early inexperience during assembly!

despite their rather fragile nature. At the output end, they are attached to a slit unit, shown in Figure 6.4. The unit restrains the fibres, again independently of the cable, and aligns them in a 5 mm x 0.125 mm slot, whose front surface forms the slit of the spectrograph. Mode-stripping (see Section 2.2) takes place where the outer 0.5 mm jacketing is removed, between the fibre restraint and the slit block. Following normal practice (though on a smaller scale), the fibres are epoxied into the slot, and the output end polished flat and perpendicular. The slit unit is completed by a camera-type bayonet mount (Pentax-K), so that it can be quickly and accurately mated with a corresponding bayonet socket on the spectrograph collimator.

As was noted in Section 3.2.2, the output ends of the fibres are placed in contact, so that they are aligned in the slit on 125 μm centres. This provides adequate separation of the spectra in the focal plane of the camera, since Condition 3.5 is easily satisfied. The DIC structure of the AWA-SD fibres eliminates optical crosstalk between adjacent fibre channels.

Acquisition system. The problem of registering the real image formed in the telescope with the copy plate carrying the fibres (again to an accuracy of 10 μm) has required the development of an acquisition system, shown schematically in Figure 6.5. The low light-level ISIT TV camera is used with a viewing microscope to look simultaneously at the output from the acquisition imageguide and a set of five fibres, placed on fiducial stars that are evenly distributed over the 6.5 deg square field. The use of six fiducial points provides considerable redundancy in the system, and allows for optimisation of the alignment in the presence of small positioning

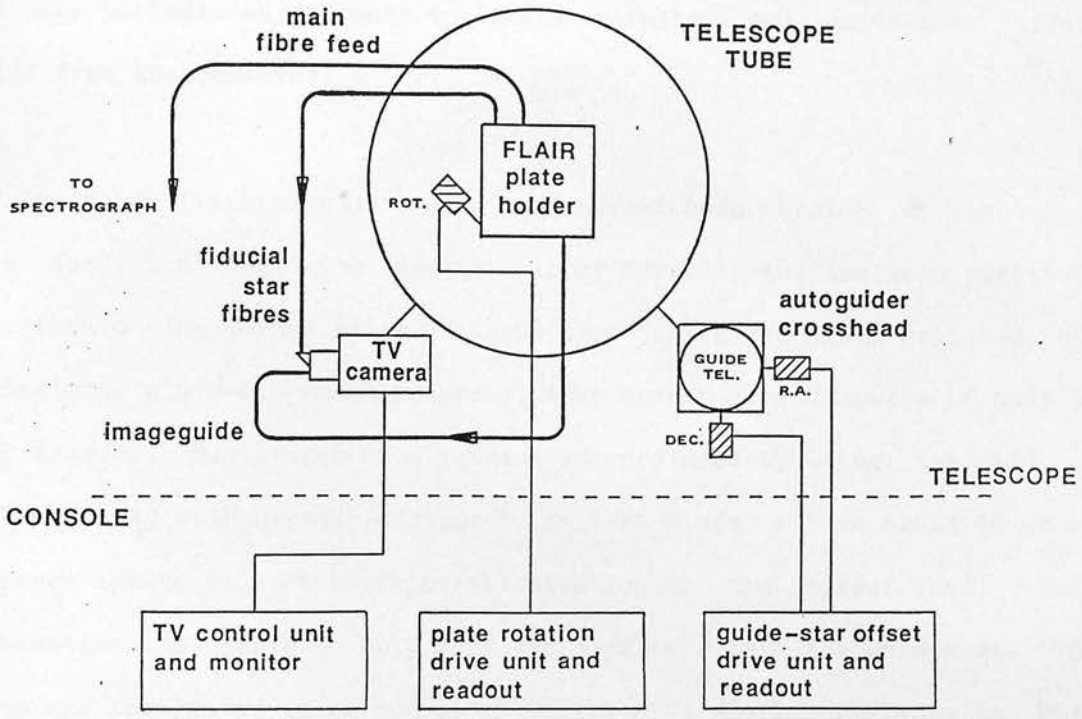

Figure 6.5 FLAIR acquisition and guidance system. (From Watson, 1986.)

errors. Once the fiducial stars are acquired, the UKST's existing auto-guider can be adjusted to track the same star that was used when the original plate was taken, and the system will then function automatically, with only periodic adjustments to plate rotation and guide-star offset needed from the observer.

The five-fibre fiducial-star bundle is a scaled-down version of the main fibre feed, 5 m long, with identical input ferrules and the same positioning method on the target stars. AWA-SD type fibres are again utilized, but to maximize plate-alignment accuracy, they have a core diameter of only 33 μm (2 arcsec). Two stages of alignment are provided by using the 125 μm outer cladding without mode-strippers, so that a star within about 60 μm of the fibre centre will cause faint illumination at the output end. Full illumination is achieved only when the star is within the core area. The fibres are terminated in an output slit unit with similar features to Figure 6.4, but very much smaller. A 2 mm square 90-degree prism cemented to the output face allows the imageguide and fiducial fibres to be brought close together in the TV field.

The imageguide itself is a Fujikura FIG-10C high-resolution (10 μm) coherent fibre bundle, 5 m long and 1.1 mm in diameter (containing about 10,000 hexagonally-packed cores), with a numerical aperture of 0.2 and a unit-length attenuation A' of 50 dB/km at 5000 Å. It is used to transfer a 74 arcsec diameter portion of the telescope field to the TV camera. During setting up, the imageguide is aligned with the image of a selected acquisition star (of about 10th magnitude) on the copy plate so that the plate image can be seen on the monitor. (The star has to be close to the edge of

the field to allow clearance of the obstructions behind the plateholder by the imageguide, which has a minimum bending radius of 200 mm.) In use, the real image of the star formed in the telescope is aligned with its plate image to give one initial point of coincidence of the plate with the sky. It is then a matter of scanning in rotation, keeping the acquisition star centred by moving the telescope, until the five fiducial fibre cores light up, when acquisition is complete.

6.4 The UKST fibre-coupled spectrograph and its detectors

Spectrograph. Unlike most telescopes for which fibre-coupled multi-object spectroscopy systems have been developed, the UKST had no existing spectrograph, and so its design could be integrated with that of the FLAIR system. As we have seen in Section 3.2.2, it was possible to use ordinary (Pentax) camera lenses for the main optical components, and thus build a very inexpensive prototype instrument. Because of their multi-layer coatings, the lenses have very high optical efficiencies, and their aberration correction is adequate for the purpose. An additional advantage of transmissive optics is the absence of a central obstruction in the spectrograph, so that no additional loss results if the shadow of the telescope central obstruction is not preserved by the fibres.

The spectrograph is shown in Figure 6.6. Its unusual features (the fast collimator and magnification greater than unity) have already been remarked upon in Section 3.2.2. In fact, the collimator and camera focal lengths are 50 and 85 mm, giving a magnification of 1.7. Plane reflectance gratings are used in Ebert configuration, with blaze to collimator and always

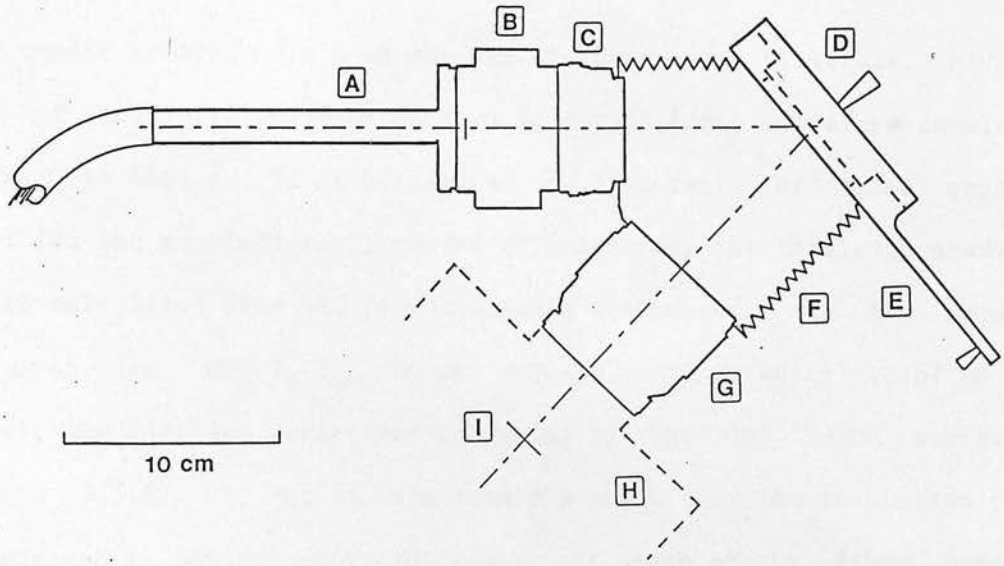

Figure 6.6 Plan view of fibre-coupled spectrograph. (A) Slit-unit located in collimator bayonet socket. (B) Collimator tube (slit-plane indicated). (C) 50 mm f/1.7 collimator lens. (D) Interchangeable grating cell. (E) Rotateable grating mount with dark-slide. (F) Flexible light-tight enclosure. (G) 85 mm f/1.4 camera lens. (H) Front of CCD cryostat or 35 mm camera body. (I) Image-plane. (From Watson, 1986.)

in first order. The axes of the two lenses are placed at 45 deg and, to allow sufficient clearance between the lenses and the grating without causing vignetting, the camera must again be fast, with a focal ratio of f/1.4 (compare Figure 3.7).

52 mm square gratings are used and six are currently available, giving a range of reciprocal dispersions from 54 to 373 Å/mm, and blaze wavelengths from 4620 to 9240 Å. Table 6.1 gives full details of these gratings. Except for the manufacturer's quoted efficiencies, the tabulated quantities are all calculated from the formulae given in Chapter 3 and its Appendix, with ϕ=45 deg, M=1.7, f_{cam}=85 mm, r=20 μm, z=22 μm and x'=12.67 mm (=576 pixels), the last two parameters referring to the GEC P8600 series CCD (Section 3.3.2). It can be seen from the table that the resolution of the spectrograph is determined by the equivalent width of the fibre projected through the system, $d\lambda_f$, since the minimum resolution element of the grating is always very much less than this. It may also be noted that, in accordance with the precepts outlined in Section 3.2.2, the sampling interval of the detector, $d\lambda_f/d\lambda_p$, generally lies between 1 and 2.

The actual resolution of the spectrograph has been demonstrated using digitized photographic spectra obtained on fine-grained film, where $d\lambda_f/d\lambda_p$ is relatively high (~10). The digitization was carried out in 8 μm steps using a PDS machine. In Figure 6.7(a), the region of the magnesium triplet in the spectrum of a bright (V=7.2) KO star, obtained with grating 1200V at 98 Å/mm, is shown. The theoretical resolution of the spectrograph at this wavelength is 3.8 Å, and the evident separation of the two short-wavelength components of the triplet ($\Delta\lambda$ = 5.4 Å) indicates that this

Table 6.1 Data on gratings for UKST fibre-coupled spectrograph

Grating	λ_L	Effic. at λ_L	λ_E	β at λ_E	$d\lambda/dx$ at λ_E	$d\beta/d\alpha$ at λ_E	$d\lambda_f$ at λ_E	$d\lambda_p$ at λ_E	λ_E/R	Spectral range
	Å	%	Å	deg.	Å/mm		Å	Å	Å	Å
300V	5000	77	4619	-18.2	372.5	0.94	18.7	8.2	0.55	4720
600V	5000	85	4619	-13.9	190.3	0.88	8.9	4.2	0.26	2411
600R	7500	76	6929	-9.5	193.4	0.83	8.5	4.3	0.38	2451
600I	10000	84	9239	-5.0	195.3	0.77	8.0	4.3	0.47	2475
1200V	5000	78	4619	-5.0	97.7	0.77	4.1	2.1	0.12	1238
2160V	5000	60	4619	10.2	53.6	0.58	1.6	1.2	0.05	679

Notes:

Gratings are designated by reciprocal groove spacing and approx. waveband.
λ_L = Littrow blaze wavelength.
λ_E = Ebert blaze wavelength.
β = angle of diffraction (= separation of grating normal and camera axis).
$d\lambda/dx$ = reciprocal linear dispersion.
$d\beta/d\alpha$ = slit projection factor.
$d\lambda_f$ = width of instrumental profile.
$d\lambda_p$ = wavelength equivalent of CCD pixel width.
λ_E/R = minimum resolution element of grating.
Spectral range is that covered by GEC CCD with dispersion along the columns.

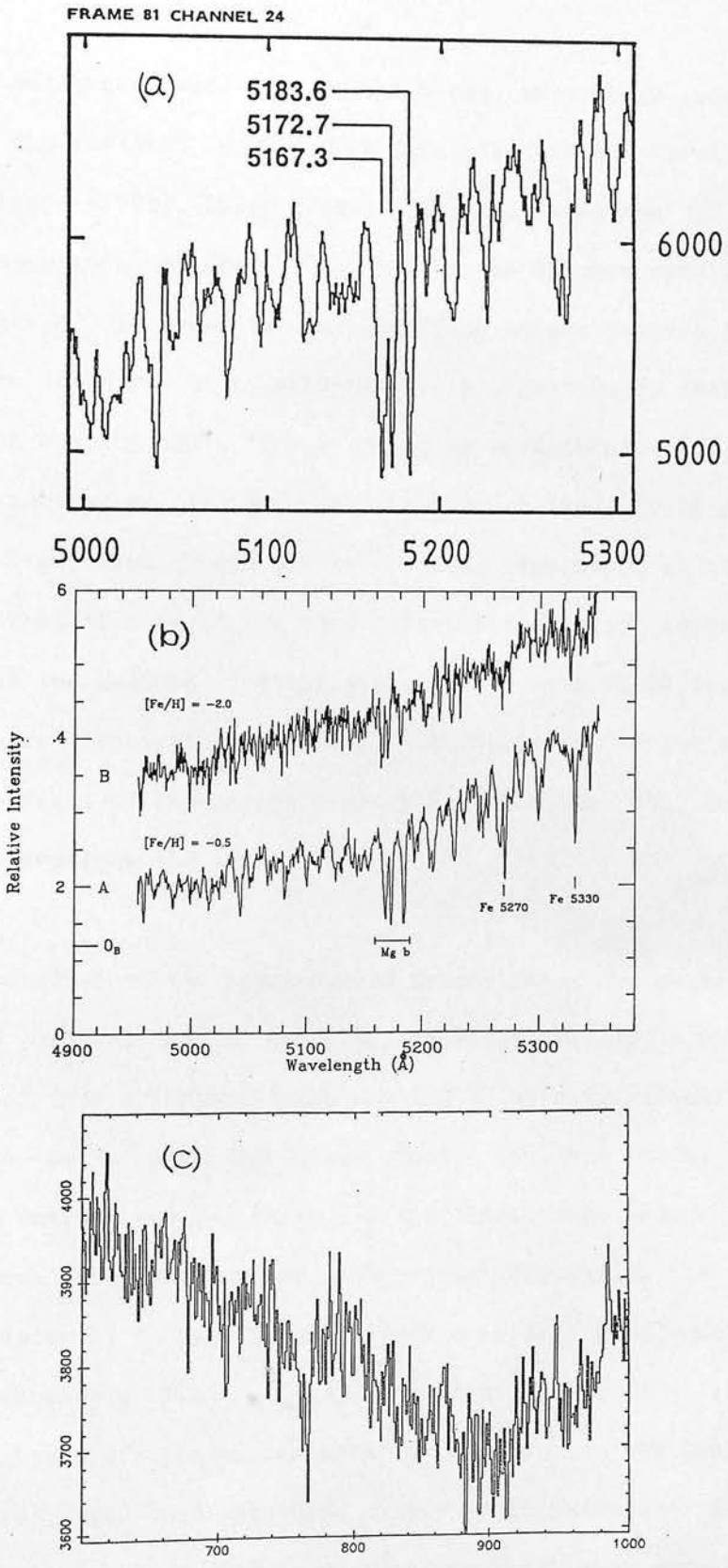

Figure 6.7 (a) Region of the magnesium triplet in the spectrum of the KO star SAO 190902, obtained with FLAIR at 98 Å/mm (from Watson, 1986). (b) K star spectra obtained with the INT (from Reid, 1985); the lower spectrum may be compared with (a), above, to demonstrate the fidelity of the FLAIR spectrum. (c) Raw PDS tracing of Na D lines in the spectrum of an anonymous F star, obtained with FLAIR at 192 Å/mm (see text).

is probably being achieved. The spectrum has very high signal-to-noise, and many of the features in it can be identified in the spectrum of a similar star (Figure 6.7(b), lower trace), obtained using the INT and included here for comparison. Figure 6.7(c) depicts the extreme resolution limit of the spectrograph. It shows the region of the sodium D-lines (left of centre) in the spectrum of an anonymous 10th magnitude F5 star, obtained at 192 Å/mm with grating 600V. The spectrum is uncalibrated (it is shown with wavelength increasing to the left), but the D-lines (with $\Delta\lambda$ =6.0 Å) are clearly resolved, even though the theoretical resolution at this wavelength is 8.8 Å. That this is at the very limit of resolution is demonstrated by the fact that the D-lines of other stars in the same FLAIR frame are either only partially resolved or are wholly unresolved; in the example shown, the random effects of photographic grain distribution, etc, have evidently conspired to separate the lines.

The high resolution of the spectrograph demonstrates the mechanical stability of its optical table mounting, described fully in Chapter 3. The versatility of this arrangement has enabled a second, identical spectrograph to be built alongside the first, so that both the CCD and photographic cameras are available all the time. The second spectrograph has also been used with another, independent CCD system (belonging to the ANU - see Chapter 7) to explore the future possibility of running two fibre feeds simultaneously from a single plateholder, thus giving 80 spatial channels. A range of spectral calibration lamps is available (Na, He, Hg-Cd and Ne), and these are used simply by illuminating the interior of the dome with its shutter closed, so that the light-path through the system is the same as that for the target objects. The Na lamp is especially use-

ful for calibrating photographic frames, where it can be used to superimpose the D-lines on the spectra of the target objects to provide a common zero-point for comparison with separate (rich-lined) arc frames, obtained at the same grating setting.

Despite the very satisfactory performance of the spectrograph in terms of resolution, it does have a number of drawbacks that might be expected from the inexpensive components used in its construction. The first of these is the poor blue transmission that will result from the high-index glasses used to achieve the requisite degree of correction in the fast SLR camera lenses (Wynne, private communication). Although no formal measurements have been made, results from FLAIR suggest that there are, indeed, substantial losses below ~4000 Å and, while the current poor blue transmission of the fibres masks this to a large extent, it is very likely to prove a serious disadvantage in the future. The second drawback has more immediate consequences, and results from a curvature of the focal surfaces with wavelength. Below ~4300 Å and above ~6500 Å, the variations in focus are particularly noticeable and, as a result, the maximum resolution can only be achieved over a limited spectral range. Again, the effect is worst in the blue. The eventual replacement of these lenses by purpose-built optics is, therefore, a high-priority item in the continuing development of FLAIR.

35 mm film camera. Although it was originally planned simply as a means of obtaining test results, the film camera has proved to be extremely useful for certain applications (notably the observation of bright objects). The camera is an ordinary Pentax 35 mm SLR body, which has been modified to allow its interior to be flushed with dry nitrogen while exposures are tak-

ing place. This is to safeguard the hypersensitizing of the emulsion from the detrimental effects of contact with moist air (see, eg, Dawe, 1984). Details of the emulsions themselves, and the hypersensitizing techniques used for FLAIR have already been given in Chapter 3.

The frame size of 35 mm film (25 mm x 36 mm) is considerably larger than the CCD format for which the spectrograph was designed, so that while the spectral ranges given in Table 6.1 are almost trebled when film is used, there will be substantial attenuation at the extremities of the spectra caused by vignetting in the camera lens. Digitization of photographic frames of spectra can be carried out in the same way as any other astronomical photographs, and facilities now exist at Cambridge for the rapid digitization (~5 minutes per frame) of FLAIR spectra using APM (Bunclark, 1986). The 35 mm film camera is currently offered as an alternative to the CCD in the PATT invitation for common-user requests.

Durham University CCD camera. This camera was built specifically for FLAIR (to an existing design) with the main aim of enabling galaxy redshifts to be obtained. It uses a GEC P8600 series device cooled to 150 K in a liquid-nitrogen cryostat mounted horizontally on the spectrograph optical table. Only the camera head itself is on the table; other equipment needed in its immediate vicinity (camera electronics, vacuum pump, etc.) does not require vibration-isolation.

The system is controlled by a PDP 11/23 computer, which communicates with the camera via a CAMAC interface; the computer is equipped with hard and floppy disc-drives, a magnetic tape drive, terminal, and data display moni-

tor. The camera runs under the control of a menu-orientated CCD program written at Durham, which allows some flexibility of operation, and permits inspection and rudimentary manipulation of the data using the PDP. Normally, the data frames are output onto tape in FITS format, for subsequent reduction on a large mainframe machine, such as a Starlink VAX node.

The camera is currently fitted with a standard, uncoated CCD chip, which is cosmetically very good but, as has already been noted, displays a high rate of CREs. It has the characteristic red response shown in Figure 3.11 (broken lines). It is expected that the chip will be replaced by one with a dye-coating to provide improved blue-sensitivity in the very near future.

6.5 Observing with FLAIR

FLAIR has now been used on the UKST a sufficiently large number of times that a well-established routine has evolved for the operation of the system, and we end this chapter with a summary of the setting-up and observing procedures. Only the prototype plateholder, 14/5, has hitherto been available for observations (3), so field changes during the night have not been possible, and FLAIR observations have consisted either of whole nights spent on single fields (a frequent arrangement during commissioning), or part-nights with conventional Schmidt photography occupying the remainder. While it is normal to carry out the former with the usual single-manning of

---

(3) 14/6, although now finished and commissioned in the telescope, awaits its fibre feeds; 14/7 is currently being fabricated.

the UKST, the latter is impossible to undertake single-handedly, and two observers are required. So far, all FLAIR observing has been carried out by the writer.

In the following summary, the stages in the preparation and execution of a FLAIR observing run using the CCD detector are given. When photography is employed, the advance preparation includes hypersensitization of the film (typically a 6-hour bake in nitrogen at 65 deg C, followed by a 10-hour soak in hydrogen with preflash immediately before each exposure), but the observations themselves are somewhat more leisurely once the initial setting-up has been accomplished, due to the long exposure times (of up to 6 hours) involved. Processing is carried out as soon as observing is finished.

The procedure for a CCD run is as follows:

(a) Advance preparation (several days or weeks before run)

Select original plate (usually a survey plate) to be used for positive copy
Select areas of target field to be used for sky fibres
(The next 2 steps are usually carried out by Trish McKenzie at UKST)
Prepare positive copy, masking selected sky areas on original to produce clear areas on copy
Check that background density, chemical fog and thickness are within tolerances
Arrange liquid nitrogen supply

(b) Before the run (1-2 days previously)

Pump down CCD cryostat
Mark and identify target objects on copy plate
Select and mark fiducial and acquisition stars
Calculate offset for each object for curvature-reversal scale-change
Remove and check fibres from previous copy plate; unload it from plateholder
Set up new copy plate in plateholder for cementing
Cement fibres on target objects, masked sky areas and fiducial stars, listing object/fibre identification

(c) Day of the run

(i) Prepare CCD:

Pump down CCD cryostat
Run up and check PDP computer
Decant liquid nitrogen and transfer to dome
Fill cryostat with liquid nitrogen; switch on camera electronics
Isolate vacuum pump and vacuum-seal cryostat during cool-down
At ~165 K connect CCD heater servo
Take test exposures and bias frames to check that all is well
Clear disc of images
Load blank tape
Allow CCD system to stabilize for >2 hours

(ii) Prepare dome:

Set up comparison lamps on telescope access gantry and test
Move acquisition console into telescope control room
Connect 5 acquisition system cables to telescope
Connect optical table nitrogen supply

(iii) Prepare plateholder:

Tension plate
Align adjustable imageguide socket with acquisition star image
Secure tangle of fibres inside plateholder and fit back cover
Temporarily coil optical cables; transfer plateholder to dome

(iv) Prepare telescope:

Connect imageguide output end to ISIT camera; secure imageguide to telescope
Load plateholder into telescope (optical cables first)
(The next 4 steps are carried out inside the telescope tube)
Bolt rotation stepper motor to plateholder
Connect up motor, rotation micrometer and rotation limit switches
Insert imageguide input-end into plateholder socket
Cover sensitometer spot projectors
Feed optical cables out through access hatch; close and seal hatch
Place safety cover on "plate unload" button
Connect fiducial-star fibre cable to ISIT camera
Switch on acquisition system; check plateholder rotates
Check TV can see plate image of acquisition star (with dome lights on and telescope shutter open)

(v) Prepare spectrograph:

Connect fibre feed cable to collimator; open telescope shutter
Insert grating
(The next 4 steps are carried out using the CCD to examine the spectra)
Adjust grating angle to obtain correct wavelength range

Adjust grating tilt to include all spectra
Adjust collimator focus for spectral region of principal interest
Adjust cryostat rotation to align spectra with CCD columns
Ensure spectrograph is light-sealed
Pressurize vibration isolation system

(d) Observing

(i) Obtain preliminary data:

Set CCD camera run parameters to write images to disc
Take CCD bias frames, dark frames, arc frames (dome closed)
Open dome to take zenith twilight sky frames if appropriate

(ii) Acquire field:

Set telescope focus, target field apparent position, guide star offsets
Slew to field with dome closed and lights on (to ensure cables do not foul)
With telescope shutter open and dome lights on, accurately mark centre of plate-image of acquisition star on TV monitor
Refill CCD cryostat before putting lights out
Open dome; acquire field as described earlier
Find guide-star in guide telescope eyepiece; adjust offsets
Engage autoguider
Peak up on fiducial stars using plateholder rotation and guide-star offset drives

(iii) Taking data:

Set CCD integration time (normally 1000 sec)
Set telescope shutter exposure time (normally 16.5 min)
Ensure dome is completely dark
Start CCD run; open telescope shutter within 5 sec
Leave dome; telescope shutter will automatically close approx. 5 sec before CCD is read out
Repeat sequence until required total integration is accumulated

(iv) Periodic chores:

Check and adjust field alignment using TV image of fiducial stars
Close dome and take arc frames
Obtain sky frames by disengaging autoguider and offsetting telescope from field
Refill CCD cryostat (approx. every 5 hours)
Output CCD images to tape (disc holds about 13 images)
Change grating (and re-adjust spectrograph) as necessary

(e) At end of observing

Take zenith twilight frames if appropriate
Close dome; take arc frames, dark frames, bias frames and flat fields
Depressurize spectrograph table

Disconnect main fibre feed from spectrograph
Remove plateholder from telescope (in reverse sequence to loading)
Release plate tension
Refill CCD cryostat before leaving

(f) At end of run

Disconnect acquisition system cables from telescope
Disconnect optical table nitrogen supply; park acquisition console
Remove comparison lamps; remove imageguide from telescope
Leave camera electronics on while CCD cryostat warms up

(g) Day after observing run

Copy any remaining images to tape
Power-down CCD system
Archive data at 6250 bpi on AAT VAX as soon as possible after run, sending original tapes and full documentation to user
Have a (short) rest!

References for Chapter 6

Bunclark PS, 1986. SERC Measuring-machines Newsletter No 9, p.10

Dawe JA, 1984. In Astr.with Schmidt-type telescopes, p.193, Reidel
Dawe JA, Watson FG, 1982. Proposal for ...(ROE internal memo, 1.7.82)
Dawe JA, Watson FG, 1984. In Astr.with Schmidt-type tels. p.181, Reidel

Eastman Kodak Co, 1973. Plates/films for sci.phot.(Kodak pub.P-315)

McLean IS, 1983. Proc.SPIE 445 (Inst.in Astr.V), p.547
McLean IS, Watson FG, 1983. The ISP/UKST fibre-optics expt.(ROE int.rep.)

Norland Products Inc, 1983. Optical adhesives data sheets

Reid IN, 1985. Telescopes, instruments, research and services (RGO)

Wallace PT, Tritton KP, 1979. MNRAS, 189, 115.
Watson FG, 1984a. MNRAS 206, 661
Watson FG, 1984b. ROE Bulletin, Oct issue, p.10
Watson FG, 1986. Proc SPIE 627 (Inst. in Astr. VI), p.787
Watson FG, 1987. SERC Bulletin Vol 3 No 7 p.7
Watson FG, Dawe JA, 1984. Proc. ASA 5, 579
Watson FG, Dawe JA, 1985. Occ.Rep.Royal Obs.Edin. No. 16 p. 1

Appendix to Chapter 6

Plate curvature reversal

Consider the situation shown in Figure 6A.1(a), where a photographic plate of thickness t is being exposed in a classical Schmidt telescope with a focal radius of curvature (and focal length) of R. The images of two objects, A and B, are formed, and are separated by a linear distance, L, on the emulsion.

If an exact positive copy of this plate (made on glass of the same thickness, t, and having a refractive index, n) is subsequently used in the telescope as an aperture plate for fibres (Figure 6A.1(b)), the reversed curvature of the emulsion side will cause the linear separation of the images of A and B on the plate to become

$$l = (R - t)L/R \qquad (6A.1)$$

by simple geometry.

However, the real images of A and B formed by the telescope on the emulsion side of the plate (where the fibres are cemented) will now be separated by

$$L' = (R - (t-t'))L/R,$$

where t' is the distance of the apparent focal surface from the front of the glass. If the plate is assumed to be flat over the small area of the converging beam at the glass surface, then

$$t' = t/n,$$

and

$$L' = (R - t + t/n)L/R \qquad (6A.2)$$

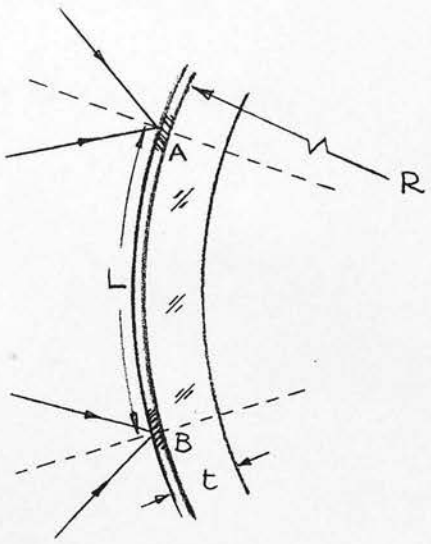

(a)

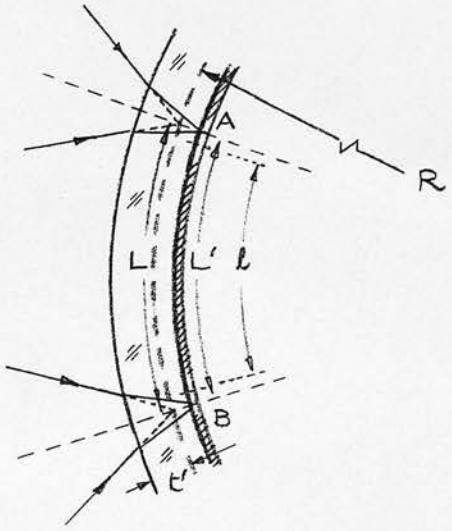

(b)

Figure 6A.1 Plate curvature reversal (see text). (a) Exposure of original plate. (b) Use of positive copy as an aperture plate.

The apparent increase in scale of the image formed in the telescope over that of the copy plate is now given by

$$L'/l = (R - t + t/n)/(R - t) = 1 + t/(R-t)n$$

or, since $R \gg t$,

$$L'/l \doteqdot 1 + t/Rn. \qquad (6A.3)$$

CHAPTER 7

Some results from FLAIR

Prefatory remarks

This chapter is devoted to some of the results that have come from FLAIR during its commissioning period. While the observations were all made by the writer, the studies are being carried out in collaboration with a large number of other scientists, and these affiliations are indicated at the head of each section. Because most of the observations were made very recently, the data reduction is, for the most part, still being undertaken by the various investigators, so much of the material presented here is rather sketchy. However, sufficient has already emerged to be able to predict with reasonable certainty those areas in which FLAIR observations are going to be of greatest value. It is also becoming clear where the greatest needs for improvement in the system lie, and the steps required to implement these are outlined in the next chapter, together with an indication of where the improvements will lead in terms of increased astronomical usefulness.

All the programmes described in the present chapter are ongoing, with new

observations planned at a later stage. In addition, there are other proposals for which observations will be made before the end of the commissioning period in August, 1987 (end of PATT Semester L). Two of these might be mentioned here. During May, 1987, FLAIR will be used in a programme to observe concentrations of bright (magnitudes 12-15), early-type stars in the galactic plane in collaboration with Gösta Lyngå (Lund Observatory). The aim here is to obtain radial velocities and luminostity criteria, so that the high resolution of the spectrograph, described in the previous chapter, will be exploited to the full. The systematic determination of stellar radial velocities will be a critical test for FLAIR, and will probably require the highest available dispersion (54 Å/mm). Later in the year, it is intended to carry out pilot observations for the writer's programme of radial velocity determination for RR Lyrae stars in the Palomar-Groningen fields, mentioned at the end of Chapter 5. The magnitude range of these objects is about 13 to 15. Both these programmes will use the Durham CCD camera, but they will be limited to using spectral features from H_β longwards (by the CCD response and the transmission of the fibres), a somewhat unsatisfactory situation. However, it is expected that valuable new data on the capabilities of FLAIR will come from the observations.

7.1 Classification of stars in the Chamaeleon dark cloud

(with D C B Whittet (Lancashire Polytechnic) et al.)

Nearby dark clouds are important to studies of low-mass star formation and pre-main sequence (PMS) evolution, and investigations of the nature and

evolution of associated interstellar material. The Chamaeleon dark cloud (RA 11 h 00 m, Dec -77 deg 00 min (1950)) is one of the closest such regions to the Sun, and contains a large number of PMS stars detected both optically (Henize and Mendoza, 1973; Schwartz, 1977) and in the infrared (Glass, 1979; Hyland, Jones and Mitchell, 1982; Baud et al., 1984). Of these, there are very few stars of early spectral type, indicating a bias towards low-mass star formation, and the apparent quiescence of the Chamaeleon region suggests that the clouds may be in a comparable evolutionary state to that in Taurus, which is similarly devoid of embedded OB stars (Elias, 1978).

A knowledge of the extinction law due to dust in the dark cloud environment is important for several reasons: (a) it provides a means of determining changes in the size distribution of the grains, and hence of investigating growth associated with mantle formation or grain coagulation; (b) derivation of the spectral-energy distributions of the PMS stars requires a detailed knowledge of the wavelength-dependence of interstellar reddening; and (c) the extinction law strongly influences measurement of the distance to the cloud, which, in turn, affects the luminosities derived for the embedded PMS stars. The extinction law in the Chamaeleon cloud has proved to be controversial, leading to distance estimates that range from 115 to 215 pc (Grasalden et al., 1975; Rydgren, 1980; Hyland, Jones and Mitchell, 1982), depending on the value assumed for the ratio total-to-selective extinction,

$$R = A(V)/E(B-V), \qquad (7.1)$$

where A(V) is visual absorption, and E(B-V) is colour excess (the amount by which B-V is increased by reddening). Indiscriminate application of the "normal" value of R (=3.1) leads to large discrepancies in the distances of stars that are clearly associated with the dark cloud.

The observing programme of which the FLAIR work formed a part was designed to investigate the nature of a selection of field stars in the direction of the Chamaeleon cloud. The data, comprising optical (UBVRI) and infrared (JHK) photometry as well as optical spectroscopy, were used to evaluate reddenings and distances, and to distinguish members and non-members of the T-association. The photometric observations were made at the Sutherland site of the South African Astronomical Observatory (SAAO), and the FLAIR spectra were combined with others obtained with the Reticon Photon Counting System (RPCS) on the SAAO's 1.9-metre telescope. The results of the spectroscopy are presented in Table 7.1.

The FLAIR spectra were obtained in January, 1986, using preflashed, hypersensitized 2415 emulsion at a reciprocal linear dispersion of 190 Å/mm, and covered the wavelength range 4000 to 7000 Å. A total of 27 sources in Chamaeleon, listed in Table 7.1(b), were included on two FLAIR frames, No. 107 (targets in Field 38 (RA 11 h 00 m, Dec -75 deg 00 min); exposure 345 min) and No. 109 (targets in Field 19 (RA 10 h 30 m, Dec -80 deg 00 min); exposure 210 min). The spectra were digitized and plotted using the APM machine at Cambridge, as described by Bunclark (1986), and some of the results are illustrated in Figure 7.1. Approximate photographic J (blue-green) magnitudes are also given. A frame containing the spectra of bright field stars (No. 20; targets in Field 601 (RA

Table 7.1 Spectroscopy of stars in the Chamaeleon dark cloud

(a) RPCS spectra

Star	Grating	Description/classification
Cha T6	3	Ca II H+K em. cores
T33	3	Ca II H+K em. cores
F10	3	K3
F13	1	F8V
F16	3	G2
F22	1	G8
F23	1,3	M5III
F25	3	G8
F28	3	K3-K5
F31	1	F5V
F33	1	G5-K0
F34	1	K3
F36	1,3	K0

(b) FLAIR spectra

Star	Frame	Description/classification
Cha T3	107	Strong Hα emission
T6	109	Hα emission
T11	109	Hα emission
T12	109	Hα emission
T15	109	Weak continuum
T21	109	Continuum; G-K
T25	107	Hα emission
T31	107	Hα, Hβ, He(5876) em.
T32	109	Hα em., Hβ, Hγ abs.; B9-A0
T34	109	Weak continuum
T35	107	Not detected
T38	107	Hα emission
T40	107	Hα, Hβ, He(5876) emission
T46	107	Hα emission
T48	107	Hα, Hβ emission
T49	107	Hα, Hβ emission
F6	107	A0V
F10	109	Continuum; G-type?
F18	109	G5-K0
F23	109	M5
F25	109	Continuum
F28	109	Continuum
F29	107	K0-K5
F30	107	F5-G5?
F33	107	G5
F34	109	Continuum
F36	107	G5

(From Whittet et al., 1987.)

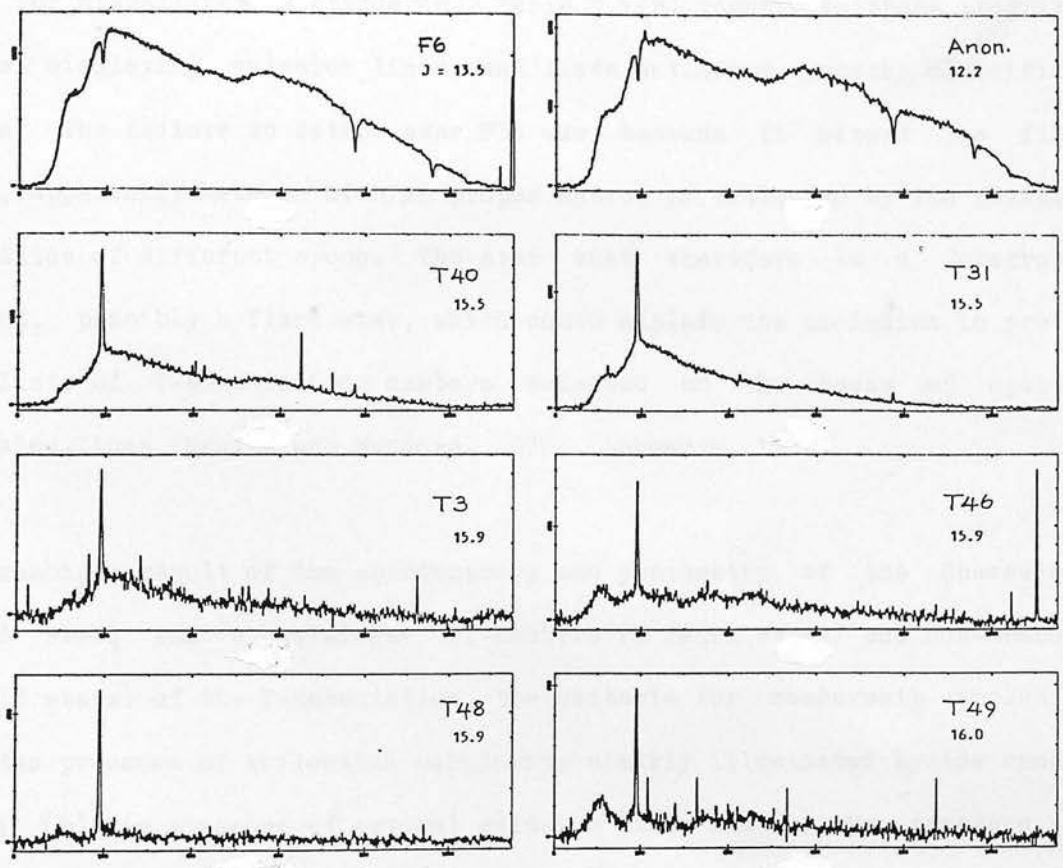

Figure 7.1 Digitized photographic FLAIR spectra of stars in the Chamaeleon dark cloud (plotted with wavelength increasing to the left). The top two are early-type field stars, while the remainder are T Tauri stars. Approximate photographic J magnitudes are shown. Random spikes in the spectra are caused by dust on the emulsion; they can be distinguished from the emission lines by their position and width. (From Bunclark, 1986.)

22 h 03 m, Dec -20 deg 00 min); exposure 30 min) was also digitized and used for classification standards. Table 7.1(b) identifies those programme stars displaying emission lines, and lists estimated spectral classifications. The failure to detect star T35 was because it missed the fibre feed, apparently because of high proper motion as indicated by its position on plates of different epoch. The star must therefore be a foreground object, possibly a flare star, which could explain its inclusion in previous lists of T-association members selected on the basis of optical emission lines (Henize and Mendoza, 1973; Schwartz, 1977).

The combined result of the spectroscopy and photometry of the Chamaeleon cloud stars was a catalogue of members (T Tauri stars) and non-members (field stars) of the T-association, the criteria for membership including (a) the presence of reflection nebulosity clearly illuminated by the candidate; (b) the presence of optical emission lines and (c) the presence of excess continuum emission at infrared wavelengths, indicating a circumstellar shell. The colour excesses, E(B-V), of all the field stars in the catalogue with reliable optical photometry and spectral classification could then be estimated, and, using a value of R, based for the most part on measurements by Vrba and Rydgren (1984), their distance moduli deduced. A plot of E(B-V) against distance modulus (not illustrated here) shows that strong reddening begins to occur at a distance modulus of 5.7 (138 pc), which may be taken as the front edge of the cloud. The mean angular extent of the cloud is equivalent to a linear size of ~4 pc at 138 pc so, assuming the cloud is approximately symmetrical, we may deduce the mean distance to be

$r = 140 \pm 12$ pc. (7.2)

This value is in excellent agreement with the distance deduced by Rydgren (1980) for the star HD 97300 (T41), which is clearly a member of the cloud, as it illuminates a bright reflection nebula, and has been used previously as a distance indicator. However, the star has been suspected of having an anomalously high value of the ratio R; using data obtained in the present programme, and the distance given in Result 7.2, we find

$R = 5.6 \pm 0.5$, (7.3)

so that the earlier suspicions are confirmed. This result supports a suggestion of Vrba and Rydgren (1984) that the value of R increases as a function of density in the cloud.

This work has been published in a paper by Whittet et al. (1987), of which the foregoing is a synopsis. The role of FLAIR in the study was clearly one to which the system is well suited; even with the limitation of photographic detection, useful spectra of stars as faint as magnitude 16 were obtained. It is noteworthy that the RPCS data given in Table 7.1(a) required 13 separate observations, whereas the 27 FLAIR spectra presented in (b) needed only two. This programme would clearly benefit from the use of the CCD detector, both from the point of view of being able to observe fainter (and more highly reddened) field stars, and from that of being able to provide better estimates of spectral classifications. Plans for such future observations are well advanced.

7.2 Spectroscopy of cluster flare stars in Orion

(with B D Carter, B J O'Mara and J E Ross, University of Queensland)

Flare stars are characterized by sporadic increases in brightness that may amount to several magnitudes, but may only last a matter of minutes. Two classes of flare star are identified: the UV Ceti stars, which are dwarf M (or occasionally K) stars observed in the solar neighbourhood, and the cluster flare stars (or "flash stars") found in open clusters and associations, and in regions of nebulosity. Thus, cluster flare stars are found in star-formation regions such as the Orion nebula (Haro, 1968) as well as in relatively older aggregations like the Pleiades and Praesepe (Haro, 1968; Gurzadyan, 1980). Cluster flare stars appear to display many times fewer outbursts than UV Ceti stars, but this may be due to selection effects caused by their greater distances, and the consequent poorer time-resolution of observations (Kunkel, 1975). They appear to encompass a short range of spectral types, with most being K dwarf stars. Many flare stars show hydrogen and ionized calcium emission lines when quiescent, and perhaps 30 percent are also irregular variables (T Tauri or RW Aurigae; Haro, 1968). It is possible that all dwarf stars may pass through a flare phase, perhaps following the T Tauri stage of stellar evolution (Ambartsumian and Mirzoyan, 1975; Haro, 1976; Mirzoyan, 1974), and so their evolutionary relationship to T Tauri and other PMS stars is of considerable interest. The very large number (~450) of cluster flare stars in Orion makes these objects suitable candidates for detailed study.

The nature of the flares displayed by the Orion stars has been investigated

by a number of authors. Haro (1964, 1968) used multiple-exposure photography with a time-resolution of 10 minutes, together with objective-prism spectroscopy, to distinguish two extreme types of flaring: (a) "normal" flares, showing an eruptive increase in the blue (but not the red) continuum, with H_α emission quickly appearing or strengthening, the rise taking place on a time-scale of a few minutes but having a slower decline; (b) "slow" flares, with an increase in the red as well as the blue continuum, taking 40 to 60 minutes to reach maximum light, and several hours to decline, with enhanced H_α emission becoming noticeable only after maximum light, but remaining visible for 1 to 2 days afterwards. The latter category is much the rarer of the two. Mirzoyan et al. (1982, 1984) used three telescopes simultaneously to obtain time-resolved photographic UBV photometry of some Orion flares. Most of the flares were of the normal, rapid kind, and showed colours similar to those of UV Ceti stars, although flares observed in two T Tauri stars had anomalous colours. Earlier photoelectric photometry by Mendoza (1968) showed colour changes that Haro (1969) attributed to peculiar flares. Some of the Orion stars have been noted to be very energetic, with changes in the U band of as much as 8 magnitudes (Gurzadyan, 1980).

It is thought that the flares displayed by UV Ceti stars have a similar origin to those seen in the chromosphere of the Sun (Mullan, 1977), with thermal mechanisms causing the optical emission (Giampapa, 1983). The outbursts shown by cluster flare stars may have a non-thermal origin, however (Haro, 1964), with synchrotron emission suggested as the mechanism (Slee et al., 1969; Slee and Higgins, 1971), though x-ray observations indicate that the enormous power radiated by flares may, in fact, be due more to the

large volume of the emitting loop (whose radius might be half that of the star) than to the existence of abnormal physical conditions in the plasma (Cohen, 1984; Feigelson, 1984). Thus, the flares shown by the Orion stars, for example, may be extreme examples of those displayed by the Sun, the larger release of energy being due to much larger size rather than fundamentally different physical processes. It is further suggested (Mullan, 1979; Gershberg and Petrov, 1976) that the "slow" flares of the Orion stars may be changes comparable with the disappearance and reappearance of starspots.

The observational data on which these ideas are based leave a good deal to be desired and, in particular, there is much scope for improvement in optical observations of flare stars. Multiple-exposure photography has limited sensitivity and accuracy and, where colours are obtained, they will not necessarily reflect the colour changes that might occur on time-scales less than the sampling interval. In any case, flare colours do not give unambiguous indications of the underlying physical processes, because of the varying relative contributions of emission lines and continua (Mullan, 1985). Objective-prism spectra, while overcoming the latter defect, likewise suffer from poor sensitivity and time-resolution.

The present programme seeks to obtain spectroscopy of Orion flare stars with a wavelength resolution of a few Angstroms or less, and time resolutions of a few minutes, much better than can be achieved using objective prisms. Observations of this kind have already been made for UV Ceti stars (see, eg, Worden, 1983), but the greater distances of cluster flare stars results in spectroscopy of these objects being considerably more difficult.

The use of multi-object methods greatly increases the likelyhood of observing an outburst. Spectra of the Orion stars would be useful even if no flares were recorded, as the quiescent spectra would permit modelling of the stellar chromosphere to match the equivalent widths and relative intensities of the Balmer lines. Comparisons with UV Ceti and T Tauri stars could also be made. Spectra of flare events would permit detailed investigation of the sequence of appearance and decay of emission lines. Again, comparisons with UV Ceti and, perhaps, solar flares could be made, and the observed characteristics of the Balmer series could be matched by modelling the physical conditions and structure of the emitting region of the chromosphere throughout the duration of the flare.

Observations for the programme have now been made using the FOCAP multi-fibre system on the AAT, and using FLAIR. Briefly, the former involved the use of 400 μm fibres together with the ASPECT software package on the IPCS (Wallace, 1985) to make time-resolved observations of 29 Orion flare stars at 33 Å/mm in November, 1985. Most of the spectra showed Balmer-line and H and K line emission when quiescent, although the relative intensities varied considerably from star to star. Other lines (eg, HeI 4026, 4471; SiI 3905 Å) were also seen. Two flares were recorded, one each on the stars T30 and T48 (identifications from Haro, 1968). The spectrum of the latter showed a gradual strengthening of the Balmer series over ~2 hours, together with the appearance of the HeI 4026 and 4471 Å lines. The H and K lines also strengthened, but reached a maximum after the hydrogen lines, and, some 5 hours after the beginning of the flare, the star had returned to its quiescent state. This outburst had many features in common with UV Ceti and solar flares, and is providing much useful data. The

results of a second FOCAP observing run in November, 1986, are still being reduced, but preliminary results indicate that a flare of star T48 was again recorded.

The FLAIR observations were made with the aim of covering a wider area of the Orion region than could be accomplished with the AAT's 40 arcmin field, at the expense of time resolution (because of the longer integrations required on the UKST). FLAIR observations of 33 flare stars in Field 768 (RA 05 h 40 m, Dec -05 deg 00 min) were made on two nights in December, 1986, using the Durham CCD as detector. Most of the stars had V magnitudes within the range 14 to 16, and eight of them (including T48) were common to the selection observed with the AAT. In addition to the flare stars themselves, fibres were placed on a spectrophotometric standard (HD 36541), and on five sky positions. During the first night, the stars were observed at 190 Å/mm, covering the approximate wavelength range 4250 to 6650 Å so as to include the first three lines of the Balmer series. The wavelength focal-curvature of the spectrograph meant that critical focus could be maintained over only a limited range of wavelengths (including H_β), and the poor blue response rendered the region around H_γ very faint. Nevertheless, eleven 1000 sec exposures were obtained with a mean time-resolution of 29 min, and these are currently being reduced to obtain values of the Balmer decrement. All the stars showed the Balmer series in emission, and, while no flare outbursts were recorded, there are evident variations in the intensity of the H_α line (and possibly in the other Balmer lines) on a timescale comparable with the sampling interval. It is activity of this kind that is extremely difficult to record with an objective prism, and it highlights the advantage gained by combining a wide-field telescope with a

CCD detector.

On the second night, thirteen 1000 sec exposures were obtained with a mean temporal resolution of 27 min, this time at a reciprocal dispersion of 98 Å/mm, covering the wavelength range 5600 to 6800 Å, and optimised for H_α. These observations were marred somewhat by a fault on the telescope that caused a 3 Hz oscillation in RA with an amplitude of up to 3 arcsec, so that the spectra are likely to be diluted by sky emission. Since this entire region of the sky has a strong background of H_α, this could cause difficulties in the desired measurement of accurate equivalent widths of the stellar H_α lines. As with the previous night's data, the reductions are proceeding; again, there are signs of variations in H_α intensity, but no increases of the kind observed in a flare.

Although final results have not yet come from this programme, it seems likely that the FLAIR data will provide useful input, once again illustrating its suitability for the observation of objects whose spectra contain emission lines, and which are distributed at ~10 deg^{-2} (Section 1.3.2). However, it also serves to highlight again the shortcomings of the system in terms of spectrograph focal curvature and poor blue sensitivity. It is proposed to undertake further FLAIR observations for the programme when the capabilities of the equipment are improved, and it is hoped, in addition, to carry out observations of the ~30 older flare stars in the Pleiades, whose much-lower number density renders multi-object spectroscopy impossible with any system other than FLAIR.

7.3 The FLAIR multi-object photometry experiment

(with R D Robinson, Anglo-Australian Observatory)

As we have seen in the previous section, most of the existing photometric data on flare stars have been obtained by photographic methods, so as to increase the likelyhood of capturing a flare by observing more than one object. The multiple-exposure technique permits successive observations to be made with a very short interval between them, but is limited in time-resolution by the actual length of each exposure, particularly on smaller telescopes. The number of successive images that can be recorded is also restricted (to ~20) by the need to avoid overlapping.

These limitations, together with the desireability of using as wide a field of view as possible, have led to the suggestion that FLAIR might be used in a photometric mode to obtain highly temporally-resolved (a few seconds) observations of known flare stars to investigate the fine structure of their light curves. Such a photometric mode, if successfully implemented, could also be used for time-resolved photometry of any other object class displaying variability on a short timescale ($\lesssim$1 day) with a number density greater than ~1 deg^{-2}. An obvious example is the set of RR Lyrae stars in the Palomar-Groningen fields mentioned earlier; FLAIR spectroscopy of these would require supporting photometry for the determination of phases, and this would be ideally suited to a FLAIR photometry system. It may be noted that the proposed technique would, like its equivalent in spectroscopy, fall into the category of a "follow-up" process, so that the discovery of objects by their variability would remain firmly within the province of

photography, or the new automated patrol techniques using CCDs (eg, McGraw, Cawson and Keane, 1986; Storey et al., private communication). Nevertheless, such a technique has evident important applications, and the experiments described here represent the first steps in investigating whether a workable system can be developed. Strictly speaking, this work is outside the scope of the present thesis, which includes no formal treatment of photometric measurement; however, it is included here as a further example of the use of FLAIR.

Until very recently, the use of fibres in astronomical photometry systems was avoided because of uncertainties about the photometric stability of a flexible lightguide. As we have seen, bends in a fibre cause changes in NA, and introduce stresses that may result in increased FRD (Section 2.2); however, the extent to which these might affect photometric accuracy in the slowly-changing environment of a telescope-mounted fibre system has probably been overestimated. Some new fibre-coupled photometers were mentioned in Section 4.4, and one of these in particular (described by Barwig, Schoembs and Buckenmayer, 1986) appears to have demonstrated quite categorically that good photometry can be carried out using fibre-coupled systems, with <1 percent accuracy reported, even in the presence of severe atmospheric transparancy variations (of up to 90 percent). The published account of this instrument includes a very complete treatment of the errors involved. This system, in common with the others mentioned, uses short lengths of fibre (a few cms), and it might be expected that the 10 m length required to couple the UKST's focal surface to the table-mounted photometer will limit the accuracy that can be achieved.

So far, the problem of aligning more than a very few objects with a multi-aperture photometry system has not been satisfactorily addressed, and this has been the main purpose of our photometry experiment to date. At the time of writing, only one observing run has been carried out, but the results have been sufficiently encouraging that more observations will be attempted within the very near future.

The experiment requires some changes in the configuration of FLAIR and, in particular, the replacement of the normal spectroscopic fibre feed, 39/40R (with its 2.7 arcsec entrance apertures), by one having the much larger apertures necessary for photometric work, so that there is no risk of images being vignetted. This new test feed (designated 10/200B) was made for the UKST by Peter Gray, and consists of ten channels of 200 μm core Spectran fibre, each of which has a projected diameter on the sky of 13.4 arcsec. The fibre feed is entirely compatible with FLAIR, having a length of 10 m, and a standard UKST slit unit (Figure 6.4) at its output end, but the fibre inputs are terminated with FOCAP ferrules rather than the FLAIR type. This is because of the evident unsuitability of the positive copy positioning technique for photometry, where extreme uniformity over the fibre entrance face is needed. This requirement, together with the relaxed positioning tolerances made possible by the larger fibres, enables a Medusa-class positioning system to be used, with a 1 mm thick FOCAP-type brass aperture plate being incorporated into a FLAIR plateholder (14/6). For the experiment, the plate was drilled at the UKST (with a positional accuracy of ~25 μm) using astrometric measurements of the target objects, the hole positions then being checked by subjecting the aperture plate itself to astrometric measurement.

Although the FLAIR acquisition imageguide can be used with the brass aperture plate, there is at present no facility for transferring fiducial stars to the ISIT TV camera. In the initial experiment, the target objects were sufficiently bright that they themselves could be used as fiducial stars, the output slit being observed visually with a magnifier while the alignment proceeded. However, there will eventually be a fiducial star bundle (using 100 μm fibres) terminating in a standard FLAIR fiducial slit unit that can be plugged into the TV microscope.

For the experiment, the UKST fibre-coupled spectrograph was reconfigured so that the fibres were imaged directly onto the CCD by the collimator and camera lenses, each fibre covering an area 15.5 pixels in diameter. A filter (RG 630) and shutter were also incorporated into the optical system. The fibres were imaged close to the readout register of the CCD, and only the first 40 rows (containing the fibre images) read out, partly to reduce the readout time and demonstrate that high time-resolution would be possible, and partly to enable a larger number (~200) of images than normal to be stored on the PDP disc.

Seven of the ten fibres were allocated to standard stars spread widely over the field, with V ranging from 7.03 to 8.40, and two were allocated to the sky. The remaining fibre was used to observe SX Phe, a β Cepheid star with a period of ~80 minutes, and a well-determined ephemeris. This object has a quasi-sinusoidal light-curve with irregular maxima, the total variation encompassing the magnitude range $6.86<V<7.47$, and it formed a very suitable target for the experiment. Observing was planned for eight bright-of-moon nights in November, 1986, but the weather prevented observing on all but

one, 1986 November 15/16. On this night, a sequence of 80 one-second exposures at two-minute intervals was obtained. The sequence was interrupted by cloud on several occasions, two of which were later established to have coincided with maxima of the star. The observations encompassed a wide range of hour angles, and no corrections to field rotation or guide star offset were made once the acquisition had been completed (because of the cumbersome alignment procedure used for the experiment). A result of this was a steady change in the positions of the star images on the fibre input faces, due to refraction effects, which was seen as a change in the annular intensity profile on the fibre output faces (see Section 2.2). At the end of the observing sequence, some of the star images were actually vignetted by the fibre cladding.

Reductions were carried out simply by summing the measured intensity over the image of each fibre, and subtracting bias, dark count and sky; the data for SX Phe were then corrected for transparency variations using the measurements of the nearest standard star. The resulting light curve is shown in Figure 7.2 and, despite the relatively large scatter of the measurements (~10 percent), the star's variability is clearly seen. Conventional photoelectric photometry, carried out earlier the same night on the ANU 0.6-metre telescope (Thompson, private communication), confirmed that the star underwent maxima at ~22h 40m, 00h 00m and 01h 20m EST, in agreement with Figure 7.2. Considering the defects in these observations (the poor weather, a residual tilt in 14/6 giving field-dependent defocusing, and the gradual drift of the images over the fibre faces) these results are remarkably good.

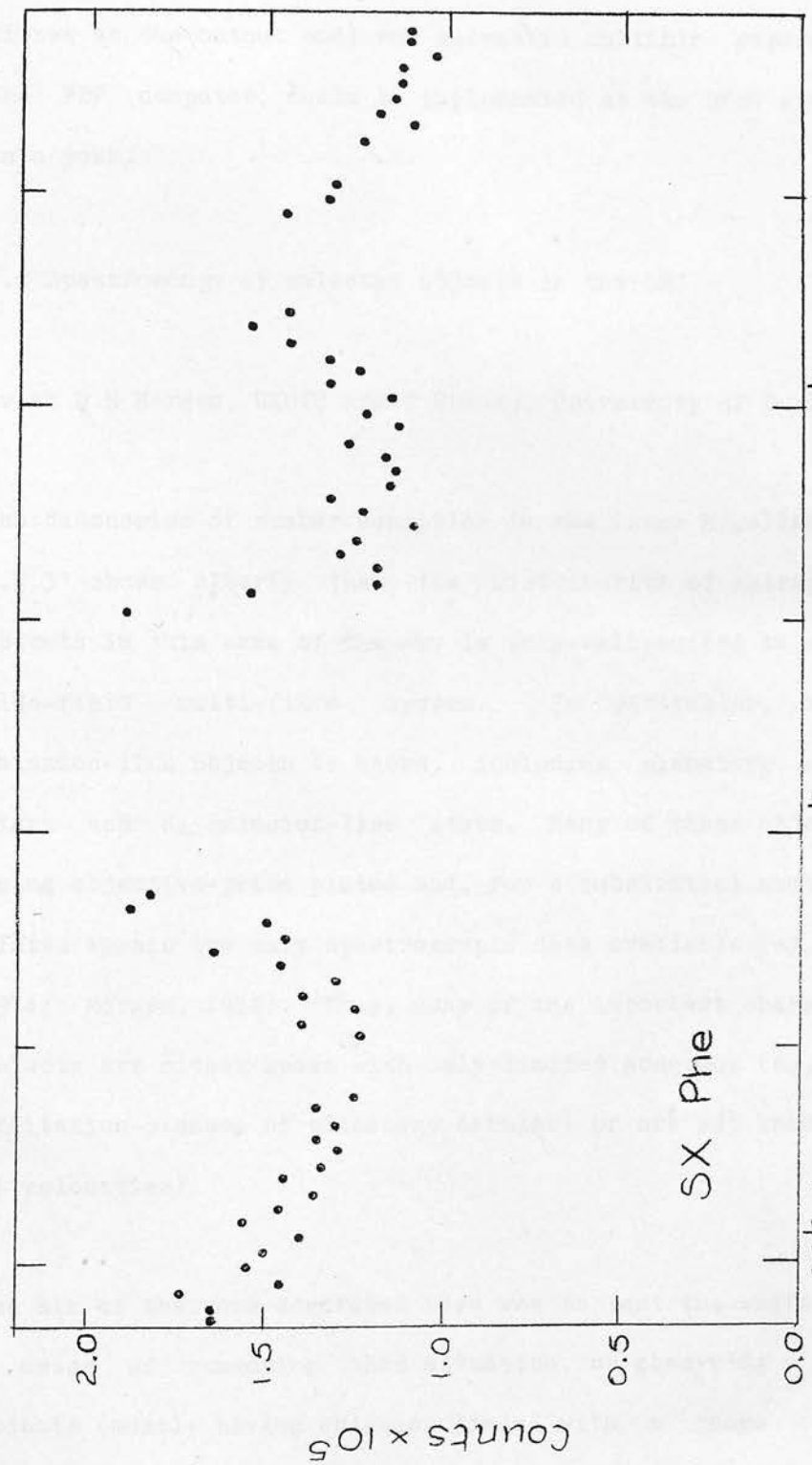

Figure 7.2 Red light-curve of the star SX Phe on 1986 November 15/16, obtained with FLAIR configured for multi-object photometry.

If subsequent tests prove successful, it is envisaged that a FLAIR multi-object photometry system, with up to 100 channels (using a matrix of fibres at the output end) and automatic multiple exposures controlled by the PDP computer, could be implemented at the UKST within as short a time as a year.

7.4 Spectroscopy of selected objects in the LMC

(with D H Morgan, UKSTU and T Shanks, University of Durham)

The discussion of number densities in the Large Magellanic Cloud in Section 1.3.3 shows clearly that the distribution of astrophysically-important objects in this area of the sky is very well-suited to spectroscopy with a wide-field multi-fibre system. In particular, a large number of emission-line objects is known, including planetary nebulae, Wolf-Rayet stars and H_α emission-line stars. Many of these objects were discovered using objective-prism plates and, for a substantial number of them, these plates remain the only spectroscopic data available (eg, Bohannan and Epps, 1974; Morgan, 1984). Thus, many of the important characteristics of the objects are either known with only limited accuracy (eg, line strengths and excitation-classes of planetary nebulae) or are not known at all (eg, radial velocities).

The aim of the work described here was to test the suitability of FLAIR as a means of remedying this situation, by observing a wide variety of LMC objects (mostly having emission lines) with a range of dispersions and integration times, thus establishing the practical limitations of a FLAIR

spectroscopic survey of the area. The observations are the most recent carried out with the system, and the reductions are still at a very early stage, but a few preliminary results have been obtained and are given here.

The selection of target objects came from a variety of sources, principally Breysacher (1981; Wolf-Rayet stars), Morgan (1984; planetary nebulae) and Bohannan and Epps (1974; H_α emission-line stars). Most were within the range $14 < V < 17$. The final list included:

5 Wolf-Rayet stars (with existing slit spectra),
3 planetary nebulae,
1 very low excitation compact nebula,
3 B III stars (with existing slit spectra),
17 H_α emission-line stars from the Bohannan and Epps catalogue (including 2 suspected VV Cephei systems),
3 LMC clusters,
2 LMC H II regions (including the central region of the 30 Doradus nebula),
1 anonymous background galaxy,
1 anonymous LMC star embedded in nebulosity,

a truly cosmopolitan selection. Had the observations been made just a few days later than they were, the list would have been further enhanced by the addition of SN 1987a, which is in the same field of view (Field 56). Observing was carried out on 1987 January 3/4 and 4/5, using the Durham CCD as detector. On the first night, spectra were obtained at 98 Å/mm, covering the wavelength range 5600 to 6800 Å to include He I 5876 and the red lines of [NII] 6548, 6583; H_α 6563; He I 6678; and [SII] 6717, 6730 Å. A fault with the PDP computer led to the loss of some frames but, by the end of the night, five 1000 sec integrations had been obtained. On the second night, observations were made at 190 and 373 Å/mm. Eight 1000 sec exposures were obtained at the first of these dispersions (the spectra covering the wavelength range 4250 to 6650 Å), and four 1000 sec exposures

were obtained at the second. Spectra at the latter dispersion, although covering a substantial fraction of the wavelength range of the CCD, are currently of limited use because of wavelength focal curvature. On the present occasion, the observations at this dispersion were degraded still further by the large hour angle of the telescope (between 4 and 5 hours), resulting in poor alignment of the targets with the fibres due to atmospheric refraction.

So far, reductions have been carried out only for the intermediate dispersion (190 Å/mm) spectra and some examples are given here. These are all taken from a single 1000 sec exposure. Figure 7.3(a) shows the spectrum of one of the candidate VV Cephei systems mentioned earlier, star 78 in the Bohannan and Epps catalogue. These systems comprise a B V star and an M star, the spectrum showing the TiO bands characteristic of the M star, together with H_α emission. In Figure 7.3(b) is the spectrum of an LMC planetary nebula, no. 52 in the list of Sanduleak, MacConnell and Philip (1978; see also Morgan, 1984). This object displays the spectral characteristics (strong [OIII] 4959, 5007 Å emission and no evidence of a continuum) which, together with its starlike appearance, categorize it as a planetary nebula (Sanduleak, 1984). Finally, in Figure 7.4(a) we present the spectrum of HDE 269888, a WC4 star showing the very broad carbon lines characteristic of these objects. The continuum magnitude is 15.7 near 5200 Å, and the FLAIR spectrum may be compared with an AAT spectrum of the same object, shown in Figure 7.4(b). This was obtained with the RGO spectrograph and IPCS under the AAO's service spectroscopy programme; the dispersion (156 Å/mm) is similar to that of the FLAIR spectrum, and it will be seen that the two are in very good agreement. The most noteworthy

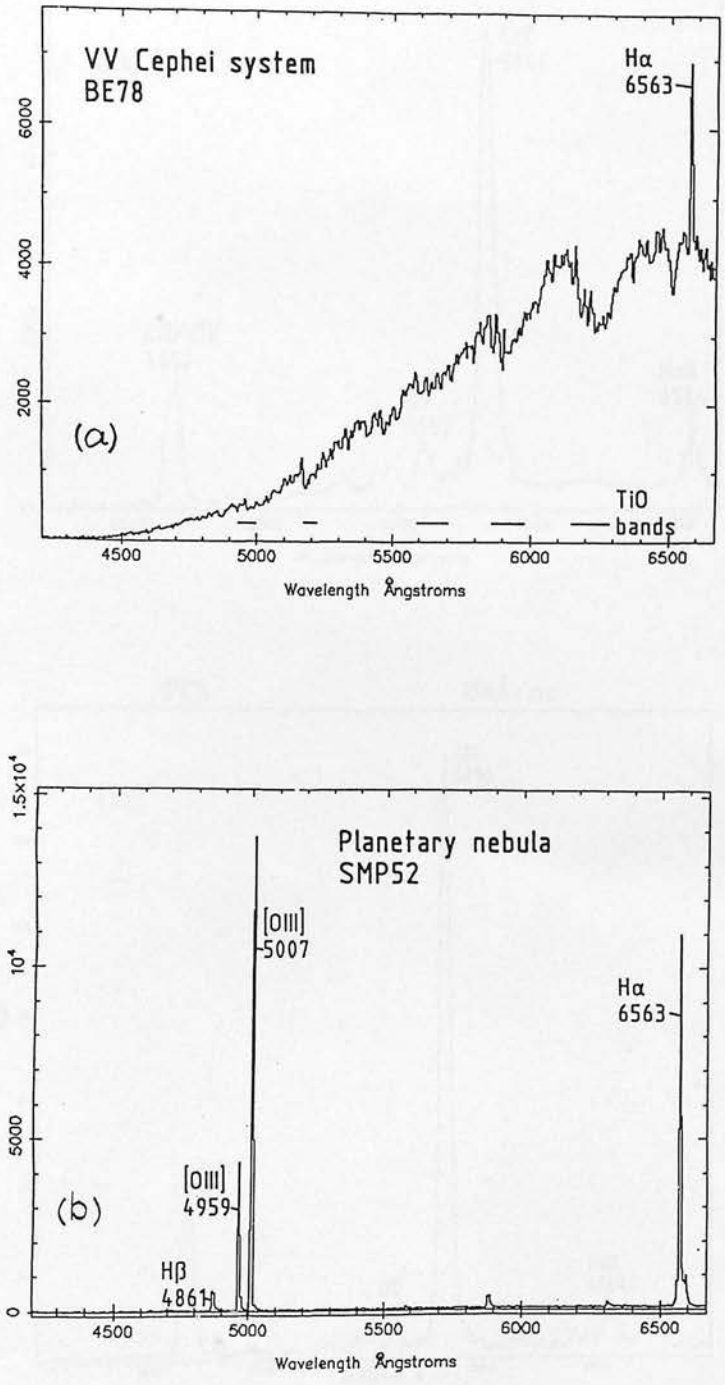

Figure 7.3(a),(b) FLAIR spectra of two objects in the LMC, obtained simultaneously in a single 1000 sec exposure. The reciprocal dispersion is 190 Å/mm (see text).

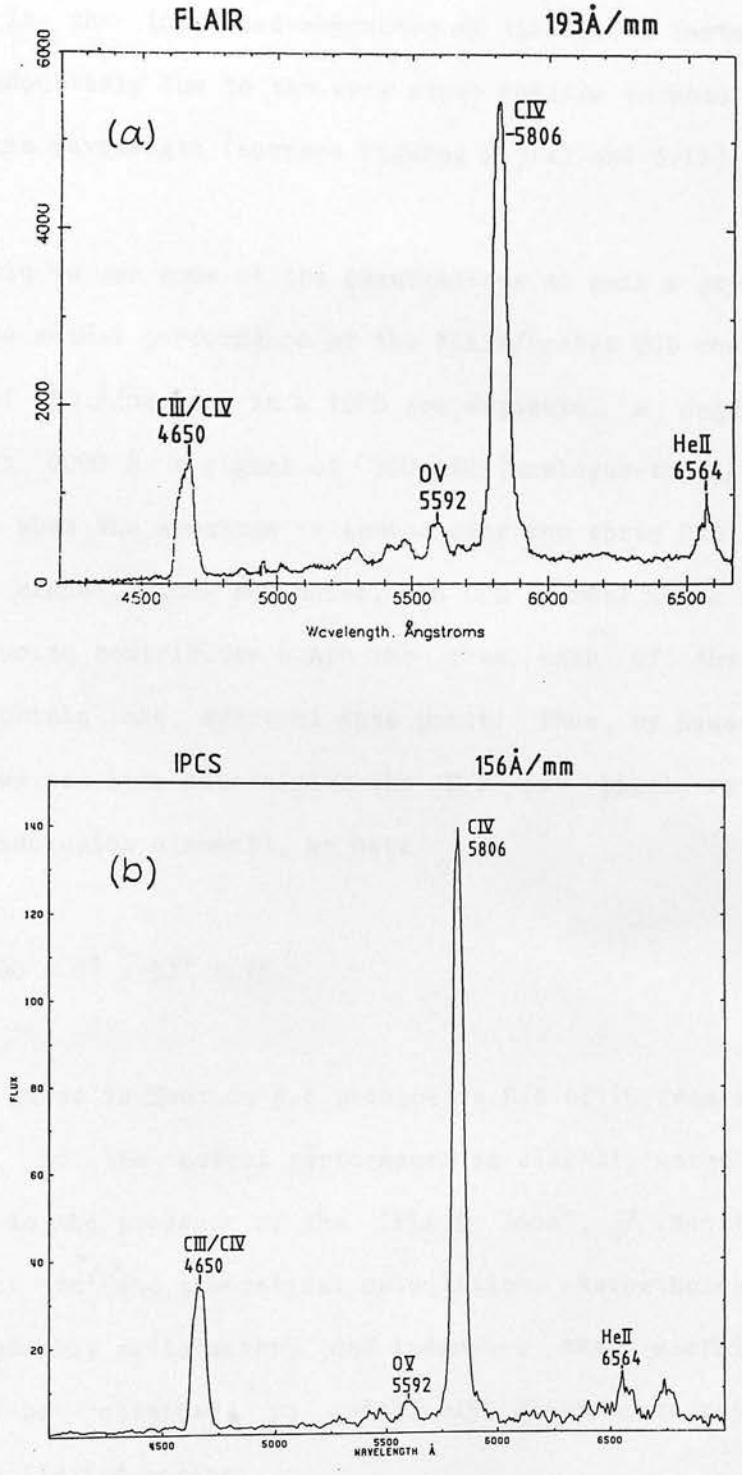

Figure 7.4 Spectra of the LMC Wolf-Rayet star HDE 269888, obtained (a) with FLAIR and (b) with the RGO spectrograph and IPCS on the AAT (see text).

difference is the increased asymmetry of the 4650 Å feature in the FLAIR spectrum, undoubtedly due to the very steep decline in sensitivity of the system at this wavelength (compare Figures 2.3(a) and 3.11).

It is possible to use some of the observations to gain a preliminary estimate of the actual performance of the FLAIR/Durham CCD combination. At a dispersion of 190 Å/mm, and in a 1000 sec exposure, a magnitude 15 star produces, at 6000 Å, a signal of ~300 ADU (analogue-to-digital units) per 4.2 Å pixel, when the spectrum is summed over the three CCD columns that it covers. Sky signal, fibre sky noise, and CCD thermal noise are negligible, but readout noise contributes 6 ADU rms from each of the three pixels summed to obtain one spectral data point. Thus, by Equation 3.18, (but noting that we are here determining the S/N per pixel rather than per wavelength resolution element), we have

$$S/N = 300/(300 + 6^2 \times 3)^{1/2} = 15. \qquad (7.4)$$

The analysis given in Section 3.4 predicts a S/N of 15 from a star of magnitude 15.7, so the actual performance is slightly worse than expected, possibly due to the presence of the "FLAIR loss", $\mathcal{F}$ (Section 6.3), not accounted for in the theoretical calculation. Nevertheless, the performance is reasonably satisfactory, and indicates that useful results are likely to be obtained in relatively short integrations in this readout-noise limited regime.

7.5 Measurement of galaxy redshifts - I

(with T Shanks, A P Oates and D Hale-Sutton, University of Durham)

The importance to studies of galaxies in clusters of the determination of large samples of their redshifts has already been briefly highlighted in this thesis, in Section 4.3. It is towards this area of study that most of the multi-object spectroscopy carried out on galaxies has been directed, largely because of the relatively limited fields of the telescopes used. There is, however, much to be achieved by studies of complete samples of galaxies over larger areas of sky, selected at random and without regard to membership of clusters. The results of this, when combined with photometry, include the determination of the three-dimensional distribution of galaxies (with the possibility of detecting large-scale and previously unknown inhomogeneities); measurement of their peculiar velocities with respect to the Hubble expansion; and the determination of the galaxy luminosity function (Peterson et al., 1986). The attribute of randomness in the selection of the area of sky, combined with that of completeness to some limiting magnitude or redshift, results in a determination of the average properties of galaxies, while the coverage of large spatial scales provides results that may fix the parameters in cosmological models (eg, Shanks, 1985).

Complete redshift surveys to date include the CfA survey mentioned in Chapter 1 (Huchra et al., 1983), which is complete to B=14.5 over much of the northern sky, and the Anglo-Australian Redshift Survey (AARS), being conducted using the AAT (Peterson et al., 1986). The latter is complete in

the survey areas to an isophotal J magnitude limit of ~17.0. The rate of progress of these surveys depends critically on the amount of telescope time available and, clearly, the observing efficiency would be much improved by using multi-object methods. In this regard, a multi-fibre system on the UKST is a very attractive proposition because, while the telescope's modest aperture will result in a fairly bright magnitude limit, the 40 square degree field permits multiplexed observing of galaxies with a number density of ~1 deg^{-2}, (which are, in any case, bright) that have to be observed singly with any other telescope (see Figures 1.3 and 1.7). This was one of the motivations for the development of FLAIR, and was certainly the main reason for the addition of the Durham University CCD camera. Trial observations of galaxies have now been made using FLAIR, and in this section we report on the most recent work. Once again, the reductions are still being undertaken, so that preliminary results are presented.

For these pilot studies, galaxies were observed in fields forming part of the AARS, the selection criteria for which are described in Peterson et al. (1986). The present observations were in Field 197 of the Southern Sky Survey, of which the central 4 deg square (the unvignetted region of the UKST field) had been surveyed for galaxies. One of the immediate drawbacks faced when contemplating a complete redshift survey with FLAIR is the selection criterion imposed by the skeleton mandrel obstruction pattern (see Section 6.3). In practice, this has reduced the number of target galaxies available in a given field, sometimes by almost 60 percent, so that two observations on different field centres would certainly be needed to increase the coverage to acceptable levels. (This situation will be eased with the introduction of the new plateholders 14/6 and 14/7, which

have fewer obstructions.) In the present observing run, 21 AARS galaxies were selected, together with 8 bright galaxies chosen by the writer in the peripheral, vignetted portion of the UKST field. Several more objects (including some of the quasars discussed in Section 7.7) were observed, together with the usual small number (in this case 2) of sky samples for simultaneous sky monitoring.

Observations were made on two nights late in 1986 (November 28/29 and December 2/3) in weather conditions that left a good deal to be desired. Nevertheless, a total integration time of 5x3000 sec was achieved at 98 Å/mm, with a further 2x2100 sec at 373 Å/mm. Normally, the most important spectral lines for use in determining galaxy redshifts are the H and K lines of Ca II, but because of the poor blue transmission of the fibres and the red response of the CCD in the current FLAIR configuration, these are not accessible. Previous experience in attempting to determine galaxy redshifts with FLAIR at 190 Å/mm had indicated that alternatives to these lines further along the spectrum (eg, Mgb, NaD), being narrower, could only be identified with certainty in spectra having extremely high signal-to-noise. The present experiment was therefore principally aimed at the identification of the lines at higher dispersion. (The two integrations at 373 Å/mm were to investigate the usefulness of low-dispersion observations of the quasars in the field; these have not yet been reduced, however).

The five 3000 sec exposures at 98 Å/mm were initially combined by taking median values on a pixel-by-pixel basis, the so-called "median filtering" technique. This method is designed to eliminate the CREs (of which there

are very many in these observations - see Section 3.3.2) and to increase the signal-to-noise in the spectra by averaging. Both these functions are carried out very effectively when the frames to be filtered have identical original signals; however, variations in the strength of the spectra in the present observations (due possibly to intermittent cloud) conspired to produce no significant improvement in signal-to-noise, so the reductions are being repeated using more conventional averaging techniques.

The results obtained so far, while encouraging, are not spectacular, with line identifications being made for 11 of the 29 galaxies observed, most of which were the slightly brighter, non-AARS galaxies near the edge of the field. No emission lines were seen in any of the spectra. Two of the better spectra (from the initial reductions) are shown in Figure 7.5(a) and (b), where it can be seen that the relatively high dispersion broadens the Mgb and NaD lines sufficiently to distinguish them from the noise. (The break in the spectrum in Figure 7.5(a) is a result of patching over the imperfectly-subtracted [OI] 5577 Å night-sky emission line.)

The redshifts, z, obtained from these observations are listed in Table 7.2. The galaxy identifications are from the AARS data in Peterson et al. (1986) for those numbers prefixed GSD; the numbers prefixed F refer to the anonymous galaxies selected by the writer. Only one of these could be identified in the usual catalogues: F7 appears in the Master List of Non-stellar Objects (Dixon and Sonneborn, 1980) as RNGC 692 (Sulentic and Tifft, 1973). The coordinates, isophotal J magnitudes (1) and types of the AARS galaxies are from Peterson et al. (1986); however, the AARS red-

---

(1) These may be converted to approximate total J magnitudes by the sub-

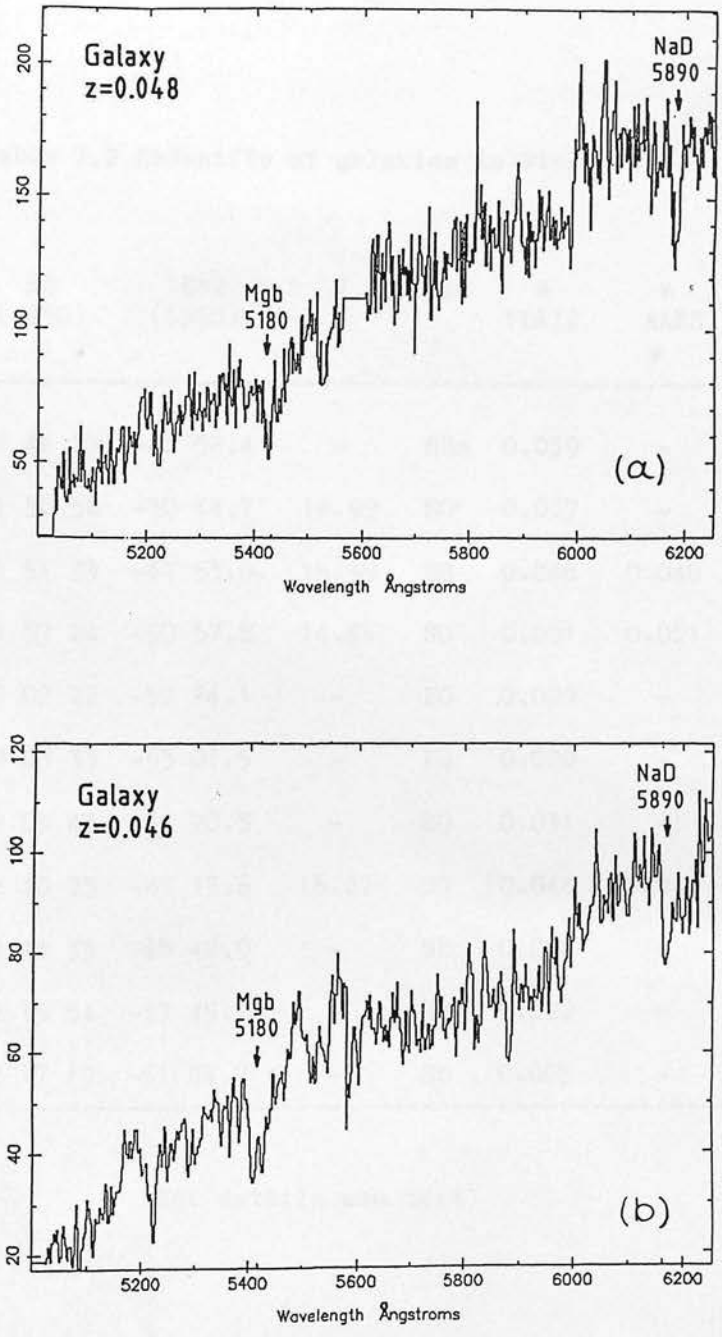

Figure 7.5 FLAIR spectra of two galaxies in the Anglo-Australian Redshift Survey, obtained at 98 Å/mm. Both are S0 galaxies; (a) is GSD012, with an isophotal (photographic) J magnitude of 15.38, and (b) is GSD040, whose isophotal J magnitude is 16.67 (see text).

Table 7.2 Redshifts of galaxies in Field 197

Ident.	RA (1950)	Dec (1950)	J	Type	z FLAIR	z AARS	Line idents.
F4 (RNGC 692)	01 46 22	-48 52.4	-	SBa	0.039	-	Mgb?
GSD055	01 50 56	-50 44.7	16.99	S0	0.067	-	Mgb?
GSD012	01 51 33	-47 53.0	15.38	S0	0.048	0.048	Mgb,NaD
GSD004	01 57 24	-50 57.8	14.45	S0	0.021	0.021	Mgb?,NaD
F8	02 02 22	-52 24.1	-	E0	0.020	-	Mgb,NaD
F1	02 03 33	-53 01.5	-	E0	0.020	-	Mgb,NaD
F3	02 05 43	-52 20.3	-	S0	0.031	-	Mgb?,NaD
GSD040	02 10 33	-49 15.6	16.67	S0	0.046	0.046	Mgb,NaD
F7	02 13 33	-48 42.9	-	Sb	0.066	-	Mgb?
F5	02 15 54	-47 45.2	-	S0	0.022	-	Mgb,NaD
F6	02 17 19	-51 04.7	-	Sb	0.065	-	Mgb?

(For details see text)

shifts quoted have not yet been published. Approximate coordinates and types of the F galaxies are from the Sky Survey plate. The redshifts, z(FLAIR), are from measurements of the individual lines identified in the spectra (last column) rather than from cross-correlation, and no formal errors have been derived. There is clearly very good agreement with the AARS data, where these exist.

Once again, it is possible to make an estimate of the actual performance achieved by calculating the S/N in these observations. In the sum of three 3000 sec exposures, a galaxy with an isophotal J magnitude of ~16 produces ~150 ADU per 2.1 Å pixel at 6000 Å. The total sky contribution for the three exposures is ~100 ADU, and there is a similar contribution from scattered light (2). Again, readout noise contributes 6 ADU rms for each of the three pixels summed to obtain one spectral data point in each 3000 sec exposure. Assuming that 1/k is small for the sky and scattered light signals, we have

$$S/N = 150/(150 + 100 + 100 + 6^2 \times 9)^{1/2} = 6, \qquad (7.5)$$

again by Equation 3.18. Because only a small area of the galaxy is sampled

---

traction of 0.3.

(2) Possible sources of this are scattering at the many cemented surfaces of the spectrograph lenses, and light leaking into the spectrograph enclosure from the dome.

by the 40 μm fibres, its integrated magnitude is of less relevance than the surface brightness, μ, and in the absence of this it is not possible to arrive at an expected value of S/N. However, we may note that the analysis in Section 3.4 predicts a S/N of 6 for an object with $\mu \sim 19.5$ magnitudes arcsec^{-2}, (under the above circumstances and taking into account a FLAIR loss estimated from the previous section), and this value of μ is comparable with expectations.

These observations highlight the limited usefulness of the present FLAIR equipment for large-scale redshift surveys. The 40 μm (2.7 arcsec) fibres sample only a small portion of each of the galaxies being observed, and their diameter might profitably be increased to 60 or even 100 μm (4.0 to 6.7 arcsec). The resulting loss in spectral resolution could be restored by increasing the grating dispersion, placing limiting slits over the fibre outputs, or (the preferred solution) changing the spectrograph magnification. More important, though, is that access to the H and K lines is clearly vital; were there lines of this width in the middle region of the optical spectrum, then almost all the galaxies observed would have yielded redshifts. Thus it appears that serious exploitation of the enormous potential of the UKST for galaxy redshift measurements must await upgrading of the equipment with new, blue-transmitting fibres and a blue-sensitive detector. We will return to these considerations in the last chapter of this thesis.

7.6 Measurement of galaxy redshifts - II

(with B A Peterson and T Mathams, Australian National University)

In addition to the studies reported in the previous section, observations of galaxies have been carried out using FLAIR in conjunction with the ANU's CCD camera (MSSSO, 1986), an "Astromed" system built commercially by C D Mackay at Cambridge. The scientific motivation for this is the same as before, viz, pilot studies for the measurement of complete redshift samples; however, the practical reasons for the experiment were (a) to use a CCD system with some blue sensitivity (the ANU CCD having a dye-coated GEC chip) and (b) to test the feasibility of operating two independent spectrographs and CCD systems simultaneously, using two 40-fibre feeds from a single plateholder.

The ANU system's MicroVAX computer and its peripherals need only a single coaxial cable to communicate with the CCD electronics, so the bulk of the equipment could remain on the UKST's ground floor, and the installation was thus very straightforward. For the experiment, observations of 32 galaxies in a (non-survey) field at RA 3 h 23.5 m, Dec -53 deg 25 min were made on the four nights of 1986 November 3/4 to 6/7, in mostly good conditions. On the first two nights, gratings 600V and 600R were used to produce a reciprocal dispersion of ~190 Å/mm, covering the approximate ranges of 4300 to 6500 Å (for the lines referred to in the last section) and 6700 to 8900 Å (in an attempt to observe the Ca II triplet at 8498-8662 Å). The third night, using 98 Å/mm, covered the same wavelength range as the Durham CCD observations, and on the last night, observations were again made at 373

Å/mm. Substantial exposure times were achieved at all dispersions.

Reduction of these observations is still proceeding, but it appears that the results will be very similar to those reported in the last section, with reliable redshifts being obtained for only a small proportion of the galaxies observed. Despite the improved blue-sensitivity of the CCD, the data were again limited by the blue attenuation of the fibres and their small diameters. The exercise allowed a number of comparisons to be made between the Durham and ANU CCD systems, the most notable of which was the lower CRE rate of the latter, already noted in Section 3.3.2. Finally, it also demonstrated that the logistics of operating two CCD s simultaneously at the UKST would be relatively straightforward, so that the extension of FLAIR to 80 fibres is an entirely feasible proposition.

7.7 Spectroscopy of quasar candidates

(with T Shanks, University of Durham)

We end this chapter with a brief account of experiments in the observation of quasars with FLAIR. Wide-field telescopes in general, and the UKST in particular, have made a major contribution to the identification of quasar candidates using a number of techniques (eg, Warren et al., 1987; see also Savage, 1987), and it is natural to ask whether the follow-up spectroscopy required for confirmation and redshift determination can be carried out with FLAIR. Currently, this work is done on larger telescopes, usually by means of single-object observations, although the AAT's FOCAP multi-fibre system has also been used (eg, Shanks et al., 1986).

It can be seen from Figure 1.5 that the difficulty with this proposal is the low number density of quasars at the magnitudes currently accessible by FLAIR; in particular, the limiting B magnitude of quasars distributed at the "ideal" FLAIR density of 1 deg^{-2} is seen to be ~18.2. While the limiting magnitude of FLAIR at the low dispersion (373 A/mm) adequate for this work has not yet been properly investigated, it may not be as faint as this, so that observations of brighter quasar candidates would have to be incorporated with other object classes requiring similar dispersion in FLAIR runs.

With this in mind, it has been usual to include a small number of quasars or quasar candidates in the target-object lists for FLAIR runs, to investigate the possible value of these observations. The first such experiment took place as long ago as November, 1985, when a magnitude 15.5 (in R) emission-line object designated 0146-487, discovered on a UKST objective-prism plate (Savage, Kalafi and Good, private communication), was included in an early photographic FLAIR frame. The FLAIR spectrum showed H_α and H_β at zero redshift, indicating the object to be an emission-line star - FLAIR's first useful scientific result.

Of the five known quasars (again selected from objective-prism plates) included with the galaxy observations described in Section 7.5, only one (designated QESD06) has yielded a spectrum that has a possible line identification. This is the C IV 1549 Å line, which appears in this spectrum at a redshift of 2.4 (in agreement with the object's known redshift of 2.39). This observation was the result of 15,000 seconds of integration at 98 Å/mm, which produced some 50 ADU in the continuum. However, the quasar

is faint, having V=18.6, so there is some hope that with a more optimal dispersion, successful observations of these targets will be made even with the prototype system.

References for Chapter 7

Ambartsumian VA, Mirzoyan LV, 1975. In Vble Stars and Stellar Ev, Reidel

Barwig H, Schoembs R, Buckenmayer C, 1986. Astron.Astrophys. 175, 327
Baud B et al., 1984. Ap J 278, L53
Bohannan B, Epps HW, 1974. Astron.Astrophys.Supp 18, 47
Breysacher J, 1981. Astron.Astrophys.Supp. 43, 203
Bunclark PS, 1986. SERC Measuring Machines Newsletter No 9, p. 10

Cohen M, 1984. Physics Reports Vol 116 No 4 P. 173

Dixon RS, Sonneborn G, 1980. Master List of Nonst. Objects, Ohio State UP

Elias JH, 1978. Ap J 224, 857

Feigelson ED, 1984. In Cool Stars, Stellar Systems and the Sun, Spr.-Verlag

Gershberg RE, Petrov PP, 1976. Soviet Astronomy Letters Vol 2 No 5 p. 195
Giampapa MS, 1983. In Activity in Red Dwarf Stars (Byrne,Rodono),Reidel
Glass IS, 1979. MNRAS 187, 305
Grasalden G, et al., 1975. AJ 80, 117
Gurzadyan GA,1980. In Flare Stars, Pergamon, Oxford

Haro G, 1964. The Galaxy and the Magellanic Clouds (Kerr,Rodgers), AAS
Haro G, 1968. In Nebulae and Interstellar Matter (Middlehurst,Aller),Chic.
Haro G, 1969. Boletin de Los Observatorios de Tonantzintla y Tacubaya 5,79
Haro G, 1976. Boletin del Instituto de Tonantzintla Vol 2 No 1 p.3
Henize KG, Mendoza EE, 1973. Ap J 180, 115
Huchra J, Davis M, Latham D, Tonry J, 1983. Ap J Supp 52, 89
Hyland AR, Jones TJ, Mitchell RM, 1982. MNRAS 201, 1095

Kunkel WE, 1975. In Variable stars and Stellar Evolution, Reidel

McGraw JT, Cawson MGM, Keane MJ, 1986. Proc SPIE 627, 60
Mendoza EE, 1968. Ap J 151, 977
Mirzoyan LV et al., 1982. Astrophysics Vol 17 No 2 p. 101
Mirzoyan LV et al., 1984. Astrophysics Vol 19 No 4 p. 411
Mirzoyan LV, 1984. Vistas in Astronomy 27, 77
Morgan DH, 1984. MNRAS 213, 491
Mullan DJ, 1977. Solar Physics 54, 183
Mullan DJ, 1985. In Unstable Current Systems and Plasma Instabilities,R'del
Mullan DS, 1979. Ap J 234, 588

Peterson BA, et al., 1986. MNRAS 221, 233

Rydgren AE, 1980. AJ 85, 444

Sanduleak N, 1984. In Struct.and Ev.of Mag.Clouds (IAU Sy.108) p.231, R'del
Sanduleak N, MacConnell DJ, Philip AGD, 1978. PASP 90, 621
Savage A, 1987. UKST Newsletter No. 9 p.11
Schwartz RD, 1977. Ap J Supp 35, 161
Shanks T, 1985. Vistas Astr. 28, 595
Shanks T, Fong R, Boyle BJ, Peterson BA, 1986. In Quasars, p.37 Reidel
Slee OB, Higgins CS, 1971. Australian Jour Physics 24, 247
Slee OB, Higgins CS, Roslund C, Lyngå G, 1969. Nature 224, 1087
Sulentic JW, Tifft WG, 1973. Revised New General Catalogue, Arizona.

Vrba FJ, Rydgren AE, 1984. Ap J 283, 123

Wallace PT, 1985. ASPECT User Manual (Manual No 15) AAO
Warren SJ, et al., 1987. Nature 325, 131
Whittet DCB, KirraneTM,KilkennyD,OatesAP,WatsonFG,KingDJ,1987.MN 224, 497
Worden SP, 1983. In Activity in Red-Dwarf Stars (Byrne, Rodono),Reidel

CHAPTER 8

Conclusion: future prospects for multi-fibre spectroscopy

8.1 Steps towards a fully-optimised FLAIR

We end this thesis with a brief survey of the prospects for multi-fibre spectroscopy in astronomy in the immediate and long-term future. First, we consider the outlook for FLAIR, the UKST's multi-object system that has formed the main topic of the thesis. As we have seen in Chapter 7, the prototype version of this instrument has now been thoroughly tested on a variety of real astronomical problems, and its strengths and weaknesses have been clearly revealed. In its present form, the system is capable of carrying out competetive spectroscopy on stellar targets down to V~16, with an extension of perhaps a magnitude if emission lines are the main spectral features of interest. This relatively modest performance is, of course, rendered much more spectacular by the fact that 40 such targets can be observed simultaneously over a substantial proportion of a 40 square degree field, so that FLAIR is capable of making a real contribution in areas like the study of PMS stars described in Chapter 7. The same holds true for extended objects with emission lines and, although the potential for multi-object work on regions of bright nebulosity is perhaps less than that

for stars, there is still clearly scope for FLAIR to play a useful role. The ability to capitalize further on the very wide field of the system by observing mixed groups of targets, like those in the LMC described in Section 7.4, is additionally useful.

Without question, however, the greatest potential of the UKST/FLAIR combination lies in the possibility of carrying out large-scale redshift surveys of moderately bright galaxies, and, as we have seen in the last chapter, the present system is not well-suited to this. Within the spectral region of greatest sensitivity, the absorption features are not broad enough to be distinguishable in any but very high signal-to-noise, and the surface brightnesses of the target objects are, for the most part, too low for this to be achieved. The prospects are not all gloomy, however, because we have demonstrated that, even with the present equipment, some redshifts can be obtained, and it appears that only relatively minor changes will be enough to make a significant improvement in performance.

These might be regarded as the first steps along the way towards a fully-engineered, optimised FLAIR system that would realise to the full the potential expected from the analyses in Section 1.5 and 3.4. Many changes to the system have been suggested in earlier chapters, but we here present a more complete summary of the various stages of improvement, beginning with those that can be made in the immediate future, and ending with the major engineering projects that will enable the very best use to be made of the telescope's potential. The stages are as follows:

(a) The first priority is the installation of a blue-sensitized GEC chip in

the Durham CCD camera; this is expected to happen in the immediate future, and its performance will be tested using the 10-channel blue-transmitting Spectran fibre feed made for the FLAIR photometry experiment, to obtain low-resolution test spectra of galaxies.

(b) To complement the enhanced blue-sensitivity, a range of blue-transmitting 40-channel fibre feeds should be fabricated. A difficulty with this is that the best blue-transmitting fibres (eg, Polymicro, Spectran) are not usually drawn in sizes less than about 100 μm, so that special orders may have to be placed to obtain fibres with "conventional" (ie, ~3 arcsec) angular diameters. However, as we have seen, there is something to be gained by using larger fibres for bright galaxies, and these, too, should be implemented. Parallel with this should be a further investigation of the cause of the cement-interlayer component of the "FLAIR loss" (Section 6.3) to determine its cause (UV irradiation intensity? Cement age? Emulsion contamination?).

(c) Steps should be taken to reduce the CRE rate in the Durham CCD camera, with possible courses of action including the installation of lead shielding around the cryostat, and the replacement of the cryostat window with a different type of glass.

(d) The foregoing improvements should render the H and K lines of CaII accessible for the routine measurement of galaxy redshifts. However, it is possible that the blue attenuation of the spectrograph's Pentax camera lenses may still prevent this, and it may be necessary to seek UV transmitting optics in the ranges of other manufacturers (eg, Nikon) for use in the

prototype spectrograph while it remains in operation.

(e) The first step towards a "final" system would be the provision of a fully-optimised spectrograph. As we have seen, the prototype, though inexpensive, has a number of drawbacks, notably curvature of the focal surface with wavelength, blue attenuation, and possible scattering at the many cemented surfaces. New designs for the fast spectrograph required, that would eliminate these defects, should be explored, preferably with the collaboration of a specialist optical system designer like C G Wynne. At this stage, it would be necessary to decide on the number of channels to be fed to the spectrograph in the optimal system; whether multiple spectrographs should be used (perhaps fabricated as a "mass-produced" item, suitable for use on other fast telescopes), and whether large-format CCDs should be catered for.

(f) Finally, as we saw in Chapter 1, the large field of the UKST makes it capable of exploiting the use of a very large number of fibres, perhaps as many as 400 (Figure 1.7). For this to be at all practicable, an automatic fibre-positioning system would have to be developed that would overcome the difficulties arising from the telescope's fine plate-scale. Clearly, a system like MX, involving remote postioners inside the telescope, is impractical, and a positioning system of the third class defined in Section 4.3 is much more realistic. At present, the design that seems most likely to succeed is an off-telescope version of AUTOFIB, into which magnetic plateholders, similar in general construction to the present FLAIR series, could be inserted to have their fibres configured, before being loaded into the telescope. The target positioning accuracy of the AAT's AUTOFIB (~25

μm) would need to be improved by a factor of 3-5 for the UKST, but all the signs are that this could be achieved by (i) extremely rigid construction, (ii) operation in a stable environment, and (iii) operation at slower speeds, since the reconfiguration time would not be as imporatant a consideration as it is on the telescope-mounted AUTOFIB. The system would be versatile and, if necessary, could undergo a development period with a smaller number of fibres, since the design of the positioner itself is independent of the number of channels in use. Unlike the present FLAIR system, there would be access to the whole field of the telescope, restricted only by the minimum separation of the fibres. The microengineering of the fibre prism units would be a formidable task, but by no means impossible and, again, mass-production techniques might be employed.

It is likely that a fully-engineered UKST FLAIR system, as broadly outlined in (e) and (f) above, would offer a gain in sensitivity of between one and two magnitudes over the current prototype, and it would have a vastly greater multiplex advantage. The kind of astronomy it could carry out would then include systematic galaxy redshift surveys, and the follow-up work on quasar candidates referred to in Section 7.7, as well as galactic studies of the kind that FLAIR is already capable of. Perhaps its greatest contribution, though, would be in the development of technology and techniques for the bigger, wide-field multi-fibre telescopes, whose construction, as we shall see, may be imminent.

8.2 New instrumentation for multi-fibre spectroscopy

We have already mentioned, at the end of Section 3.1.3, some of the new large telescopes that may incorporate fibre couplers into their design. The increased awareness of the possibilities of fibres, together with the more general appreciation of the efficiency of wide-field observations, as originally demonstrated by Fellgett (1970), has led to some quite radical thinking, such as the use of individual fibre input correctors for use in a telescope with a single large spherical mirror (Angel, 1982). Such systems have the potential to be extended to very large apertures (~ 20 m), but it appears likely that resources for telescopes of this size would be more likely to be directed towards more conventional, narrow field instruments with good-quality imaging capabilities, as well as the potential for carrying out spectroscopy on very faint objects.

New wide-field telescopes, too, are likely to remain of more conventional design so as to be able to undertake the survey-imaging role in which the Palomar and UK Schmidt telescopes have been so spectacularly successful over the last three decades. Two events that have brought the possibility of such a telescope much closer to reality are (i) the development of the three-mirror design by Willstrop (1984, 1987), and (ii) the development of techniques for the manufacture of borosilicate glass mirrors of ~8 m diameter by Angel et al. (1982). The procurement of a large, wide-field telescope, possibly a 5-metre Willstrop, is now highlighted by the Royal Astronomical Society as the highest-priority new project for UK ground-based astronony (RAS, 1986). At an estimated cost of £20M, the new telescope would incorporate photographic and CCD (drift-scan) imaging, as

well as a multi-fibre capability with a multiplex advantage of ~1000. We have seen, in earlier chapters, how the Willstrop design is well-suited to multi-fibre work; its implementation would be further assisted by experience gained with the fully-engineered FLAIR system described in the last section.

Other developments, besides the procurement of new telescopes, are likely to influence progress in the instrumental aspects of astronomical multi-fibre spectroscopy. It was mentioned in Chapter 2 that the trend in fibre development for the communications industry is towards longer wavelengths using new materials. In particular, experiments with fluoride glasses have produced low attenuations of 0.1 dB/km at 2.5 μm and 0.3 dB/km at 3.6 μm, and there is potential for losses as low as 0.01 dB/km at 4.4 μm (Aggarwal, 1982). These wavelengths are similar to those of atmospheric transmission windows in the near infrared (ROE, 1985) and, given the recent deployment of 2-dimensional detectors sensitive in the 1-5 μm region (McLean, 1987), it is possible to imagine, in principle, at least, the use of fibres for multi-object near-infrared spectroscopy using a cooled-grating system (eg, Wade, 1983; Mountain et al., 1983). The practicality of such a scheme would clearly depend on the number density of suitable sources and the field size of the telescopes used; it would also probably rely heavily on the multi-fibre beamswitching technique mentioned in Chapter 5 (Footnote 3) for background subtraction.

Returning to optical wavelengths, the developments in multi-fibre photometry reported in Sections 4.4 and 7.3, may, as we have seen, have significant astronomical applications, particularly when a wide-field tele-

scope is available. The use of a dispersing element to provide simultaneous multi-colour measurements has been described by Baruch et al. (1986) and Barwig, Schoembs and Buckenmayer (1987), the former using a grating to disperse images of the fibre outputs onto a CCD, and the latter using a prism with fibre-coupled photomultiplier tubes. It appears, however, that the use of avalanche photodiodes (eg, Personick, 1977) might be more suitable when large numbers of object fibre channels (each of which feeds several colour channels) are used. These devices have the sensitivity and large band-width required for astronomical observation. Furthermore, new waveguide devices that might be referred to as "spectrographs on a chip" are now being developed for wavelength-division multiplexing in communications systems (Tomlinson, 1977). These have the required characteristics for low-resolution spectrophotometry (albeit in astronomically unconventional wavebands), converting a single fibre input to a multi-colour, multi-fibre output (Suhara, Viljanen and Leppihalme, 1982; Fujii and Minowa, 1983). The devices have dimensions of a few mm, and their fabrication, like that of avalanche photodiodes, will eventually be sufficiently inexpensive that large numbers could be employed in multi-object spectroscopy systems. The confinement of light from the target objects within a waveguide, from its entry into the fibre feed in the telescope to the point at which it is detected, is a particularly attractive proposition, resulting in low losses and extreme convenience in use.

Following on from this, we may note, in conclusion, that the electro-optics and communications industries are currently in a particularly volatile state, with integrated systems and non-linear devices receiving much attention, and optical computing apparently just around the corner. It is

always possible that some of the exotic products of these industries will turn out to have surprising applications in astronomy - in exactly the same way as fibres have done.

8.3 The astronomical outlook

At the outset of this thesis, we presented a detailed evaluation of the prospects for multi-fibre spectroscopy, given the distribution of number densities of astrophysically-important classes of objects, and the field sizes of available telescopes. The prognosis was good, and we have seen in Chapters 4, 5 and 7 how the technique has been applied to real astronomical problems, and has, generally speaking, met with success. Most of its shortcomings can be remedied with further technological development, and there seems little doubt that it is a technique that is here to stay.

If the new, wide-field, 1000-fibre survey telescopes that we have discussed do, in fact, materialize, there will be an explosion of spectroscopic data that would have seemed inconceivable to most of those astronomers whose work appears in Table 1.1. Studies of the history and large-scale structure of the Universe *via* the spectra of quasars and galaxies will be advanced by access to a very large data set, permitting detailed statistical investigations to be carried out. Studies of the evolution of clusters of galaxies will be similarly aided, and for galaxies nearer than the Virgo cluster, there is a possibility of obtaining data on statistically significant samples of their own populations - globular clusters, H II regions, planetary nebulae and stars. In studies of our own Galaxy, it will be possible to undertake programmes investigating the detailed element abundances

of stars and star-clusters of different ages, and our understanding of the local and large-scale kinematics of the Galaxy will be much enhanced.

Access to such data could transform our view of the Universe in almost as big a way as that predicted at the outset for the Hubble Space Telescope (Longair, 1982). It is possible that we stand on the brink of changes in our understanding of nature as great as any in the long history of science.

References for Chapter 8

Aggarwal ID, 1982. Laser Focus, November issue, p.115
Angel JRP, 1982. In Inst.for Ast.with Large Opt.Tels., p.117, Reidel
Angel JRP, et al., 1982. In Inst.for Ast.with Large Opt.Tels. p.33, Reidel

Baruch JEF et al., 1986. Internal Report, University of Leeds
Barwig H, Schoembs R, Buckenmayer C, 1987. Astr.Astrophys. 175, 327

Fellgett PB, 1970. In Opt.Insts.and Techniques, p.475, Oriel, Newcastle
Fujii Y, Minowa J, 1983. Applied Optics 22, 974

Longair MS, 1982. In Space Telescope Observatory, NASA CP-2244, p.121

McLean I, 1987. UKIRT Newsletter No 15
Mountain CM, Bingham RG, Sanchez-Magro C, Selby MJ, 1983. Proc SPIE 445, 93

Personick SD, 1977. Proc IEEE 65, 1670

RAS, 1986. Report on the Sci. Priorities for UK Ast.Res. for 1990-2000
Royal Observatory Edinburgh (ROE), 1985. Research and Facilities, p.57

Suhara T, Viljanen J, Leppihalme M, 1982. Applied Optics 21, 2195

Tomlinson WJ, 1977. Applied Optics 16, 2180

Wade R, 1983. Proc SPIE 445 (Inst.in Astr.V), p.47
Willstrop RV, 1984. MNRAS 210, 597
Willstrop RV, 1987. MNRAS 225, 187

List of abbreviations and acronyms

AAO	Anglo-Australian Observatory
AARS	Anglo-Australian Redshift Survey
AAS	Australian Academy of Science
AAT	Anglo-Australian Telescope
ADC	atmospheric dispersion compensator
ADU	analogue-to-digital unit
ANU	Australian National University
APM	Cambridge automatic plate measuring machine
ARC2	2-dimensional wavelength-calibration routine in SPICA
AS	all-silica (fibre)
ASPECT	area spectroscopy software package for IPCS
AUTOFIB	Durham University/AAO automatic fibre positioning system
AWA	Amalgamated Wireless of Australia
bpi	bits per inch (tape density)
BS	Bright Star Catalogue
CCD	charge-coupled device
CES	coudé echelle spectrograph
CfA	Harvard-Smithsonian Center for Astrophysics
CFHT	Canada-France-Hawaii Telescope
COSMOS	ROE high-speed automatic measuring machine (Coordinates, Sizes, Magnitudes, Orientations, Shapes)
CRE	cosmic-ray event
CTIO	Cerro-Tololo Inter-American Observatory
CVD	chemical vapour deposition
DIC	depressed-index cladding
DQE	detective quantum efficiency
DSCL	Starlink image-processing package
DUSDERS	Durham University spectral data reduction package
ESO	European Southern Observatory
FIS	fibre image-slicer
FLAIR	fibre-linked array-image reformatter
FLOAT	fibre-linked optical array telescope
FOCAP	fibre-optic coupled aperture plate

FORS	faint-object red spectrograph
FRD	focal-ratio degradation
FWHM	full-width at half-maximum
GCVS	General Catalogue of Variable Stars
GRIN	graded refractive-index (lenses)
HD	Henry Draper Catalogue
HST	Hubble Space Telescope
IEEE	Institute of Electrical and Electronics Engineers
INT	Issac Newton Telescope
IPCS	Image Photon Counting System
ISEC	intensified SEC
ISIS	WHT triple spectrograph
ISIT	intensified SIT
JKT	Jacob Kapteyn Telescope
KPNO	Kitt Peak National Observatory
LDSS	Low-Dispersion Survey Spectrograph
LMC	Large Magellanic Cloud
LSR	local standard of rest
MAT	Multi-Aperture Telescope
MK	Morgan-Keenan spectral classification system
MSSSO	Mount Stromlo and Siding Spring Observatories
MTF	modulation transfer function
MX	Steward Observatory automatic fibre positioning system
NA	numerical aperture
ND	neutral density (filter)
NGC	New General Catalogue
NNTT	National New Technology Telescope
NOAO	National Optical Astronomical Observatories
OPTOPUS	ESO multi-fibre spectroscopy system
PATT	Panel for the Allocation of Telescope Time
PCS	polymer-clad silica
PDS	photometric data system
PMS	pre-main sequence
RA	right ascension
RAS	Royal Astronomical Society
RCA	Radio Corporation of America
RGO	Royal Greenwich Observatory
rms	root mean square
RNGC	Revised New General Catalogue
ROE	Royal Observatory, Edinburgh
RPCS	Reticon Photon-Counting System
SAAO	South African Astronomical Observatory

SAO	Smithsonian Astrophysical Observatory (Catalogue)
SEC	secondary electron conduction
SERC	Science and Engineering Research Council
SDRSYS	scanner data reduction system
SIT	silicon intensified target
SLR	single lens reflex (35mm camera)
SMC	Small Magellanic Cloud
SPICA	Starlink spectral data reduction package
SPIE	Society of Photo-Optical Instrumentation Engineers
TAURUS	Imaging Fabry-Perot spectrometer (Taylor-Atherton Uariable-resolution Radial Uelocity System!)
UKIRT	United Kingdom Infra-Red Telescope
UKST	United Kingdom Schmidt Telescope
UKSTU	UK Schmidt Telescope Unit
UVX	ultraviolet excess
VPO	vapour-phase oxidation
WHT	William Herschel Telescope
XCORR	Cross-correlation routine in SPICA

Glossary of symbols

(The section in which each definition appears is given in parentheses)

a	aperture of a telescope (1.4)
a	radial coordinate on input end of a fibre (2.2)
a,b	constants in sinusoidal intensity function (3.3.1)
a,b	constants in diode law (3.3.2)
a(r)	absorption along the line of sight (1.3.1)
A	Oort's constant of galactic rotation (1.3.2)
A	attenuation of a fibre (dB) (2.1)
A	area of a general optical element (2.3) or telescope primary, excluding central obstruction (3.4)
A_t	area of telescope primary (2.3)
A'	unit length attenuation of a fibre (dB/km) (2.3)
A,B	signal in channels A,B of a detector system (5A)
A(m,C)	differential number density of objects C (1.3.1)
A(V)	absorption in the V band (7.1)
$\mathbb{A}$	atmospheric transmission (3.4)
b	beam inclination (3.1.2)
B	apparent magnitude in the B (blue) band (1.3.2)
B	beam coupling efficiency (2.4)
B_i	input beam coupling efficiency (3.4)
B_o	output beam coupling efficiency (3.4)
B'	limiting B magnitude (1.5)
C	class of objects (1.3.1)
d	groove spacing of a grating (3A)
d^{-1}	reciprocal spacing (grooves/mm) (3A)
d_{cam}	grating-camera distance (3.2.2)
d_{coll}	collimator-grating distance (3.2.2)
$d\beta/d\alpha$	slit projection factor (3A)
$d\beta/d\lambda$	angular dispersion (3A)
$d\beta/dm'$	angular separation of minima (3A)
$d\lambda/dx$	reciprocal linear dispersion of a spectrograph (3A)
$d\lambda_f$	projected equivalent width of a fibre (3.2.2)
$d\lambda_f/d\lambda_p$	sampling interval of detector (3.2.2)
$d\lambda_p$	equivalent width of a detector pixel (3.2.2)
D	photographic density (1.4)
D	loss due to focal ratio degradation (2.3)
D_{cam}	camera pupil diameter (3.2.2)

D_{coll}	collimator pupil diameter (3.2.2)
D_{grat}	height of grating (3.2.2)
D(r,C)	relative density function of objects C (1.3.1)
D(z,C)	vertical density function of objects C (1.3.2)
e	polar-axis elevation for correction of rotation due to atmospheric refraction (3.1.2)
e	fibre positioning or alignment error (3.4)
E	entrance coupling efficiency (2.4)
E_A, E_B	total efficiencies of channels A,B of a detector system (5A)
E(B-V)	colour excess (7.1)
$\mathbb{E}$	overall optical efficiency (3.4)
f_{cam}	camera focal length (3.2.2)
f_{coll}	collimator focal length (3.2.2)
$\mathcal{f}$	focal ratio of beam from fibre (3.2.2)
$\mathcal{f}_c$	collimator focal ratio (3.4)
$\mathcal{f}_T$	telescope beam focal ratio (3.4)
F	area of field of a telescope (1.3.1)
F	flux density of a discrete source (3.4)
$\mathcal{F}$	"FLAIR loss" at cemented fibre input face (6.3)
$\mathbb{F}$	fibre feed overall efficiency (3.4)
G	grating optical efficiency (3.2.1)
h	half-width of a slit (2.5)
(h,δ)	hour angle and declination on the sky (3.1.2)
H_o	Hubble constant (1.2)
i	number of objects observed with a multi-object system (1.4)
i	electrical dark current in a CCD (3.3.2)
I	apparent magnitude in the I (near infrared) band (1.3.2)
I	intensity in an image (2.4), in a sinusoidal intensity pattern (3.3.1) or of an extended source (3.4)
j	number of channels in a multi-object system (1.4)
J	apparent magnitude in the photographic J (blue-green) band, defined by IIIa-J emulsion and GG395 filter (1.3.2)
J	light-loss due to placing a slit over a fibre (2.5)
(J,H,K)	apparent magnitudes in the infrared J,H and K bands (7.1)
k	constant of proportionality in total image intensity (2.4)
k	Boltzmann's constant (3.3.2)
k	number of sky fibres (3.4)
l	length of a fibre (km) (2.3)
l_D	modal-diffusion length in a fibre (2.2)
(l,b)	galactic longitude and latitude (1.3.1)
L	luminosity of a spectrometer (3.2.1)
L'	separation of telescopic images on the back of the plate (6A)
L,l	separation of images on a plate before and after curvature reversal (6A)
m	apparent magnitude (1.3.1)

m	order of diffraction (3A)
m'	limiting magnitude of a telescope (1.5)
m'	order of minima in grating intensity pattern (3A)
m_{pg}	photographic apparent magnitude (1.3.2)
$\bar{m}_{pg}$	mean photographic magnitude (5.1)
m_{vis}	visual apparent magnitude (1.3.2)
m	dummy variable magnitude (1.3.1)
M	absolute magnitude (1.3.1)
M	magnification of a spectrograph (3.2.2)
M	modulation of a sinusoidal intensity function (3.3.1)
M_B	absolute magnitude in the B (blue) band (1.3.2)
M_R	absolute magnitude in the R (red) band (1.3.2)
M_V	absolute magnitude in the V (visual) band (1.3.3)
n	number of readouts of a CCD (3.4)
n_D	refractive index at wavelength of sodium D-lines (2.2)
n_0	refractive index of space containing fibre (2.2)
n_1	refractive index of fibre core (2.2)
n_2	refractive index of fibre cladding (2.2)
N	number of lines in a grating (3A)
NA	numerical aperture of an optical system (2.2)
N(m,C)	integrated number density of objects C (1.3.1)
p	packing fraction (2.1)
p	area of fibre output face projected through spectrograph, in pixels (3.4)
P_i	input optical power (2.1)
P_o	output optical power (2.1)
q	responsive quantum efficiency of a detector (3.3.1)
q_o	cosmological deceleration parameter (1.2)
q_D	detective quantum efficiency of a detector (3.3.1)
Q_S	optical efficiency of a spectrometer (3.2.1)
Q_T	optical efficiency of telescope (3.1.1)
r	heliocentric distance (1.3.1)
r	radius of fibre core (2.2)
r	readout noise in a CCD (3.3.2)
(r,θ)	polar coordinates (4.3)
R	apparent magnitude in the R (red) band (1.3.2)
R	radius of a bend in a fibre (2.2)
R	radius of curvature of focal surface (3.1.2)
R	resolving power of a grating (3A)
R	required signal in a detector system (5A)
R	ratio of total-to-selective absorption (7.1)
R_F	fraction of incident light which undergoes Fresnel reflection (2.3)
R_o	Sun's distance from the galactic centre (5.1)
s	angle subtended by fibre radius on the sky (2.4)
S	scattering loss at fibre face (2.3)
S_i/N_i	signal-to-noise ratio of input signal (3.3.1)
S_o	signal at detector produced by integrated object flux (3.4)
S_o/N_o	signal-to-noise ratio of output signal (3.3.1)
S_S	signal at detector produced by integrated sky flux (3.4)

$\mathbb{S}$	spectrograph transmission (3.4)
t	temperature of a CCD (3.3.2) or ambient temperature (3.4)
t	exposure time (3.4)
t	thickness of a plate (6A)
T	transmission of plate (1.4) or fibre (2.3)
$\mathbb{T}$	telescope transmission (3.4)
$\mathfrak{T}$	time in a long-term process (3.4)
U	apparent magnitude in the U (ultraviolet) band (7.1)
V	space volume (1.3.1)
V	apparent magnitude in the V (visual) band (1.3.3)
V	vignetting efficiency (= 1-vignetting loss) (3.1.2)
x,y	coordinates in direction of dispersion and vertical direction in a spectrograph (1.4)
(x,y)	Cartesian coordinates (4.5)
(x',y')	physical dimensions of a detector (3.2.2)
z	distance above galactic plane (1.3.2)
z	radial distance in a Gaussian, in units of σ (2.4)
z	pixel size (3.2.2)
z	redshift (7.5)
Z	Meaburn's figure of merit for spectrometers (3.2.1)
α	effective aperture of a telescope (1.5)
α	angular distance from field centre (3.1.2)
α	linear thermal expansion coefficient (3.1.2)
α	angle of incidence (3A)
β	angle of diffraction (3A)
β'	angle of diffraction at edge of camera field (3A)
$\beta(C)$	scale height above galactic plane of objects C (1.3.2)
γ	contrast of a photographic emulsion (3.3.2)
δ	half (angular) field of spectrograph collimator (3.2.2)
$\Delta\lambda$	wavelength range (3.4) or separation (6.4)
Δm	magnitude loss (3.1.2)
Δm_{pg}	amplitude of RR Lyrae photographic light curve (5.3)
ΔS	Preston's metallicity index for RR Lyrae stars
Δt	temperature difference (3.1.2)
Δv	amplitude of RR Lyrae velocity curve (5.3)
ϵ	half (angular) field of spectrograph camera (3A)
ϵ_x	angular half-field of spectrograph camera in x direction (3.2.2)
ϵ_y	angular half-field of spectrograph camera in y direction (3.2.2)
ζ	angular radius of a target object (3.4)
θ	blaze angle (3A)
θ_o	angle of incidence of light entering a fibre (2.2)

θ_1 angle of refraction of light entering a fibre (2.2)

λ wavelength (1.4)
λ' wavelength at edge of camera field (3A)
λ_E first-order Ebert blaze wavelength (3A)
λ_L first-order Littrow blaze wavelength (3A)

μ apparent surface brightness of an extended object (mag arcsec^{-2})(2.4)

ν spatial frequency of a sinusoidal intensity function (3.3.1)
$\nu(r,M,C)$ space density of objects C (1.3.1)

(ξ,η) standard coordinates in the field of a telescope (3.1.2)

Π plate-scale of a telescope (2.4)
Π_o radial velocity of the LSR in a galactocentric cylindrical coordinate system (5.1)

ρ radial coordinate on output end of a fibre (2.2)
ρ reflectance of a surface (3.1.1)
ρ radial velocity of a star (5.4)

σ standard deviation (2.4)
σ spacing of fibres along the slit (3.2.2)
σ velocity dispersion (5.4)
σ_f fibre sky-subtraction noise (3.4)
$\Sigma(C)$ surface density of objects C (1.3.2)

τ transmittance of a surface (3.1.1)

ϕ critical angle of fibre core-cladding interface (2.2)
ϕ angular separation of collimator and camera axes (3A)
$\phi(M,C)$ luminosity function of objects C (1.3.1)
Φ_E flux received at detector from an extended object (3.4)
Φ_P flux received at detector from a point source (3.4)

ω solid angle (1.3.1)
Ω solid angle of beam accepted by detector (2.3)
Ω solid angle on sky subtended by fibre entrance face (3.4)
Ω_S solid angle on sky of light accepted by a spectrograph (2.3)